TECHNISCHE UNIVERSITÄT MÜNCHEN

TUM School of Engineering and Design

Test-Based Controller Parameter Retuning Using Non-Parametric Frequency Domain Methods

Agnes Christine Steinert, Dipl.-Ing. Univ.

Vollständiger Abdruck der von der TUM School of Engineering and Design der Technischen Universität München zur Erlangung des akademischen Grades einer

Doktorin der Ingenieurwissenschaften

genehmigten Dissertation.

Vorsitzender:	Prof. Dr.-Ing. Oskar J. Haidn
Prüfer der Dissertation:	1. Prof. Dr.-Ing. Florian Holzapfel
	2. Assoc. Prof. Peter Chudý, Ph.D.

Die Dissertation wurde am 30.09.2021 bei der Technischen Universität München eingereicht und durch die TUM School of Engineering and Design am 13.01.2022 angenommen.

Abstract

In today's engineering applications many controllers are still realized as linear multi-variable control laws. The parameters of the linear control law – the controller gains - are often designed based on linear models of the system using classical methods from linear system theory. High fidelity models are often not available or are subject to considerable model uncertainties, due to cost and time constraints. These controllers typically suffer from performance deficits or do not satisfy their initial requirements when applied to a real-world system environment during trails. The reasons are considerable deviations between the real plant dynamics and the models applied during controller design and assessment.

With respect to these uncertainties, different robust control design approaches exist, which synthesize controllers that exhibit high robustness and satisfactory performance despite expected uncertainties. With this approach, controller parameters are chosen to meet the design objectives for all a priori assumed uncertainties. This is often time intense and requires a trade-off between safety (i.e. robustness) and other control objectives like performance, especially when the model parameters are very uncertain. Furthermore, the design is not perfectly laid-out for the actual real plant dynamics.

To improve the performance of a linear controller on the true system, this thesis presents a novel methodology towards a clear, systematic, data-driven tuning process of controller parameters, based on real measurement data from tests under closed-loop conditions. The advantage of our approach is its non-parametric nature, i.e. it does not rely on a parametrized plant model. This allows to take into account the true order of the system in contrast to parametrized plant models, which approximate the true system typically with a low order simulation model. Consequently, these models are lacking information about higher order dynamics, for example aeroelastic modes, actuator or sensor dynamics, that might be present in the experiment data. Using non-parametric representations, this information can be retained.

The proposed optimization problem imposes the relevant design criteria by minimizing the deviation between the desired closed-loop frequency response and the anticipated tuned closed-loop behavior for a new set of controller parameters in the frequency domain. The deviation is quantified by a metric, considering a weighted squared error in magnitude and phase of the respective frequency responses. Furthermore, we propose a regularization by adding a penalization term, constraining the tuned gains to reasonable bounds around

the initial gains. Finally, stability criteria are enforced by supplementary constraints.
In addition, we propose a method to calculate the non-parametric, anticipated, tuned closed-loop frequency response, for an updated set of controller parameters. This method is based on closed-loop experiments, with an initial controller and the assumption that it is linear and exactly known.
For a single-input-single-output closed-loop system (with a linear controller, error feedback and feed-forward) an analytical expression for the bias between the anticipated and true updated closed-loop frequency response has been derived. We show that the bias is small for small changes in the feedback controller, large initial feed-forward gains or large signal-to-noise ratios.
The controller parameter retuning is demonstrated for a longitudinal baseline controller on a real flexible large aircraft. The longitudinal baseline controller is part of a modular flight control system and was flight tested on four different CS-23 aircraft. The retuning process is analyzed via Monte Carlo simulations on a high-fidelity, six degrees of freedom simulation environment. The simulation also includes real world effects like noise, structural and aeroelastic modes, backlash and light turbulence. Finally, the test-based retuning concept is successfully demonstrated with real flight tests.

Zusammenfassung

In den meisten realen Anwendungen der Regelungstechnik werden die Regler als lineare, multivariable Strukturen umgesetzt. Die Parameter dieser linearen Regelgesetze werden dabei auf Basis von linearen Modellen der realen Systeme, unter Verwendung klassischer Methoden aus der linearen Regelungstheorie, ausgelegt. Hochpräzise Systemmodelle sind oft nicht Verfügbar oder unterliegen signifikanten Modelungenauigkeiten, um den Kosten- und Zeitrahmen im Projektgeschäft einzuhalten. Die daraus hervorgehenden, ausgelegten Regler leiden typischerweise unter Performanzdefiziten oder erfüllen die an sie gestellten Anforderungen nicht, wenn sie während der Erprobung den realen Umgebungsbedingungen und Systemverhalten ausgesetzt werden. Dies begründet sich in den beträchtlichen Abweichungen zwischen der realen Streckendynamik und den Modellen, die während der Auslegung und Verifikation verwendet wurden. Um die Unsicherheiten bereits bei der Auslegung zu berücksichtigen, existieren verschiedene robuste Regelungsauslegungsverfahren, die einen hohen Grad an Robustheit gegenüber Modellunsicherheiten aufweisen und zufriedenstellende Performanz bieten. Nichtsdestotrotz verlangen diese Verfahren zumeist einen Kompromiss zwischen Sicherheit (Robustheit) und anderen Regelungszielen (insbesondere der Performanz). Gerade bei großen Modellunsicherheiten führt dies zu schlecht ausgelegten Regelstrecken die weit hinter den Möglichkeiten eines ideal für das reale System abgestimmten Reglers zurückbleiben.
Diese Arbeit stellt eine neue Methode für die systematische, auf Messdaten basierende Reglerauslegung vor, um basierend auf Experimenten mit dem geschlossenen Regelkreis die Reglerparameter zu optimieren. Der Ansatz ist nichtparametrisch, d.h. er ist unabhängig von der Identifikation eines parametrisierten Streckenmodells. Hierdurch wird die tatsächliche Ordnung der realen Stecke berücksichtigt, im Gegensatz zu Ersatzmodellen, die bei parametrischen Methoden zum Einsatz kommen, und von niedrigerer Ordnung sind. Dort führt die Reduktion zu einem Informationsverlust von Systemcharakteristika, z.B. Aeroelastische Modi, Aktuator oder Sensordynamik, die jedoch in den Messdaten der Tests enthalten sind und daher durch den nichtparametrischen Ansatz erhalten werden können.
Für die neue Methode wird ein Optimierungsproblem formuliert, dass die relevanten Auslegungskriterien durch die Minimierung der Abweichung zwischen dem gewünschten Verhalten und dem erwarteten, optimierten Verhalten des geschlossenen Regelkreises im Frequenzbereich erreicht und neue Reglerparameter ermittelt. Es wird durch eine Metrik

quantifiziert, die auf dem gewichteten, quadrierten Fehler der Amplitude und Phase der jeweiligen Frequenzantworten basiert. Ein zusätzlicher Regularisierungsterm begrenzt die Reglerparameter während der Optimierung auf sinnvolle Bereiche. Ebenso werden Stabilitätskriterien durch zusätzliche Contraints eingehalten.
Zudem wird eine Methode vorgestellt, um die nichtparametrische Frequenzantwort des geschlossenen, neu-parametrierten Regelkreises zu schätzen. Die Abschätzung erfolgt auf Basis von Testdaten des geschlossenen Kreises und eines initialen Reglerparameter-Satzes unter der Annahme, dass der Regler bekannt und linear ist. Durch eine analytische Herleitung wird gezeigt, dass der Bias zwischen der geschätzten und der tatsächlichen Frequenzantwort unter gewissen Randbedingungen klein ist.
Alle Verfahren werden an einem Basisregler für die Längsdynamik eines aeroelastischen Flugzeuges mit großer Streckung demonstriert und im realen Flugversuch erprobt. Der Basisregler, als Komponente eines modularen Flugsteuerungssystems, wurde in vier verschiedenen CS-23 Luftfahrzeugen erfolgreich Testflügen unterzogen.
Die Simulationen zur Demonstration der Methoden wird an verschiedenen 6-Freiheitsgraden-Simulationsmodellen mit diversen Störeffekten (Strukturschwingungen, Sensorrauschen, Aktuatorspiel, etc.) durchgeführt.

Acknowledgemets

This work is the result of one interesting challenge during my employment at the Institute of Flight System Dynamic of the Technical University of Munich. Therefore, I would first like to thank Prof. Dr.-Ing. Florian Holzapfel for the opportunity to work at his institute on a variety of immensely interesting and challenging topics and research projects, in a highly motivating, open-minded and inspiring atmosphere. I also want to thank him for his technical inputs and exceptional support in all my concerns - technical or personal nature. Especially, I want to credit his efforts for making the compatibility between family and career possible, and enabling his employees to succeed in mastering both.
Furthermore, I would like to thank Prof. Dr.-Ing. Oskar J. Haidn for chairing the thesis committee and Assoc. Prof. doc. Ing. Peter Chudý, Ph.D., MBA for being the second examiner and reviewing this thesis.
I also want to express my thanks to Moritz Speckmaier and Daniel Gierszewski who devoted their time to perform the flight tests, whose results round up the thesis and provided a couple of insights. Without their commitment and the kind support of Grob Aircraft SE this would have not been possible. Moreover, I want to thank the German Federal Ministry for Economic Affairs and Energy (BMWi) for funding the related work of this thesis including flight tests, within the Federal Aeronautical Research Program LuFO V-I.
Several other people supported my research on a theoretical-technical level. In this context, I like to thank my (former) colleagues in the flight control group, Dr.-Ing. Simon Schatz, Dr.-Ing. Volker Schneider, Nils Mumm, Alexander Zollitsch, Erik Karlsson and Lars Peter for their support and the discussions during the initial development of the baseline controller that was used as an application in this thesis. Specifically, I want to thank Rasmus Steffensen for the numerous discussions, his critical questioning of the theory and the motivating atmosphere, which were extremely valuable and contributed a lot to this work. It has been incredible fun to work with him on different projects and topics.
I also wish to thank my friends and family that supported me throughout the work on this thesis. Specifically, I want to thank my parents and my brother, who always supported me and my children, and enabled my studies from the beginning of my diploma studies until this work. With all my heart, I finally thank my children and my husband for their love, patience and distraction, which kept my spirits up and helped me to clear my mind.

Contents

List of Figures

List of Tables

Symbols, Indices and Acronyms

Acronyms

AFCS	Automatic Flight Control System
CAP	Control Anticipation Parameter
CbT	Correlation-based data-driven Tuning
DFT	Discrete Fourier Transform
DTFT	Discrete Time Fourier Transform
ETFE	Empirical Transfer Function Estimate
FCC	Flight Control Computer
FCS	Flight Control System
FFT	Fast Fourier Transform
FRF	Frequency Response Function
FRIT	Fictitious Reference Iterative Tuning
FSD	Flight System Dynamics
FT	Fourier Transform
HMI	Human Machine Interface
IFT	Iterative Feedback Tuning
i.i.d.	independent identically distributed
INDI	Incremental Nonlinear Dynamic Inversion
LFT	Linear Fractional Transformation
lin	linear
LOES	Low-Order Equivalent System
LTI	Linear Time Invariant
MC	Monte Carlo
MIMO	Multiple Input Multiple Output
MOC	Means of Compliance
MTOW	Maximum Take Off Weight
MUAD	Maximum Unnoticeable Added Dynamics
nl	nonlinear
OPV	Optionally Piloted Vehicle
PE	Prediction Error Method

SIMO	Single Input Multiple Output
SISO	Single Input Single Output
SGT	Small Gain Theorem
SNR	Signal-to-Noise Ratio
STC	Supplemental Type Certificate
TFM	Transfer Function Matrix
TUM	Technical University of Munich
VRFT	Virtual Reference Feedback Tuning

Symbols

$*$	General placeholder
A_m	Gain margin
C	Controller transfer function
c	constraint
C_{**}	Pseudo variance of complex random variable *
C_k	k'th fourier coefficient
δ	Dirac impulse
$\mathbb{E}[*]$	Expected value of *
f	Independant variable, mostly frequency in Hz
f_H	First harmonic frequency
f_S	Sampling frequency
$\mathcal{F}\{*\}$	Fourier transform of *
G	plant transfer function
G_{cl}	closed-loop transfer function
I	Identity matrix
$\Im(*)$	Imaginary part of *
J	Cost function
j	Imaginary unit
K_{**}	Variance of complex random variable *
μ	Specific mean value
N	Number of samples
$\mathcal{N}$	Normal distribution
ω	Independant variable, mostly frequency in radian per second
$\boldsymbol{p}$	Parameter vector
Φ_m	Phase margin
$\boldsymbol{Q}$	Controller gain penalty weighting matrix
R	number of maneuver repetitions
$\Re(*)$	Real part of *
s	Operator variable in the Laplace domain
σ^2	Specific variance value
t	Independant variable, mostly time in seconds
T_S	Sampling time
u	control input
$var[*]$	Variance of *
$w(t)$	Rectangular window
w_A	relative weight for magnitude squared-errors
$\mathrm{w}_\gamma(\omega_k)$	Frequency dependent relative weight
w_ϕ	relative weights for phase squared-errors
y	system output
III	Dirac comp

Indices

0	initial
ap	amended plant
cl	closed-loop
cmd	command
des	desired
DFT	Discrete Fourier Transform
DTFT	Discrete Time Fourier Transform
FT	Fourier Transform
HOS	High Order System
LGE	Lower Gain Envelope
LOES	Low Order Equivalent System
LPE	Lower Phase Envelope
nom	nominal
UGE	Upper Gain Envelope
UPE	Upper Phase Envelope

Chapter 1

Introduction

1.1 Motivation and Problem Statement

Since the beginning of aviation more than 100 years ago, aeronautics experienced an enormous technological progress. One of the numerous developments was the evolution of flight controls from mechanical linkages between the pilot control inceptor and the control surfaces towards fly-by-wire systems. Mechanical linkages have been replaced by an electronic interface, where the desired movements of control surfaces are computed and transmitted to actuation elements driving the aircraft's control surfaces by electronic signals. The associated flight control algorithms underwent a tremendous development. The degree of automation steadily increased from stability and control augmentation concepts to autopilot and auto-land systems, to optionally piloted and unmanned aerial systems. Increasing computational speed and resources inside the flight control computers, better sensor and more sophisticated data busses accelerated the process and opened a variety of new possibilities.

Driven by fly-by-wire systems since the days of the Concorde Aircraft in the 1960s, aircraft manufacturers established proven processes for the development of flight control systems and the associated flight control algorithms implemented in hardware or software. For a long time these developments did not progress to the general aviation market due to cost, weight or space constraints in small and medium-sized aircraft. In recent decades, however, this dilemma has slowly changed with the availability of off-the-shelf basic autopilot systems from several companies. Still, the general aviation market is far away from a widespread use of fully digital fly-by-wire systems. The recent trend towards unmanned aerial vehicles and optionally piloted vehicles, driven by the wish for new personal transportation forms or cost-effective logistics for remote areas, will demand new flight control concepts and processes. In the commercial airliner segment, companies can easily afford long and substantially expensive flight test campaigns to develop and fine-tune their control algorithms. This is neither possible in terms of time nor financial effort in the general aviation market, especially when future unmanned platforms must be cost-effective with

a fast time to market. The industry is in urgent need of new methodologies, which can be integrated in a sophisticated, yet cost-effective process to establish their digital flight control systems in future platforms.

For any aerial system exceeding a certain take off mass, flight control systems must be certified (i.e. approved) by the relevant authorities. Certification refers to the process of providing substantial evidence to the authorities, showing that the aircraft and its components like the flight control laws and algorithms comply with governmental regulations and industry standards. Furthermore, it aims to assure that the flight control laws and algorithms were developed in a suitable process to minimize human error and guarantee a minimum performance level and an adequate level of safety. Authorities issue certification specifications for certain aircraft classes (distinguished for example by weight, number of passengers, intended use, etc.), which define means of compliance (MOC) in order to adhere to the specification. There is no legal obligation to follow the guidelines and industry standards referred to in the MOC, but any manufacturer is strongly advised to do so in order to facilitate and streamline the certification process. For the certification process, a key element is requirements-based verification. The intended behavior of the flight control algorithms needs to be precisely defined by a set of requirements before its actual development can be started. During the different verification phases and activities throughout the development process, the flight control algorithms are tested against these requirements. A subset of these requirements for example define certain robustness specifications, while other requirements specify for example the required performance of the flight control algorithm. For the baseline specification of the intended behavior of a flight control law, one usually resorts to standards such as SAE AS94900 [SAE07], SAE ARP94910 [SAE12], MIL-F-8785C [US 80] or MIL-HDBK-1797 [US 97]. These standards provide minimum performance and robustness criteria for the flight control algorithm of a given aircraft type, defined mostly in the time and frequency domain. Accepted metrics for demonstrating robustness of the flight control law are for example lower limits for phase and gain margin (according to SAE AS94900) which can only be applied to classical linear controllers. Also the testing of the performance requirements is easier for classical linear controllers, due to their linearity and lower complexity compared to nonlinear controllers. Flight control algorithms are therefore often realized as linear multi-variable controllers [Bal03], separated into longitudinal and lateral motion. The parameters of the linear control law – the controller gains - are designed based on linear models of the system using methods from linear system theory. Flight control algorithms are usually cascaded systems with outer loops consisting of an autopilot or trajectory controller [BAL11, Ch. 1], [Sch18a] and a baseline controller which translates the outer loop commands into surface deflection commands.

In commercial aviation the development process of baseline controllers is driven by a large scale process compliant to the standards which is complex and extremely costly. Different divisions and departments focus each on distinct elements of the development process like modeling and system identification, linearization and system analysis, gain design and assessment etc. resulting in high personnel expenses. Expensive tools, specialized for supporting the particular tasks in the different divisions and process steps increase the costs further ([SKFL03],[FVBS02, Ch. 1, Ch. 2],[Bal03]). Furthermore, extensive flight test campaigns are performed to allow full estimation of the aerodynamic parameters and time intensive and costly modelling efforts are executed for all system components.
However, this approach would be too expensive for general aviation aircraft or UAVs. Due to the lower affordable modelling and development efforts compared to classical aviation high fidelity models are often not available or subjected to considerable model uncertainties. In general, all unmodelled or unconsidered effects during controller design and verification, due to cost and time constraints, might lead to a degraded controller performance in real-world flight tests. On the one hand the most obvious examples for unconsidered effects that may lead to a degraded tracking performance are atmospherical disturbances like gusts or turbulence. On the other hand the most obvious examples for unmodelled effects that may cause problems when the controller is applied within flight tests are effects introduced by the real hardware like backlash or aeroelastic modes. Also, parametric uncertainties especially with respect to aerodynamic and propulsive characteristics are an important example as they might cause considerable deviations between the real aircraft dynamics and the models applied during controller design and assessment.
Controller designed only based on these available models typically suffer from performance deficits or at worst case do not satisfy their requirements when applied to the real environment within flight tests due to the present model uncertainties. With respect to these uncertainties, approaches exist to develop flight controllers in such a way that they exhibit high robustness and satisfactory performance despite some expected uncertainties. For this purpose the controller parameters are selected in many approaches to meet the design objectives for all a priori assumed uncertainties. This approach is often time intense and requires advanced control design skills from the engineer. But most important it often requires a dissatisfying trade off between safety (i.e. robustness) and other control objectives like performance, especially when the model parameters are very uncertain, instead of being perfectly designed for the actual real aircraft dynamics.
Especially baseline controller count as the component of flight control algorithms which rely the most on the aircraft dynamics. Therefore, they are sensitive to the models used for gain design and assessment and consequently on the uncertainties, inaccurately or even unmodelled effects and disturbances. Because the baseline controller is the most inner part of a Flight Control System, all other components, especially the autopilot and trajectory control, depend on the closed- loop baseline controller dynamics and behavior regarding

their parametrization and design [KSB+18]. As a consequence the baseline controller is attributed with a high criticality. Additionally, the inner-loop is responsible for good disturbance rejection before they manifest themselves in the outerloop control variables [kar].

Therefore, a gain update method is highly desirable that assures that in particular the baseline closed- loop controller dynamics of the real aircraft in real flight correspond as close as possible to the nominal designed closed- loop behavior. Not only in order to be compliant to all inner-loop requirements, but also regarding the fulfillment of the requirements and performance and stability criteria related to the outer loops, as the assumed inner-loop dynamics serve as a basis for their gain design and assessment. To account for the strict cost constraints, the environments of general aviation and UAV are subjected to, this method shall not rely on very accurate models derived over extensive, expensive flight test campaigns.

1.2 State of the Art

In model based control design the controller is designed based on a model of the plant. This nominal plant model, often linear, is only an approximation of the true plant, which is usually nonlinear and of higher order. Often this discrepancy between the true plant and the plant model is approximated by an uncertainty model. In general, it is straight forward to design a linear controller based on a linear nominal plant model, such that the controlled nominal plant model satisfies specific requirements and control objectives. To fulfill this task, one or a combination of the various classical control design approaches can be used. Since the nominal plant is only an approximation of the true system, the designed controller which is perfect for the nominal plant model might reveal a degraded performance on the real system because of the discrepancies between the model and the true system. In the worst case it might even not satisfy the control objectives, it was designed for, on the true plant or even be unstable. In commercial aviation therefore much effort and money is put into

- system identification and the modelling to get very accurate models of the aircraft and uncertainty models
- controller design and assessment with regard to the uncertainties

In general aviation as well in the area of smaller UAV this is not affordable and we need to deal with relatively high and unknown uncertainties in the models. Many other applications, beside the aviation domain, share this issue. Some of the most popular approaches that evolved over time, that account for uncertainties in control are

- adaptive control
- auto-tuning
- robust control
- iterative schemes of identification and control
- data-driven controller tuning

In the following an overview is given.

1.2.1 Adaptive Control

In adaptive control in general, the parameters of a controller are continuously or recursively adjusted to accommodate disturbances and changes in the plant dynamics, resulting in a time-varying controller. There are two main streams of adaptive control:

- direct adaptive control
- indirect adaptive control

1.2.1.1 Direct Adaptive Control

In direct adaptive control, controller parameters are adjusted directly from data obtained in closed-loop operation, such that control design and identification are entwined.

1.2.1.2 Indirect Adaptive Control

The indirect adaptive tuning procedure handles identification and control as separated steps. In the identification part, parameters of the plant model are updated online by recursive parameter estimation. Then in the control part, based on this updated model, the controller parameters are updated with some appropriate control design method.

The field of adaptive control has been extensively investigated in the past decades and much effort has been put in topics like proving or investigating properties as global stability, asymptotic stability, convergence, boundedness of signals, magnitude of the bounded signals, convergence time and many more. For a long time one main concern in adaptive control that was raised according to [SB93], has been, that despite its potential to improve an existing controller it cannot be excluded that a deficient performance could occur. It is often difficult to guarantee that the transient dynamics inherit a desired behavior.

1.2.2 Automatic Tuning

With automatic tuning usually a gain design is described that on user demand automatically tunes the controller parameters based on experiments. It can be roughly divided into

- Frequency response methods
- Parameter estimation methods
- Rule-based methods

1.2.2.1 Frequency-Based Method

A well known frequency based method is the relay method, originally developed by [sH84]. This method is especially suitable for PID tuning. As it is based on test-based measurements it is hence practical where little is known about the system characteristics. It does not require an system identification step. Instead, a nonlinear feedback denoted as relay type, generates a limit cycle oscillation, hence pushes the system is to the limit of stability. The period and amplitude of the oscillation are determined when a steady-state oscillation is obtained, providing a test-based measurement of the ultimate period and gain. Based on these values the PID controller parameters can be determined, e.g. using the Ziegler-Nichols frequency response method. The main limitation of these methods is given by the fact that the tuning is performed at a fixed frequency. This leads to problems related

to actuator saturation, sluggish responses or excessive derivative action. More advanced methods, like the enhanced Åström method [TLW96] achieve better performance in the frequency- and time-domain, though some more effort is required.

1.2.2.2 Parameter Estimation Method

In this context, parameter estimation methods are procedures, where the parameters of a plant model are estimated and then based on this model the controller parameters are obtained by some appropriate control design method.

1.2.2.3 Rule-Based Method

The so called rule-based methods do not use an explicit model of the plant. When transients, set-point changes or load disturbances for example occur, the behavior of the controlled process is observed (e.g overshoot, decay ratio, time constant, oscillation frequency) and if it deviates from the specifications the controller parameters are automatically adjusted using some rules of thumb.

1.2.3 Robust Control

The robust control paradigm arose already back in 1980's, introducing different techniques for dealing with bounded system uncertainty. For an overview see e.g. [DFT13] and [ZD98]. Most control design techniques in this domain have in common, that a controller is synthesized such that specific control design objectives are satisfied not only for the nominal plant model but also for all plant variations described by an uncertainty model that approximates the discrepancy between the nominal model and true plant. The related control design approaches mainly differ in the controller structure, the control objectives they seek to satisfy and in the different descriptions for the uncertainty modelling they address.
The book [DFT13] addresses the fundamental issue of performance/stability robustness trade off with focus on single input and output systems and the technique of loop-shaping, while [ZD98] deals with multi-variable control. It introduces essentials of H_∞ control theory, and other important state of the art robust control techniques as the ν- gap metric and ν- synthesis, structured singular value μ and μ- synthesis. In robust control design one accepts that the (nominal) models, applied during gain design and assessment, are not accurate and will not entail all the dynamics of the real plant. Almost all related methods utilize a description of the model uncertainty that quantifies the mismatch between model and plant. This is incorporated into the gain design and assessment in order to assess robust stability and performance of the controlled plant or to check the gain design against requirement satisfaction. The nominal model and uncertainties are assumed in most robust control paradigms to be given a priori. Since the 80's extensive research was made in this field bringing up concepts as

- Loopshaping design [DFT13], [SP07], [GM89]
- Linear Quadratic Gaussian (LQG) Control [AM07], [KS72]
- structured singular value (μ), μ-synthesis, H_2 and H_∞ control theory [ZD98], [SP07]
- ν- gap metric and ν- synthesis [ZD98]

to name a selection of the main streams which are the most widely applied control design techniques for aircraft flight control [Bal03]. The classical ideas behind the different domains are briefly sketched in the following, giving the basic idea of the concepts.

1.2.3.1 Loopshaping Design

The core idea in the loop shaping approach is to obtain a compensator such that imposed requirements on the open-loop singular values are satisfied. These open-loop singular values requirements are derived from closed-loop objectives. Different advanced methods for performing the loop shaping design exist like e.g. the loop transfer recovery method in LQG design [KS72] or using the so- called normalized co-prime factor H_∞ robust stabilization problem [MG92].

1.2.3.2 LQG Control

The classical LQG control is a optimization- and signal-based approach where the exogenous signals (process noise, e.g. measurement noise and disturbance signals) are assumed to be stochastic with known statistical properties and the error terms enter the cost function in terms of the 2-norm. A shortcoming of the LQG controller, which is a combined optimal state estimation (Kalman filter) and optimal feedback controller (LQR), is the lack of satisfactory robustness properties as there are no guaranteed stability margins [Doyle 1978].

1.2.3.3 Structured Singular Value Theory

The structured singular value theory in combination with a unified framework allows the treatment of robust stability and robust performance analysis for systems with structured uncertainty. In the context of flight control law clearance problems μ — analysis can easily address frequency domain criteria for example the stability margin criterion [FVBS02]. Therefore, the influence of uncertain model parameters on the closed-loop dynamics is captured via so-called linear fractional transformation (LFT) based uncertainty models. The captured uncertainties can be structured or unstructured. The structured uncertainties describe uncertainties in parameters such as inertia, center of gravity, stability derivatives etc., which are known within a specific range. The unstructured uncertainties in contrast originate from unmodelled dynamics in the model. The small gain theorem

(SGT), defines a robustness criterion for a closed-loop model containing unstructured uncertainty. The resulting level of conservatism in the robustness analysis can be reduced if the uncertainties are structured, meaning that the uncertainty modelling has a certain structure as it is the case for many uncertainties of aerospace systems as mentioned before. For these cases based on structured LFT based uncertainty models the structured singular value robustness measure can be derived with the multi-variable Nyquist stability theorem [FVBS02]. Moreover, the structured singular value can be interpreted in terms of classical gain/phase margin and Nichols exclusion region robustness specifications as done in [FVBS02]. In contrast to gridding approaches traditionally used by industry, which generally only test for all combinations of the extreme values of the uncertain parameters, that the criterion is not violated, μ -analysis supplies the possibility to check if all exclusion regions in the Nichols plane have been avoided for all possible combinations of the values of the parametric uncertainties.

1.2.3.4 H_2 and H_∞ Control Theory

The LQG problem constitutes a special case of H_2 optimal control. The H_∞ optimization can constitute a fundamental tool for μ-synthesis ([ZD98]) and originated back in the 1980' motivated by the shortcomings of LQG control. Both H_∞ and H_2 control require the solutions to two Riccati equations and involve based on a state-space realization of a generalized plant a minimization of H_∞ and H_2 norms respectively. Furthermore, both techniques provide controllers of equal state dimension as the generalized plant and exhibit a similar structure as the LQG controller. In contrast to H_2 control where the optimal controller is unique, it is theoretically and numerically complicated to provide an optimal H_∞ controller. Thus, in general a sub-optimal controller is obtained [SP07]. But on the other hand the H_∞ approach is preferred over the more traditional H_2 norm when uncertainties need to be addressed [SP07]. The objective of the H_∞ robust stabilization problem [GM89] is to maximize the stability margin of normalized co-prime factor plant descriptions, thus stabilizing a set of perturbed models and not only the nominal plant.

1.2.3.5 ν- gap Metric and ν- Synthesis

The gap metric was introduced for the study of the robustness of stability of feedback systems subjected to uncertainties [El-85]. It was motivated by the fact that examples can be constructed, where the norm of the difference between two systems is a poor measure of their distance as it approaches infinity though the systems are close together. Situations were identified, where the gap metric constitutes a better suited metric for the distance between two linear systems than a metric based on norms. In addition, the gap metric can be applied to unstable systems. Seeking for more efficient ways for computing the gap with better numerical and analytical properties, the gap metric was modified, resulting in the ν-gap metric which has a clear frequency response interpretation [Vin93].

It introduces the ν-gap distance, which can be interpreted as a kind of measure of the importance of the difference in behavior of two systems. The ν-gap can be applied to measure the difference between a perturbed (uncertain) system and the corresponding nominal system [FVBS02]. It offers the possibility to analyze stability margin criteria , and it is a linear frequency domain method.

Summary - Robust Control Most of the concepts have in common that based on a nominal plant specific uncertainties are assumed in the one or other way. The uncertainty model, that approximates the possible discrepancy between nominal plant model and expected true plant, in this context is often denoted as plant envelope. The real plant is often assumed to lie within this plant envelope. The model and uncertainties are commonly assumed to be given a priori. Based on the assumed structure and values of the uncertainties a control design is performed that assures that the addressed control objectives are satisfied for a specific set of uncertainties.
A draw back of these approaches is that in general they lead to conservative controller designs that are not perfectly parametrized for the real plant, which is only one realization within the uncertainty set. Another risk of these methods is that in case, the discrepancy between nominal model and real plant was modelled too inaccurately, such that the real plant lies outside the assumed plant envelope, the resulting controller still might not satisfy specific control objectives when applied to the true system. Furthermore, the workload and complexity of these approaches is higher compared to a design of a linear controller based on a linear nominal plant model using standard, classical methods. In general, it is straight forward to design a linear controller, based on a linear nominal plant model, that satisfies some specific control objectives such that the corresponding nominal closed-loop system of nominal plant model and designed controller, inherits a perfect, desired behavior. At the beginning of Chapter 3 an example is discussed, that further illustrates the mentioned drawbacks.
In many applications, like the light UAV or general aviation sector, the nominal models are often very inaccurate. Furthermore, the uncertainty structure and exact distribution is often not well known because of the high costs related to system identification and because the related extensive flight test campaigns are not affordable. The consequence of the large uncertainties is, that the uncertainty model has to cover a large plant envelope. The use of large plant envelopes, however, leads to a conservative controller. Besides the large uncertainties to be covered, under-modelling is another issue. Under-modelling might arise from

- underestimated uncertainties
- neglected higher order dynamics in the nominal plant model
- neglected nonlinear effects like backlash in the actuation

Due to the approximate character of the model, one might risk violating the control objectives on the real system. But even in case that the true system is captured exactly by the uncertainty model, the performance would only lie within some specified boundaries and might be conservative, i.e. it will not correspond to the perfect, desired response that can be achieved for the nominal plant model. It will be just acceptable. A desirable situation though would be to be able to design the controller such that when applied to the true plant the desired response could be achieved while keeping the costs and therefore the effort and workload for controller design and assessment as low as possible.

The domain of robust control and model-based control design are in general an important application area and motivator for the identification of models using experiment data. The reason is that model-based control design assumes that a reliable model of the considered plant is available. As a basis for robust control design, additionally a quantification or suitable measure for the model uncertainty and its uncertainty structure is required.

1.2.4 System Identification

System identification is, as control design, an enormous scientific field which rapidly grew since the 1950s. There exist different possibilities how to divide or classify this domain into different research areas. One possibility with focus on the methods used within this thesis is shown in Figure 1.1. First it is possible to distinguish between time domain and frequency domain methods. The time domain system identification methods are a huge domain, which of course can be divided into many subdomains. Since the applied methods within this thesis are frequency domain methods an overview over the time domain methods is omitted, as it would clearly go beyond the scope of this thesis. For an overview the

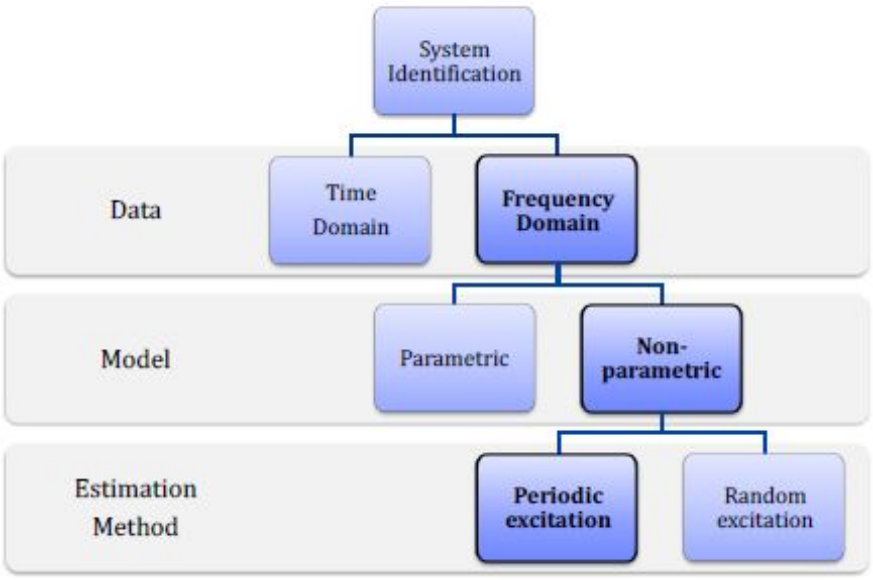

Figure 1.1: *Classification of considered system identification method. [Mer19]*

interested reader is referred to [Lju99], which counts as a standard reference work for time domain system identification. With focus on flight dynamics applications [KM06] can be named as classical literature. Frequency domain methods use logged experimental time domain data to calculate the frequency response, by application of discrete Fourier Transforms or spectral analysis, to name the most popular methods. There exist a variety of standard reference literature on this topic since it enjoyed high popularity in engineering, research and industry since the 1950s. References are for example [PS12] and [SM$^+$05]. [RT06] applies frequency domain methods on flight dynamics identification, with focus on rotor-crafts.
Motivated by model based and/or robust control design many identification concepts addressed methods to provide a nominal model of a plant with unknown dynamics and its uncertainty region. For a long time, the research in the domain of system identification, has put emphasis on characteristics such as consistency and efficiency, with regard to the identification of the real plant based on the measurement data and guarantees on the specified error/uncertainty bounds. Work focused also on more accurate identification methods with tighter error bounds of the mismatch of estimated model and the real plant. This was motivated by the fact that in model-based control design the performance attained by controllers when applied to the real plant will rely on the nominal model and the assumed uncertainties during control design. The higher the uncertainties the more conservative will be the controller as it seeks to satisfy requirements for the complete uncertainty set.

1.2.5 Interplay-Area of System Identification and Robust Control

In almost all domains including aerospace and flight control, control design and system identification are often separated research areas, despite their actually strong interactions and inter-dependencies. In the 1990's the interplay-area of system identification and robust control actually gained growing interest. Aiming an interaction between robust control design and system identification a problem area indicated by "*identification for control*" (from an identification point of view) or "*experiment-based control design*" (from a control design point of view) evolved. These fields explicitly address a joint design of identification and control. The importance of that topic was advocated in [Gev93]. Until 2003 almost approximately 1500 paper only on the topic of identification for control have been published according to [Gev05]. The key promoter for this development might have been the plenary [Gev92] at the 1991 IFAC Symposium on System Identification. It defined an agenda for research addressing the numerous open questions and key issues in this area.

1.2.6 Identification for Control

The area of "identification for control" was initially motivated by the insight that even with very simple models, high performance control can often be readily achieved, given that the driving dynamical features of the system are accurately captured [Gev05]. Consequently, since the model is always only an approximation of the true system, the identification shall be tuned towards the intended application of the model. The reason is that the intended application of the model determines the required quality of the model or frequency range, where the model error shall be small.
The area of identification for control gained a lot of interest and according to [Gev05] three main streams developed:

- experiment design
- control-oriented uncertainty sets
- definition of control-oriented identification criteria

One early attempt related to the area of **experiment design** was presented in [GL86], where the experimental conditions for the identification where computed, taking controller performance into account. The controller performance was taken into account by minimizing the performance degradation, caused by the fact that the controller was computed only based on an estimate of the true system and not the true system itself. This approach as well as several other optimal control- oriented experiment design for identification methods suffer according to [Gev05] from the fact that the optimal experimental conditions depend on the unknown system.
An important paradigm, which was formulated during that time and which is also driving the concept in this thesis, is that when designing a controller based on a model, finally all that matters is the achieved performance of this controller on the true system rather than the quality or structure of the used model. This paradigm led to concepts and applications, where only the control performance objective was assumed to be known and the model as well as the controller to be implemented were assumed as unknown. This led, according to [Gev05], to the following formulation of the control-oriented identification procedure: "*Given a control performance objective, design the identification in such a way that the worst case performance achieved by the model-based controller on the validated uncertainty set of models is as high as possible*".
Further research was directed toward **control-oriented uncertainty sets** and was motivated by the observation that the design of the identification experiment influences the model uncertainty set, which influences the set of admissible controllers and their worst case performance on all models in the set. This further research work concentrated on the interplay between model uncertainties and robust control in terms of the definition of so called "control-oriented uncertainty sets" and computation of the corresponding model

quality measures as a function of the experimental conditions [Gev05]. The field of experiment design addresses topics as for example optimal input design for system identification for open-loop identification and for closed-loop identification.
In the domain of **control-oriented identification**, the identified parametric model is assumed to be good if the closed-loop system of the designed controller with the identified model is nearly the same as with the true system. Furthermore, it is argued that the identification objective should be a function of the control performance objective. The resulting work focused on the definition and computation of control-oriented nominal models and on "*the design of identification criteria that minimize a (control-oriented) measure of the model error*" according to [Gev05]. Already back in the 90's the developed concepts aimed to define identification criteria for the plant model that minimize the difference between the achieved and designed closed-loop. Thereby, the achieved closed-loop denotes the controlled real plant and the designed closed-loop is the nominal plant model controlled by the same controller as the real plant. This difference between the two closed -loops, is usually expressed in terms of a norm of some control performance criteria. It was found out that this way the control performance objective "*shapes the bias error distribution of the nominal model*" [Gev05]. As a result the nominal model is characterized by a bias error that is reduced especially in frequency regions where it is important to have an accurate estimate in order to obtain a better controller. Especially closed-loop experiment-based identification was found to provide good models for control design, because in many approaches through the closed-loop experiment the identification criterion automatically included a frequency weighting by the closed-loop sensitivity function [HGd96]. The results of the domain of the control-orientated identification were used in many approaches in the field of experiment-based control design.
Furthermore, they led to

- a revival of closed-loop identification [FL99], [Hea00], [Hea01a], [Hea01b], [Hea02], [Hea03], [WG02], [WG04] (after observing that identification under closed-loop conditions might be beneficial for many control performance objectives [HGd96])
- the development of iterative schemes of controller and model updates, which can be subordinated to the domain of experiment-based control design

1.2.7 Experiment-Based Control Design

The domain of experiment-based control design is widespread. Also, the before mentioned concepts like adaptive control, auto-tuning using relay methods for example, or the rule- based methods can be regarded as experiment-based control design methods. Related concepts are categorized into iterative and non-iterative, into parametric and non-parametric, into model-based (indirect) and data-driven (direct) as detailed below.

In [FHK14], a study is presented which compares model-based and data-driven controller tuning. The obtained main conclusions of this study are:

- If a model with not accurately known structure is identified using an ML estimator, the data-driven approach is capable to statistically outperform the model-based result regarding the final control cost, though the parameters' variance remains larger in the data-driven approach.

- Because under-modelling cannot be circumvented with a low-order model, data-driven methods may provide better solutions in real applications

The study though only considers stable systems and open-loop experiments under the assumption that the control objective is achievable. It was stated that a generalization of the made conclusions is not straightforward.

1.2.7.1 Model-Based (Indirect) Schemes

An interesting area called "iterative schemes of controller and model updates" gained a lot of interest in the 90's. [VS95] gives a detailed overview of these iterative schemes and introduces a generic form and framework within which most of the procedures can be described. The iterative methods were developed driven by the desire of a joint identification and control design, since classical methods in system identification and control design are optimizing either the model or the controller while the other component is fixed. Because an simultaneous optimization of both elements is not possible, [VS95], this led to the development of iterative schemes directed toward an repeated and sequential optimization of the controller and the model. For the identification of the model, thereby the results from the domain of **control-oriented identification** were applied. Because of the sequential and iterative character, these approaches were often interpreted as an indirect adaptive control scheme with a time-scale separation between controller redesign and identification in closed-loop [Gev05]. The generic form in [VS95] summarizes these iterative schemes. The concept in this thesis might be interpreted as a method to successfully implement this scheme in a non-parametric manner with only one iteration. The basic idea for the iterative schemes is as follows. Based on experiments of the true plant P with a controller C, a control performance index $J(P, C)$ is calculated. This performance index is then improved by tuning the controller based on the identified model from the experiment $\hat{P}$. From closed-loop experiments first an approximate plant model $\hat{P}$ is identified. Based on this plant model the control performance cost, mainly expressed as a norm of the control performance index $J(\hat{P}, C)$ of plant model and controller, is minimized. The minimization is performed by a control design method providing an updated version of the controller that was initially tested in the experiment. Driven by the fact, that what really matters is the performance achieved by the controller in conjunction with the real system, i.e. the achieved closed-loop performance, the key element of these concepts is a special triangle equation [Sch92, p. 25-27]. From this triangle equation it becomes obvious that instead of minimizing the control performance cost of the true plant and controller $||J(P, C)||$, which represents the achieved performance, two other expressions can be minimized instead:

- First, the *performance degradation cost* $\min_{\hat{P}} ||J(P,C) - J(\hat{P},C)||$, is minimized with respect to the plant model $\hat{P}$, such that a new plant model is obtained from the closed-loop experiment. This kind of identification criterion measures the mismatch between true system and model. This mismatch is measured in terms of the difference, between the control performance costs of the true system and model when controlled by the same controller. It originates from the domain of control-oriented identification, where data from closed-loop experiments is used for identification. It aims to identify a plant model such that the resulting closed-loop system of model and controller is as close as possible to the real experimental closed-loop system.

- Second, the estimated plant model is used to update the controller. This is performed by minimizing the designed performance cost $\min_{C} ||J(C,\hat{P})||$, with respect to the controller, such that a new controller is obtained. This ensures a high *nominal performance*.

Once a pair of plant model and new controller is derived, it is evaluated as a candidate solution to the joint problem of identification and control design. Besides a high *nominal performance*, also a robust performance is desired, meaning the *achieved performance* shall be close to the designed performance. This is enforced by requiring the *performance degradation cost* with the new controller to be small compared to the designed nominal performance. In general these concepts will yield controller where the designed nominal performance cost is minimized, but often there is no prior guarantee that this new controller will also achieve this performance when applied to the real plant. Therefore, often an additional robustness analysis needs to verify this.
Different iterative schemes have been developed following this basic concept but differing in [VS95]

- the choice of control performance cost

- the way the closed-loop identification is treated

For example in [LAKM93] the performance cost and hence control design is based on the internal mode control (IMC) paradigm. The approach in [ZBG91] bases its control design strategy on an infinite horizon LQ-control objective and [SB93] on a H_∞ robust control design method, [BB90].
A common characteristic is though, that a joint performance criterion for both parts - identification and control design - is used, as already described. In the iterations often the performance level of the closed-loop is gradually increased such that already achieved performances are constantly improved rather than aiming immediately for an ideal, but possibly unachievable desired performance. For example in [LAKM93] or [SB93] the desired closed-loop bandwidth is gradually increased with each iteration of identification and control design.

The iterative way of increasing the performance addresses cases, where the achievable performance is unknown in advance. The iterative character also allows for a cautious control performance improvement. Caution in the controller update is necessary, because it is performed based on a model of the true plant and this plant model only approximates the true plant in the operating condition. Another reason why a cautious controller update or a cautious performance improvement might need to be performed, is that the true plant might contain some nonlinearities or higher order dynamics, which are not reflected in the model. As a consequence of these approximations, one might risk a high performance degradation, e.g. that the performance of true plant with controller might not be very close to the designed performance (of controller with plant model), if the controller is changed too much. For small changes of the controller it is assumed that the plant model is accurate enough such that in the vicinity of the controller that was used for identifying this plant model the true closed-loop will behave as the designed closed-loop.
Another common factor of the iterative schemes is, that most approaches use a model based controller design and therefore estimate a parametric model of the plant. Often prediction error methods with a least-squares prediction error criterion are used for identification like in [LAKM93] or in [ZBG91]. In [SB93] the closed-loop identification is performed based on a coprime factorization that is dual to the Youla parametrization of stabilizing compensators [Vid11].
A problem that often emerges from the intermediate step of identifying a parametrized plant model is, that if the model structure is assumed incorrectly or the assumed model order cannot reflect or approximate the real plant dynamics accurately enough, this causes modelling errors. This under-modelling of the plant might lead to a loss of information that was actually present in the data and to a limitation of the achieved performance.
In fact, "*it has turned out to be surprisingly difficult to guarantee that for model-based control design methods, with a model of restricted complexity, the performance is near optimal*" [Hja98]. But despite the fact that in general these iterative schemes do not converge to the achievable minimum of the performance cost, as derived in [HGG95], the concepts found their way into many process control applications (see e.g. [Gev05] for an overview of these applications). A key driver might have been that in these kinds of applications an extensive amount of closed-loop data is generated that can be easily used to improve the controller.

1.2.7.2 Data-Driven (Direct) Schemes

The so called data-driven control methods were developed as an alternative to the model-based approach. These techniques are denoted as "direct" because the data collected on the plant is used to directly tune a parametrized controller, without an intermediate plant-identification step. These techniques can be distinguished into iterative and non-iterative (one-shot schemes). The most popular methods are:

- a) Iterative Feedback tuning (IFT)
- b) Virtual reference feedback tuning (VRFT)
- c) correlation-based data-driven tuning (CbT)

a) Iterative Feedback Tuning Iterative Feedback Tuning (IFT) schemes as described in [Hja98], use collected closed-loop experimental data on the true plant to directly tune a parametrized controller, without a plant- identification step. The core idea of the IFT concept originates from the situation that the control design objective is the minimization of some criterion. The controller parameters are updated based on a gradient based approach, where the gradient of the criterion with respect to the controller parameters has to be calculated. The core idea is, to approximate this gradient by using the system itself instead of an identified parametric model, by performing a specific, additional gradient experiment. With this direct approach it is avoided to have to solve an identification step first, which itself requires an iterative minimization procedure. Moreover, when the controller is changed a new local model of the criterion is created from new experimental data. It was found in [Hja98] that such methods are less sensitive compared with model-based methods. Regarding the calculation of the gradient, one of the first concepts was to do a numerical approximation of the gradient by evaluating the criterion for perturbations of the parameter vector and then calculating a difference approximation. The need for these additional gradient experiments is especially impractical in applications, like aircraft, where tests are expensive. Furthermore, the number of experiments is proportional to the number of parameters, what becomes expensive and impractical for a larger number of parameters. In the context of safety critical applications like aircraft, another problem might be seen in the gradient experiments, where perturbed gains are tested without clearance or stability guarantees.
In [HGG94] an LQG type design criterion is used together with closed-loop experiments in order to perform controller updates in an iterative manner such that the criterion converges to a local minimum, completely without requiring any model of the system. The criterion includes as first term a quadratic norm of the error between the response of the true system and the desired response (tracking error) and as a second term the quadratic norm of the input signal to account for control effort. The gradient of the criterion is based on closed-loop experiments directly and the approach is thus not model-based. The objective can be manipulated between iterations in order to improve performance.
In [Hja02] which gives an overview over the iterative feedback tuning (IFT) methods it is shown, that with the proposed experiment-based gradient estimation an unbiased estimate is obtained. This is a key property of the IFT and allows to prove that under certain conditions the scheme converges to a stationary point of the design criterion, regardless of the order of the true LTI plant and the complexity of the controller. Furthermore, IFT has proven to be robust to the properties of the plant compared with model-based meth-

ods. As explained in [Hja02], and as simulations and practical experiments indicated, it even performed well on numerous nonlinear systems like on the DC-servo with backlash [HGGL98] for example. Further applications of IFT are listed in [Hja02].

b) Virtual Reference Feedback Tuning The virtual reference feedback tuning (VRFT), [CLS00], is another data-driven controller-tuning method, where no model identification of the plant is needed and that gained a lot of interest. The idea behind this "direct" method is to reformulate the problem of designing a model-reference feedback controller into a standard system-identification problem. It aims to identify the optimal parameters of the controller such that the two-norm of an approximate model reference criterion is minimized. The model reference criterion constitutes the difference between the reference model, which describes the desired closed-loop behavior, and the achieved closed-loop system based on the controller with the current parameter setting. The VRFT approaches apply a specific filtering of the measured signals to calculate a time domain criterion that approximates the model reference criterion. The filter usually depend on the reference model and different variants of this filtering evolved. The controller parameters are calculated via minimization of this time domain criterion using non-standard prediction error methods (PEM). Due to the dependency of the noise model on the controller parameters the noise model has to be estimated correctly to derive consistent estimates of the optimal controller parameters. Several concepts evolved, which propose different approaches to deal with the problems introduced by the measurement noise. The so-called instrumental variable approaches for example use multiple measurements, incorporating that the noise of the different experiments is not correlated. But in general the VRFT approaches are a "one shot" method, meaning non-iterative, in contrast to the IFT approaches.

c) Correlation-Based Data-Driven Tuning Approach [KvB07] presents the correlation-based data-driven tuning approach (CbT) for fixed-order controller. The key element is a convex correlation criterion, with respect to linearly parametrized controllers, that approximates the model-reference control criterion. The main characteristics of this approach are according to [KvB07]

- it minimizes the correlation between the model-reference error and the reference signal instead of the two-norm of the model-reference error like in VRFT,
- an estimate of a correlation criterion is minimized using the least-squares algorithm
- for finite data length, however, the estimate of the correlation criterion is biased, but based on a frequency-domain description of this bias it was shown that it will in general improve the robustness of the closed-loop system
- it cannot be applied to nonlinear systems

d) Other Concepts In [KPVDF17] a one-shot direct data-driven gain tuning concept in the **Loewner framework**, based on frequency domain data, is presented. As the VRFT, the proposed control technique is a model-reference based tuning scheme, where the control objective is expressed in terms of a reference transfer function. This reference transfer function represents the desired behavior of the closed-loop. Based on an open-loop experiment, plant input and output time domain data is measured and the frequency response of the plant is calculated. Thus, a non-parametric plant estimate is obtained. Based on this plant frequency response and the desired closed-loop reference transfer function an ideal controller frequency response is calculated. This obtained controller frequency response is ideal in that sense that the closed-loop frequency response calculated from the plant and ideal controller frequency response will match the desired frequency response. The core of the concept is the following step, where the ideal controller is approximated by a linear time-invariant system. This identification is performed via the Loewner framework in the frequency domain.

The Loewner approach, which is originally used for model approximation and reduction by constructing a state-space model from frequency –domain data is here applied to identify the controller. It constitutes an interpolation approach, where the model performs a barycentric Lagrange interpolation and allows balancing between model complexity and accuracy by specifying the controller model order. This design technique is applicable to systems, where the controller structure is not fixed a priori. Furthermore, as other data-driven tuning concepts it does not allow for stability and robustness analysis.

Another popular concept is the **fictitious reference iterative tuning** (FRIT) [Kan13].

e) Applications to Flight Control Experiment-based methods have been also applied in Flight control. [IPR+16] for example, presents a comparison study of the VRFT and CbT methods with application to an attitude control law of a variable-pitch quadrotor. It was found that both methods provide similar tracking and disturbance rejection capabilities. The CbT method though, appeared to show better robustness in the presence of low signal-to-noise ratios (SNR).
[ZIPL20] performs a data-driven MIMO attitude control- design for a multirotor UAV based on a VRFT method. Because of unavoidable inertial couplings originating from nonlinear effects and a non-perfect knowledge of the principal axes frame such a decoupled controller may perform unsatisfactory in reality, such that a retuning might be necessary. The VRFT method has been extended to allow the execution of data–collection experiments under closed-loop conditions, because experiments for the tuning of such attitude controllers can be executed safely only under closed-loop conditions. The design results in a controller with MIMO FIR structure with integral action.

Another iterative experiment based tuning concept with application to flight control is presented in [Gra18]. Based on closed-loop flight tests with an initial controller a Low-Order

Equivalent System (LOES) model of the closed-loop short-period dynamics is identified using a least-squares solution. The control objective is a desired closed-loop short period pole location, expressed in terms of two design parameters: natural frequency and damping ratio, but could be also chosen as other criteria like overshoot or settling time. The control objective is achieved via an optimization. Therein a quadratic cost function of the deviation of the design parameters from their desired value is minimized with respect to the controller parameters using a Gauss-Newton optimization. A weighting based on the residual covariance matrix, which describes the uncertainty on the estimated design parameters, is incorporated into the cost function to prioritize more accurate data over less accurate. The gradient of the cost function with respect to the controller parameters, which is needed to update the controller parameters, is obtained from flight tests. This includes that at each optimization step each controller parameter is sequentially perturbed around its current value. For each perturbation an additional repetition of the maneuver is performed with an subsequent identification of the corresponding closed-loop LOES and the gradient can be computed using finite differences. The calculation of the gradient, hence, requires the test to be repeated for each controller parameter variation at each iteration. For higher numbers of parameters this could easily become extensive and cost intensive. This could be circumvented according to [Gra18] by deriving an analytical expression for these sensitivities by differentiating the corresponding equations of motion as performed in [Gra15].

Summary - Data-Driven Schemes A critical step in direct data-driven control tuning methods, which are based on model reference tuning such as VRFT and IFT tuning, is the choice of a suitable closed-loop reference model. The difficulty arises from the fact that the reference model should on one hand reflect the desired closed-loop performance, but on the other hand it should also take into account the capability of the unknown plant dynamics to reproduce the desired closed-loop behavior with the tuned controller, hence be achievable. Consequently, the definition of the reference model is not straightforward, since it would require knowledge of the plant, which the data-driven framework aims to eliminate. Furthermore, in general no stability constraints are enforced in the algorithms, such that stability of the closed-loop resulting from the algorithms with a given reference model and controller structure, is not a priori guaranteed. This makes the tuning result of these tuning algorithms and the achieved performance levels reliant on the choice of an adequate reference model.
In [SPB18] therefore, an approach based on VRFT is proposed that optimizes a reference model and a controller at the same time. This is achieved by minimizing a performance index with respect to controller and reference model parameters. The performance index includes two terms. The first term is composed of the tracking error and control input efforts that would be present if the reference model was matched perfectly by the closed loop. The second term penalizes the expected mismatch between the reference model and

the true closed-loop.
But not only the choice of the reference model in data-driven reference-model based tuning methods influences the achieved performance levels. Also, the chosen controller structure has a high impact, since the reference model will be approximated with a different bias by the resulting closed-loop systems. Other issues that might become critical are non-minimum phase plants [CEGB11].

1.3 Objectives

This thesis is to be considered in the context of a linear baseline controller that is developed as a component of a highly modular flight guidance and auto flight control system for optionally piloted general aviation (CS-23) aircraft and unmanned systems.
The development process shall cope with the demands arising with the addressed aircraft systems, i.e. general aviation aircraft. Especially the issue that extensive flight test campaigns for model identification are not affordable and modelling efforts are time and cost restricted shall be addressed. As a consequence only low fidelity and low order models, with large uncertainties will be available for the control design. A controller obtained with classical model-based methods might therefore underperform when applied to the true system. In order to improve the performance of the controller a retuning might be necessary. Other reasons, why a retuning of a controller might be necessary are

- Uncertainties in the plant model used for initial controller design
- reduced plant order, as effects like structural and aero-elasticity are in general not part of the parametric model
- reduced plant performance due to e.g. components ageing
- variable plant performance due to changes in the operating conditions that are not reflected by the simulation, e.g. different payloads, environment
- changes in plant performance due to modifications

Objective 1: To accomplish this task, a method shall be developed towards a systematic, flight test experiment based retuning process of the controller gains.

In [FHK14] it was found that experimental data- driven control approaches without an intermediate step of parametrized plant model identification might lead to better results regarding the achievement of the final control objective on the true system. The reason is that parametrized plant models always represent only an approximation of the true system and under-modelling cannot be avoided with a low-order model. Hence, the information about high order dynamics, e.g. aeroelastic modes, actuator or sensor dynamics or nonlinearities, e.g. backlash, delays that might be present in the experimental data is often neglected or gets lost in the model representation.
Objective 2: Therefore, the method shall be data-based and non- parametric, hence not include an intermediate step of parametrized plant model identification.

In most of the above-mentioned situations, where an initial controller already exists and where the objective is to improve its performance, an approach where closed-loop test can be performed is attractive. Closed-loop tests are attractive in these situations, because

they allow to perform the experiment to collect the data without requiring a special testbed and without requiring to modify the system. This significantly simplifies the retuning process and reduces the costs.
Objective 3: As a consequence the developed method shall allow to update initial low fidelity model based controller gains, based on real measurement data from closed-loop flight test. For the same reasoning, concepts where only the controller parameters are updated, and the controller structure remains unchanged are beneficial.

Objective 4: The retuning procedure shall be in a deterministic manner and include the impact of deviations of the real system dynamics from the assumed model on the controller behavior automatically. The aim is to achieve compliance of the controlled system with all relevant requirements in the real environment. Therefore, the baseline closed-loop dynamics of the real aircraft in real flight shall correspond as close as possible to the nominal designed closed-loop behavior.

As we saw in the State- of the Art many experiment-based model reference tuning approaches lack of the incorporation of stability or robustness constraints. Hence, the stability of the true closed-loop with retuned controller is not a priori guaranteed. This is not acceptable for an aircraft.
Objective 5: Therefore, the approach needs to account for stability margins.

1.4 Contributions of this Thesis

With respect to the previously defined objectives, the main contribution of this thesis is a novel experiment based controller retuning method. A methodology towards a clear, systematic, experiment and non-trial and error based tuning process of the controller parameters, based on real measurement data from tests under closed-loop conditions is proposed. The aim of the developed method is to improve existing underperforming controllers by retuning.

A beneficial characteristic of the concept is that the proposed method is non-parametric. The controller parameters are updated directly from closed-loop input–output data, without the intermediate step of a parametric plant-model identification. Since the performance of model-based controllers is highly dependent on the model accuracy, one drawback of an intermediate model identification is a possible plant-model mismatch due to inaccuracy in identified model structure or parameters. This problem is mitigated by the developed concept by the fact that the closed-loop test data is exploited directly without resorting to a parametrized plant model. This allows to take into account the true order of the system in contrast to approaches based on a parametrized plant model which are typically low order approximations of the system. Moreover, the demand for extensive, costly flight test campaigns (to identify a very accurate model by full estimation of aerodynamic parameters, as performed in civil aviation) is mitigated. Hence, the method is suitable for the currently highly emerging market of novel small to medium sized Manned and Unmanned Aerial Vehicles as well as Optionally Piloted Vehicles for General aviation aircraft, which are very cost-sensitive compared to large transport aircraft.

C1: Proposal of a novel test-based gain retuning procedure for linearizable control laws The objective is to update controller parameters of an initial controller, such that closed-loop performance requirements are satisfied on the true system. Based on tests performed on the true system under closed-loop conditions with the initial controller, the closed-loop and open-loop frequency response is estimated. Based on this, the anticipated closed-loop frequency response and stability margins for an updated set of controller parameters is calculated and used together with a desired closed-loop frequency response within an optimization problem to adjust these controller parameters to obtain an improved controller response as detailed below. The desired closed-loop frequency response shall satisfy all performance requirements such that by minimizing the deviation between the anticipated tuned closed-loop response and the desired one sufficiently, the performance requirements are also satisfied on the true system.

C2: Formulation of an optimization problem for test-based gain-retuning A specific optimization problem is proposed, which imposes the relevant design criteria through a suitable optimization formulation such that deviations of the real system dy-

namics from the assumed model are automatically included in the gain retuning. The proposed optimization problem seeks to determine controller parameters such that the deviation between the desired closed-loop frequency response and the anticipated closed-loop behavior for a new controller parameter set in the frequency domain is minimized. The deviation is quantified by a metric considering a weighted squared error in magnitude and phase of the respective frequency responses. The proposed deviation metric was already used successfully in the context of low order equivalent system (LOES) identification by [RT06]. In that context the deviation between measured frequency response and LOES frequency response is minimized with respect to the plant parameters. The idea in the context of this thesis is to use a similar structure to minimize the deviation between a desired closed-loop frequency response and an anticipated closed-loop frequency response, which is detailed below, with respect to the controller parameters. Furthermore, a regularization is proposed by adding a penalization term, keeping the tuned gains within reasonable bounds around the initial gains. Finally, stability criteria are enforced by supplementary constraints.

C3: Method to calculate the non-parametric, anticipated closed-loop frequency response for an updated controller parameter set A method to calculate the non-parametric, anticipated tuned closed-loop frequency response for an updated controller parameter set, based on closed-loop experiments with an initial controller is proposed. First, based on experimental data a non-parametric closed-loop frequency response estimate of the true plant with initial controller is calculated. Based on this estimate, the anticipated closed-loop frequency response for an updated set of controller parameters can be calculated, assuming that the controller, that was applied during the experiment is linear and exactly known.

C4: Development of an analytic expression for the bias of the anticipated closed-loop estimate For a single-input-single-output closed-loop system with a linear controller with error feedback and feed-forward an analytical expression for the bias between the anticipated and true updated closed-loop frequency response has been derived. It is shown that the bias is small for small changes in the feedback controller, large initial feed-forward or large signal-to-noise ratios.

C5: Practical Demonstration on different aircraft including flight tests The controller parameter retuning is demonstrated for a longitudinal baseline controller on a real flexible large aircraft. The longitudinal baseline controller is part of a modular flight control system and was flight tested on four different CS-23 aircraft. The controller entails all components that are necessary for real applications, e.g. roll off filters to attenuate noise, notch filters, control allocation, trim compensation etc.. The concept is analyzed for this application via Monte Carlo simulations on a high fidelity 6 Degrees of Freedom

simulation environment including real world effects like noise, structural and aeroelastic modes, backlash and light turbulence. Finally, the concept is successfully demonstrated with real flight tests.

1.5 Structure of this Thesis

The remainder of this thesis is organized as follows: In Chapter 2 the theoretical background regarding the estimation of the Frequency Response Function of a linear dynamic system is established. Section 2.1 focusses on the Empirical Transfer Function Estimate (ETFE) under open-loop conditions. In Section 2.2 the ETFE is discussed in more detail and the challenges in calculating the ETFE are discussed regarding the most relevant effects and error sources. Finally, Section 2.3 addresses the estimation of the frequency response of the plant under closed-loop conditions.

Chapter 3 presents the proposed test-based controller retuning concept. Section 3.1 gives an overview over the proposed procedure. The theoretical contents presented in the following sections are demonstrated based on an illustrative example system, which is introduced in Section 3.2. First, Section 3.3 introduces the made design choices and assumptions. It is followed by the description of the closed-loop test maneuvers in Section 3.4, which are used for estimation of the initial closed-loop frequency response estimate. Section 3.5 describes the estimation of the non-parametric frequency domain estimate of the closed-loop of true plant with initial controller and its statistical properties. The non-parametric frequency domain estimate of the closed-loop of true plant with updated controller parameters is derived in Section 3.6, as well as its statistical properties. This predicted closed-loop behavior is used as described in Section 3.8, via an optimization, to determine new controller parameters. The optimization problem that is formulated for this purpose incorporates constraints on the phase and gain margins to enforce the required stability criteria on the obtained new system with updated controller parameters. These are addressed in Section 3.7. Finally, Section 3.9 and 3.10 present evaluation criteria and and possible adaptations for further applications.

Chapter 4 demonstrates the developed test-based controller retuning concept for an inner-loop controller of a modular, cascaded flight guidance and control system for optionally piloted general aviation (CS-23) aircraft and unmanned systems, that was successfully tested in several flight test campaigns for different platforms. First Section 4.1 briefly presents the demonstration platforms for which the flight control system was developed and demonstrated on. Section 4.2 introduces the controller environment and Section 4.3 the simulation framework. Section 4.4 and 4.5 focus on the longitudinal and lateral inner-loop, respectively. Each of the both sections presents the controller structure, the test-based retuning concept and simulation and flight test results.

Finally, Chapter 5 concludes this thesis, summarizing its achievements as well as open problems and proposes perspectives for future research.

Chapter 2

Theoretical Preliminaries

This chapter addresses the theoretical Preliminaries regarding the estimation of the Frequency Response Function of a linear dynamic system. Section 2.1 focusses on the Empirical Transfer Function Estimate (ETFE) under open-loop conditions, giving and overview and first idea of the concept. In Section 2.2 the ETFE is discussed in more detail and the challenges in calculating the ETFE are discussed regarding the most relevant effects and error sources. Finally, Section 2.3 addresses the estimation of the frequency response of the plant under closed-loop conditions.

2.1 Measuring the Frequency Response Function of a Linear Dynamic System

Estimating the Frequency Response Function (FRF) of a linear dynamic system together with quantifying the quality of that estimate is "*an old problem that is considered to be well solved and completely understood*" [SVBP09]. The inaccuracy in an estimated transfer function can be quantified precisely in terms of bias and variance. In the following subsections the preliminaries for measuring the FRF by an ETFE, are given and related issues are discussed. As it constitutes an old and well understood problem different solutions exist to elude many pitfalls.

2.1.1 Frequency Response Function of a Linear System

The transfer functions of continuous time systems are defined in terms of the Laplace-transform of their input and output signals:

$$G_{yu}(s) = \frac{Y(s)}{U(s)} \tag{2.1}$$

The transfer function of a system characterizes its frequency response. At any frequency ω, $G(s = j\omega)$ is a complex number and hence can be represented by its amplitude and phase according to

$$G(j\omega) = |G(j\omega)|e^{j\angle G(j\omega)} \tag{2.2}$$

The frequency response of the system is given by

$$Y(j\omega) = G(j\omega)U(j\omega) = |G(j\omega)||U(j\omega)|e^{j(\angle G(j\omega)+\angle U(j\omega))}. \tag{2.3}$$

In the discrete case, transfer functions are defined in terms of the z-transform of their input and output signals:

$$G_{yu}(z) = \frac{Y(z)}{U(z)}. \tag{2.4}$$

The bilateral form of the z transform of a signal x is defined as:

$$X(z) = \sum_{n=-\infty}^{+\infty} x[n]z^{-n} \tag{2.5}$$

where $x[n]$ is the $n'th$ time sample of the signal x.

2.1.2 Empirical Transfer Function Estimate

According to Section 2.1.1 the discrete case transfer functions are defined in terms of the z-transform of their input and output signals according to (2.4). To calculate the exact z transform of a signal x the entire dataset from $n = -\infty$ to $n = \infty$ is required as shown in (2.5). In real applications, however only a finite length record can be measured and processed. The discrete transfer functions can be estimated based on finite, discrete measurement data by the so called empirical transfer function estimate (ETFE), [Lju99],

$$\hat{G}_{yu}(j\omega_k) = \frac{Y_{DFT}(j\omega_k)}{U_{DFT}(j\omega_k)} \tag{2.6}$$

where the z- transforms are approximated by the Discrete Fourier Transforms (DFTs) of the input and output signals. The Discrete Fourier Transform (DFT) can be considered as a special case of the z-transform. It calculates the z-transform for a finite number of data samples for z on the complex unit circle, i.e. for $z = e^{j\omega}$ with angular frequency $\omega \in \mathbb{R}$. Consider a discrete time sequence

$$x(t), t = 0, T_s, 2T_s, ..., (N-1)T_s \tag{2.7}$$

with sampling time T_s, sampling frequency $f_s = \frac{1}{T_s}$ and N samples. Note, as it might be confusing, that it takes not $T_w = NT_s$ time to collect the N samples of the data, but $T_w - T_s$. This is visualized in Figure 2.1. This means that for measuring periodic signals with period T_w only a finite time sequence of $T_w - T_s$ is necessary.

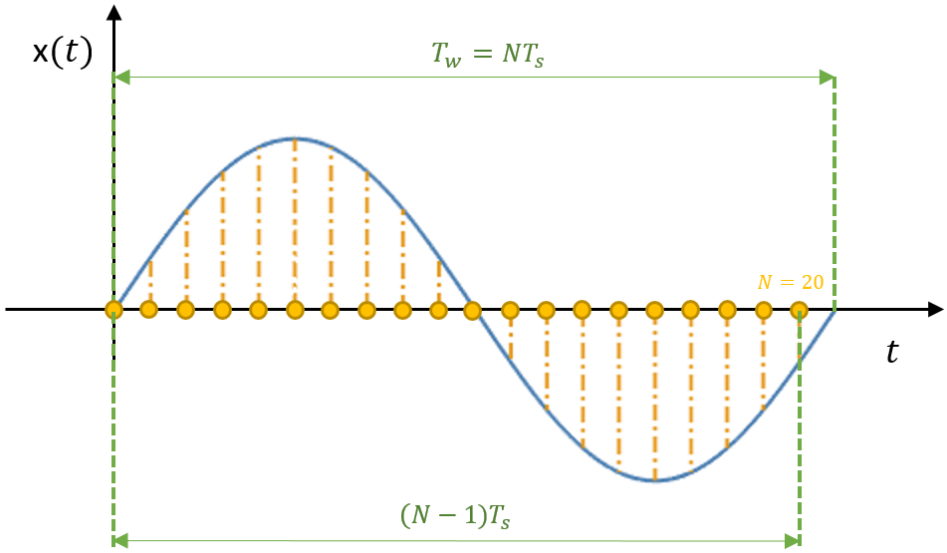

Figure 2.1: *Visualization of T_w.*

The DFT, which is calculated from the discrete time sequence of $x(t)$, evaluates at a discrete frequency set f_k, as integer multiples of the first harmonic frequency $f_H = \frac{1}{T_w} = \frac{1}{NT_s}$, i.e. the discrete sequence

$$f_k = kf_H = k\frac{1}{NT_s}, k = 0, ..., N-1 \tag{2.8}$$

The DFT at the discrete angular frequency $\omega_k = 2\pi f_k$ is calculated according to [PS12] as

$$\begin{aligned} X_{DFT}[k] &= X_{DFT}[j\omega_k] \\ &= \frac{1}{\sqrt{N}} \sum_{n=0}^{N-1} x(nT_s) e^{-j\omega_k(nT_s)} \\ &= \frac{1}{\sqrt{N}} \sum_{n=0}^{N-1} x(nT_s) e^{-\frac{j2\pi kn}{N}}, k = 0, ...N-1 \end{aligned} \tag{2.9}$$

Thereby, a scaling factor of $\frac{1}{\sqrt{N}}$ is used, which returns an averaged amplitude [SVBP09]. Note, that different definitions for the scaling factor can be found in the literature. The *fft* algorithm of MATLAB, which calculates the discrete Fourier transform (DFT) using a fast Fourier transform (FFT) algorithm, applies a different scaling factor for example, and calculates the DFT according to

$$X_{DFT}[k] = \sum_{n=1}^{N} x((n-1)T_s) e^{j\frac{2\pi(k-1)(n-1)}{N}} \tag{2.10}$$

Note, that here $X_{DFT}[k]$ denotes the Fourier coefficient at $\omega_k = 2\pi f_k$, where

$$f_k = (k-1)f_H = (k-1)\frac{1}{NT_s}, k = 1, ..., N \tag{2.11}$$

which is due to the fact that matlab does not support zero indexing. Note, that the DFT evaluates at frequencies which are multiple integers of the first harmonic frequency $f_H = \frac{1}{NT_s}$, which is inversely proportional to the number of measurements N. Consequently the frequency resolution of the DFT is increased if N is increased (while keeping the same sampling rate).
According to [Lju99] the term "*empirical*" in ETFE shall indicate that no other assumptions on the system are made except linearity. It should be noted, that the scaling of the DFT, which, as mentioned, varies in the literature, has no influence on the ETFE estimates when the same scaling for the input and output signals are used.

The ETFE is a non-parametric model. Non-parametric models often share the property that the number of "parameters" grows with the recorded data length. In the case of the ETFE we saw that the frequency resolution of the DFT is inversely proportional to the data length. Consequently, the number of frequencies, where the ETFE estimate is calculated grows proportional to the data length [SVBP09]. In contrast, parametric models are defined by a finite number of parameters. The number of parameters does not depend on the data length. Instead, the number of parameters depends, for example in the case of a transfer function model for a linear dynamic system, on the system characteristics, like the number of poles and zeros. However, the ETFE based on the DFT spectra of the input and output signal measurements as given in (2.6) differs from the true transfer function $G_{yu}(j\omega_k)$. There are different sources for these errors. In the following section the most relevant effects and their influences on the DFT and the ETFE are discussed.

Example 2.1. ***Discrete Fourier Transform of cosine signal***
The following simple example will be used throughout the following sections to illustrate the presented theory with regard to the different concepts of measuring the FRF, their relations, differences and drawbacks or issues. As example a cosine signal will be used, as periodic functions can be expressed as the sum of sines and cosines through Fourier Series. Since later, multi-sine signals will be used in the flight test-based gain tuning concept, this simple example is suitable to illustrate the presented theory and to demonstrate the expected issues. Consider a cosine signal of the form

$$x(t) = A_x \cos(2\pi f_x t) \tag{2.12}$$

with amplitude A_x and angular frequency $\omega_x = 2\pi f_x$ where f_x is chosen as an integer multiple of the first harmonic frequency f_H in this example and $f_x \leq f_s/2$. The second assumption is important in order to prevent aliasing as will be shown and explained later.

With $f_x = m_x f_H = m_x \frac{1}{NT_s}$, $m_x \in \{m_x \in \mathbb{N} \mid m_x \leq \frac{N}{2}\}$ *the sampled signal* $x(t)$ *is expressed as*

$$x(nT_s) = A_x \cos(2\pi f_x(nT_s)) = A_x \cos(2\pi \frac{m_x n}{N}) \tag{2.13}$$

The DFT according to Equation (2.10) *or* (2.9) *will provide the two-sided spectrum. Meaning that the amplitude*$|X_{DFT}|$ *plotted over* f_k *will be zero except for* $f = f_x$ *and* $f = f_s - f_x$. *The peak at these frequencies will have a value of*

$$|X_{DFT}(f_x)| = |X_{DFT}(f_s - f_x)| = \frac{A_x}{2} N \tag{2.14}$$

in case the FFT algorithm of MATLAB was used and

$$|X_{DFT}(f_k)| = |X_{DFT}(f_s - f_x)| = \frac{A_x}{2} \sqrt{N} \tag{2.15}$$

in case that Equation (2.9) *was used for calculating the DFT. The latter case is demonstrated in the following:*
Derivation. Based on the relations

$$e^{j\omega} = \cos(\omega t) + j \sin(\omega t) \tag{2.16}$$

and

$$e^{-j\omega} = \cos(\omega t) - j \sin(\omega t) \tag{2.17}$$

sines and cosines can be rewritten as complex exponentials:

$$e^{j\omega t} + e^{-j\omega t} = 2\cos(\omega t) \Rightarrow \cos(\omega t) = \frac{e^{j\omega t} + e^{-j\omega t}}{2} \tag{2.18}$$

and

$$e^{j\omega t} - e^{-j\omega t} = 2j \sin(\omega t) \Rightarrow \sin(\omega t) = \frac{e^{j\omega t} - e^{-j\omega t}}{2j} \tag{2.19}$$

The DFT of the cosine signal (2.13) *using* (2.9) *is*

$$\begin{aligned} X_{DFT}(k) &= \frac{1}{\sqrt{N}} \sum_{n=0}^{N-1} (A_x \cos(2\pi \frac{m_x n}{N})) e^{-\frac{j2\pi kn}{N}} \\ &= \frac{A_x}{\sqrt{N}} \sum_{n=0}^{N-1} (\frac{e^{j(2\pi \frac{m_x n}{N})} + e^{-j(2\pi \frac{m_x n}{N})}}{2}) e^{-\frac{j2\pi kn}{N}} \\ &= \frac{A_x}{2\sqrt{N}} \sum_{n=0}^{N-1} (e^{-j2\pi \frac{(k-m_x)n}{N}} + e^{-j2\pi \frac{(k+m_x)n}{N}}) \end{aligned} \tag{2.20}$$

For $k = m_x$ *it can be immediately seen that the first term of the sum becomes* N. *For* $k \neq m_x$

$$\sum_{n=0}^{N-1} e^{-j2\pi \frac{(k-m_x)n}{N}} = 0 \tag{2.21}$$

holds, which can be derived using the formula for geometric series given by

$$\sum_{n=0}^{N-1} r^n = \frac{1-r^N}{1-r} \tag{2.22}$$

for $r \neq 1$. *With* $r = e^{-j2\pi\frac{(k-m_x)}{N}}$, (2.22) *becomes*

$$\sum_{n=0}^{N-1} (e^{-j2\pi\frac{(k-m_x)}{N}})^n = \frac{1-e^{-j2\pi(k-m_x)}}{1-e^{-j2\pi\frac{(k-m_x)}{N}}} = \frac{1-e^{-j2\pi k}e^{j2\pi m_x}}{1-e^{-j2\pi\frac{(k-m_x)}{N}}} \tag{2.23}$$

Since k *and* m_x *are integers and* $e^{j2\pi p} = 1$ *for any integer* p, (2.23) *will be* 0 *except for* $k = m_x$ *where* $r = 1$ *and the sum becomes* N.
Multiplication of the second exponential term in (2.20) *with* $1 = e^{j2\pi n}$ *results in*

$$\sum_{n=0}^{N-1} e^{-j2\pi\frac{(k+m_x)n}{N}} e^{j2\pi n\frac{N}{N}} = \sum_{n=0}^{N-1} e^{-j2\pi\frac{(k-(N-m_x)n}{N}} \tag{2.24}$$

Using again the geometric series formula it can be shown that (2.24) *is* N *for* $k = N - m_x$ *and* 0 *for* $k \neq N - m_x$. *Consequently* (2.20) *becomes* $A_x\sqrt{N}/2$ *for* $k = m_x$ *or* $k = N - m_x$ *and* 0 *for all other* k*:*

$$X_{DFT}(k) = \begin{cases} \frac{A_x}{2}\sqrt{N} & \text{for } k = m_x \text{ or } k = N - m_x \\ 0 & \text{otherwise} \end{cases} \tag{2.25}$$

The DFT in (2.20), *hence, provides the two-sided spectrum, meaning that there will be a peak at* f_x *and at* $f_s - f_x$. *For reconstructing the amplitude of the signal* x *the amplitude of the conjugate complex* $X_{DFT}(k)$ *for the first half of frequencies needs to be doubled. Thereby, the amplitudes at the first frequency at* $f_0 = 0$ *and* $f_{N/2} = f_s/2$ *are excluded from doubling and are considered only once. Division of the so obtained amplitude by* $\sqrt{N}$ *if Equation* (2.9) *was used or rather by* N *if the FFT algorithm of MATLAB was used, results in a value which exactly corresponds to* A_x. *Note, that the MATLAB "angle" command, interprets the signal as a cosine. Hence, when calculating the phase of the complex number* X_{DFT} *using "angle" and the signal* x *was a sinus, then the resulting phase will be shifted by* 90 *degrees* ($\pi/2$) *as* $\sin(x + \phi) = \cos(x + \phi - \pi/2)$.

2.2 Challenges in Measuring the Frequency Response Function

To understand the most relevant effects and error sources when calculating the ETFE it is essential to understand how the Fourier Transform (FT), the discrete Time Fourier Transform (DTFT) and the discrete Fourier Transform (DFT) are connected and what their application, purpose and reasoning is.

2.2.1 Fourier Transform and Fourier Series

Many time-varying signals have a spectrum, meaning that the signal can be expressed depending on a continuum of frequencies. The Fourier transform allows to transform a time-varying signal, which is a representation in "time domain", into the "frequency domain", meaning a function depending on the frequency. The inverse of the Fourier transform allows to transform the signal back into time domain. Hence, the representations in frequency and time domain are for many types of functions equivalent [Osg19]. The Fourier transform or spectrum of an infinite long continuous signal $x(t)$ is defined as [Pap62, p. 1]

$$X_{FT}(f) = \mathcal{F}\{x(t)\} = \int_{-\infty}^{\infty} x(t)e^{-j2\pi ft}dt \tag{2.26}$$

and in terms of angular frequency $\omega = 2\pi f$ as

$$X_{FT}(\omega) = \mathcal{F}\{x(t)\} = \int_{-\infty}^{\infty} x(t)e^{-j\omega t}dt \tag{2.27}$$

It is possible to represent the signal $x(t)$ by its inverse

$$x(t) = \mathcal{F}^{-1}\{X_{FT}(f)\} = \int_{-\infty}^{\infty} X_{FT}(f)e^{j2\pi ft}df \tag{2.28}$$

In terms of angular frequency the integral becomes with change of variables by substitution with $\frac{d\omega}{df} = 2\pi$, hence $df = \frac{d\omega}{2\pi}$

$$x(t) = \mathcal{F}^{-1}\{X_{FT}(\omega)\} = \frac{1}{2\pi}\int_{-\infty}^{\infty} X_{FT}(\omega)e^{j\omega t}d\omega \tag{2.29}$$

Note, that in literature different definitions can be found, introducing a factor of $\frac{1}{2\pi}$ in (2.27) instead in (2.29), or $\frac{1}{\sqrt{2\pi}}$ in both equations. Even a change of the sign of the exponent is possible [Pap62]. As a consequence the confusion is often very high. This is emphasized by a very representative sentence from the Flying qualities of piloted aircraft handbook, MIL-STD-1797A, published by the US department of defense, when

dealing with the implementation matters of atmospheric disturbance models and with spectral forms: "*This matter is particularly confusing because spectral forms are written in a number of ways - one-sided or two-sided, in terms of spatial or temporal frequency, or in terms of angular or cyclical frequency. ...* ***Finally, when using the more complex models it seems nearly impossible to formulate a program without an error involving a factor of*** 2 ***or*** π ***"***[US 97, p. 694]. Therefore, this thesis starts with the definition of the Fourier transform and Fourier series, to provide in a complete and consistent manner the addressed relations. In the appendix detailed derivations of the given relations can be found, because in literature often important or tedious steps are left out, which makes it difficult to understand why the stated formulas or why certain relations hold.
Fourier transforms were motivated by the study of Fourier series, where complicated but periodic functions with period T can be expressed as the sum of sines and cosines. Under certain conditions a signal $x(t)$ can be such written as the sum [Pap62, p. 1]

$$x(t) = \sum_{n=-\infty}^{\infty} C_n e^{j\omega nt} \tag{2.30}$$

with $\omega = 2\pi f = \frac{2\pi}{T}$ and where the coefficients are given by

$$C_n = \frac{1}{T} \int_{-T/2}^{T/2} x(t) e^{-j\omega nt} dt \tag{2.31}$$

The Fourier transform is often interpreted as the decomposition of waves into sinusoids or as a transformation from time domain to frequency domain. Sines and cosines can be rewritten as complex exponentials:

$$e^{j\Phi} = cos(\Phi) + jsin(\Phi) \tag{2.32}$$

where the current angle is $\Phi = 2\pi t$ and the wave $e^{j\Phi}$ completes one cycle per second if t is measured in seconds.

Example 2.2. ***Fourier Transform of cosine signal***
For our cosine signal example $x(t) = A_x cos(2\pi f_x)$, which was introduced in Section 2.1.1, the Fourier transform at angular frequency $\omega = 2\pi f$ is given as

$$X_{FT}(f) = \mathcal{F}\{x(t)\} = \int_{-\infty}^{\infty} A_x cos(2\pi f_x) e^{-j2\pi ft} dt \tag{2.33}$$

Using (2.18), (2.33) *becomes*

$$\begin{aligned} X_{FT}(f) &= \int_{-\infty}^{\infty} A_x \frac{e^{-j2\pi f_x t} + e^{j2\pi f_x t}}{2} e^{-j2\pi ft} dt \\ &= \frac{A_x}{2} \int_{-\infty}^{\infty} (e^{-j2\pi(f+f_x)t} + e^{-j2\pi(f-f_x)t}) dt \end{aligned} \tag{2.34}$$

It is commonly known in literature, that the infinite integral of the complex exponential function is (see Lemma B.0.1):

$$\int_{-\infty}^{\infty} e^{-j2\pi ft} dt = \delta(f) \tag{2.35}$$

where $\delta(f)$ is the Dirac impulse, Definition A.0.1. Using (2.35) *in* (2.34) *leads to*

$$X_{FT}(f) = \frac{A_x}{2} \left(\delta(f + f_x) + \delta(f - f_x)\right) \tag{2.36}$$

This result shows that there will be two infinite peaks at $f = \pm f_x$. The amplitude of the cosine signal can be reconstructed from the Fourier transform by integrating over the frequency of the cosine signal as follows

$$\begin{aligned} \int_{-f_x-\epsilon}^{-f_x+\epsilon} X_{FT}(f) df + \int_{f_x-\epsilon}^{f_x+\epsilon} X_{FT}(f) df &= \frac{A_x}{2} \left(\int_{-f_x-\epsilon}^{-f_x+\epsilon} \delta(f + f_x) df + \int_{-f_x-\epsilon}^{-f_x+\epsilon} \delta(f - f_x) df \right) \\ &+ \frac{A_x}{2} \left(\int_{f_x-\epsilon}^{f_x+\epsilon} \delta(f + f_x) df + \int_{f_x-\epsilon}^{f_x+\epsilon} \delta(f - f_x) df \right) \\ &= A_x \end{aligned} \tag{2.37}$$

The integral was found using the sifting property, Property A.0.1, of the Dirac impulse, resulting in property (A.4) *given by*

$$\int_{t_1}^{t_2} \delta(t - t_0) dt = 1 \tag{2.38}$$

for $t_1 < t_0 < t_2$. Note, that if the investigated signal is composed of a sum of multiple cosines, there will be diracs at each frequency, associated with their respective amplitude.

2.2.2 Sampling - Relation between DTFT and FT

Section 2.1.2 introduced the ETFE as the ratio of the DFT spectra of the output and input signal measurements (2.6). Ideally the ETFE would be calculated using the Fourier transforms of the signals. Due to different reasons it is not possible to calculate the FT in many real world applications: First, for digital systems, continuous signals of physical quantities can only be measured at discrete time steps at some sampling frequency f_s. The signal behavior between these time steps is unknown and only the measured discrete values are stored and processed in computers. Additionally, the measured signals are not infinitely long. Hence, it is not possible to calculate the Fourier transform $X_{FT}(\omega)$ of the continuous signal $x(t)$, and instead the frequency response of a transfer function is estimated over the ETFE by calculating the discrete Fourier transforms of the finite length sampled input and output signals. When calculating the DFT different essential errors in the calculated Fourier spectra can occur if for example the sampling or the observation/measurement time is chosen inappropriately. This section deals with the sampling effects. The next section will further investigate the effects related to finite observation length.
In order to understand the effects, when calculating the DFT of a sampled signal, we will first investigate the discrete time Fourier transform (DTFT), as this deals with the sampling process, and how the DTFT differs from the FT of the continuous signal. In contrast to the DFT the DTFT assumes an infinite long signal. But the DFT and DTFT have in common that they are applied to a signal which is a discrete sequence. The DTFT according to [Rao08, p. 194] can be defined by

$$\begin{aligned} X_{DTFT}(\omega) &= \sum_{n=-\infty}^{\infty} x[n] e^{-j\omega(nT_s)} \\ X_{DTFT}(f) &= \sum_{n=-\infty}^{\infty} x[n] e^{-j2\pi f(nT_s)} \end{aligned} \tag{2.39}$$

where $\omega = 2\pi f = \frac{2\pi}{T}$ and $x[n]$ is a discrete sequence of the measured signal's samples given by

$$x[n] = x(nT_s) \tag{2.40}$$

with the sampling time T_s. Note, that the DTFT in (2.39) is continuous in ω or f. It shall be not confused with the sampling frequency $f_s = 1/T_s$ of the discrete sequence (2.40). Another common definition of the DTFT is given by [Pou18, p. 17-1]

$$X_{DTFT}(\bar{\omega}) = \sum_{n=\infty}^{\infty} x[n] e^{-j\bar{\omega}n} \tag{2.41}$$

where $\bar{\omega} = \omega T_s$ is the frequency in radians per sample and not radians per second like in (2.39). By Lemma C.0.1, the DTFT (2.39) can be equally expressed by

$$T_s X_{DTFT}(f) = \sum_{k=-\infty}^{\infty} X_{FT}(f - kf_s) \tag{2.42}$$

This result shows that by calculating the DTFT (2.39) with the discrete sequence $x[n]$ of the sampled signal $x(nT_s)$, the Fourier transform $X_{FT}(f)$ of the continuous signal $x(t)$ is still entailed. But there will be also copies of $X_{FT}(f)$ with a distance of kf_s as the sum in (2.42) constitutes a periodic repetition of $X_{FT}(f)$. Note, that dependent on the definition of the DTFT you choose, there may exist a scaling between the DTFT and FT coefficients. For this specific choice of the DTFT (Equation (2.39)) there will be a scaling factor of T_s. Figure 2.2 shows the FT and DTFT for the cosine signal $x(t) = A_x \cos(2\pi f_x)$ from our example with $f_x < f_s/2$. The continuous FT transform of $x(t)$ is depicted as the blue spectrum, see also Equation (2.37). The DTFT is the green spectrum and results from the repetition of the FT with period kf_s. To obtain the FT from the DTFT only frequencies from $-f_s/2$ to $f_s/2$ shall be considered, due to the repetitions.

Figure 2.3 shows the FT and DTFT for the cosine signal $x(t) = A_x \cos(2\pi f_x)$ from our example with $f_x > f_s/2$. As the DTFT results from the folding of the FT with period kf_s the DTFT will entail non-zero values in the frequency range from $-f_s/2$ to $f_s/2$, though the FT is zero in this frequency range. This makes it difficult to determine the original frequency of the cosine signal. If the signal is restricted to contain only frequencies smaller than $f_s/2$ this problem does not occur. Figure 2.4 visualizes this folding effect in a schematic. Assume that in blue the Fourier Transform of some signal is given. We see that the signal entails also frequencies larger than $f_s/2$. The DTFT for the frequency range $-f_s/2$ to $f_s/2$ is depicted in green. It obviously differs from the FT of the signal as the high frequency content of the FT is folded down to the considered frequency range. This is called aliasing. **It can be summarized that aliasing can be avoided in case that the frequency content of the considered signal is below $f_s/2$, meaning that the signal is *band limited*. The frequency $f_{Ny} = f_s/2$ is called *Nyquist frequency*.**

In literature the sampling of a continuous signal $x(t)$ is often modelled as a multiplication with a dirac comb

$$\mathrm{III}_{T_s}(t)x(t) \tag{2.43}$$

where

$$\mathrm{III}_{T_s}(t) = \sum_{n=-\infty}^{\infty} \delta(t - nT_s) \tag{2.44}$$

A dirac comb is an impulse train, where the dirac impulses are periodically repeated with period T_s. Note, that this is not equal to the sampled signal $x(nT_s)$. It is rather a mathematical representation that is often used in literature to gain insight into the properties of the DTFT/DFT. The Fourier transform of (2.43) is equal to the DTFT of

the sampled sequence $x(nT_s)$ by Lemma F.0.1.

$$\mathcal{F}\{\mathrm{III}_{T_s}(t)x(t)\} = X_{DTFT}(f) \tag{2.45}$$

We will use this construct in the next section to obtain more insight into the effects related to finite observation length.

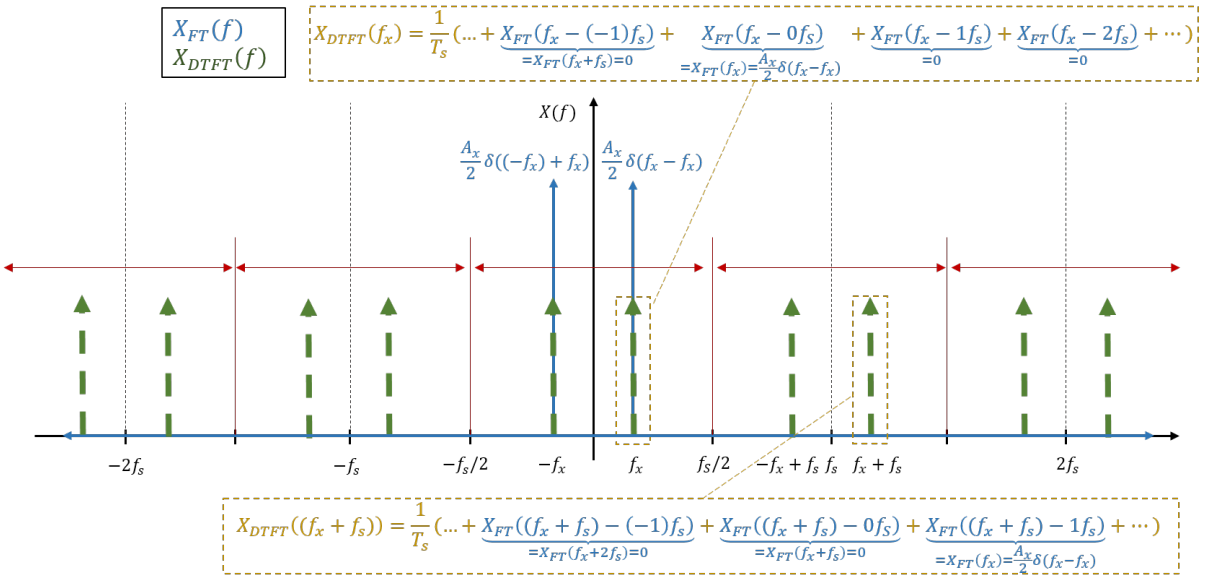

Figure 2.2: *Fourier Transform and Discrete Fourier Transform of cosine example signal with* $f_x < f_s/2$.

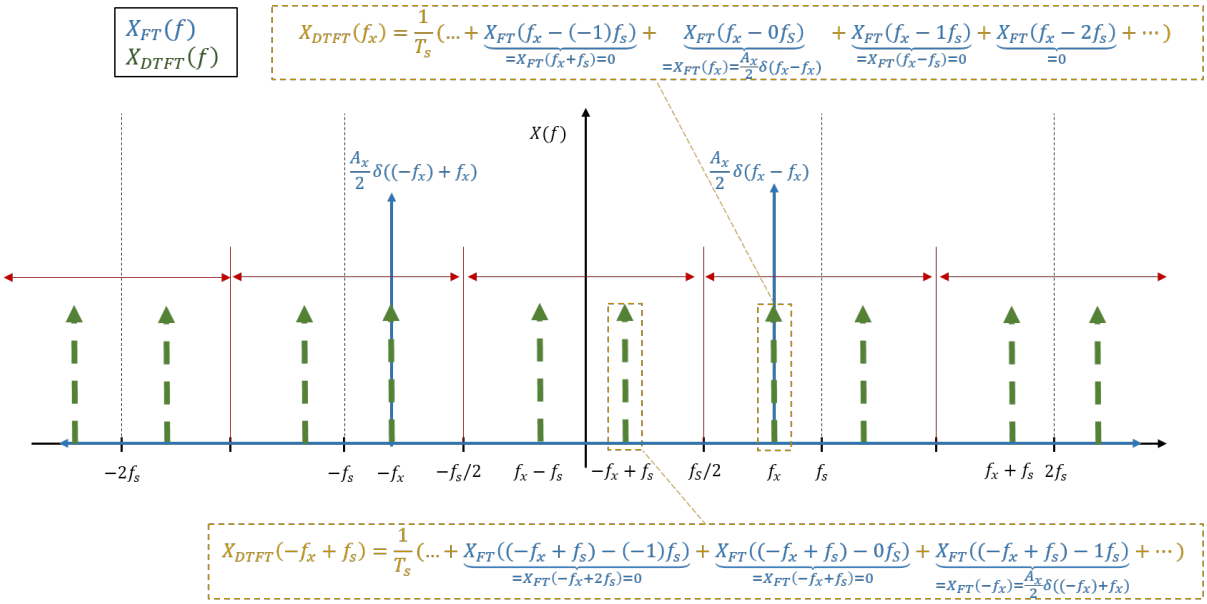

Figure 2.3: *Fourier Transform and Discrete Fourier Transform of cosine example signal with* $f_x > f_s/2$.

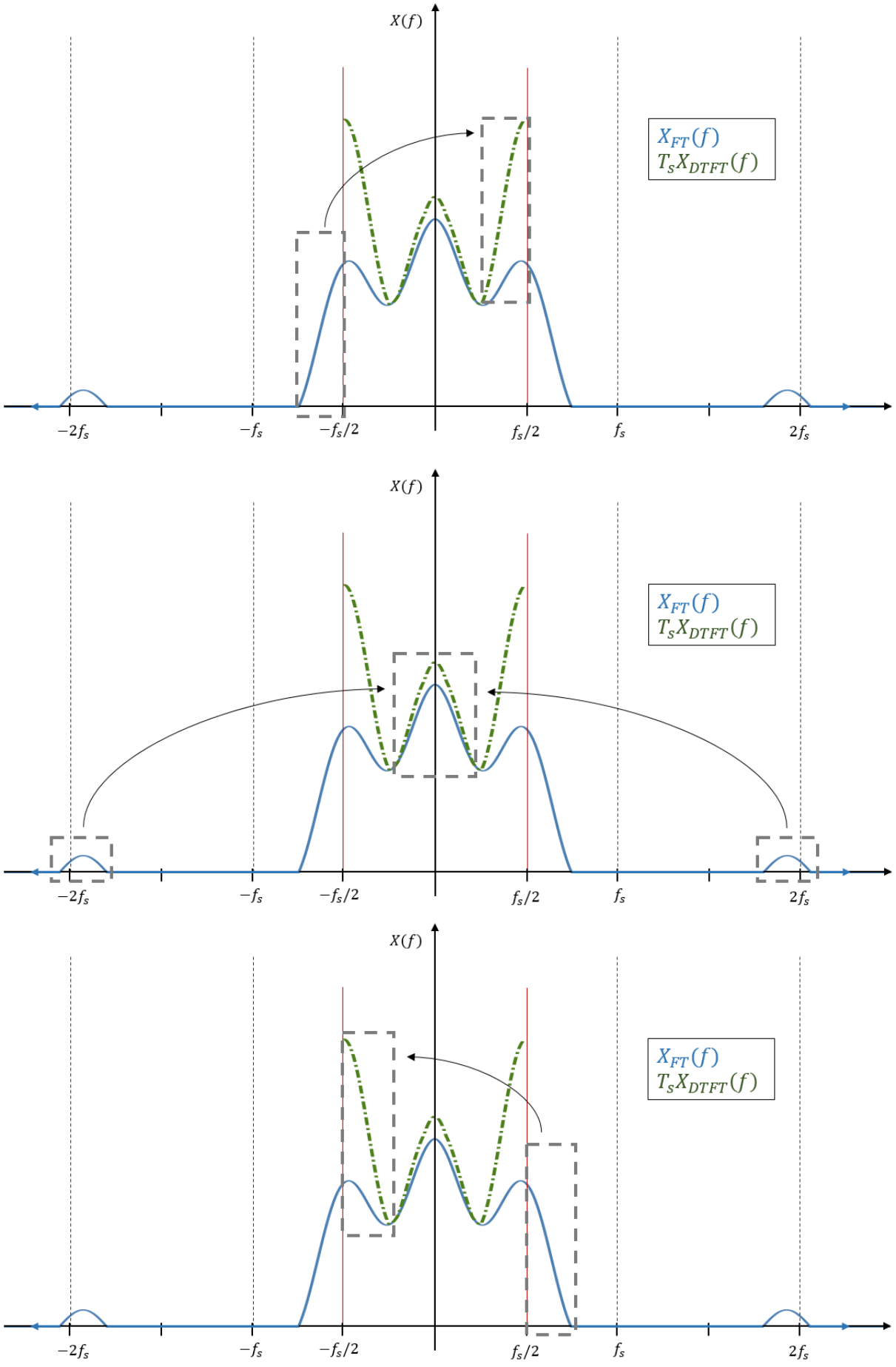

Figure 2.4: *Visualization of aliasing.*

2.2.3 Truncation (Finite Length Signals)

In Section 2.2.2 the DTFT was introduced as a possibility to calculate the Fourier transform of a signal $x(t)$, where only the discrete samples $x(nT_s)$ are available. Conditions for which the FT can be obtained over the DTFT were discussed as well as errors (aliasing) that might occur if the sampling frequency is chosen inappropriately or the signal is not band limited. But the DTFT requires an infinite long discrete sequence of $x(t)$. This is not possible in applications. Measurement records are restricted to a finite length. This section shows that with the Discrete Fourier Transform (DFT) the values of the Fourier Transform at discrete frequencies can be obtained for finite length, band limited, sampled periodic signals if the measurement or observation time is chosen appropriately. Furthermore, the modelling of finite length signals using so called windowing functions is discussed. The resulting construct is used to gain insight into errors that occur if the number of available samples of the signal $x(t)$ is inappropriate. These effects are called leakage.

2.2.3.1 Relation between DTFT and DFT

In Section 2.2.2 the DTFT was introduced by

$$X_{DTFT}(f) = \sum_{n=-\infty}^{\infty} x[n] e^{-j2\pi f(nT_s)} \tag{2.46}$$

with the discrete sequence $x[n] = x(nT_s)$ which is composed of the samples of $x(t)$ at sampling frequency $f_s = \frac{1}{T_s}$. As introduced in Section 2.2.2, by Lemma C.0.1, the DTFT corresponds to

$$X_{DTFT}(f) = \frac{1}{T_s} \sum_{r=-\infty}^{\infty} X_{FT}(f - r f_s) \tag{2.47}$$

meaning that the FT of the continuous signal $x(t)$ can be reconstructed by application of the DTFT to the infinite discrete sequence $x(nT_s)$. Therefore, the signal needs to be band limited such that no frequencies larger than the nyquist frequency $f_{Ny} = \frac{f_s}{2}$ are contained in the signal. Otherwise, the aliasing effect will introduce errors to the frequency spectrum. If the signal $x(t)$ is periodic with period $T_w = NT_s$, meaning

$$x(t) = x(t + mT_w) \tag{2.48}$$

with $m \in \mathbb{Z}$, where $\mathbb{Z}$ is the set of integers, and where N is the number of measured equidistant samples of $x(t)$, and when the DTFT is evaluated at discrete frequencies

$$f_k = k f_H \tag{2.49}$$

which are integer multiples of the harmonic frequency $f_H = \frac{1}{T_w}$, then by Lemma H.0.1, the following relation holds

$$X_{DTFT}(f_k) = \frac{1}{\sqrt{N}T_s}\delta(0)X_{DFT}[k] = \frac{1}{NT_s}\delta(0)\sum_{n=0}^{N-1} x[n]e^{-\frac{j2\pi kn}{N}} \tag{2.50}$$

This relation holds under the condition that the signal $x(t)$ is periodic with period $T_w = NT_s$ and shows that X_{DFT} (2.9), will equal X_{DTFT} scaled with factor $\frac{1}{\sqrt{N}T_s}\delta(0)$. This means that for periodic signals with period T_w only a finite time sequence of $x(t)$ of $T_w - T_s$ is necessary to exactly calculate the DTFT, which would otherwise require an infinite time sequence of $x(t)$. We have now arrived at a construct that is implementable on a digital computer and that, as desired, exactly recovers the FT under certain conditions as was shown in Section 2.2.2. Note, as it might be confusing, that it takes not T_w time to collect the N samples of the data, but $T_w - T_s$. This is visualized in Figure 2.1.

2.2.3.2 Leakage

A finite time sequence can be modelled as a multiplication of the infinite sequence $x(nT_s)$ with a rectangular window function $w(t)$, see Figure 2.5. This window function equals one

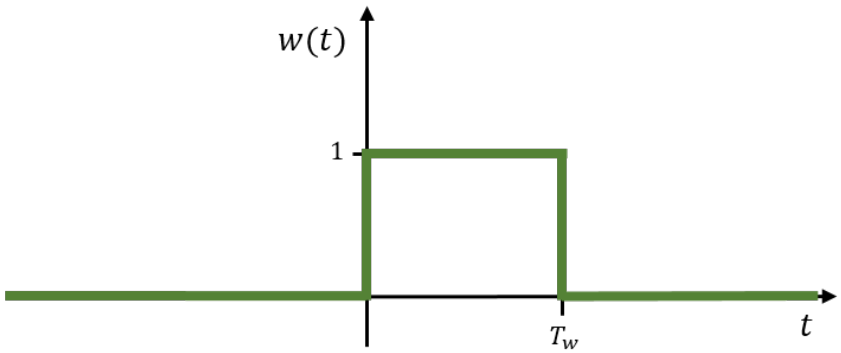

Figure 2.5: *Rectangular window function in time domain.*

during the experiment and is zero outside the observation interval $[0, T_w]$, where $T_w = NT_s$ is the window length with the sampling time T_s and where N is the number of samples of $x(t)$. The rectangular window function is defined by

$$w(t) = \begin{cases} 1 & \text{for } 0 \leq t < T_w \\ 0 & \text{otherwise} \end{cases} \tag{2.51}$$

Other window functions exist for different purposes. In most cases the window functions are non-zero during the observation and zero outside the measurement interval. From (2.45) we know that the DTFT of $x(nT_s)$, equals the Fourier transform of the continuous signal $x(t)$ multiplied with a dirac comb, which is often used as a model of the sampling

process:

$$X_{DTFT}(f) = \mathcal{F}\{\mathrm{III}_{T_s}(t)x(t)\} = \mathcal{F}\{\sum_{n=-\infty}^{\infty} \delta(t - nT_s)x(t)\} \tag{2.52}$$

If we now additionally apply the rectangular window function to $x(t)$, we obtain a continuous time mathematical model of the truncated sampled sequence of $x(t)$:

$$\tilde{x}(t) = \mathrm{III}_{T_s}(t)x(t)w(t) \tag{2.53}$$

By Lemma J.0.1, the FT of (2.53), equals the DFT, (2.9), of $x(nT_s)$ at the discrete frequencies $f = kf_H$, $k \in \mathbb{Z}$ and scaled with factor $\sqrt{N}$:

$$\tilde{X}_{FT}(kf_H) = \mathcal{F}\{\mathrm{III}_{T_s}(t)x(t)w(t)\} = \sqrt{N}X_{DFT}[k] \tag{2.54}$$

Note, that the Fourier transform of $\tilde{x}$, by Lemma K.0.1, can also be expressed by

$$\begin{aligned} \tilde{X}_{FT}(f) &= \mathcal{F}\{\mathrm{III}_{T_s}(t)x(t)w(t)\} \\ &= \mathcal{F}\{\mathrm{III}_{T_s}(t)x(t)\} * \mathcal{F}\{w(t)\} \\ &= \int_{-\infty}^{\infty} X_{DTFT}(\bar{f})T_w\mathrm{sinc}(\pi(f - \bar{f})T_w)e^{-j\pi(f-\bar{f})T_w}d\bar{f} \end{aligned} \tag{2.55}$$

At the discrete bin frequencies $f = kf_H$, $k \in \mathbb{Z}$, the Fourier transform (2.55) equals

$$\begin{aligned} \tilde{X}_{FT}(kf_H) &= \int_{-\infty}^{\infty} X_{DTFT}(\bar{f})T_w\mathrm{sinc}(\pi(kf_H - \bar{f})T_w)e^{-j\pi(kf_H-\bar{f})T_w}d\bar{f} \\ &= T_w\int_{-\infty}^{\infty} X_{DTFT}(\bar{f})g(\bar{f}, kf_H)d\bar{f} \end{aligned} \tag{2.56}$$

where

$$g(\bar{f}, kf_H) = \mathrm{sinc}(\pi(kf_H - \bar{f})T_w)e^{-j\pi(kf_H-\bar{f})T_w} \tag{2.57}$$

This result provides insight into the occurring effects due to windowing or finite time domain data samples. These are visualized and explained based on our example with the cosine signal $x(t) = A_x cos(2\pi f_x)$. In Section 2.2.2 the DTFT of this signal was depicted for the cases: $f_x < \frac{f_s}{2}$ and $f_x > \frac{f_s}{2}$ in order to visualize the aliasing effect, which is connected to the sampling process. Here we will focus on the case that $f_x < \frac{f_s}{2}$, because we aim to investigate the effects related to the finite observation length. Furthermore, we will distinguish 2 cases:

- $f_x = mf_H = m\frac{1}{T_w} = m\frac{1}{NT_s}$, $m \in \mathbb{Z}$, meaning, the signal $x(t)$ is periodic with period T_w. Thus, f_x is a multiple integer of the harmonic frequency $f_H = \frac{1}{T_w}$
- $f_x \neq mf_H$, meaning, the cosine frequency is not a multiple integer of f_H.

The function $g(\bar{f}, f = kf_H)$, (2.57), is depicted in Figure 2.6 over $\bar{f}$, at the discrete bin frequencies $f = kf_H$ for $k = 0$, $k = 1$ and $k = 2$. For each of these frequencies, the absolute value, the real part and the imaginary part of (2.57) are shown. Note, that for

$\bar{f} = lf_H$, $l \in \mathbb{Z}$, the real and imaginary parts and hence the absolute value of $g(\bar{f}, f)$ are zero, except for $\bar{f} = f = kf_H$, where the absolute value and the real value equal 1. Note also, how $g(\bar{f}, kf_H)$ is shifted with k.

Figure 2.7 depicts in blue, the FT of the cosine signal $x(t) = A_x cos(2\pi f_x)$, where $f_x = 2f_H < \frac{f_s}{2}$, and in green the respective DTFT. As already explained in Section 2.2.2 the DTFT of $x(nT_s)$ will recover the FT of $x(t)$ with a scaling in the frequency interval $-\frac{f_s}{2} < f < \frac{f_s}{2}$, as $f_x < \frac{f_s}{2}$. Figure 2.7 is separated into 3 subplots, showing $X_{FT}(\bar{f})$, $X_{DTFT}(\bar{f})$ and $\left|g(\bar{f}, kf_H)\right|$ and $\tilde{X}_{FT}(kf_H)$ for $k = 0$, $k = 1$ and $k = 2$. The first subplot shows $\left|g(\bar{f}, kf_H)\right|$ and $\tilde{X}_{FT}(kf_H)$ for $k = 0$. At the bin frequencies $\bar{f} = lf_H$, $l \in \mathbb{Z}$, $g(\bar{f}, 0)$ is zero except for $l = k = 0$, because of

$$\text{sinc}(\pi(0f_H - lf_H)T_w) = \frac{\sin(-\pi l f_H T_w)}{-\pi l f_H T_w} = \frac{\sin(\pi l)}{\pi l} = \begin{cases} 1 & \text{for } l = 0 \\ 0 & l \in \mathbb{Z} \setminus \{0\} \end{cases} \tag{2.58}$$

Consequently, as can be directly seen in the same subplot, the multiplication of $X_{DTFT}(\bar{f})$ with $g(\bar{f}, 0)$ will result in zero for all $\bar{f}$. Hence, the integral (2.56) and consequently $\tilde{X}_{FT}(f = 0)$ are zero, too.

The second subplot in Figure 2.7 shows $\left|g(\bar{f}, kf_H)\right|$ and $\tilde{X}_{FT}(f = kf_H)$ for $k = 1$. Compared to $\left|g(\bar{f}, 0)\right|$, $\left|g(\bar{f}, f_H)\right|$ is shifted by f_H to the right. Again it can be seen that $\tilde{X}_{FT}(f = f_H)$ will be zero as $g(\bar{f}, f_H)$ is zero for $\bar{f} = lf_H$, except for $l = k = 1$, because

$$\text{sinc}(\pi(1f_H - lf_H)T_w) = \frac{\sin(\pi(1-l)f_H T_w)}{\pi(1-l)f_H T_w} = \frac{\sin(\pi(1-l))}{\pi(1-l)} = \begin{cases} 1 & \text{for } l = 1 \\ 0 & l \in \mathbb{Z} \setminus \{1\} \end{cases} \tag{2.59}$$

The third subplot in Figure 2.7 shows $\left|g(\bar{f}, kf_H)\right|$ and $\tilde{X}_{FT}(kf_H)$ for $k = 2$, meaning at frequency $2f_H$, which is the chosen cosine frequency f_x. The resulting value of the Fourier transform of $\tilde{x}(t)$ at this frequency will equal

$$\begin{aligned} \tilde{X}_{FT}(f = 2f_H) &= T_w \int_{-\infty}^{\infty} X_{DTFT}(\bar{f}) g(\bar{f}, 2f_H) d\bar{f} \\ &= T_w \int_{-\infty}^{\infty} \frac{1}{T_s} \sum_{r=-\infty}^{\infty} X_{FT}(\bar{f} - rf_s) g(\bar{f}, 2f_H) d\bar{f} \end{aligned} \tag{2.60}$$

where (2.47) was inserted for X_{DTFT}. For our cosine example the FT is given by (2.36) and f_x is chosen as $f_x = 2f_H$. Hence,

$$\begin{aligned}\tilde{X}_{FT}(f=f_x) &= \frac{T_w}{T_s}\int_{-\infty}^{\infty}\sum_{r=-\infty}^{\infty}\frac{A_x}{2}(\delta(\bar{f}-rf_s+f_x)+\delta(\bar{f}-rf_s-f_x))g(\bar{f},2f_H)d\bar{f}\\ &= N\int_{-\infty}^{\infty}\sum_{r=-\infty}^{\infty}\frac{A_x}{2}(\delta(\bar{f}-rf_s+2f_H)+\delta(\bar{f}-rf_s-2f_H))g(\bar{f},2f_H)d\bar{f}\end{aligned} \tag{2.61}$$

The sampling frequency is a multiple integer of the harmonic frequency, $f_s = Nf_H$, because $f_H = \frac{1}{NT_s} = \frac{1}{N}f_s$. Hence, (2.61) can be written as

$$\tilde{X}_{FT}(f=f_x) = N\int_{-\infty}^{\infty}\sum_{r=-\infty}^{\infty}\frac{A_x}{2}\left(\delta(\bar{f}-(rN-2)f_H)+\delta(\bar{f}-(rN+2)f_H)\right)g(\bar{f},2f_H)d\bar{f} \tag{2.62}$$

This shows that the dirac impulses will be only non-zero at frequencies $\bar{f} = (rN-2)f_H$ with $r \in \mathbb{Z}$. These frequencies are multiple integers of f_H. The term $g(\bar{f},2f_H)$ instead is zero for all $\bar{f} = lf_H$ except for $\bar{f} = 2f_H$, where it equals 1. Hence, (2.62) can be reduced to

$$\begin{aligned}\tilde{X}_{FT}(f=f_x) &= N\int_{-\infty}^{\infty}\frac{A_x}{2}(\delta(\bar{f}+2f_H)+\delta(\bar{f}-2f_H))d\bar{f}\\ &= NA_x\end{aligned} \tag{2.63}$$

where the integral was found using the sifting property of the dirac impulse, Property A.0.1, Equation (A.4). Next the case is considered that f_x is not an multiple integer of f_H. Figure 2.8 shows the FT of the corresponding continuous time signal $x(t)$, the DTFT of the infinite long time sequence $x(nT_s)$ and $\left|g(\bar{f},0)\right|$. It can be seen that at frequency $f = 0f_H$ the Fourier transform of $\tilde{x}(t)$, $\tilde{X}_{FT}(0)$ will not be zero, because f_x is not a multiple integer of f_H and the bins of X_{DTFT} at the frequencies $f_x + nf_s$ are now consequently not multiplied with a zero value of $g(\bar{f},0)$.

Thus, the integral in (2.56) will produce a non-zero value for $\tilde{X}_{FT}(0)$. This effect is called leakage. The same holds for other frequencies. Due to the leakage, the DFT of $x(nT_s)$, which equals $\tilde{X}_{FT}$ with some scaling (see (2.54)), will not allow to reproduce the FT of $x(t)$ or to identify the frequencies of the signal and the respective amplitudes.

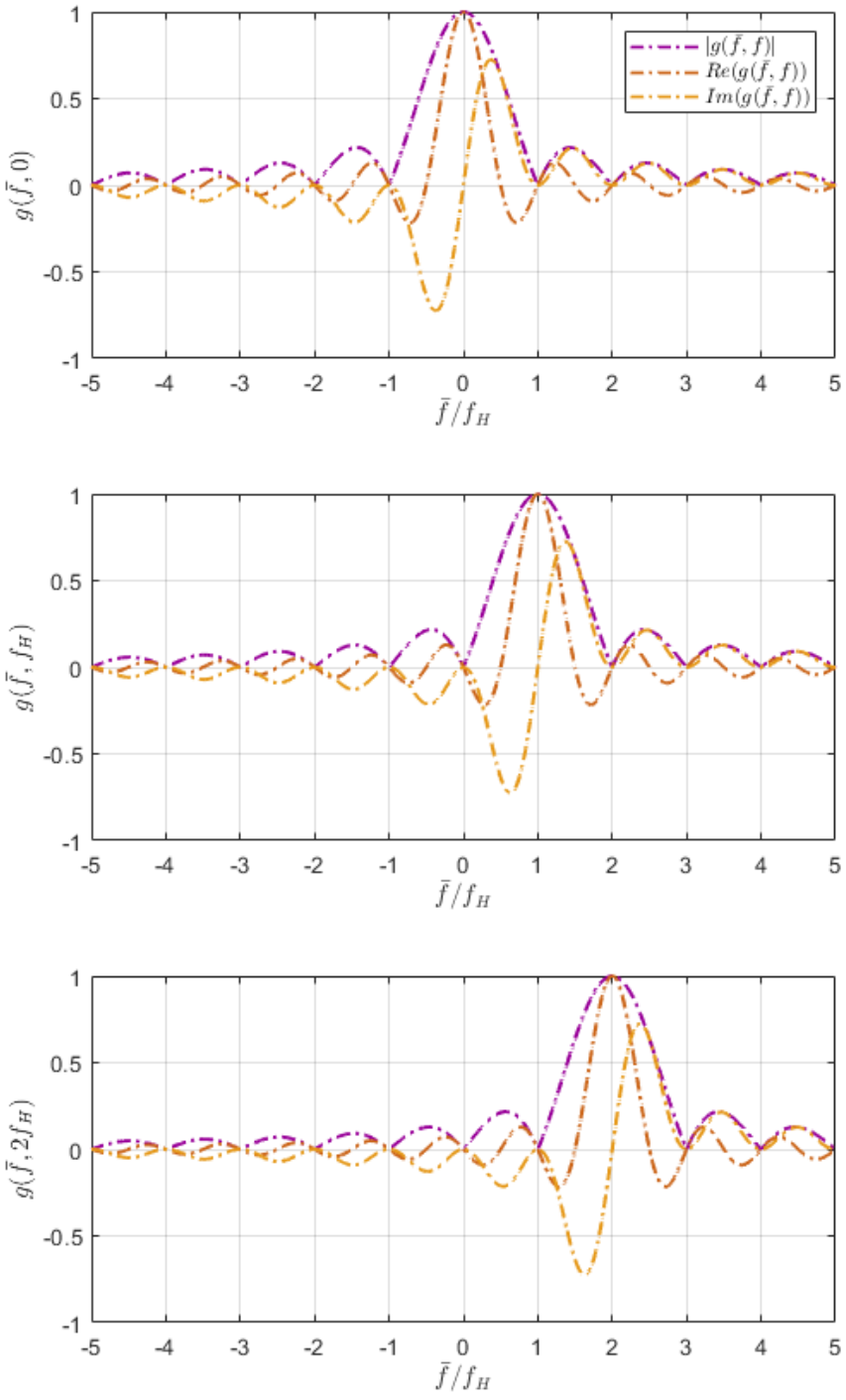

Figure 2.6: *Absolute value, real part and imaginary part of* $g(\bar{f}, f)$ *for* $f = 0$, $f = f_H$, $f = 2f_H$.

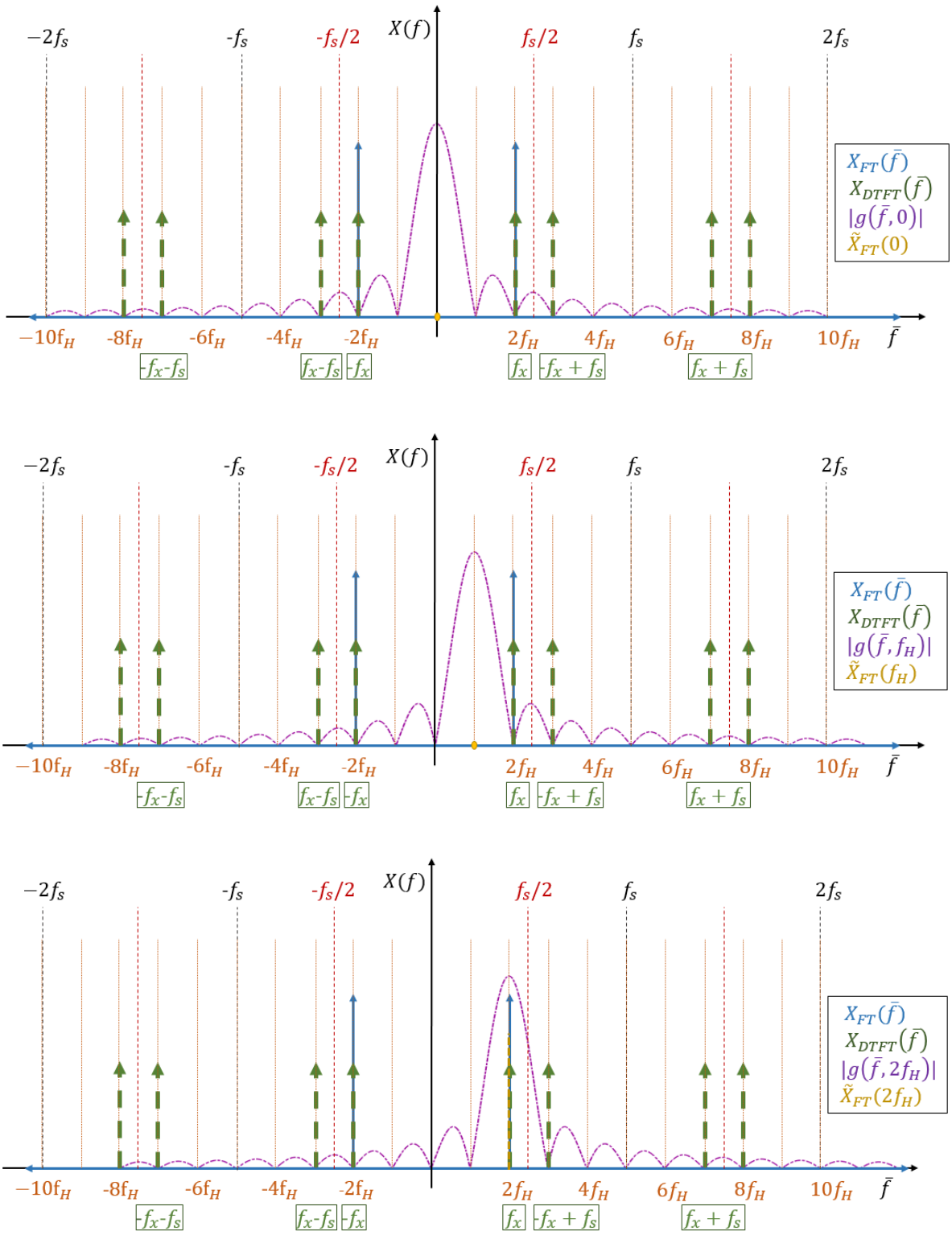

Figure 2.7: *Fourier transform of* $\tilde{x}(t)$ *at frequencies* $f = 0$, $f = f_H$, $f = 2f_H$, *for* $f_x = 2f_H$.

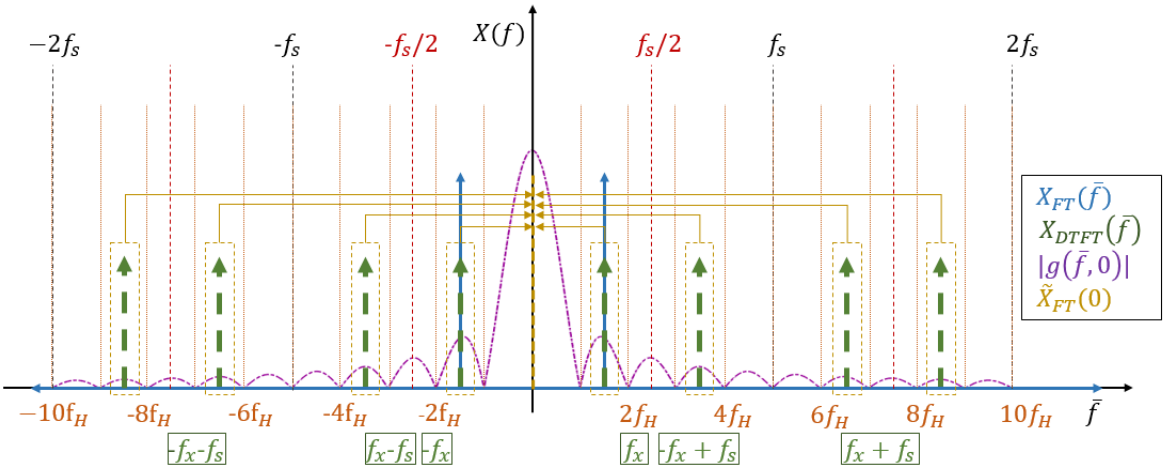

Figure 2.8: *Visualization of leakage on Fourier transform of $\tilde{x}(t)$ at frequency $f = 0$, for $f_x \neq mf_H$.*

2.2.3.3 Avoiding Leakage with Periodic Excitations when Measuring the ETFE

The ETFE was defined in Section 2.1.2 according to [Lju99] by

$$\hat{G}_{yu}(j\omega_k) = \frac{Y_{DFT}(j\omega_k)}{U_{DFT}(j\omega_k)} \tag{2.64}$$

It estimates the frequency response function (FRF) from input signal $u(t)$ to output signal $y(t)$. Though, different scaling exist for the DFT see (2.9) or (2.10) for example, they have no influence on the FRF if the same scaling are used in the DFT´s of the input and output. To avoid aliasing, the excitation signal $u(t)$ and $y(t)$ should be bandlimited such that the frequency content is below the nyquist frequency which is half of the sampling frequency $f_{Ny} = f_s/2$. If the excitation signal is periodic with period T_w and the system is linear such that $y(t)$ is also periodic with same period, the spectrums $U(j\omega)$ and $Y(j\omega)$ are non-zero only at the discrete frequencies $2\pi k f_H = 2\pi k \frac{1}{T_w}$, which are integer multiples of the harmonic frequency f_H or the inverse of the period length T_w. The respective spectrums will be line spectrums consisting of bins at the respective harmonic frequencies. Furthermore, if full periods of the periodic signals are observed, such that $T_w = NT_s$, where N is the number of measured samples, no leakage will occur in the DFT's of u and y and the FRF at the regular frequency grid of discrete frequencies $\omega_k = 2\pi k f_H$, $k \in 0 \ldots N-1$. Therefore, it is recommended whenever possible to use periodic excitation signals and to observe integer multiples of their periods to avoid leakage [PS12].

In this thesis multisine signals, as will be presented in Section 3.4 are used as excitation signals $u(t)$, where the frequencies of the sine signals are multiple integers of the harmonic frequency f_H

$$f_m = m f_H, m \in \mathbb{S} \tag{2.65}$$

and $\mathbb{S}$ is the set of the integer numbers from $0...N-1$. Since the DFT might be affected by leakage at frequencies that are not an integer of f_H the ETFE shall only be calculated at discrete frequencies, which are a multiple integer of f_H. Furthermore, the ETFE is not defined at frequencies, where the DFT of u is zero, meaning at frequencies that are not excited by the input signal u. Therefore, the ETFE is only calculated at the frequencies f_m. Consequently, no information about the FRF at non- excited integer frequencies or intermediate, non –integer frequencies can be obtained. In the next section the influence of noise on the ETFE will be investigated.

2.2.4 Effect of Noise on ETFE for Open-loop Plant Estimates

In the previous sections the ETFE was introduced as a possibility to estimate the non-parametric frequency response of a linear dynamic system using the DFTs of the logged input and output time domain data of a realization of the linear dynamic system. It was concluded that the logged data shall be band-limited to avoid aliasing and a periodic excitation with period $T_w = NT_s$ shall be used to avoid spectral leakage, assuming that the

transients have died out. This section describes how noise on the logged data influences the ETFE. As described before, the frequency response function (FRF) at the kth harmonic frequency $\omega_k = 2\pi k f_H$ is given by the ratio of the DFTs at the respective frequency of the output and input time domain data:

$$G(j\omega_k) = \frac{Y_{DFT}(j\omega_k)}{U_{DFT}(j\omega_k)} \tag{2.66}$$

For dynamic systems, in general, noise can originate from different sources, and it can be considered in different ways. The noise disturbs the logged data. As a consequence the measured DFTs $U_{m,DFT}(j\omega_k)$,$Y_{m,DFT}(j\omega_k)$ will differ from the true ones $U_{DFT}(j\omega_k)$,$Y_{DFT}(j\omega_k)$. Thus, the ETFE

$$\hat{G}(j\omega_k) = \frac{Y_{m,DFT}(j\omega_k)}{U_{m,DFT}(j\omega_k)} \tag{2.67}$$

will differ from the true FRF $G(j\omega_k)$. The resulting effects on the ETFE are characterized in terms of the bias and the variance [GPS92]. The bias of the ETFE is calculated as the difference between the expected value of the estimate and the true FRF

$$b(\hat{G}(j\omega_k)) = \mathbb{E}[\hat{G}(j\omega_k)] - G(j\omega_k) \tag{2.68}$$

The variance is determined as

$$var[\hat{G}(j\omega_k)] = var[\Re(\hat{G}(j\omega_k))] + var[\Im(\hat{G}(j\omega_k))]. \tag{2.69}$$

The variance and expected value for a random complex variable are defined in the Appendix, Definition M.0.16 and Definition M.0.20. The literature, dealing with the calculation of the bias and variance and with different strategies attempting to reduce them, is extensive as they depend on a variety of different factors. First it is important under which conditions the variance and bias are considered, whether due to noise only, or including other effects. One example for other effects could be transients caused by the initiation of the maneuver. In this thesis it is assumed that in the data used for estimation these transients have vanished, such that the transient errors are negligible.
Moreover, it is important to distinguish whether a periodic or non-periodic excitation signal is considered. Due to the above mentioned reasons (avoidance of leakage), in this thesis only periodic signals are considered. Furthermore, periodic excitations offer a variety of other significant advantages in system identification compared to non- periodic excitations as shown in [SPG94] with regard to multisine signals. As we use multisine signals as excitation within this thesis, Section 3.4 will be dedicated to this topic. Besides the multisine signal, which can be regarded as one of the most general representations for periodic excitations according to [SPG94], many other periodic excitations are possible such as periodic random signals, periodic chirp signals, etc.. In general these signals can be classified into deterministic and random excitations. Both variants are broadly used

in system identification. Depending on the class of the chosen excitation signal different concepts for estimation of the FRF with different averaging techniques are investigated in the literature, besides the ETFE, which is mainly used in the context of multisine signals. A rough overview can be gained from these references [PA03], [Bra11], [SVBP09], [SGS18] and [GPS92]. Figure 2.9 summarizes these classifications and highlights the focus within this thesis.

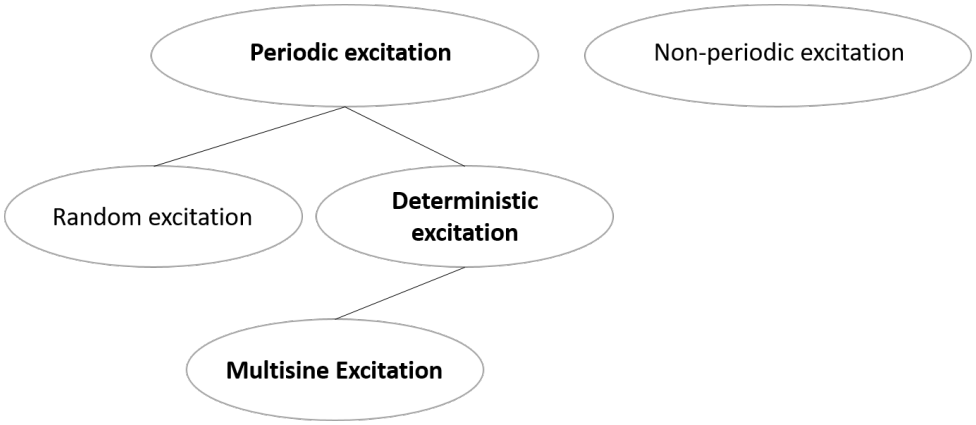

Figure 2.9: *Visualization of excitation signal classification.*

Regarding the bias and variance resulting from noise, when considering the ETFE for a multisine excitation signal , an important further factor is the noise characteristics (probability distribution) and how the noise acts on the measured signal. Within this thesis the noise is considered as an additive perturbation on the sampled discrete time domain signal $y[n]$ generated by the transfer function G with input u:

$$y_m[n] = y[n] + n_y[n] \tag{2.70}$$

where $n_y[n]$ represents the contribution of the noise. Another important criterion is whether the noise acts on the measured output time domain signal only or if there is also noise on the input signal. In cases where noise acts on both the input and output signals, a distinction needs to be made whether the input and output noise are correlated or not, see Figure 2.10.

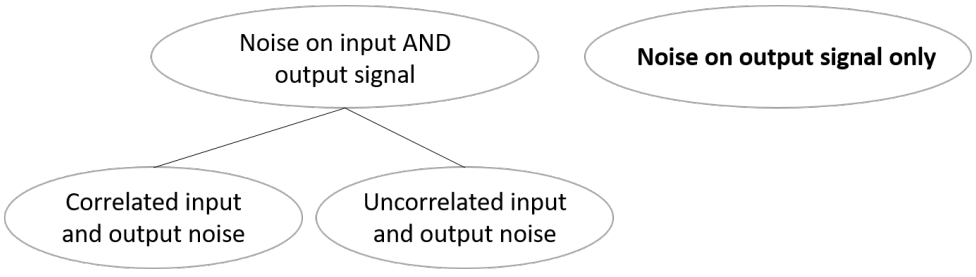

Figure 2.10: *Visualisation of noise classification.*

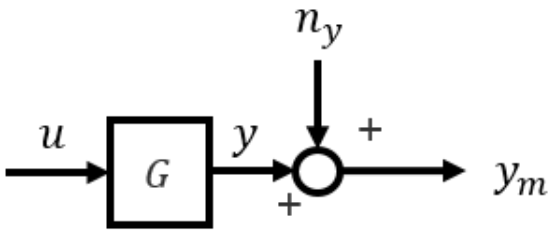

Figure 2.11: *System response with noise.*

The following sections deal with the bias and variance of the ETFE for a multisine excitation, with noise acting on the output data. The next section starts with introducing the characteristics of the DFT of a measured signal with additive noise with specific properties. Section 2.2.4.2 calculates the bias and variance of the ETFE based on these results. Finally, in Section 2.2.5 basic averaging techniques are summarized.

2.2.4.1 DFT of Measured Signal with Additive Noise

As explained in the previous section we consider the discrete time sequence of N samples of the measured output signal to be perturbed by noise according to

$$y_m[n] = y[n] + n_y[n] \tag{2.71}$$

as depicted in Figure 2.11. It is assumed that no noise is acting on the logged input data, such that

$$u_m[n] = u[n]. \tag{2.72}$$

The objective is to calculate the bias and variance of the resulting ETFE which is given by the ratio of the DFTs of $y_m[n]$ and $u_m[n]$. Therefore, we first focus in this section on the DFT of $y_m[n]$. As no noise is acting on the measured input signal, the DFT of $u_m[n]$ equals the DFT of $u[n]$:

$$U_{m,DFT}[k] = U_{DFT}[k]. \tag{2.73}$$

In Appendix M, some helpful definitions are given to assure a common understanding in the theoretical basics used in the following derivations. The DFT at the discrete angular frequency $\omega_k = 2\pi\frac{k}{NT_s}$, of the real valued discrete time sequence of the measured output signal $y_m[n]$ with N samples is calculated according to (2.9) by

$$Y_{m,DFT}[k] = \frac{1}{\sqrt{N}} \sum_{n=0}^{N-1} y_m[n] e^{-j\frac{2\pi kn}{N}} \tag{2.74}$$

With the noise acting as an additive disturbance on the undisturbed output signal $y[n]$, (2.71), the DFT of $y_m[n]$ will be composed of the DFT of $y[n]$ and $n_y[n]$ according to

$$\begin{aligned} Y_{m,DFT}[k] &= \frac{1}{\sqrt{N}} \sum_{n=0}^{N-1} (y[n] + n_y[n]) e^{-j\frac{2\pi kn}{N}} \\ &= \frac{1}{\sqrt{N}} \sum_{n=0}^{N-1} y[n] e^{-j\frac{2\pi kn}{N}} + \frac{1}{\sqrt{N}} \sum_{n=0}^{N-1} n_y[n] e^{-j\frac{2\pi kn}{N}} \\ &= Y_{DFT}[k] + N_{y,DFT}[k] \end{aligned} \tag{2.75}$$

Normally Distributed i.i.d. Noise Sequence: If the N discrete samples of the sequence $n_y[n]$ are independent, identically distributed random variables (i.i.d.), see Definition M.0.12, with normal distribution, see Appendix M.0.10, with zero mean $\mu = 0$ and variance σ^2, then by Lemma N.1.1, the real and imaginary part of the DFT of $n_y[n]$ at frequency $\omega_k = \frac{2\pi}{NT_s}k$ will be also normally distributed as follows

$$\begin{aligned} \Re(N_{y,DFT}[k]) &\sim \mathcal{N}(0, \frac{\sigma^2}{2}) \\ \Im(N_{y,DFT}[k]) &\sim \mathcal{N}(0, \frac{\sigma^2}{2}) \end{aligned} \tag{2.76}$$

Furthermore,

- $N_{y,DFT}[k]$ is a circular symmetric complex random variable (see Definition M.0.24) by Lemma N.2.1
- $\Re(N_{y,DFT}[k])$ and $\Im(N_{y,DFT}[k])$ are independent real-valued random variables by Lemma N.3.1 and hence uncorrelated by Lemma M.0.5
- $\Re(N_{y,DFT}[k])$ and $\Im(N_{y,DFT}[k])$ are jointly normal by Lemma N.5.1

From Equation (2.75) and (2.76), because the expectation operator is linear, Property M.0.1, and because for the variance Equation (M.11) holds, it follows that the real and imaginary parts of the complex random variable $Y_{m,DFT}[k]$ are uncorrelated and normally distributed according to

$$\begin{aligned} \Re(Y_{m,DFT}[k]) &\sim \mathcal{N}(Y_{DFT}[k], \frac{\sigma^2}{2}) \\ \Im(Y_{m,DFT}[k]) &\sim \mathcal{N}(Y_{DFT}[k], \frac{\sigma^2}{2}) \end{aligned} \tag{2.77}$$

Filtered Normally Distributed i.i.d. Noise Sequence (Coloured Noise): Assume that the noise sequence n_y is acting on the system response y as depicted in Figure 2.12, where n_w is filtered by a stable and proper linear time invariant (LTI) system W. The sequence $n_w[n]$ is an i.i.d. sequence, see Definition M.0.12, with normal distribution, see Appendix M.0.10, with zero mean $\mu = 0$ and variance σ^2. Then as shown in [Bri81],

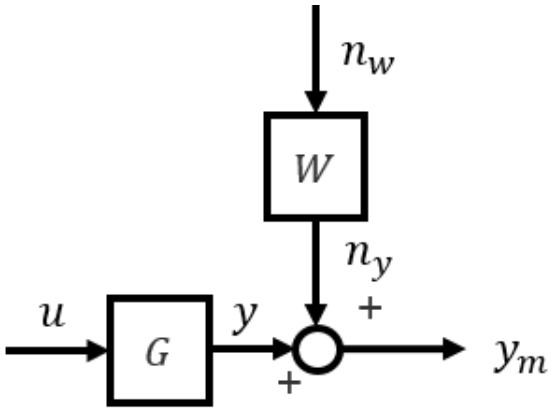

Figure 2.12: *System response with filtered noise.*

[dv95] the DFT $N_{y,DFT}$ of $n_y[n]$ converges for $N \to \infty$, where N is the number of samples, in distribution to a normal distribution with zero mean and with variance and covariance of the real and imaginary parts of $N_{y,DFT}$ given by

$$\begin{aligned} &\mathbb{E}[\Re(N_{y,DFT}[k])\Re(N_{y,DFT}[k])] = \mathbb{E}[\Im(N_{y,DFT}[k])\Im(N_{y,DFT}[k])] = \frac{\sigma^2}{2}|W(j\omega_k)|^2 \\ &\mathbb{E}[\Re(N_{y,DFT}[k])\Im(N_{y,DFT}[k])] = 0 \end{aligned} \tag{2.78}$$

where the real and imaginary parts are asymptotically uncorrelated and jointly normally distributed, hence asymptotically independent [dv95].

2.2.4.2 Bias and Variance of ETFE due to Noise

As introduced in the previous sections, the non-parametric frequency response of a linear dynamic system is estimated as the ETFE, using the DFTs of the logged input and output time domain data. It is assumed that no noise acts on the input data, but that noise acts on the output data according to (2.71). The ETFE results in

$$\hat{G}(j\omega_k) = \frac{Y_{m,DFT}[k]}{U_{m,DFT}[k]} = \frac{Y_{DFT}[k] + N_{y,DFT}[k]}{U_{DFT}[k]} = G(j\omega_k) + \frac{N_{y,DFT}[k]}{U_{DFT}[k]} \tag{2.79}$$

where Equation (2.66), (2.73) and (2.75) were used and where $G(j\omega_k)$ is the true value of the FRF, for periodic excitations and assuming that transients died out.

Normally Distributed i.i.d. Noise Sequence: First we consider the case, where the N discrete samples of the noise sequence $n_y[n]$ are independent, identically distributed random variables (i.i.d.) with normal distribution

$$n_y[n] \sim \mathcal{N}(0, \sigma^2) \tag{2.80}$$

The DFT, $U_{DFT}[k]$, is a complex number and can be expressed by its amplitude and phase as

$$U_{DFT}[k] = |U_{DFT}[k]|e^{j\angle U_{DFT}[k]} \tag{2.81}$$

such that

$$\begin{aligned}\hat{G}(j\omega_k) &= G(j\omega_k) + N_{y,DFT}[k] \cdot (|U_{DFT}[k]|^{-1} e^{-j\angle U_{DFT}[k]}) \\ &= G(j\omega_k) + |U_{DFT}[k]|^{-1} (N_{y,DFT}[k] \cdot e^{-j\angle U_{DFT}[k]})\end{aligned} \tag{2.82}$$

Because the complex random variable $N_{y,DFT}[k]$ is circularly symmetric, by Lemma N.2.1, then the distribution of $N_{y,DFT}[k] \cdot e^{-j\angle U_{DFT}[k]}$ equals the distribution of $N_{y,DFT}[k]$, according to Definition M.0.24, i.e. its real and imaginary part are uncorrelated and according to Equation (2.76)

$$\begin{aligned}\Re(N_{y,DFT}[k] \cdot e^{-j\angle U_{DFT}[k]}) &\sim \mathcal{N}(0, \frac{\sigma^2}{2}) \\ \Im(N_{y,DFT}[k] \cdot e^{-j\angle U_{DFT}[k]}) &\sim \mathcal{N}(0, \frac{\sigma^2}{2})\end{aligned} \tag{2.83}$$

The input signal magnitude $|U_{DFT}[k]|^{-1}$ is a real valued constant for a fixed k. By Property M.0.1 of the expected value operator and Property M.0.2, Equation (M.11), of the variance, the second term in Equation (2.82):

$$G_n(j\omega_k) = \frac{N_{y,DFT}[k] \cdot e^{-j\angle U_{DFT}[k]}}{|U_{DFT}[k]|} \tag{2.84}$$

is then distributed according to

$$\begin{aligned}\Re(G_n(j\omega_k)) &\sim \mathcal{N}(0, \frac{1}{2}\frac{\sigma^2}{|U_{DFT}[k]|^2}) \\ \Im(G_n(j\omega_k)) &\sim \mathcal{N}(0, \frac{1}{2}\frac{\sigma^2}{|U_{DFT}[k]|^2})\end{aligned} \tag{2.85}$$

Thus, $\hat{G}(j\omega_k)$, is distributed according to

$$\begin{aligned}\Re(\hat{G}(j\omega_k)) &\sim \mathcal{N}(\Re(G(j\omega_k)), \frac{1}{2}\frac{\sigma^2}{|U_{DFT}[k]|^2}) \\ \Im(\hat{G}(j\omega_k)) &\sim \mathcal{N}(\Im(G(j\omega_k)), \frac{1}{2}\frac{\sigma^2}{|U_{DFT}[k]|^2})\end{aligned} \tag{2.86}$$

This result shows that for the case of an additive normally distributed i.i.d. noise sequence with zero mean, on the output signal only, the ETFE provides an unbiased estimate, i.e.

$$b(\hat{G}(j\omega_k)) = \mathbb{E}[\hat{G}(j\omega_k)] - G(j\omega_k) = 0 \tag{2.87}$$

where the bias was defined in Equation (2.68). Furthermore, the real and imaginary parts of the estimate $\hat{G}(j\omega_k)$ are uncorrelated and normally distributed with equal variance of

$$var[\Re(\hat{G}(j\omega_k))] = var[\Im(\hat{G}(j\omega_k))] = \frac{1}{2}\frac{\sigma^2}{|U_{DFT}[k]|^2} \tag{2.88}$$

The variance of the estimate can be thus reduced by

- increasing the signal-to-noise ratio, i.e.

$$\frac{|U_{DFT}[k]|}{\sigma} \tag{2.89}$$

Note, that the variance of the noise signal σ^2 is often given by the used sensors. The amplitude of the input signal, $|U_{DFT}[k]|$, cannot be increased arbitrarily, because with higher excitation amplitudes the system might drift away from its operational point after a shorter period of time. Furthermore, the amplitude needs to be carefully chosen with regard to the chosen excitation frequencies in order to inhibit that the actuators hit their limits and rate saturations, because this would introduce nonlinearities, such that the estimate is not applicable. Also, other nonlinearities might affect the measured responses in case the excitation amplitudes are chosen too high.

Filtered Normally Distributed i.i.d. Noise Sequence: Assume that the noise sequence $n_y[n]$ is acting on the system response y as depicted in Figure 2.12, where n_w is filtered by a stable and proper linear time invariant (LTI) system W. The sequence $n_w[n]$ is an i.i.d. sequence, see Definition M.0.12, with normal distribution, see Appendix M.0.10, with zero mean $\mu = 0$ and variance σ^2, such that $n_y[n]$ is stationary and normally distributed. First we calculate the expected value of the resulting estimate $\hat{G}(j\omega_k)$, Equation (2.79), i.e

$$\mathbb{E}[\hat{G}(j\omega_k)] = \mathbb{E}[G(j\omega_k)] + \mathbb{E}[\frac{N_{y,DFT}[k]}{U_{DFT}[k]}]. \tag{2.90}$$

The expected value of $V[k] = \frac{N_{y,DFT}[k]}{U_{DFT}[k]}$ is

$$\begin{aligned}
\mathbb{E}[V[k]] &= \mathbb{E}\left[\frac{N_{y,DFT}[k]}{U_{DFT}[k]}\right] \\
&= \mathbb{E}\left[\frac{N_{y,DFT}[k]U^*_{DFT}[k]}{U_{DFT}[k]U^*_{DFT}[k]}\right] = \mathbb{E}\left[\frac{(N_r[k] + jN_j[k])(u_r[k] - ju_j[k])}{|U_{DFT}[k]|^2}\right] \\
&= \mathbb{E}\left[\frac{(N_r[k]u_r[k] + N_j[k]u_j[k]) + j(N_j[k]u_r[k] - N_r[k]u_j[k])}{|U_{DFT}[k]|^2}\right]
\end{aligned} \tag{2.91}$$

To improve readability $[k]$ is omitted in the following, whenever it is clear from the context. The real random variables N_r and N_j are the real and imaginary part of $N_{y,DFT}$, which is the DFT of the noise sequence $n_y[n]$, and u_r and u_j are the real and imaginary part

of U_{DFT}, which is the DFT of the input sequence $u[n]$, which are constant for a fixed k. According to Property M.0.7

$$\mathbb{E}[V] = \mathbb{E}[\Re(V)] + j\mathbb{E}[\Im(V)] = \mathbb{E}\left[\frac{(N_r u_r + N_j u_j)}{|U_{DFT}|^2}\right] + j\mathbb{E}\left[\frac{(N_j u_r - N_r u_j)}{|U_{DFT}|^2}\right] \tag{2.92}$$

Because of the linearity property of the expected value operator, Equation (2.92) corresponds to

$$\mathbb{E}[V] = \frac{u_r}{|U_{DFT}|^2}\mathbb{E}[N_r] + \frac{u_j}{|U_{DFT}|^2}\mathbb{E}[N_j] + j\frac{u_r}{|U_{DFT}|^2}\mathbb{E}[N_j] - j\frac{u_j}{|U_{DFT}|^2}\mathbb{E}[N_r]. \tag{2.93}$$

Because $n_y[n]$ is a stationary and normally distributed sequence

$$\begin{aligned} \mathbb{E}[N_r[k]] &= \frac{\mu}{\sqrt{N}}\sum_{n=0}^{N-1}\cos(\frac{2\pi kn}{N}) = 0 \\ \mathbb{E}[N_j[k]] &= \frac{\mu}{\sqrt{N}}\sum_{n=0}^{N-1}\sin(\frac{2\pi kn}{N}) = 0 \end{aligned} \tag{2.94}$$

holds according to Lemma O.1.1, for $k \neq 0$. Hence, using Equation (2.94) in Equation (2.93) results in

$$\mathbb{E}[V] = \mathbb{E}[\frac{N_{y,DFT}}{U_{DFT}}] = 0 \tag{2.95}$$

such that Equation (2.90) becomes

$$\mathbb{E}[\hat{G}] = \mathbb{E}[G] = G \tag{2.96}$$

meaning that the ETFE (2.79) is unbiased.
Note, that the expected value of the DFT of the noise sequence $n_y[n]$, and thus $\mathbb{E}[V[k]]$ is zero for $k \neq 0$, even if $n_y[n]$ has non-zero mean and for a finite number of samples N.

The covariance matrix $\Sigma_{V_r V_j}$ of $V = \frac{N_{y,DFT}}{U_{DFT}} = V_r + jV_j$ is according to Equation (M.62)

$$\Sigma_{V_r V_j} = \begin{bmatrix} \sigma_{v_r}^2 & cov[V_r, V_j] \\ cov[V_j, V_r] & \sigma_{v_j}^2 \end{bmatrix} \tag{2.97}$$

Using that V has zero mean, Equation (2.95), the elements of this covariance matrix are given by Lemma O.4.1 as

$$
\begin{aligned}
var[V_r] = \sigma_{v_r}^2 &= \frac{1}{2}\Re(K_{VV} + C_{VV}) = \frac{1}{2}\frac{\mathbb{E}\left[N_{y,DFT}N_{y,DFT}^*\right]}{|U_{DFT}|^2} + \frac{1}{2}\Re\left(\frac{\mathbb{E}[N_{y,DFT}N_{y,DFT}]}{u_r^2 - u_j^2 + 2ju_ru_j}\right) \\
var[V_j] = \sigma_{v_j}^2 &= \frac{1}{2}\Re(K_{VV} - C_{VV}) = \frac{1}{2}\frac{\mathbb{E}\left[N_{y,DFT}N_{y,DFT}^*\right]}{|U_{DFT}|^2} - \frac{1}{2}\Re\left(\frac{\mathbb{E}[N_{y,DFT}N_{y,DFT}]}{u_r^2 - u_j^2 + 2ju_ru_j}\right) \\
cov[V_r, V_j] &= \frac{1}{2}\Im(-K_{VV} + C_{VV}) = \frac{1}{2}\Im\left(\frac{\mathbb{E}[N_{y,DFT}N_{y,DFT}]}{u_r^2 - u_j^2 + 2ju_ru_j}\right) \\
cov[V_j, V_r] &= \frac{1}{2}\Im(K_{VV} + C_{VV}) = \frac{1}{2}\Im\left(\frac{\mathbb{E}[N_{y,DFT}N_{y,DFT}]}{u_r^2 - u_j^2 + 2ju_ru_j}\right)
\end{aligned}
\tag{2.98}
$$

where K_{VV} and C_{VV} are the variance and pseudo variance defined in Definition M.0.20 and M.0.21, respectively. Note, that $\mathbb{E}[N_{y,DFT}N_{y,DFT}^*]$ and $\mathbb{E}[N_{y,DFT}N_{y,DFT}]$ depend on the noise characteristics and properties. For the considered case, the variance and covariance of the real and imaginary parts of $N_{y,DFT}$ are given by Equation (2.78) for the asymptotic case, i.e. $N \to \infty$. Further, the DFT $N_{y,DFT}$ of n_y converges for $N \to \infty$, in distribution to a normal distribution. Because the mean of $N_{y,DFT}$ is zero, we identify $\mathbb{E}[N_{y,DFT}N_{y,DFT}^*]$ as the variance of $N_{y,DFT}$, Definition M.0.20, and $\mathbb{E}[N_{y,DFT}N_{y,DFT}]$ as the pseudo variance, Definition M.0.21. Hence, by Lemma M.0.11 and Lemma M.0.12 the **asymptotic** variance and pseudo variance of $N_{y,DFT}$ is given by

$$
\begin{aligned}
\mathbb{E}\left[N_{y,DFT}N_{y,DFT}^*\right] &= var[\Re(N_{y,DFT})] + var[\Im(N_{y,DFT})] \\
&= \mathbb{E}[\Re(N_{y,DFT})\Re(N_{y,DFT})] + \mathbb{E}[\Im(N_{y,DFT})\Im(N_{y,DFT})] \\
&= \sigma^2|W|^2 \\
\mathbb{E}\left[N_{y,DFT}N_{y,DFT}\right] &= var[\Re(N_{y,DFT})] - var[\Im(N_{y,DFT})] + 2jcov[\Re(N_{y,DFT}), \Im(N_{y,DFT})] \\
&= \mathbb{E}[\Re(N_{y,DFT})\Re(N_{y,DFT})] - \mathbb{E}[\Im(N_{y,DFT})\Im(N_{y,DFT})] \\
&\quad + 2j\mathbb{E}[\Re(N_{y,DFT})\Im(N_{y,DFT})] = 0
\end{aligned}
\tag{2.99}
$$

Note, that according to Lemma O.3.1, in case that $n_y[n]$ is a stationary sequence, Definition M.0.11, with uncorrelated samples and with a normal distribution $\mathcal{N}(\mu, \sigma^2)$

$$
\begin{aligned}
\mathbb{E}[N_{y,DFT}N_{y,DFT}^*] &= \sigma^2 \\
\mathbb{E}[N_{y,DFT}N_{y,DFT}] &= 0
\end{aligned}
\tag{2.100}
$$

holds. Using Equation (2.99) and (2.98) we obtain

$$\begin{aligned} var[V_r] = var[V_j] &= \frac{1}{2}|W|^2 \frac{\sigma^2}{|U_{DFT}|^2} \\ cov[V_r, V_j] &= cov[V_j, V_r] = 0 \end{aligned} \tag{2.101}$$

Because, the real and imaginary parts of $N_{y,DFT}$ are asymptotically uncorrelated and jointly normally distributed, hence asymptotically independent [dv95], the real and imaginary parts of the estimate in (2.79) will be also **asymptotically** normally distributed according to

$$\begin{aligned} \Re\{\hat{G}(j\omega_k)\} &\sim \mathcal{N}(\Re\{G(j\omega_k)\}, \frac{1}{2}|W(j\omega_k)|^2 \frac{\sigma^2}{|U_{DFT}[k]|^2}) \\ \Im\{\hat{G}(j\omega_k)\} &\sim \mathcal{N}(\Im\{G(j\omega_k)\}, \frac{1}{2}|W(j\omega_k)|^2 \frac{\sigma^2}{|U_{DFT}[k]|^2}) \end{aligned} \tag{2.102}$$

with uncorrelated real and imaginary parts, i.e.

$$\mathbb{E}[\Re\{\hat{G}(j\omega_k)\}\Im\{\hat{G}(j\omega_k)\}] = 0 \tag{2.103}$$

2.2.5 Averaging the ETFE

In Section 2.2.4.2 it was shown that the ETFE provides an unbiased FRF estimate if only the output signal is perturbed by an additive normally distributed i.i.d. noise sequence with zero mean. This section shows that the variance of the estimate can be reduced by repeating the experiment and calculating the averaged ETFE. The averaged ETFE is calculated according to

$$\hat{G}(j\omega_k) = \frac{\frac{1}{R}\sum_{r=0}^{R-1} Y_{m,DFT}^{[r]}[k]}{\frac{1}{R}\sum_{r=0}^{R-1} U_{m,DFT}^{[r]}[k]} \tag{2.104}$$

where for each of the R repetitions of the maneuver, the respective DFTs $Y_{m,DFT}^{[r]}[k]$ and $U_{m,DFT}^{[r]}[k]$ are calculated, which are mutually independent for $r = 0 \dots R-1$. Because it is assumed that no noise acts on the logged input data

$$\frac{1}{R}\sum_{r=0}^{R-1} U_{m,DFT}^{[r]}[k] = \frac{1}{R}\sum_{r=0}^{R-1} U_{DFT}[k] = U_{DFT}[k] \tag{2.105}$$

holds and Equation (2.104) can be expressed by

$$\hat{G}(j\omega_k) = \frac{1}{R}\sum_{r=0}^{R-1} \frac{Y_{m,DFT}^{[r]}[k]}{U_{DFT}[k]} = \frac{1}{R}\sum_{r=0}^{R-1} \hat{G}^{[r]}(j\omega_k) \tag{2.106}$$

For each repetition of the maneuver the real and imaginary parts of the ETFE, $\hat{G}^{[r]}(j\omega_k)$, are normally distributed and uncorrelated according to Equation (2.86). Since $\hat{G}^{[r]}(j\omega_k)$ are mutually independent for $r = 0, \dots R-1$, because $Y^{[r]}_{m,DFT}[k]$ are mutually independent for $r = 0, \dots R-1$, the real and imaginary parts of $\hat{G}(j\omega_k)$ will be also normally distributed and uncorrelated by Lemma M.0.8, with the following expected value and variance according to Property M.0.1, Equation (M.11) and Lemma M.0.2:

$$\begin{aligned}
\Re(\hat{G}(j\omega_k)) &\sim \mathcal{N}(\frac{1}{R}\sum_{r=0}^{R-1}\Re(G(j\omega_k)), \frac{1}{R^2}\sum_{r=0}^{R-1}\frac{1}{2}\frac{\sigma^2}{|U_{DFT}[k]|^2}) \\
&\sim \mathcal{N}(\Re(G(j\omega_k)), \frac{1}{2R}\frac{\sigma^2}{|U_{DFT}[k]|^2}) \\
\Im(\hat{G}(j\omega_k)) &\sim \mathcal{N}(\Im(G(j\omega_k)), \frac{1}{2R}\frac{\sigma^2}{|U_{DFT}[k]|^2})
\end{aligned} \tag{2.107}$$

Hence, by increasing the number of the repetitions of the maneuver the variance of the estimate can be decreased. Note, that increasing the number of repetitions increases the duration of the experiment and thus the costs of the test campaign. Furthermore, the number of repetitions shall be chosen carefully, such that the drift from the operational point stays within acceptable bounds.

Note, that for the case that noise is also acting on the logged input data, the bias of the ratio of the averaged DFTs of the input and output data, (2.104), does not equal the bias of the average of the ETFEs of each repetition, (2.106), as was shown in [GPS92]. The case that both the input and output signal are additively perturbed by noise is often denoted as the open-loop *error-in-variables case*. The derivation of the bias and variance of $\hat{G}(j\omega_k)$ is in this case more involved and even more complex if the input and output noise are correlated. For additive, complex normal distributed errors on the measured Fourier coefficients of the input and output signals, obtained by a DFT for example, [GPS92] derives analytical expressions for the bias of non-parametric frequency response estimates using different averaging techniques, based on a Taylor's series expansion. The case that the input-output errors are mutually uncorrelated as well as the case that they are correlated is considered. In [GKP96a] approximations for the variance of non-parametric estimate of the open-loop error-in-variables case are discussed. The input and output disturbances are considered uncorrelated. The variance for this case is shown to be **infinite** if the errors are complex normally distributed, even if the signal-to-noise ratio is large. Further the effects of introducing a so-called exclusion zone on the variance are discussed. In [Hea01b], it is emphasized that some low order approximations in the literature for the variance of indirect estimates derived from closed-loop system estimates shall be treated with some care and that statements in the literature that these estimates are unbiased shall be interpreted as meaning asymptotically unbiased.

2.2.6 Distributions of the Magnitude and Phase of the ETFE

We usually calculate the averaged ETFE according to (2.104) and investigate the amplitude and phase of the resulting complex random variable. Note, that the averaging is not performed on the amplitudes and phases, but over the complex numbers. The reason is that, given a proper complex normal random variable $Z = X + jY$, see Definition M.0.23, where $\mathbb{E}[Z]$ is the mean of the complex random variable Z, the marginal distribution of its magnitude $|Z| = \sqrt{X^2 + Y^2}$ will be a Rician distribution, see Appendix M.0.22. The mean of the Rician distributed magnitude

$$\mathbb{E}[|Z|] = \mathbb{E}[\sqrt{X^2 + Y^2}] \tag{2.108}$$

will not correspond to the magnitude of the expected value of the ETFE Z given by

$$|\mathbb{E}[Z]| = |\mathbb{E}[X] + j\mathbb{E}[Y]| = \sqrt{\mathbb{E}[X]^2 + \mathbb{E}[Y]^2}. \tag{2.109}$$

where $\mathbb{E}[Z]$ will give an unbiased estimate, as we derived in Section 2.2.4.2 and hence $|\mathbb{E}[Z]|$ will give an unbiased estimate of the magnitude. The marginal distribution of the phase $\Theta = Arg(Z) \in [0, 2\pi)$ is discussed in detail in Appendix M.0.23. An important parameter in the context of the pdfs of the magnitude and phase, is κ,

$$\kappa = \frac{\nu}{\sigma} \tag{2.110}$$

which is denoted in this context as the signal-to-noise ratio, but shall not be confused with the signal-to-noise ratio introduced in (2.89). In (2.110), ν is the magnitude of the expected value of the complex random variable $Z = X + jY$, i.e $\nu = |\mathbb{E}[Z]|$, and σ^2 is the variance of its real and imaginary part, i.e. $var[X] = var[Y] = \sigma^2$. If the SNR is high then both the marginal distribution of the magnitude and the marginal distribution of the phase can be approximated by a normal distribution, see Lemma M.0.16 and Lemma M.0.17. Such that the magnitude $|Z|$ constitutes a normally distributed random variable with mean ν and variance σ^2. The phase then constitutes a random variable with mean $Arg(\mathbb{E}[Z]) = Arg(\mathbb{E}[X]+j\mathbb{E}[Y])$ and variance $(\sigma/\nu)^2 = 1/\kappa^2$. In Appendix M.0.21, M.0.22 and M.0.23, the joint distribution of the Amplitude and Phase as well as the respective marginal distributions are discussed in detail.

2.3 Closed-loop Identification

In the previous section, the averaged ETFE was discussed as a technique to estimate the non-parametric frequency response of a dynamical system. The focus was on the classical identification framework meaning:

- the system, whose response is estimated, is operated in open-loop
- the excitation input is exactly known
- only the output observations are noisy

The framework is depicted in Figure 2.11. In this section we turn our attention from the field of non-parametric techniques in open-loop system identification to the field of closed-loop identification. Since decades the problem of identifying a plant model using data from closed-loop experiments is in the focus of research. The following factors might motivate or necessitate that the identification is performed under closed-loop conditions:

- unstable or poorly damped plant
- safety reasons
- operational reasons
- reduced costs (no additional test set up in code required, in order to perform open-loop experiment)
- if identified plant shall be used in control design (In [HGd96] it was argued that for model based control design, better results with regard to controller performance can be obtained if the model was obtained from experiments under closed-loop conditions instead of open-loop experiments. Thereby the controller performance is measured by a specific performance metric which is the variance of the error between the desired closed-loop time response and actual closed-loop response with a controller derived from the identified model. [Gev93] and [VS95] support the idea that for the purpose of control design, closed-loop identification shall be preferred over open-loop identification.)

The field of identification under closed-loop conditions can be subdivided into model-based and non-parametric methods. In the following we will focus on non-parametric identification. This choice is motivated by the fact that in contrast to non-parametric approaches, model-based approaches require prior assumptions on the model- order and structure. Information that was contained in the measured data might consequently get lost if these assumptions are wrong. Furthermore, it was argued in [FHK14] that data-driven tuning achieves better results regarding the final control cost on the real system than model-based solutions under some conditions. Of course, as also mentioned

in [FHK14] a generalization of the statement that data-driven non-parametric concepts outperform model-based concepts is not straight forward and shall be considered with care.
Within the domain of non-parametric estimation, different approaches exist: for example spectral methods or approaches using the DFT and ETFE as described in the previous sections. We will focus on the ETFE using the DFT.
The considered framework under which the closed-loop experiments might be performed is depicted in Figure 2.13. According to [Lju99] the approaches to closed-loop identification can be separated into three main categories:

- Direct Approach
- Indirect Approach
- Joint Input-Output Approach

Direct Approach Here the plant is estimated directly, using the measured plant input u and plant output y from a closed-loop experiment. The reference input r of the closed-loop system, as well as the controller are hence, in general not necessary for the identification of the plant. As this concept requires no knowledge about the controller, this approach is advantageous in cases where the controller is complex or unknown. Some difficulties in this approach arise from the influence of noise on the measured signals. Since the measured output signal is fed back, the input signal u will be correlated with the output signal y.

Indirect Approach The indirect approach can be divided into two steps and requires that the controller is exactly known and of a linear form.

- First, the reference input r of the closed-loop system and the closed-loop response y are used to identify the closed-loop system.
- In the second step the plant is calculated from the estimated closed-loop obtained in the first step using the knowledge about the controller that was applied in the closed-loop experiment.

For the identification of the closed-loop system in the first step, any identification method that works in open-loop may be used since the reference input and the measured output signal are uncorrelated.
This second approach is often disfavored, as any deviation from a linear controller due to anti-windup schemes, delimiters, input saturations or other nonlinearities, directly propagate to the estimated plant. As the applied controller in this thesis is linear and exactly known, and the identification maneuvers are concepted in a way that limitations or saturations are not hit, this approach is used.

Joint Input-Output Approach The joint Input-Output Identification recovers the system from a joint system, which considers y and u as outputs of a system which is driven by r and noise.

In the following sections, we assume

- the reference input $r(t)$ is a periodic excitation, e.g. a multisine signal
- the measurements to be synchronized
- the transients to be negligible
- the leakage to negligible
- i.i.d. normally distributed noise sequence n_w with zero mean

In the following we will consider the closed–loop system depicted in Figure 2.13, which is assumed to be closed-loop stable. For the measured output the following relation holds

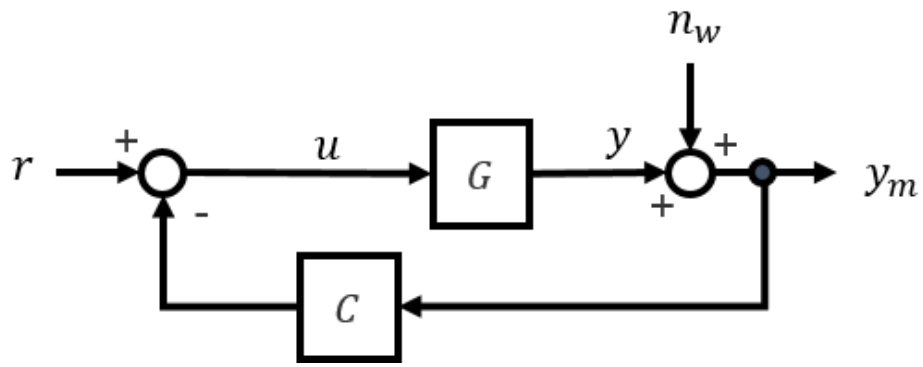

Figure 2.13: *Standard closed-loop framework.*

$$Y_m = GU + N_w \tag{2.111}$$

where Y_m, U, N_w are the Laplace transforms of the measured output $y_m(t)$, plant input $u(t)$ and random process $n_w(t)$. G is the linear transfer function of the plant, whose frequency response we wish to identify. Note, that for better readability the dependency on the Laplace variable (s) is omitted. In closed-loop the following relation holds for the input u

$$U = R - CY_m \tag{2.112}$$

where C is the controller transfer function. The measured output y_m can be expressed as

$$Y_m = G(R - CY_m) + N_w \tag{2.113}$$

where (2.112) was inserted into (2.111). Hence,

$$Y_m = \frac{G}{1+GC}R + \frac{1}{1+GC}N_w = G_{cl}R + S_cN_w = G_{cl}R + N_y \tag{2.114}$$

can be obtained, which has the block diagram representation in Figure 2.14, and where

$$G_{cl} = \frac{G}{1+GC} \tag{2.115}$$

is the closed-loop transfer function and

$$S_c = \frac{1}{1+GC} \tag{2.116}$$

is the sensitivity. Furthermore, by inserting Equation (2.111) into (2.112) the closed-loop relation

$$U = R - CGU - CN_w \tag{2.117}$$

is obtained and hence

$$U = \frac{1}{1+GC}R - \frac{C}{1+GC}N_w = S_cR - CS_cN_w = S_cR + N_u \tag{2.118}$$

can be obtained, which has the block diagram representation in Figure 2.15.

2.3.1 Direct Non-parametric Plant Estimate under Closed-loop Conditions

In this section we are concerned with the non-parametric direct plant estimate obtained from closed-loop experiments. The direct plant estimate is calculated as the ETFE according to

$$\hat{G}(j\omega_k) = \frac{Y_{m,DFT}(j\omega_k)}{U_{m,DFT}(j\omega_k)} \tag{2.119}$$

where $Y_{m,DFT}$ and $U_{m,DFT}$ are the DFT spectra of the measured time domain data $y_m(t)$ and $u_m(t)$, at discrete time samples, obtained from the closed-loop experiment with excitation $r(t)$. The measured input and output DFT spectra can be expressed, [PS01], in terms of

$$\begin{aligned} Y_{m,DFT}(j\omega_k) &= Y_{DFT}(j\omega_k) + N_{y,DFT}(j\omega_k) \\ U_{m,DFT}(j\omega_k) &= U_{DFT}(j\omega_k) + N_{u,DFT}(j\omega_k) \end{aligned} \tag{2.120}$$

The direct plant estimate (2.119), hence corresponds to

$$\hat{G}(j\omega_k) = \frac{Y_{DFT}(j\omega_k) + N_{y,DFT}(j\omega_k)}{U_{DFT}(j\omega_k) + N_{u,DFT}(j\omega_k)} \tag{2.121}$$

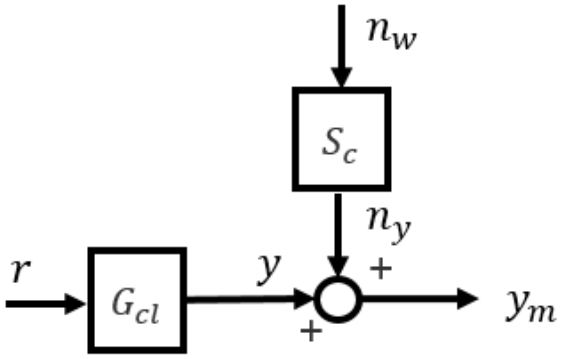

Figure 2.14: *Closed-loop framework representation.*

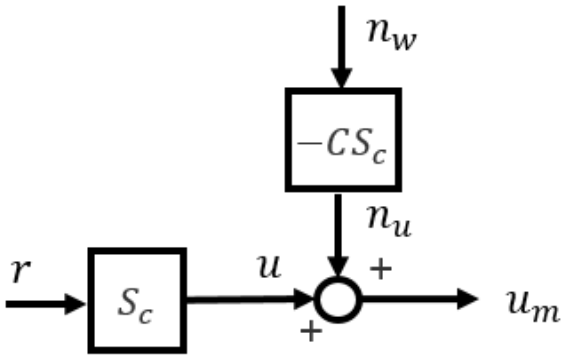

Figure 2.15: *Alternative closed-loop framework representation.*

This formulation corresponds to the errors-in-variables model formulation, [GKP96a], with linearly correlated input and output noise, since

$$N_y = S_c N_w \tag{2.122}$$

and

$$N_u = -CS_c N_w \tag{2.123}$$

according to Equation (2.114) and (2.118). Such a problem has been extensively studied in the literature, see [PS01] or [PS12] or [GKP96a] for example. Statements in the literature that such estimates are unbiased should be interpreted according to [Hea01b] as meaning asymptotically unbiased only (i.e. for an infinite number of sub-records or repetitions: $\hat{G}(j\omega_k) = \lim_{R\to\infty} \frac{\frac{1}{R}\sum_{r=0}^{R-1} Y_{m,DFT}^{[r]}(j\omega_k)}{\frac{1}{R}\sum_{r=0}^{R-1} U_{m,DFT}^{[r]}(j\omega_k)}$) and therefore be treated with some care.

Bias of Direct Non-parametric Estimate in Case of i.i.d. Normally Distributed Noise Sequence with Zero Mean and Variance σ_n^2: In [PS01] it is argued that an exact expression for the relative bias of (2.121) is

$$b(k) = \mathbb{E}[\frac{\hat{G}(j\omega_k) - G(j\omega_k)}{G(j\omega_k)}] = -\exp(-\frac{|U_{DFT}(j\omega_k)|^2}{\sigma_U^2(j\omega_k)}) \left(1 - \rho(j\omega_k) \frac{\frac{|U_{DFT}(j\omega_k)|}{\sigma_U(j\omega_k)}}{\frac{|Y_{DFT}(j\omega_k)|}{\sigma_Y(j\omega_k)}}\right) \quad (2.124)$$

for $k \neq 0, \frac{N}{2}$, where N is the number of samples of the measured data and the finite second-order moments are

$$\begin{aligned} \sigma_U^2(j\omega_k) &= \mathbb{E}[|N_{u,DFT}(j\omega_k)|^2] \\ \sigma_Y^2(j\omega_k) &= \mathbb{E}[|N_{y,DFT}(j\omega_k)|^2] \\ \sigma_{YU}^2(j\omega_k) &= \mathbb{E}[N_{y,DFT}(j\omega_k) N_{u,DFT}^*(j\omega_k)] \end{aligned} \quad (2.125)$$

where $N_{u,DFT}^*$ is the conjugate complex of $N_{u,DFT}$. The correlation coefficient of the normalized input and output errors $\frac{N_{u,DFT}}{U_{DFT}}$ and $\frac{N_{y,DFT}}{Y_{DFT}}$ is

$$\rho(j\omega_k)) = \frac{\sigma_{YU}^2(j\omega_k)}{\sigma_U(j\omega_k)\sigma_Y(j\omega_k)} \exp(-j\angle G(j\omega_k)) \quad (2.126)$$

In the following the argument $(j\omega_k)$ is omitted to increase readability. The signal n_y results from filtering n_w, which is a i.i.d. normally distributed noise sequence with zero mean and variance σ_n^2, by S_c, see Figure 2.14 and Equation (2.122). We then know [Bri81],[dv95], that $\sigma_Y^2 = \mathbb{E}[|N_{y,DFT}|^2]$ is **asymptotically**, i.e. for $N \to \infty$, where N are the number of samples,

$$\sigma_Y^2 = \mathbb{E}[|N_{y,DFT}|^2] = |S_c|^2 \sigma_n^2 \quad (2.127)$$

according to (2.99). Similarly, σ_U^2 is asymptotically

$$\sigma_U^2 = \mathbb{E}[|N_{u,DFT}|^2] = |CS_c|^2 \sigma_n^2 \quad (2.128)$$

see Figure 2.15 and Equation (2.123) and

$$\sigma_{YU}^2 = \mathbb{E}[N_{y,DFT} N_{u,DFT}^*] = -C^* |S_c|^2 \sigma_n^2 \quad (2.129)$$

With the relations (2.127) to (2.129) the correlation coefficient (2.126) becomes

$$\begin{aligned} \rho(j\omega_k) &= \frac{-C^*(j\omega_k)|S_c(j\omega_k)|^2 \sigma_n(j\omega_k)}{\sqrt{|C(j\omega_k)|^2 |S_c(j\omega_k)|^2 \sigma_n^2(j\omega_k) |S_c(j\omega_k)|^2 \sigma_n^2(j\omega_k)}} \exp(-j\angle G(j\omega_k)) \\ &= -\frac{C^*(j\omega_k)}{|C(j\omega_k)|} \exp(-j\angle G(j\omega_k)) \end{aligned} \quad (2.130)$$

Defining

$$\alpha = \exp\left(-\frac{|U_{DFT}|^2}{\sigma_U^2}\right) = \exp\left(-\frac{|U_{DFT}|^2}{|C|^2|S_c|^2\sigma_n^2}\right) \tag{2.131}$$

the relative bias in Equation (2.124) becomes

$$\begin{aligned} b &= -\alpha\left(1 - \left(-\frac{C^*}{|C|}\right)\exp\left(-j\angle G\right)\frac{\frac{|U_{DFT}|}{\sqrt{|C|^2|S_c|^2\sigma_n^2}}}{\frac{|Y_{DFT}|}{\sqrt{|S_c|^2\sigma_n^2}}}\right) \\ &= -\alpha\left(1 - \left(-\frac{C^*}{|C|^2}\right)\exp\left(-j\angle G\right)\frac{|U_{DFT}|}{|Y_{DFT}|}\right) \\ &= -\alpha\left(1 - \left(-\frac{1}{C}\right)\exp\left(-j\angle G\right)\frac{|U_{DFT}|}{|Y_{DFT}|}\right) \\ &= -\alpha\left(1 - \left(-\frac{1}{C}\right)\frac{1}{G}\right). \end{aligned} \tag{2.132}$$

where $|C|^2 = CC^*$ and $|Y_{DFT}|/|U_{DFT}| = |G|$ was used. Finally, using the relation

$$b(j\omega_k) = \mathbb{E}[\frac{\hat{G}(j\omega_k) - G(j\omega_k)}{G(j\omega_k)}] = \mathbb{E}[\frac{\hat{G}(j\omega_k)}{G(j\omega_k)} - 1] = \mathbb{E}[\frac{\hat{G}(j\omega_k)}{G(j\omega_k)}] - 1 = \frac{1}{G(j\omega_k)}\mathbb{E}[\hat{G}(j\omega_k)] - 1 \tag{2.133}$$

the expected value of $\hat{G}$ is obtained according to [PS01] by

$$\mathbb{E}[\hat{G}] = G(b+1) = G(-\alpha\left(1 - \left(-\frac{1}{C}\right)\frac{1}{G}\right) + 1) = G(1-\alpha) + \alpha\left(-\frac{1}{C}\right) \tag{2.134}$$

Because the excitation is assumed to be periodic and transients are assumed to have died out, U_{DFT} is given by

$$U_{DFT} = DFT(S_cR) = S_cR_{DFT} \tag{2.135}$$

according to Equation (2.118), such that α, given in Equation (2.131), can be reduced to

$$\alpha = \exp\left(-\frac{|S_cR_{DFT}|^2}{|C|^2|S_c|^2\sigma_n^2}\right) = \exp\left(-\frac{|R_{DFT}|^2}{|C|^2\sigma_n^2}\right) \tag{2.136}$$

This result shows that if the signal-to-noise ratio: $\sigma_n/|R_{DFT}|$ is large, α becomes small and $\mathbb{E}[\hat{G}]$ approaches G, see Equation (2.134). As shown in [PS01], the bias of an errors-in-variables estimator according to

$$\hat{G}(j\omega_k) = \frac{\frac{1}{R}\sum_{r=0}^{R-1} Y_{m,DFT}^{[r]}(j\omega_k)}{\frac{1}{R}\sum_{r=0}^{R-1} U_{m,DFT}^{[r]}(j\omega_k)} \tag{2.137}$$

where $Y^{[r]}_{m,DFT}(j\omega_k)$ and $U^{[r]}_{m,DFT}(j\omega_k)$ are the DFT spectra of R synchronized input /output records of an integer multiple of the known excitation period, decreases exponentially with R because in this case [PS01]

$$\alpha = \exp\left(-R\frac{|R_{DFT}|^2}{|C|^2\sigma_n^2}\right) \tag{2.138}$$

holds. Furthermore, the bias will be asymptotically (i.e. $R \to \infty$) zero as α goes to zero.

Variance of Direct Non-parametric Estimate: In [PS01] it is proposed that for the estimator (2.137), under the given assumptions, the expression

$$\sigma^2_G(j\omega_k) = \frac{|G(j\omega_k)|^2}{R}\left(\frac{\sigma^2_Y(j\omega_k)}{|Y_{DFT}(j\omega_k)|^2} + \frac{\sigma^2_U(j\omega_k)}{|U_{DFT}(j\omega_k)|^2} - 2\Re\left(\frac{\sigma^2_{YU}(j\omega_k)}{Y_{DFT}(j\omega_k)U^*_{DFT}(j\omega_k)}\right)\right) \tag{2.139}$$

could be used to calculate uncertainty regions, for "sufficiently large" number of records R. The expression (2.139) is obtained as the variance of the taylor series expansion, restricted to the first order terms, of $\hat{G}$ around the true value G, [PS01]. Note, that σ^2_G is not the variance of $\hat{G}$ obtained with the estimator (2.137). The variance of $\hat{G}$ of this estimator is shown in [PS01] to be infinite.

2.3.2 Indirect Non-parametric Plant Estimate under Closed-loop Conditions

In this section we are concerned with the non-parametric indirect plant estimate of the closed-loop framework depicted in Figure 2.13. For such a closed-loop system, the closed-loop transfer function is related to the plant and controller transfer function, $G(j\omega_k)$ and $C(j\omega_k)$ according to (2.115), which is repeated here for convenience.

$$G_{cl}(j\omega_k) = \frac{G(j\omega_k)}{1 + G(j\omega_k)C(j\omega_k)} \tag{2.140}$$

Assuming that an closed-loop frequency response estimate $\hat{G}_{cl}(j\omega_k)$ is available, a frequency response estimate of the plant can be obtained by solving (2.140) for G

$$\hat{G}(j\omega_k) = \frac{\hat{G}_{cl}(j\omega_k)}{1 - \hat{G}_{cl}(j\omega_k)C(j\omega_k)} \tag{2.141}$$

Assume that

- The closed-loop estimate $\hat{G}_{cl}(j\omega_k)$ is given by

$$\hat{G}_{cl}(j\omega_k) = G_{cl}(j\omega_k) + G_{B,cl}(j\omega_k) + \epsilon_k \tag{2.142}$$

where $G_{cl}(j\omega_k)$ is the true closed-loop frequency response and $G_{B,cl}(j\omega_k)$ is a constant bias.

- The complex random variable ϵ_k has normally distributed real and imaginary parts, which might be correlated.
- Both the real and imaginary part of ϵ_k have zero mean.

For this case, [Hea01b] derived the expected value (in terms of an Cauchy Principle Value) of the indirect non-parametric plant estimate in (2.141). It is given in Lemma P.1.1. Similar results were found by [Dou80], [DB90].

Bias of Indirect Non-parametric Estimate in Case of i.i.d. Normally Distributed Noise Sequence with Zero Mean and Variance σ_n^2: Assume that

- the noise sequence n_w in the closed-loop system in Figure 2.13 is i.i.d. normally distributed with zero mean and variance σ_n^2
- the reference input $r(t)$ is a periodic excitation, e.g. a multisine signal and is exactly known
- leakage is negligible
- transients are negligible

We further assume that the closed-loop frequency response is estimated by the ETFE

$$\hat{G}_{cl}(j\omega_k) = \frac{Y_{m,DFT}(j\omega_k)}{R_{DFT}(j\omega_k)} \tag{2.143}$$

where $Y_{m,DFT}(j\omega_k)$ and $R_{DFT}(j\omega_k)$ are the DFTs of the signals r and y_m depicted in Figure 2.13. Because of the relation (2.114) for the measured output signal y_m under the given closed-loop structure, the closed-loop estimate will result in

$$\hat{G}_{cl}(j\omega_k) = \frac{Y_{DFT}(j\omega_k)}{R_{DFT}(j\omega_k)} + \frac{N_{y,DFT}(j\omega_k)}{R_{DFT}(j\omega_k)} \tag{2.144}$$

where $Y(j\omega) = G_{cl}(j\omega)R(j\omega)$ and $N_y(j\omega)$ results from filtering n_w by the sensitivity S_c, see Figure 2.14. Because R is periodic and transients are assumed to have died out, $\frac{Y_{DFT}(j\omega_k)}{R_{DFT}(j\omega_k)}$ corresponds to the true closed-loop frequency response $G_{cl}(j\omega)$:

$$\hat{G}_{cl}(j\omega_k) = G_{cl}(j\omega) + \frac{N_{y,DFT}(j\omega_k)}{R_{DFT}(j\omega_k)} = G_{cl}(j\omega_k) + \epsilon_k \tag{2.145}$$

Because n_w is a i.i.d. normally distributed noise sequence with zero mean and variance σ_n^2, the expected value of $\epsilon_k = \frac{N_{y,DFT}}{R_{DFT}}$ is according to (2.95):

$$\mathbb{E}[\epsilon_k] = 0 \tag{2.146}$$

The variance and correlation of the real and imaginary parts of ϵ_k are asymptotically, i.e. for $N \to \infty$, where N are the number of samples, according to [Bri81], [dv95], Equation (2.145) and (2.122), given by

$$\begin{aligned} &\mathbb{E}[\Re(\epsilon_k)\Re(\epsilon_k)] = \mathbb{E}[\Im(\epsilon_k)\Im(\epsilon_k)] = \sigma(j\omega_k)^2 = \frac{1}{2}|S_c(j\omega_k)|^2 \frac{\sigma_n^2}{|R_{DFT}(j\omega_k)|^2} \\ &\mathbb{E}[\Re(\epsilon_k)\Im(\epsilon_k)] = 0 \end{aligned} \tag{2.147}$$

and asymptotically jointly normally distributed. The expected value of the indirect plant estimate (2.141) will then be according to Lemma P.2.1

$$\mathbb{E}[\hat{G}(j\omega_k)] = \alpha(j\omega_k)G(j\omega_k) + (1 - \alpha(j\omega_k)) \left(-\frac{1}{C(j\omega_k)} \right) \tag{2.148}$$

where α is

$$\alpha = 1 - \exp(-\frac{1}{2}\frac{1}{\sigma^2}|\frac{S_c}{C}|^2) \tag{2.149}$$

and using Equation (2.147)

$$\begin{aligned} \alpha &= 1 - \exp(-\frac{1}{2}\frac{1}{\sigma^2}|\frac{S_c}{C}|^2) = 1 - \exp(-\frac{1}{2}\frac{1}{\frac{1}{2}\frac{\sigma_n^2}{|R_{DFT}|^2}|S_c|^2}|\frac{S_c}{C}|^2) \\ &= 1 - \exp(-\frac{1}{\sigma_n^2}|\frac{R_{DFT}}{C}|^2) \end{aligned} \tag{2.150}$$

Note, that for better readability $(j\omega_k)$ was omitted in the last equations.

Variance of Indirect Non-parametric Plant Estimate: [Hea01b] shows that the variance of the previously discussed indirect plant estimate is infinite. A similar result (infinite variance) has been obtained by [GKP96b] in the context of errors-in-variables estimates and in [PS01] for errors-in-variables estimates with correlated input and output noise. As we have seen in Section 2.3.1 the direct estimate problem can be expressed in terms of this latter case. For such cases, i.e. in the absence of a well- defined variance, [GKP96b] has proposed an "exclusion zone" around the singularity to regularize the problem and render the variance of such estimates finite. In context of indirect identification under closed-loop conditions this idea was investigated by [WG02]. Thereby they consider the closed-loop set-up depicted in Figure 2.16. The respective indirect estimate, for this set up, resulting from the inversion of the closed-loop relationship

$$G_{cl}(j\omega_k) = \frac{G(j\omega_k)C(j\omega_k)}{1 + G(j\omega_k)C(j\omega_k)} \tag{2.151}$$

is

$$\hat{G}(j\omega_k) = \frac{\hat{G}_{cl}(j\omega_k)}{C(j\omega_k)(1 - \hat{G}_{cl}(j\omega_k))} \tag{2.152}$$

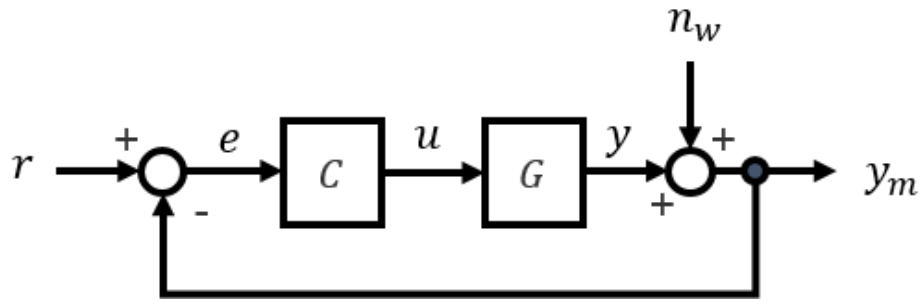

Figure 2.16: *Closed-loop framework.*

From this expression it becomes clear that a singularity exists for $\hat{G}_{cl} = 1$. Therefore, the true closed-loop transfer function is required to be bounded away from one at the considered frequencies. Consequently, an exclusion zone around the singularity can be introduced, meaning that any value of $\hat{G}_{cl}$ in the vicinity of one, i.e

$$|\hat{G}_{cl}(j\omega_k) - 1| < \epsilon \tag{2.153}$$

can be discarded in order to regularize the distribution of $\hat{G}$. Assuming that neither $\hat{G}_{cl}$, nor the true closed-loop G_{cl}, lies within some exclusion region in the complex plane, surrounding the point one, [WG02] develop an expression for the resulting bias and variance. [WG02] argue that under some conditions the bias is essentially unchanged from the result of [Hea01b], presented in the previous sections, and the effect of the chosen exclusion zone is examined. [WG02] express the variance of the estimate with this exclusion zone as an integral over an infinite series expansion and show that using this regularization technique the resulting variance of the estimate is bounded. However, this approach for the given controller structure, requires considering frequencies where neither $\hat{G}_{cl}$, nor the true closed-loop G_{cl}, lies within some exclusion region in the complex plane, surrounding the point one. This is problematic, since in most control design problems one objective is to maximize the frequency region where the closed-loop frequency response equals 1 in order to obtain a high bandwidth and steady-state accuracy. Hence, such a problem formulation of the indirect plant estimate might be impractical, because the plant estimate can be only obtained at higher frequencies. However, it is important to note that the singularity depends on the problem formulation and controller structure. For example, adding a constant feedforward gain H to the structure in Figure 2.16, as depicted in Figure 2.17, results in the closed-loop relationship

$$G_{cl}(j\omega_k) = \frac{G(j\omega_k)(C(j\omega_k) + H)}{1 + G(j\omega_k)C(j\omega_k)} \tag{2.154}$$

with indirect estimate

$$\hat{G}(j\omega_k) = \frac{\hat{G}_{cl}(j\omega_k)}{(C(j\omega_k) + H) - C(j\omega_k)\hat{G}_{cl}(j\omega_k)} \tag{2.155}$$

Consequently, for such a controller structure the singularity for the indirect plant esti-

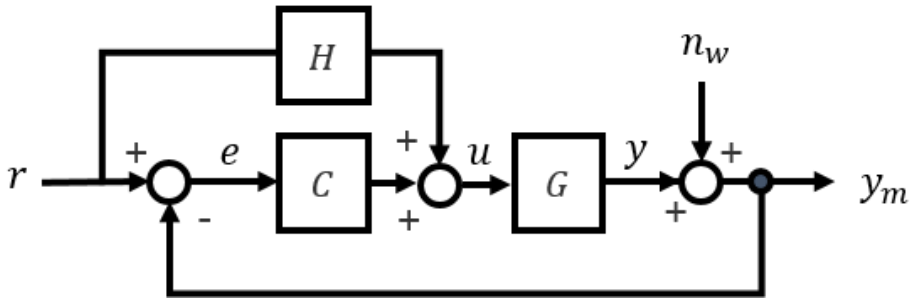

Figure 2.17: *Closed-loop framework with feed forward.*

mate occurs at $\hat{G}_{cl}(j\omega_k) = (C(j\omega_k) + H)/C(j\omega_k) = 1 + H/C(j\omega_k)$.

For a problem formulation as depicted in Figure 2.13, with closed-loop relationship

$$G_{cl}(j\omega_k) = \frac{G(j\omega_k)}{1 + G(j\omega_k)C(j\omega_k)} \tag{2.156}$$

and indirect estimate

$$\hat{G}(j\omega_k) = \frac{\hat{G}_{cl}(j\omega_k)}{(1 - C(j\omega_k)\hat{G}_{cl}(j\omega_k))} \tag{2.157}$$

[Hea03] also addresses the idea of introducing an exclusion zone around the singularity, i.e. $\hat{G}_{cl}(j\omega_k) = \frac{1}{C(j\omega_k)}$. Hence, the data is discarded if the estimate $\hat{G}_{cl}(j\omega_k)$ is sufficiently close to $\frac{1}{C(j\omega_k)}$. Assuming that the real and imaginary part of the estimate $\hat{G}_{cl}(j\omega_k)$ are independently normally distributed with equal variance σ^2, [Hea03] derives, from the probability density function of the closed-loop estimate, an expression for the variance of the indirect estimate, when such an exclusion zone is introduced. Furthermore, an approximation of the variance (via asymptotic expansion) for an "appropriately" ranged exclusion zone and for large values of the term

$$\beta = \frac{1}{2\sigma^2}|G_{cl} - \frac{1}{C}|^2 \tag{2.158}$$

meaning, for cases where G_{cl} is sufficiently far from $\frac{1}{C}$ or the variance of $\hat{G}_{cl}$ is sufficiently small, is given.

In [Hea00] the probability density function of the indirect plant estimate $\hat{G}$ for a closed-loop system as depicted in Figure 2.13 is derived, assuming that the real and imaginary part of the estimate $\hat{G}_{cl}(j\omega_k)$ are independently normally distributed with equal variance σ^2. It is shown, that this probability density function can be described as a horseshoe encircling the inverse of the controller. Another important result presented in [Hea00] is that

this probability density function approximates a complex normal distribution, with mean G and variance $\sigma^2|1+GC|^4$, if the signal-to-noise-ratio is sufficiently high. Nevertheless, the variance of $\hat{G}$ is in theory infinite.

Chapter 3

Test-Based Controller Retuning Concept

This chapter presents the main contribution of this thesis - the Test-Based Gain Retuning Concept (C1-C4). We will start with an introductory motivational scenario. Imagine you designed a linear controller based on a linear nominal plant model of the considered system, such that all addressed requirements are satisfied by the resulting closed-loop system of the designed controller and nominal plant model, hence providing a desired behavior. Now during tests, where the designed controller is applied to the real system it turns out that the closed-loop system, of designed controller and true plant, does not perform as desired. That means, that the measured response deviates from the desired response such that for example some addressed performance requirements that were all satisfied on the nominal plant model, are now on the real system not satisfied. This is a situation, where the method that is presented in the following can be used. The method allows to retune the controller gains or parameters in an automated and easy manner based on closed-loop tests of the initial controller and true system, such that the true closed-loop response with the retuned controller will be closer to the desired one.

First, how could that happen that the designed controller does not perform as desired in reality? In many applications, the models provided for controller design are inaccurate, and the uncertainties are not known exactly. The task is to design a controller based on the given model - but often in the project there is no money or work-packages allocated regarding extensive controller design and assessment or regarding system identification campaigns to obtain an accurate model. The discrepancy between the assumed model during controller design and the real dynamics and the lack of resources to improve the model or apply more advanced controller design and assessment techniques, leads to a degradation of the controller performance on the true system.

For the nominal model however, especially in the domain of flight control, it is in general straight forward to obtain controller parameters that satisfy all relevant requirements, by applying classical linear gain design techniques. This means that a nominal closed-loop behavior can be obtained – when applying the so designed controller to the nominal plant

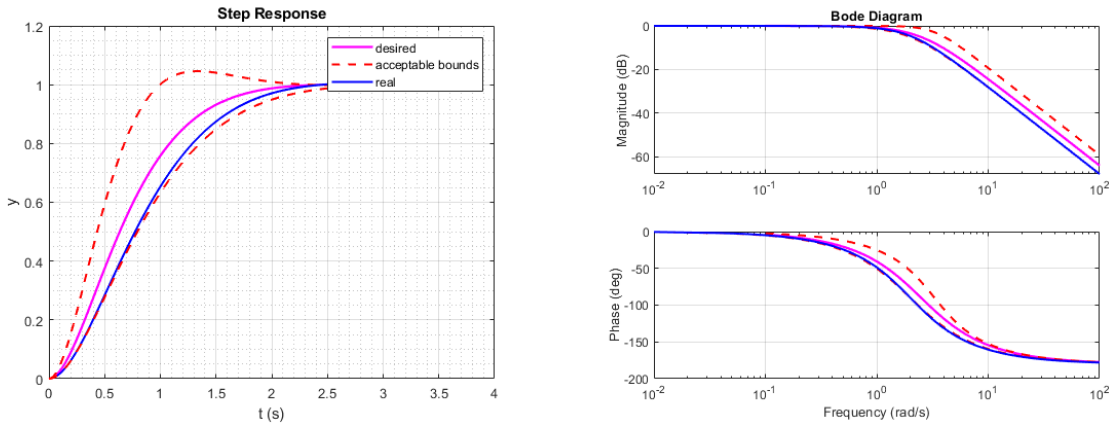

Figure 3.1: *Schematic of desired and real closed-loop behavior.*

model – that satisfies all requirements. Hence, it provides a desired behavior for the true system, see Figure 3.1 (magenta). If there are outer control loops like an autopilot for example, this nominal inner-loop behavior could also serve as a basis for their respective gain design.

As mentioned before it is very unlikely that the real plant will exactly behave like the nominal plant model. In case the uncertainties of the plant model are known, the information about the uncertainties could be used to perform one of the various robust gain design concepts. These aim to make sure that for all possible plant variations, according to the given uncertainties and assumed uncertainty structure, the closed-loop performance and margins will be within some acceptable bounds, see Figure 3.1 (red-dashed). This requires first the availability of the corresponding resources, since the related work load is slightly higher than in the case of designing controller gains for one plant model only, namely the nominal plant model. If outer control loops exist, their respective gain design, too, needs consequently to account for a range of possible closed-loop responses of the inner-loop. This also increases the workload, compared to the case where only one closed-loop behavior is expected. Furthermore, such designs often lead to a conservative performance and result in a compromise only. Meaning, depending on the true plant parameters the response will deviate from the perfect, desired one, see Figure 3.1 (blue). It will be only adequate, i.e within the required boundaries - in case the assumed uncertainties and uncertainty structure was correct. In case the uncertainties were underestimated or some of the system dynamics were neglected, it could happen that the closed-loop behavior of the true plant violates the boundaries such that some requirements are not met. At the end the ideal situation is considered to be a controller, fine tuned in such a way that the closed-loop behavior on the true plant is as close as possible to the desired behavior. Especially if the outer-loops were designed based on this desired closed-loop behavior, they would be expected to perform as desired on the true system if the true inner-loop would behave as the design one.

Conventionally, the first idea would direct towards an attempt to further reduce the uncertainties by trying to identify the plant parameters more accurately. This would require flight test campaigns which are expensive. Moreover, there are usually more plant parameters than controller gains. It should be also mentioned, that a model-based control design includes an intermediate approximation and optimization, namely the intermediate step of identifying a parametrized model, which requires an assumption for the model structure and model-order. It is hence considered as beneficial if this intermediate approximation step could be skipped when fine-tuning the controller gains. Furthermore, it is sought for a method that allows to fine tune the controller gains based on experiments on the true system under the expected operational conditions such that it is made sure that really the true closed-loop behavior is improved, and the true model order is taken into account.

For these situations: namely where the real closed-loop response with an initial model-based controller deviates from the desired response, a method is presented where the gains are retuned in an automated manner based on test data such that the true closed-loop response with these new gains approaches the desired one. At the same time the satisfaction of the stability margins of this retuned controller on the true system is addressed.

3.1 Concept

This section gives an overview over the test-based controller retuning concept (C1). We find it useful to introduce first of all the terminology summarized in Table 3.1 that will be used throughout this thesis. The basic principle of the controller retuning procedure is depicted in Figure 3.2.

First it is assumed that based on an available linear nominal plant model G_{nom} an initial linear controller $C_0 = C_0(\boldsymbol{p_0})$ is designed. Using classical model-based controller design techniques the respective initial controller gains or parameters, $\boldsymbol{p}_0$, can be obtained. It is further assumed that the resulting closed-loop $G_{cl,des}$ of nominal plant model and initial controller satisfies all addressed requirements and hence provides a desired closed-loop behavior. Tests on the true system with true plant G and initial controller C_0 might reveal that the true closed-loop system $G_{cl,0}$ does not perform as desired, due to differences between the nominal plant model and the true system, such that a retuning of the controller is required. This constitutes a typical situation where the test-based retuning method can be applied. The procedure is as follows:

1. First of all closed-loop tests on the true plant G with the initial controller C_0 are performed by injection of specially designed test maneuvers.

2. Based on the known applied reference input r and the logged measurement data of the closed-loop output signal y_m, a non-parametric frequency response estimate $\hat{G}_{cl,0}(j\omega_k)$ is obtained, at discrete frequencies ω_k that will be defined later. Note,

Nomenclature	**Explanation**
G_{nom}	parametrized nominal plant model
$\boldsymbol{p}$	controller parameters
$C_0 = C(\boldsymbol{p}_0)$	initial controller with initial parameters $\boldsymbol{p}_0$, obtained from model-based control design using G_{nom}
$G_{cl,des}$	desired closed-loop, e.g. closed-loop of nominal plant model G_{nom} and initial controller C_0
G	true plant
$G_{cl,0}$	true closed-loop of true plant G with initial controller C_0
$\hat{G}_{cl,0}$	estimated closed-loop based on measurement data from closed-loop tests with true plant G and initial controller C_0
$\hat{G}$	estimated plant based on $\hat{G}_{cl,0}$
$\tilde{C} = C(\tilde{\boldsymbol{p}})$	retuned controller: parametrized with optimized controller parameters $\tilde{\boldsymbol{p}}$
$\tilde{G}_{cl}$	true closed-loop of true plant G with retuned controller $\tilde{C}$
$\hat{\tilde{G}}_{cl}$	estimate of tuned closed-loop $\tilde{G}_{cl}$, based on $\hat{G}_{cl,0}$, C_0 and $\tilde{C}$, also denoted as anticipated tuned closed-loop

Table 3.1: *Nomenclature.*

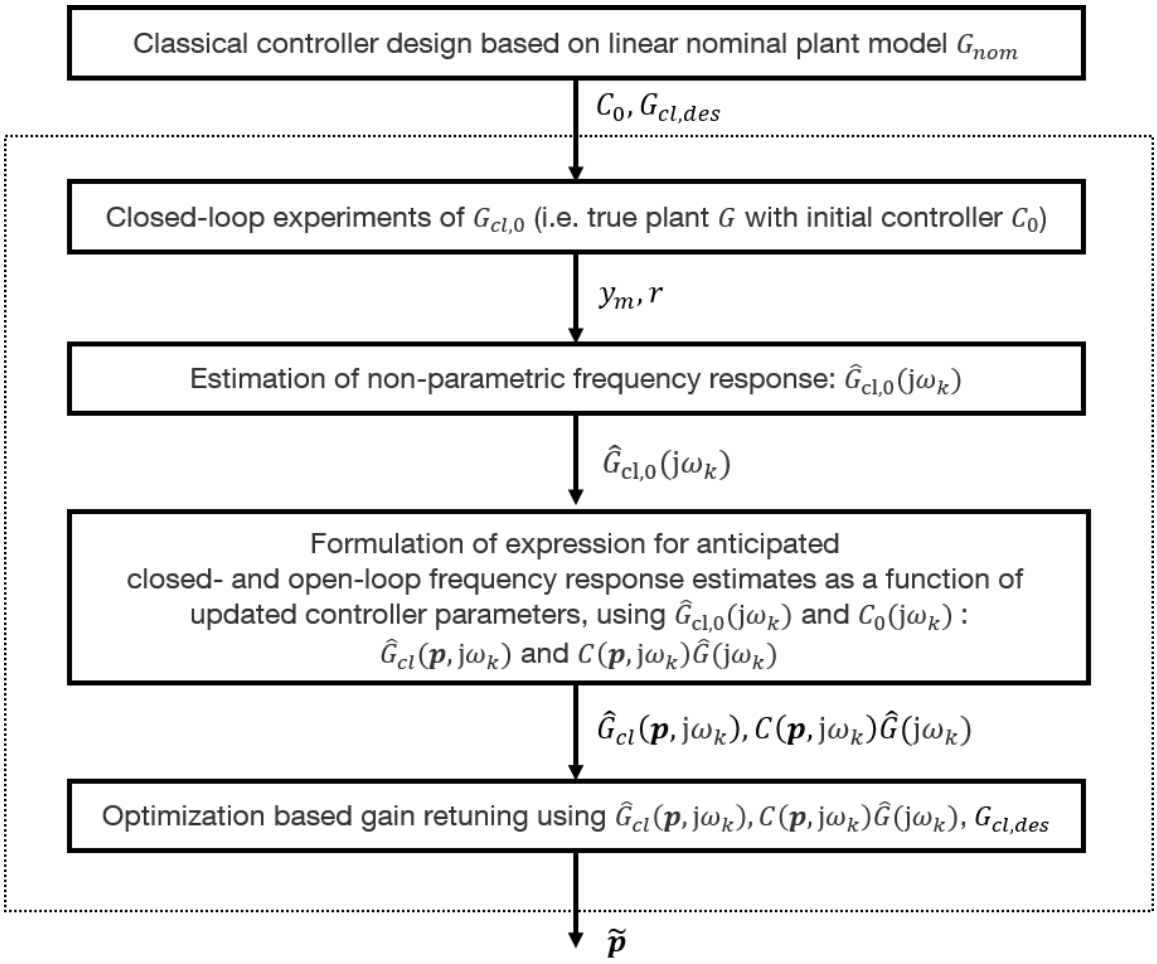

Figure 3.2: *Schematic of test-based controller parameter retuning concept.*

that in the following the argument $(j\omega_k)$ is omitted whenever it is clear from the context. The frequency response estimate $\hat{G}_{cl,0}$ is a non-parametric representation of the true closed-loop system $G_{cl,0}$, of the true plant G with the initial controller C_0. Note, that this estimate is independent of a specific model structure or model-order assumptions.

3. Assuming that the initial parameters set and structure of the controller C_0, that was applied in the test is of a linear form and known exactly, an anticipated closed–loop frequency response $\hat{G}_{cl}(C(\boldsymbol{p}))$ for an updated controller $C = C(\boldsymbol{p})$ with arbitrary parameter values $\boldsymbol{p}$ can be calculated as well as an anticipated open-loop frequency response $C\hat{G}$, which is used to calculate the anticipated margins. As we will see in Section 3.6 and 3.7 these estimates ($\hat{G}_{cl}$ and $C\hat{G}$) can be calculated based on $\hat{G}_{cl,0}$, C_0 and C directly. These relations are used within an optimization, which seeks to retune the controller parameters in an automated, systematic manner, such that all relevant requirements will be met by the true retuned closed-loop system. The proposed optimization problem and fitness function imposes the relevant design criteria by minimizing the deviation between the desired closed-loop $G_{cl,des}$ and the anticipated tuned closed-loop $\hat{G}_{cl}(C(\boldsymbol{p}))$ in the frequency domain and with respect to the controller parameters $\boldsymbol{p}$. A regularization is incorporated into the cost function to retain the retuned gains within reasonable bounds around the initial gains. The fulfillment of relevant stability criteria, calculated using the estimate $C(\boldsymbol{p})\hat{G}$, is enforced by constraints. The solution of the optimization process provides the possibly optimal controller parameters $\tilde{\boldsymbol{p}}$.

The following sections will address each of these steps in more detail, supported by a simple illustrative example that is presented in the next section.

3.2 Illustrative Example

This section presents the example system that will demonstrate the theory presented in the following sections.

3.2.1 System Structure

We consider the closed-loop system depicted in Figure 3.3. The considered plant dynamics are the linearized short period dynamics of an fixed-wing aircraft given by

$$\begin{bmatrix} \dot{\alpha} \\ \dot{q} \end{bmatrix} = \begin{bmatrix} Z_\alpha & 1+Z_q \\ M_\alpha & M_q \end{bmatrix} \begin{bmatrix} \alpha \\ q \end{bmatrix} + \begin{bmatrix} 0 \\ M_\eta \end{bmatrix} \eta \tag{3.1}$$

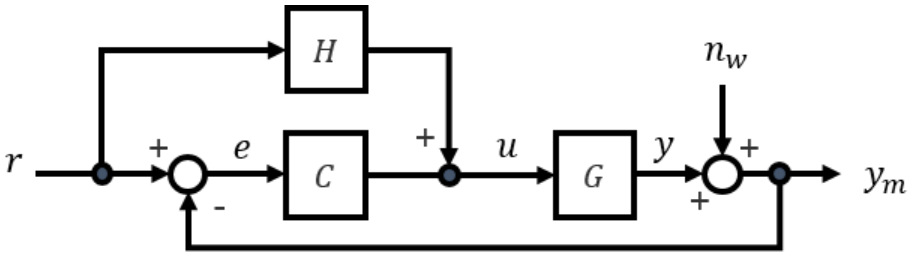

Figure 3.3: *Closed-loop block diagram.*

Parameter	Value
Z_α	-1.068
Z_q	-0.022
M_α	-4.160
M_q	-1.689
M_η	-3.914

Table 3.2: *Nominal Model parameters.*

where $\alpha = \alpha(t)$ is the angle of attack, $q = q(t)$ is the pitch rate and the input $u = \eta = \eta(t)$ is the elevator deflection. Note, that for better readability, the argument (t) was omitted. The measured output signal is the pitch rate, with an additive noise signal $n_w = n_w(t)$

$$y_m = y + n_w = q + n_w = \begin{bmatrix} 0 & 1 \end{bmatrix} \begin{bmatrix} \alpha \\ q \end{bmatrix} + n_w \tag{3.2}$$

The parameter values of the nominal plant model that equals (3.1) are summarized in Table 3.2. In the Laplace domain we can express the nominal plant dynamics by

$$Y(s) = G_{nom}(s)U(s) \tag{3.3}$$

where $G_{nom}(s)$ is given by

$$G_{nom}(s) = \begin{bmatrix} 0 & 1 \end{bmatrix} (s\mathbf{I} - \begin{bmatrix} Z_\alpha & 1 + Z_q \\ M_\alpha & M_q \end{bmatrix})^{-\mathbf{1}} \begin{bmatrix} 0 \\ M_\eta \end{bmatrix} \tag{3.4}$$

The considered controller is a simple pitch rate controller, where the reference input signal $r = q_c$, is a pitch rate command and the feedback signal $y_m = q$ is the measured pitch rate. The control law obeys in the Laplace domain

$$\begin{aligned} U(s) &= C(s)(R(s) - Y_m(s)) + H(s)R(s) \\ &= (C(s) + H(s))R(s) - C(s)Y_m(s) \\ &= T(s)R(s) - C(s)Y_m(s) \end{aligned} \tag{3.5}$$

Parameter	Value
k_0	-0.31
$k_{I,0}$	-0.18
h_0	-1.48

Table 3.3: *Initial controller parameters.*

where $C(s)$ is a PI controller:

$$C(s) = k + \frac{k_I}{s} \tag{3.6}$$

with feedback gain k and integral gain k_I, and where $H(s)$ is a constant feed forward gain h. The controller transfer behavior from the reference signal r to control signal u is described by

$$T(s) = C(s) + H(s) \tag{3.7}$$

We define the controller parameter vector as

$$\boldsymbol{p} = \begin{bmatrix} \boldsymbol{p}_c & p_h \end{bmatrix} \tag{3.8}$$

with

$$\begin{aligned} \boldsymbol{p}_c &= \begin{bmatrix} k & k_I \end{bmatrix} \\ p_h &= h \end{aligned} \tag{3.9}$$

3.2.2 Initial Model-based Controller Parameters and Nominal Closed-loop

Based on the nominal plant model the controller parameters are determined, such that the short period poles of the resulting closed-loop system of nominal plant model and controller are conjugate complex with desired natural frequency ω_0 corresponding to a CAP of 1, (providing Handling 1 qualities), and a damping ratio of $\zeta = \frac{\sqrt{2}}{2}$. The feed forward gain introduces a zero to the closed-loop system transfer behavior from commanded pitch rate q_c to measured pitch rate. The value of the feed forward gain is determined such that the resulting zero cancels the closed-loop pole, introduced by the controller integrator. The reason for the cancellation of the integrator pole is, that it is undesired that this additional pole can be anticipated by the pilot. The resulting gain margin of nominal plant and controller is larger than $6dB$ and the resulting phase margin is larger than 45 deg. The obtained initial model-based controller parameters are summarized in Table 3.3. In closed-loop, see Figure 3.3, we have the relation

$$Y_m = GC(R - Y_m) + GHR + N_w \tag{3.10}$$

from which the relation

$$Y_m = \frac{G(C+H)}{1+GC}R + \frac{1}{1+GC}N_w = G_{cl}R + S_cN_w = G_{cl}R + N_y \tag{3.11}$$

can be obtained, with sensitivity

$$S_c = \frac{1}{1+GC} \tag{3.12}$$

and closed-loop transfer function

$$G_{cl} = \frac{G(C+H)}{1+GC} \tag{3.13}$$

The block diagram representation of Equation (3.11), is depicted in Figure 2.14. Note, that the dependency on the Laplace operator (s) was omitted for better readability. The frequency response of the nominal closed-loop system, i.e.

$$G_{cl,des} = \frac{G_{nom}(C_0+H_0)}{1+G_{nom}C_0} \tag{3.14}$$

is revealed in the bode-diagram in Figure 3.4. This frequency response specifies the desired behavior, that we would like to achieve on the true plant by retuning the controller gains.

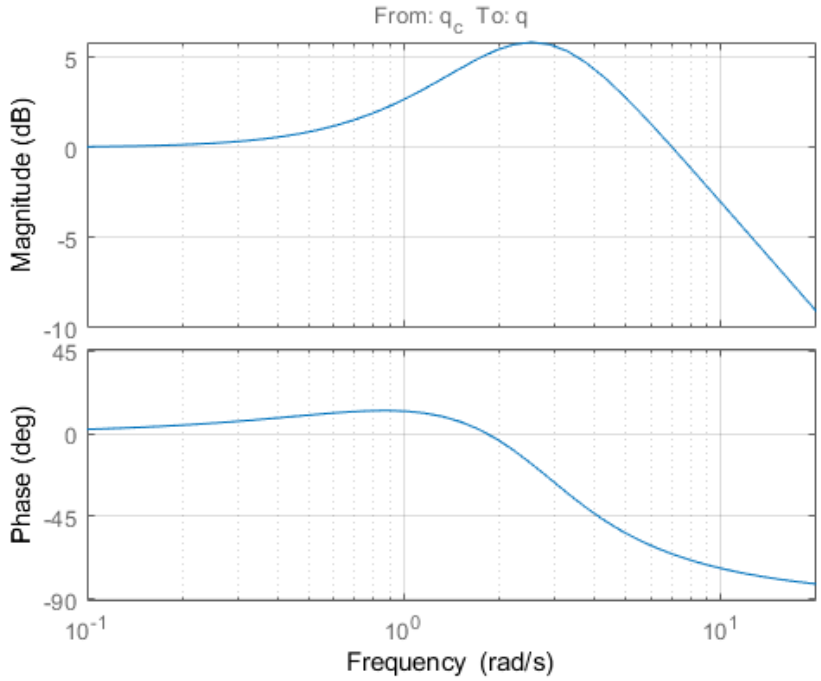

Figure 3.4: *Desired closed-loop frequency response.*

3.3 Assumptions and Design Choices

This section summarizes the assumptions and design choices, resulting from the discussions in Section 2.2. These are applicable for the considerations in the following sections. In the following sections we will be concerned with indirect frequency domain non-parametric estimates of the open-loop for calculation of the stability margins and closed-loop response - both for a new parameter set for the controller. These estimates will have in common, that they are calculated based on an estimate of the closed-loop frequency response from experimental data obtained under the closed-loop conditions as depicted in Figure 3.3. We choose to calculate this closed-loop estimate by an averaged ETFE as described in Section 2.2.5 according to

$$\hat{G}_{cl}(j\omega_k) = \frac{\frac{1}{R}\sum_{r=0}^{R-1} Y_{m,DFT}^{[r]}[k]}{\frac{1}{R}\sum_{r=0}^{R-1} R_{DFT}^{[r]}[k]} = \frac{\frac{1}{R}\sum_{r=0}^{R-1} Y_{m,DFT}^{[r]}[k]}{R_{DFT}[k]} \tag{3.15}$$

where $Y_{m,DFT}^{[r]}$ is the DFT of the $r'th$ record of the measured output signal y_m and R_{DFT} is the DFT of the exactly known reference input r. The chosen estimation method is the ETFE because of its simplicity and good properties, see Section 2.2, under the following conditions: We assume the leakage errors to be negligible because the excitation signal is chosen to be periodic. Specifically we chose it to be a multi-sine. The system is assumed to be linear and full periods of the excitation signal are measured, i.e. the record time length T_w and the multi-sine are chosen such, that T_w is a multiple integer of the periods of the sines contained within the multi-sine. Each record contains a finite number of discrete samples of the measured signals y_m and r. The measured signals are assumed to be synchronized. Furthermore, we assume leakage due to transients from maneuver initiation to be negligible. This error can be reduced by discarding an appropriate number of initial records. Since the reference signal is generated and logged by the FCC it is assumed to be exactly known. The output signal is assumed to be disturbed by noise as depicted in Figure 3.3. The noise sequence is assumed to be i.i.d. normally distributed with zero mean. We summarize the made assumptions:

- linear system dynamics
- finite number of discrete samples are measured
- synchronized measurements
- transients due to maneuver initiation are negligible
- full periods of the periodic excitation signal are measured
- errors due to leakage are negligible
- chosen estimation method for initial closed-loop estimate is the averaged ETFE

- reference signal and initial controller, that is applied in the closed-loop experiment, are exactly known

- output signal is additively perturbed by an i.i.d. normally distributed noise sequence with zero mean and variance σ_n^2.

3.4 Closed-loop Test-Maneuver

According to Section 3.1, see also Figure 3.2, the first step of the test-based controller retuning is to perform closed-loop tests of the true plant G with the initial controller C_0, H_0, see Figure 3.3. Carefully predesigned test maneuvers are injected over the reference input r. According to Section 3.3 the finite, discrete, sampled measured output signal sequence $y_m[n]$ is perturbed by noise as depicted in Figure 3.3.

The following section is extracted from my publication [GHSM21]: " [*The closed-loop system is excited over the reference input r using a periodic signal, in specific a multisine signal. During execution of the maneuver, the closed-loop response y_m is logged*]. The multisine input signal is calculated as proposed in [Mor12]. It is composed of the sum of harmonic sinusoids with individual phase shifts Φ_k according to

$$r_T(t) = \sum_{k=1}^{n_\omega} A_k \sin\left(\frac{2\pi l_k}{T} t + \Phi_k\right), t \in [0, T] \tag{3.16}$$

where A_k is the amplitude of the k-th sinusoidal component, T is the window length, and $l_k \in \mathbb{S}, \mathbb{S} \subset \mathbb{N}$ with $k = 1, \ldots, n_\omega$. These values are selected as follows:

Time Length T of the Excitation and Selected Frequency Set: T is the time length of the excitation, i.e. the maneuver, which defines the first harmonic frequency as $\omega_{min} = 2\pi/T$ for the sinusoids in Equation (3.16).
The frequency set with n_ω selected frequencies is chosen as $\omega_k = l_k \cdot \omega_{min}$, $l_k \in \mathbb{S}, \mathbb{S} \subset \mathbb{N}$ with $k = 1, \ldots, n_\omega$ such that the frequencies of interest, where the dynamics to be estimated are expected to lie, are covered. Note, that the available frequencies for the sinusoids in Equation (3.16) are harmonically related, i.e. integer multiples of ω_{min}. This ensures that the excitation signal contains integer numbers of full periods to avoid leakage, see Section 2.2.3.3. [*The time length of the excitation together with the selected frequency set, hence, determines the frequency spacing of the ETFE according to Section 2.2.3.3. It shall be selected such that the frequency grid is fine enough to capture the dynamics of the system to be estimated. The finer the grid, the longer is the required maneuver duration. This increases the test time and costs on one hand, on the other hand with too long maneuver lengths, one might risk an unacceptable drift away from the reference or trim condition, resulting in bad estimates. Hence, the maneuver length shall be chosen as a compromise of these contradicting factors. Furthermore, the selected frequencies shall*

cover the dynamics of interest of the system to be estimated, which determines the considered frequency interval. Together with the required signal-to-noise ratio, which determines the required amplitude of the excitation, it has to be made sure that actuator constraints, such as limits and rate saturations are not violated, as this would introduce nonlinearities, resulting in an erroneous estimate.]

Phase angles Φ_k: If the phase angles Φ_k were chosen randomly, then in general, the selected harmonic sinusoids could add together at some points leading to an input with relatively large amplitudes. This is undesired because it can cause a drift of the dynamic system too far from the selected reference condition. Therefore, the phase angles Φ_k for each of the selected harmonic components are chosen according to [Mor12]. The basic idea of this approach is to minimize the relative peak factor (RPF) with respect to Φ_k. The RPF is a measure of the efficiency of an input for dynamic modeling purposes in terms of the amplitude range of the input divided by a measure of the input energy. [*Low relative peak factors are desirable and efficient for estimating dynamic model parameters because the objective is to excite the dynamic system with good input energy over a variety of frequencies while minimizing the input amplitudes in the time domain to avoid driving the dynamic system too far away from the reference condition, [Mor12].*]

Amplitudes A_k: To achieve a uniform power distribution according to [Mor12], all A_k are selected identical as

$$A_k = A/\sqrt{n_\omega} \quad \forall k \tag{3.17}$$

where n_ω is the number of sinusoidal components included in the summation (3.16). A is the amplitude of the reference input r, to be chosen such that sufficient signal-to-noise ratio on the measured system response is achieved. [*Furthermore, it has to made sure that these amplitudes are selected such that together with the selected frequencies the resulting excitation does not lead to a violation of actuator constraints.*]" [end of quotation from my publication [GHSM21]]

The final maneuver will consist of R repetitions of the multisine signal $r_T(t)$, resulting in a total maneuver length of RT. The R measurement records are used to calculate the averaged ETFE, see Section 2.2.5. As shown in Section 2.2.5 the variance of the averaged ETFE can be decreased by increasing the number of repetitions R. But on the other hand the maneuver length is increased, such that again a compromise between costs, drift away from the reference condition, variance reduction and maneuver length T, meaning the frequency grid, needs to be found.

3.5 Non-parametric Frequency Domain Estimate of Closed-loop of True Plant with Initial Controller

In the second step of the proposed test-based controller retuning method, according to Section 3.1 and Figure 3.2, the measurement data, obtained by the closed-loop experiment described in Section 3.4, is used to calculate the closed-loop frequency response estimate of the true plant G with initial controller C_0, H_0. This closed-loop estimate is obtained, according to Section 3.3, as the averaged ETFE

$$\hat{G}_{cl,0}(j\omega_k) = \frac{\frac{1}{R}\sum_{r=0}^{R-1} Y_{m,DFT}^{[r]}(j\omega_k)}{\frac{1}{R}\sum_{r=0}^{R-1} R_{DFT}^{[r]}(j\omega_k)} \tag{3.18}$$

where $Y_{m,DFT}^{[r]}$ and $R_{DFT}^{[r]}$ are the DFT's of the $r'th$ record of the sampled time domain data of the measured output signal $y_m[n]$ and reference input $r[n]$. According to Section 3.3, the reference input r is assumed to be exactly known. Hence, we obtain for the averaged ETFE of the closed-loop frequency response

$$\hat{G}_{cl,0}(j\omega_k) = \frac{\frac{1}{R}\sum_{r=0}^{R-1} Y_{m,DFT}^{[r]}(j\omega_k)}{R_{DFT}(j\omega_k)} \tag{3.19}$$

Because of Equation (3.11) and because the excitation is periodic and transients are assumed to have died out, the estimate (3.19) corresponds to

$$\hat{G}_{cl,0}(j\omega_k) = G_{cl,0}(j\omega) + \epsilon_k \tag{3.20}$$

where $G_{cl,0}$ is the true closed-loop and where

$$\epsilon_k = \frac{1}{R}\sum_{r=0}^{R-1} \epsilon_k^{[r]} = \frac{1}{R}\sum_{r=0}^{R-1} \frac{N_{y,DFT}^{[r]}(j\omega_k)}{R_{DFT}(j\omega_k)} \tag{3.21}$$

According to Figure 2.14 and Equation (3.11), n_y results from filtering the noise sequence n_w, which is i.i.d. normally distributed with zero mean, $\mu_n = 0$ and variance σ_n^2, by the sensitivity $S_{c,0}$. Hence, as shown in the previous chapter, Equation (2.146), we know that

$$\mathbb{E}[\epsilon_k^{[r]}] = \mathbb{E}[\frac{N_{y,DFT}^{[r]}(j\omega_k)}{R_{DFT}(j\omega_k)}] = 0 \tag{3.22}$$

and because of the linearity property of the expected value operator and Property M.0.1:

$$\mathbb{E}[\epsilon_k] = \mathbb{E}[\frac{\frac{1}{R}\sum_{r=0}^{R-1} N_{y,DFT}^{[r]}(j\omega_k)}{R_{DFT}(j\omega_k)}] = 0 \tag{3.23}$$

Further according to [Bri81],[dv95] and as was shown in Equation (2.147), the variance and correlation of the real and imaginary parts of $\epsilon_k^{[r]}$ are **asymptotically**, i.e. for $N \to \infty$, where N are the number of samples, given by

$$\begin{aligned} \mathbb{E}[\Re(\epsilon_k^{[r]})\Re(\epsilon_k^{[r]})] = \mathbb{E}[\Im(\epsilon_k^{[r]})\Im(\epsilon_k^{[r]})] &= \frac{1}{2}|S_{c,0}(j\omega_k)|^2 \frac{\sigma_n^2}{|R_{DFT}(j\omega_k)|^2} \\ \mathbb{E}[\Re(\epsilon_k^{[r]})\Im(\epsilon_k^{[r]})] &= 0 \end{aligned} \tag{3.24}$$

and asymptotically jointly normally distributed. Because of the property given in Equation (M.11) and Lemma M.0.2 the variance and covariance of the real and imaginary parts of the sum in Equation (3.21) is given by

$$\begin{aligned} \mathbb{E}[\Re(\epsilon_k)\Re(\epsilon_k)] = \mathbb{E}[\Im(\epsilon_k)\Im(\epsilon_k)] &= \frac{1}{2R}|S_{c,0}(j\omega_k)|^2 \frac{\sigma_n^2}{|R_{DFT}(j\omega_k)|^2} \\ \mathbb{E}[\Re(\epsilon_k)\Im(\epsilon_k)] &= 0 \end{aligned} \tag{3.25}$$

The sensitivity $S_{c,0}$ is given in Equation (3.12) by

$$S_{c,0}(j\omega_k) = \frac{1}{1 + G(j\omega_k)C_0(j\omega_k)} \tag{3.26}$$

where C_0 is the exactly known initial controller, that was applied in the closed-loop experiment, and whose parameters we would like together with H_0 to retune. The closed-loop estimate (3.19), is hence asymptotically complex normally distributed with uncorrelated real and imaginary parts with equal variance and mean value corresponding to the true closed-loop frequency response $G_{cl,0}$, i.e.:

$$\begin{aligned} \mathbb{E}[\hat{G}_{cl,0}(j\omega_k)] &= G_{cl,0}(j\omega_k) \\ var[\Re(\hat{G}_{cl,0}(j\omega_k))] = var[\Im(\hat{G}_{cl,0}(j\omega_k))] &= \sigma^2 = \frac{1}{2R}|S_{c,0}(j\omega_k)|^2 \frac{\sigma_n^2}{|R_{DFT}(j\omega_k)|^2} \\ cov[\Re(\hat{G}_{cl,0}(j\omega_k))), \Im(\hat{G}_{cl,0}(j\omega_k))] &= 0 \end{aligned} \tag{3.27}$$

This result shows that by increasing the SNR or the number of the repetitions of the maneuver, the variance of the estimate can be decreased. Note, that increasing the number of repetitions increases the duration of the experiment and thus the costs of the test campaign. Furthermore, the number of repetitions and hence maneuver duration shall be chosen carefully such that the drift from the reference condition stays within acceptable bounds.

Example 3.1. ***Sample Properties of Initial Closed-loop Estimate***

In this example we are concerned with the closed-loop estimate $\hat{G}_{cl,0}$ of the system, described in Section 3.2. The closed-loop estimate is obtained with the averaged ETFE as described in Section 3.5. The initial controller parameters that are applied in the experiment are given in Table 3.3. The parameter values of the considered true plant G are

Parameter	Value
Z_α	-1.068
Z_q	-0.022
M_α	-3.952
M_q	-1.858
M_η	-4.109

Table 3.4: *True plant parameters.*

given in Table 3.4. They correspond to an 5% *decrease in* M_α*, an* 10% *increase in* M_q *and an* 5% *increase in* M_η*, compared to the nominal plant model parameters given in Table 3.2. We consider two cases, that differ in the signal-to-noise ratio only:*

1. $\frac{|R_{DFT}|}{\sigma_n} = 1$
2. $\frac{|R_{DFT}|}{\sigma_n} = 10$

where R_{DFT} *is the DFT of the reference input signal, which is the multi-sine signal described in Section 3.4, and* σ_n^2 *is the variance of the noise sequence* $n_w[n]$ *for which the assumptions given in Section 3.3 hold. The first maneuver is discarded to reduce leakage errors from transients due to maneuver initiation. The number of used records is* $R = 1$*.* $N = 6250$ *samples are considered for the simulation and DFT to emulate the asymptotic condition required by Equation* (3.27)*. The experiment is simulated* $M = 2000$ *times, such that* 2000 *closed-loop estimates are obtained for each SNR. These are investigated in the following. According to Equation* (3.27)*, the expected value of* $\hat{G}_{cl,0}$ *is the true value* $G_{cl,0}$*. Figure 3.5 and 3.6 compare for a SNR of 1 and a SNR ratio of 10, the true value* $G_{cl,0}$ *with the sample mean*

$$\bar{\hat{G}}_{cl,0}(j\omega_k) = \frac{1}{M}\sum_{m=1}^{M} \hat{G}_{cl,0}^{[m]}(j\omega_k) \tag{3.28}$$

where $\hat{G}_{cl,0}^{[m]}(j\omega_k)$ *is the estimate of the respective* m'*th simulation. We see, that the sample mean corresponds to the true value* $G_{cl,0}$*. Asymptotically (for* $N \to \infty$*), according to Equation* (3.27)*, the variance of the real and imaginary parts are equal and given by:*

$$\sigma^2 = \frac{1}{2R}|S_{c,0}(j\omega_k)|^2 \frac{\sigma_n^2}{|R_{DFT}(j\omega_k)|^2} \tag{3.29}$$

Figure 3.7 compares for a SNR of 1 and a SNR of 10, this theoretical value of the variance with the sample variances

$$\begin{aligned} \bar{\sigma}_r^2 &= \frac{1}{M-1}\sum_{m=1}^{M}\left(\Re(\hat{G}_{cl,0}^{[m]}(j\omega_k)) - \Re(\bar{\hat{G}}_{cl,0}(j\omega_k))\right)^2 \\ \bar{\sigma}_i^2 &= \frac{1}{M-1}\sum_{m=1}^{M}\left(\Im(\hat{G}_{cl,0}^{[m]}(j\omega_k)) - \Im(\bar{\hat{G}}_{cl,0}(j\omega_k))\right)^2 \end{aligned} \tag{3.30}$$

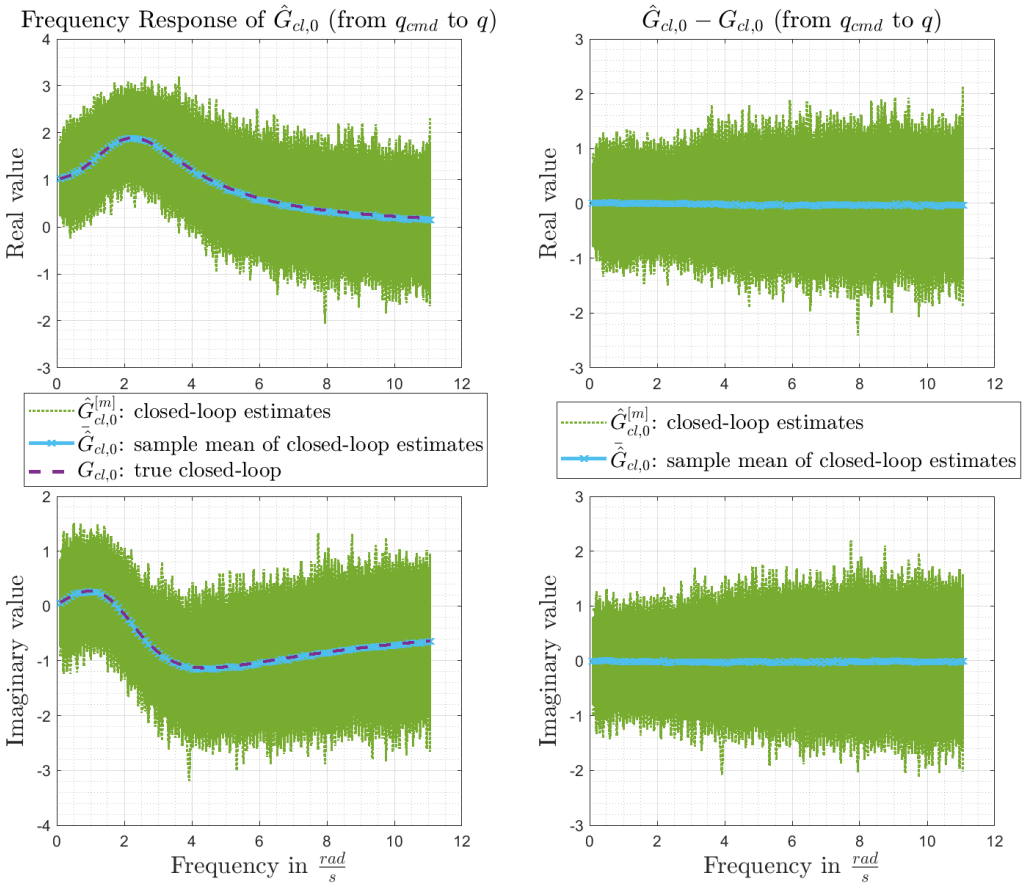

Figure 3.5: *Closed-loop estimate for SNR of 1.*

We see, that the sample variance is centered around the theoretical value for both cases. Further, the variance increases with frequency because of the increasing magnitude of the sensitivity $S_{c,0}(j\omega_k)$, which is depicted in Figure 3.8. Figure 3.9 shows the probability density function of the real values of all M estimates $\hat{G}^{[m]}_{cl,0}(j\omega_k)$ at frequency ω_k corresponding to the $5'th$ harmonic frequency. Figure 3.9 reveals that the distribution of the samples approximates a normal distribution with mean (3.27) *and variance* (3.29)*, which is depicted in green. Figure 3.10 shows the sample covariance between real and imaginary parts of $\hat{G}_{cl,0}$, i.e.*

$$\bar{\sigma}^2_{ri} = \frac{1}{M-1}\sum_{m=1}^{M}\left(\Re(\hat{G}^{[m]}_{cl,0}(j\omega_k)) - \Re(\bar{\hat{G}}_{cl,0}(j\omega_k))\right)\left(\Im(\hat{G}^{[m]}_{cl,0}(j\omega_k)) - \Im(\bar{\hat{G}}_{cl,0}(j\omega_k))\right) \tag{3.31}$$

for a SNR of 1 and a SNR of 10. As expected they are almost zero.

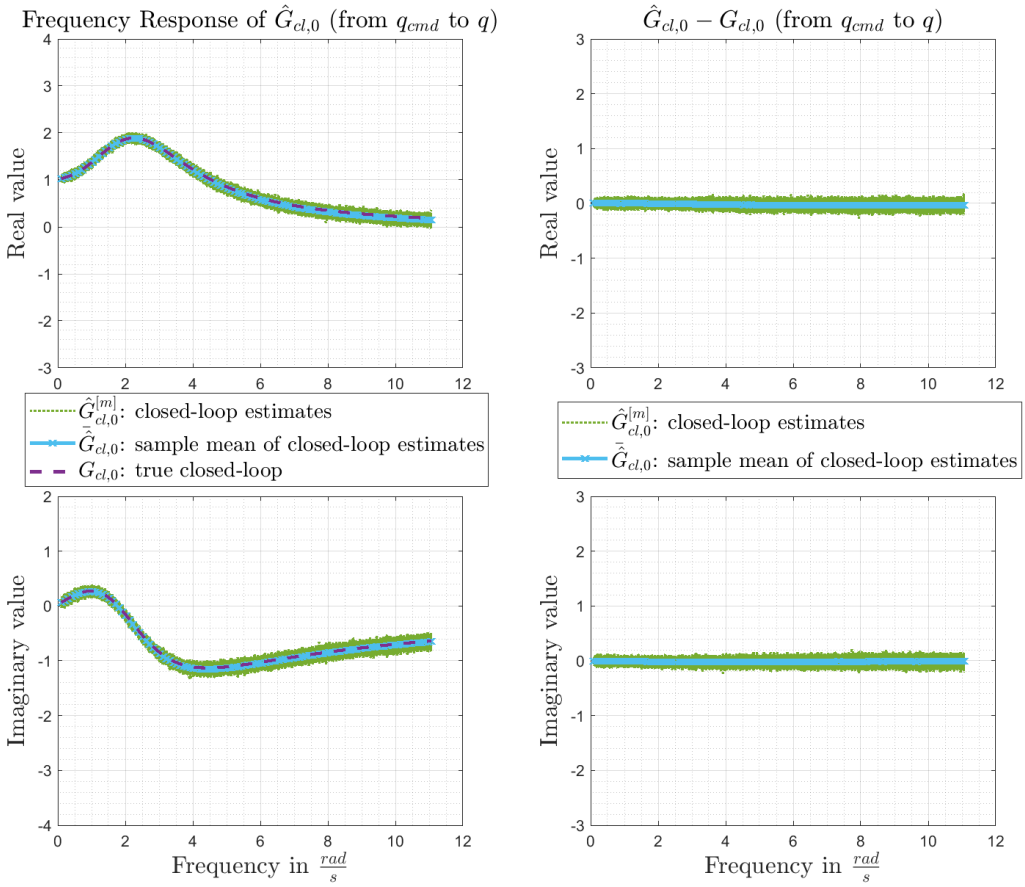

Figure 3.6: *Closed-loop estimate for SNR of 10.*

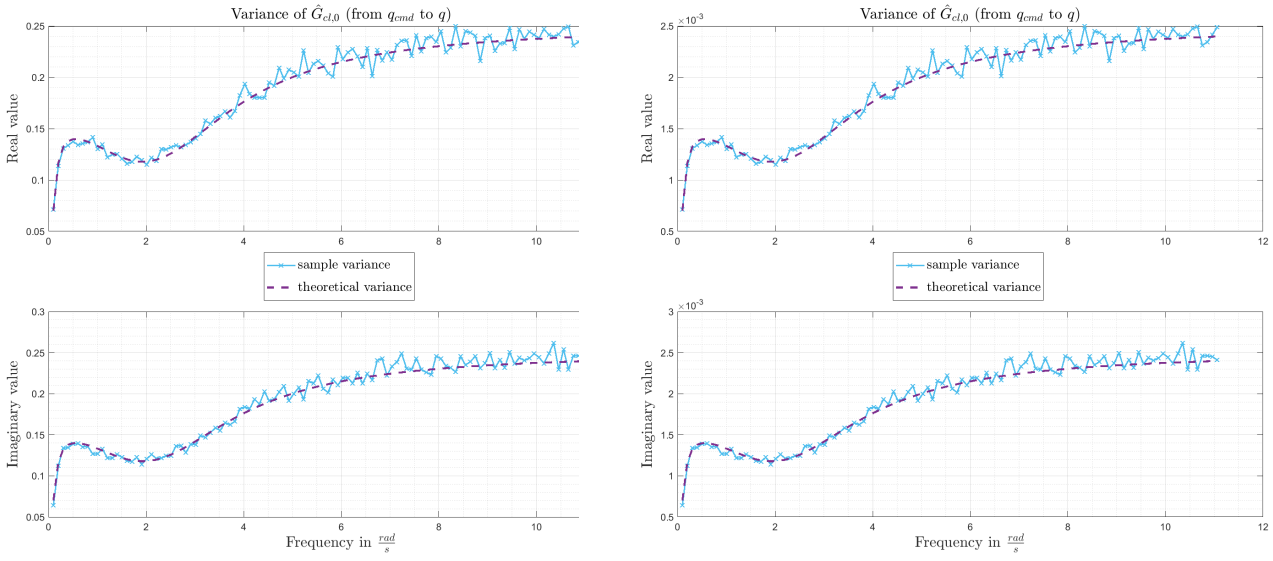

Figure 3.7: *Sample variance of real parts and of imaginary parts, Left: SNR of 1; Right: SNR of 10.*

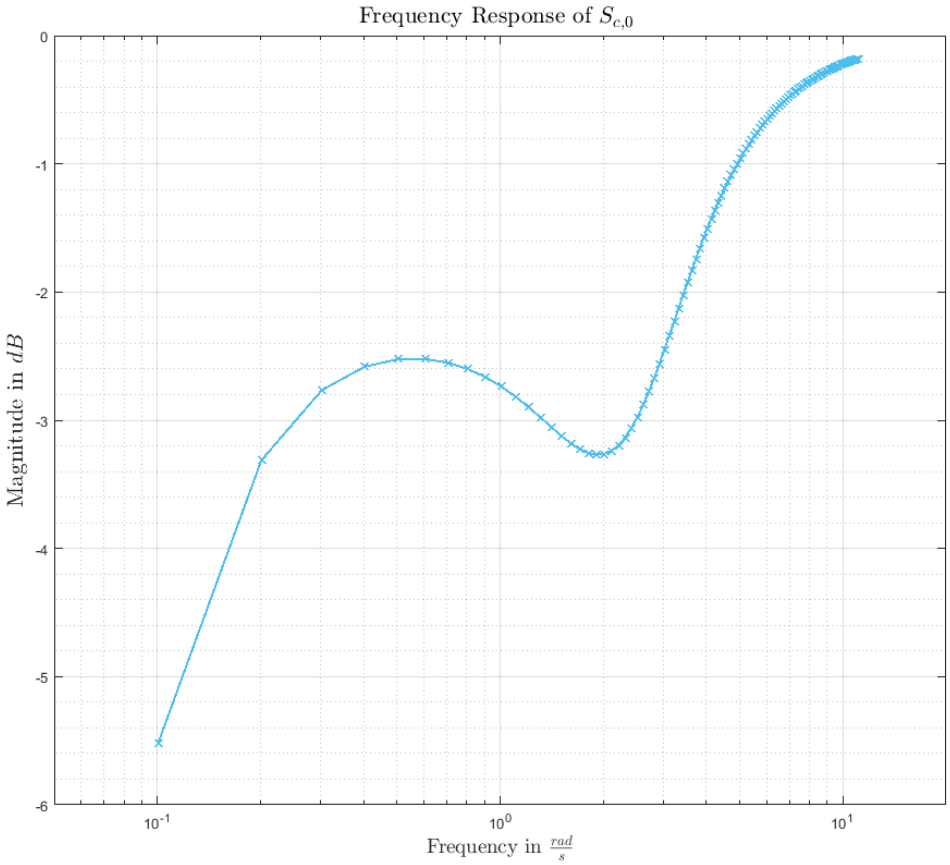

Figure 3.8: *True sensitivity* $S_{c,0}(j\omega_k)$.

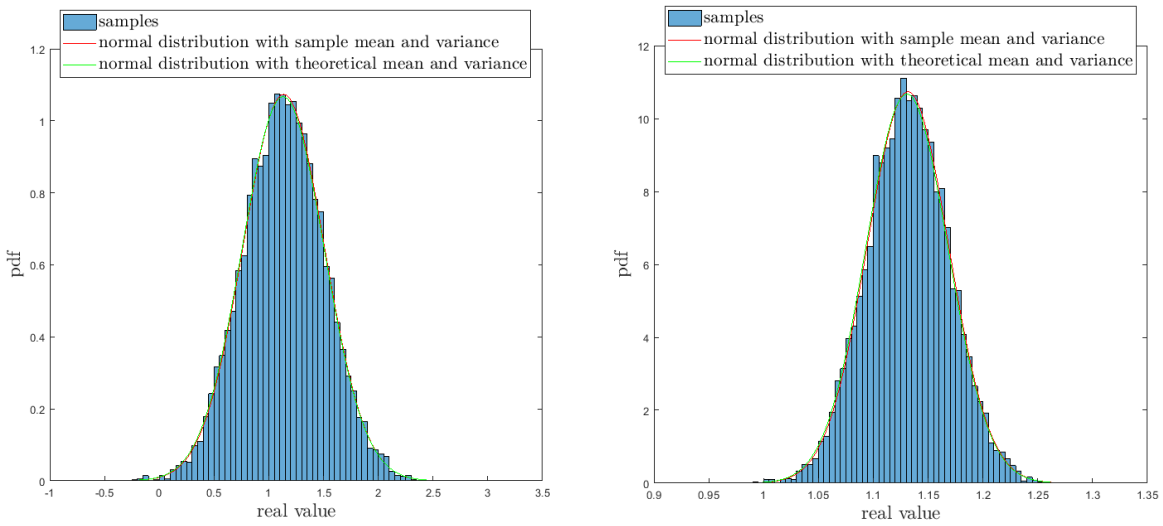

SNR of 1 SNR of 10

Figure 3.9: *Probability density function of real values of closed-loop estimates at* $5'th$ *harmonic frequency* ($M = 10000$ *simulations), Left: SNR of 1; Right: SNR of 10.*

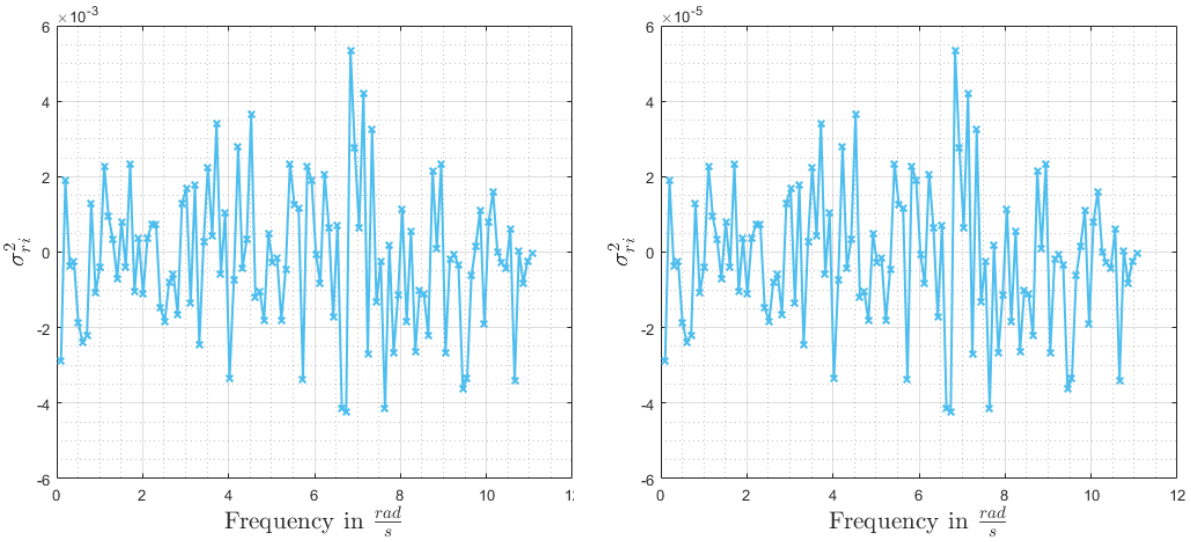

Figure 3.10: *Sample covariance of real and imaginary part of initial closed-loop estimates, ($M = 10000$ simulations), Left: SNR of 1; Right: SNR of 10.*

3.6 Non-parametric Closed-loop Frequency Response Estimate of True Plant with Updated Controller

In the previous section we were concerned with the closed-loop estimate $\hat{G}_{cl,0}$ of the true plant G with the initial controller C_0, H_0. This estimate was obtained based on closed-loop experimental data of the true system with controller C_0, H_0. The following section presents how based on this estimate, $\hat{G}_{cl,0}$, an anticipated closed-loop frequency response $\hat{\tilde{G}}_{cl}$, for a new set of controller parameters $\tilde{\boldsymbol{p}}$, can be obtained. This anticipated, new closed-loop frequency response $\hat{\tilde{G}}_{cl}(j\omega_k, \tilde{\boldsymbol{p}})$ is used in an optimization, as will be discussed in Section 3.8, to obtain the optimal controller parameters. Based on the difference of the anticipated closed-loop frequency response $\hat{\tilde{G}}_{cl}(j\omega_k, \tilde{\boldsymbol{p}})$, for controller parameters $\tilde{\boldsymbol{p}}$, and the desired frequency response, the optimal controller parameters are determined. The question that instantaneously arises and will be addressed in this section, is how the anticipated closed-loop frequency can be calculated (C3) and how close the anticipated closed-loop frequency response $\hat{\tilde{G}}_{cl}(j\omega_k, \tilde{\boldsymbol{p}})$ will be to the true closed-loop frequency response $\tilde{G}_{cl}(j\omega_k, \tilde{\boldsymbol{p}})$ of true plant G and controller with updated parameters (C4). Note, that the complete sections 3.6.1, 3.6.2, 3.6.3 and related appendices are extracted from my manuscript [SSH]. ["

3.6.1 Estimate of Anticipated Updated Closed-loop

For the system in Figure 3.3 we have in closed-loop the relation given in Equation (3.11) by

$$G_{cl,0}(j\omega_k) = \frac{G(j\omega_k)(C_0(j\omega_k) + H_0(j\omega_k))}{1 + G(j\omega_k)C_0(j\omega_k)} = \frac{G(j\omega_k)T_0(j\omega_k)}{1 + G(j\omega_k)C_0(j\omega_k)} \tag{3.32}$$

where

$$T(j\omega_k) \triangleq C(j\omega_k) + H(j\omega_k) \tag{3.33}$$

is the controller transfer behavior from reference input r to control signal u, see Equation (3.7) and Equation (3.5). In the following we will omit the argument $(j\omega_k)$ for better readability. By solving relation (3.32) for G

$$\begin{aligned} G_{cl,0}(1 + GC_0) &= GT_0 \\ G_{cl,0} &= GT_0 - GC_0G_{cl,0} \\ G_{cl,0} &= G(T_0 - C_0G_{cl,0}) \\ G &= \frac{G_{cl,0}}{T_0 - C_0G_{cl,0}} \end{aligned} \tag{3.34}$$

a relation for G is obtained, which depends on the controller $C(\boldsymbol{p}_{c,0}) = C_0, H(p_{h,0}) = H_0$ and the resulting closed-loop frequency response, $G_{cl,0}$, of G with this controller. Based on relation (3.34) for the plant G, the closed-loop frequency response, $\tilde{G}_{cl}$, for an updated set of controller parameters, which we denote as $C(\tilde{\boldsymbol{p}}_c) = \tilde{C}$, $H(\tilde{p}_h) = \tilde{H}$, can be obtained

as follows:

$$\begin{aligned}\tilde{G}_{cl} &= \frac{G\tilde{T}}{1+G\tilde{C}} \\ &= \frac{\frac{G_{cl,0}}{T_0-C_0G_{cl,0}}\tilde{T}}{1+\frac{G_{cl,0}}{T_0-C_0G_{cl,0}}\tilde{C}} \\ &= \frac{G_{cl,0}\tilde{T}}{T_0-C_0G_{cl,0}+G_{cl,0}\tilde{C}} \\ &= \frac{G_{cl,0}\tilde{T}}{T_0-(C_0-\tilde{C})G_{cl,0}} \\ &= \frac{\tilde{T}}{T_0}\frac{G_{cl,0}}{1-\frac{(C_0-\tilde{C})}{T_0}G_{cl,0}}\end{aligned} \tag{3.35}$$

Hence, based on an non-parametric estimate for the closed-loop frequency response $\hat{G}_{cl,0}$, obtained from closed-loop experiments of the true system G with initial controller C_0, H_0, as described in Section 3.5, the closed-loop frequency response for an updated controller parameter set, $\tilde{C}, \tilde{H}$ can be calculated by

$$\hat{\tilde{G}}_{cl} = \frac{\tilde{T}}{T_0}\frac{\hat{G}_{cl,0}}{1-F_0\hat{G}_{cl,0}} \tag{3.36}$$

where

$$F_0 \triangleq \frac{C_0-\tilde{C}}{T_0} \tag{3.37}$$

and where

$$\begin{aligned}T_0 &\triangleq C_0 + H_0 \\ \tilde{T} &\triangleq \tilde{C} + \tilde{H}\end{aligned} \tag{3.38}$$

3.6.2 Bias of Anticipated Updated Closed-loop

Lemma 3.6.1. *Suppose we have the closed-loop system depicted in Figure 3.3, with an unknown plant G. The closed-loop behavior $G_{cl,0}$ from reference input r to system output y_m is described by Equation* (3.32)*. Then, for an updated controller $\tilde{C}$, $\tilde{H}$, the closed-loop behavior $\tilde{G}_{cl}$ from reference input r to system output y_m is given by* (3.35) *with* (3.38)*. Suppose we have at specific frequencies an estimate $\hat{G}_{cl,0}(j\omega_k)$ of $G_{cl,0}$, for example obtained as described in Section 3.5, such that it is given by*

$$\hat{G}_{cl,0}(j\omega_k) = G_{cl,0}(j\omega_k) + \epsilon_k \tag{3.39}$$

The real and imaginary parts of ϵ_k are jointly normally distributed with zero mean

$$\mathbb{E}[\Re(\epsilon_k)] = \mathbb{E}[\Im(\epsilon_k)] = 0 \tag{3.40}$$

with equal variance

$$var[\Re(\epsilon_k)] = var[\Im(\epsilon_k)] = \sigma^2 = \frac{1}{2R}\frac{\sigma_n^2}{|R_{DFT}(j\omega_k)|^2}|S_{c,0}(j\omega_k)|^2 \tag{3.41}$$

and uncorrelated

$$cov[\Re(\epsilon_k), \Im(\epsilon_k)] = 0. \tag{3.42}$$

Then the expected value of $\hat{\tilde{G}}_{cl}$*, estimated by Equation* (3.36)*, is given by*

$$\mathbb{E}[\hat{\tilde{G}}_{cl}] = \alpha\tilde{G}_{cl} + (1-\alpha)(-\frac{1}{\tilde{F}}) \tag{3.43}$$

where

$$\alpha = 1 - \exp\left(-\frac{1}{2\sigma^2}|\frac{1 - F_0 G_{cl,0}}{F_0}|^2\right) \tag{3.44}$$

and

$$\begin{aligned} F_0 &\triangleq \frac{C_0 - \tilde{C}}{T_0} \\ \tilde{F} &\triangleq \frac{C_0 - \tilde{C}}{\tilde{T}} \end{aligned} \tag{3.45}$$

where T_0 *and* $\tilde{T}$ *are the open-loop controller transfer behavior from reference input* r *to control signal* u*, given by Equation* (3.38)*. Note, that the dependency* $(j\omega_k)$ *is omitted for readability.*

Proof. The following proof has been structured to use the similarities with [Hea01b], where the expected value of an non-parametric, indirect plant estimate $\hat{G}$ was calculated for a closed-loop system structure as depicted in Figure 2.13.
The probability density function of $\hat{G}_{cl,0}$, evaluated at $z \in \mathbb{C}$ is given by (see Lemma M.0.14)

$$f_{\hat{G}_{cl,0}}(z) = \frac{1}{2\pi\sqrt{det(\mathbf{\Sigma})}} e^{-\frac{1}{2}\begin{bmatrix}\Re(z-\mu_z)\\ \Im(z-\mu_z)\end{bmatrix}^T \mathbf{\Sigma}^{-1}\begin{bmatrix}\Re(z-\mu_z)\\ \Im(z-\mu_z)\end{bmatrix}} \tag{3.46}$$

where μ_z, is the expected value of the complex random variable $\hat{G}_{cl,0}$, given by

$$\mu_z = \mathbb{E}[\hat{G}_{cl,0}] = G_{cl,0} \tag{3.47}$$

as can be directly seen from Equation (3.39), incorporating that ϵ_k has zero mean. The covariance matrix Σ is given by

$$\begin{aligned}\mathbf{\Sigma} &= \begin{bmatrix} var[\Re(z)] & cov[\Re(z),\Im(z)] \\ cov[\Im(z),\Re(z)] & var[\Im(z)] \end{bmatrix} \\ &= \begin{bmatrix} \sigma^2 & 0 \\ 0 & \sigma^2 \end{bmatrix}\end{aligned} \tag{3.48}$$

as can be directly seen from Equation (3.41) and (3.42). The expected value of $\hat{\tilde{G}}_{cl}$ is according to Definition M.0.17 and Equation (3.36)

$$\mathbb{E}[\hat{\tilde{G}}_{cl}] = \mathbb{E}[\frac{\tilde{T}}{T_0}\frac{z}{1-F_0 z}] = \frac{\tilde{T}}{T_0}\int_{\mathbb{C}} \frac{z}{1-F_0 z} f_{\hat{G}_{cl,0}}(z)dz \tag{3.49}$$

with the probability density function $f_{\hat{G}_{cl,0}}(z)$ given in Equation (3.46) and where the differential element dz is to be understood as $dz = d\bar{x}d\bar{y}$. Hence, (3.49) expresses not a complex contour integral but a double integral over $\mathbb{R}^2$.
For $F_0 \neq 0$

$$\begin{aligned}\mathbb{E}[\hat{\tilde{G}}_{cl}] &= \frac{\tilde{T}}{T_0}\int_{\mathbb{C}} \frac{z}{1-F_0 z}\frac{F_0}{F_0} f_{\hat{G}_{cl,0}}(z)dz \\ &= -\frac{\tilde{T}}{T_0}\frac{1}{F_0}\int_{\mathbb{C}} \frac{1-F_0 z-1}{1-F_0 z} f_{\hat{G}_{cl,0}}(z)dz \\ &= -\frac{\tilde{T}}{T_0}\frac{1}{F_0}(\int_{\mathbb{C}} 1 f_{\hat{G}_{cl,0}}(z)dz - \int_{\mathbb{C}} \frac{1}{1-F_0 z} f_{\hat{G}_{cl,0}}(z)dz) \\ &= \frac{\tilde{T}}{T_0}(-\frac{1}{F_0} + \frac{1}{F_0}\int_{\mathbb{C}} \frac{1}{1-F_0 z} f_{\hat{G}_{cl,0}}(z)dz)\end{aligned} \tag{3.50}$$

where

$$\int_{\mathbb{C}} 1 f_{\hat{G}_{cl,0}}(z)dz = 1 \tag{3.51}$$

was used, and partial fraction decomposition was applied to factor out 1 from the second to the third equal sign in (3.50).
Put

$$\begin{aligned} x &\triangleq \frac{1}{\sigma}(\bar{x} - \Re(G_{cl,0})) \\ y &\triangleq \frac{1}{\sigma}(\bar{y} - \Im(G_{cl,0}))\end{aligned} \tag{3.52}$$

such that

$$\begin{aligned} \bar{x} &= \Re(z) = \sigma x + \Re(G_{cl,0}) \\ \bar{y} &= \Im(z) = \sigma y + \Im(G_{cl,0})\end{aligned} \tag{3.53}$$

and

$$\begin{aligned} d\bar{x} &= \sigma dx \\ d\bar{y} &= \sigma dy \end{aligned} \tag{3.54}$$

Then

$$\begin{aligned} \mathbb{E}[\hat{\tilde{G}}_{cl}] &= \frac{\tilde{T}}{T_0}(-\frac{1}{F_0} + \frac{1}{F_0}\int_{-\infty}^{\infty}\int_{-\infty}^{\infty}\frac{1}{1-F_0(\bar{x}+j\bar{y})}f_{\hat{G}_{cl,0}}(\bar{x},\bar{y})d\bar{x}d\bar{y}) \\ &= \frac{\tilde{T}}{T_0}(-\frac{1}{F_0} + \frac{1}{F_0}\int_{-\infty}^{\infty}\int_{-\infty}^{\infty}\frac{1}{1-F_0(\sigma(x+jy)+G_{cl,0})}f_{\hat{G}_{cl,0}}(x,y)\sigma^2 dxdy) \end{aligned} \tag{3.55}$$

The probability density function of $\hat{G}_{cl,0}$, given by Equation (3.46), can be expressed using (3.48),(3.47) and (3.53) by

$$f_{\hat{G}_{cl,0}}(\bar{x},\bar{y}) = \frac{1}{2\pi\sigma^2}\exp\left(-\frac{(\bar{x}-\Re(G_{cl,0}))^2+(\bar{y}-\Im(G_{cl,0}))^2}{2\sigma^2}\right) \tag{3.56}$$

and in terms of x, y by

$$\begin{aligned} f_{\hat{G}_{cl,0}}(x,y) &= \frac{1}{2\pi\sigma^2}\exp\left(-\frac{x^2\sigma^2+y^2\sigma^2}{2\sigma^2}\right) \\ &= \frac{1}{2\pi\sigma^2}\exp\left(-\frac{x^2+y^2}{2}\right) \end{aligned} \tag{3.57}$$

In polar coordinates given by

$$\begin{aligned} r^2 &= x^2+y^2 \\ \theta &= \arg(x+jy) \\ x &= r\cos\theta \\ y &= r\sin\theta \end{aligned} \tag{3.58}$$

and with

$$dxdy = rd\theta dr \tag{3.59}$$

the expected value given in Equation (3.55) can be expressed by

$$\begin{aligned} \mathbb{E}[\hat{\tilde{G}}_{cl}] = \frac{\tilde{T}}{T_0}(&-\frac{1}{F_0} \\ &+ \frac{1}{F_0}\int_0^{\infty}\int_{-\pi}^{\pi}\frac{1}{1-F_0\sigma r(\cos\theta+j\sin\theta)-F_0G_{cl,0}}\frac{1}{2\pi}e^{(-\frac{r^2}{2})}rd\theta dr) \end{aligned} \tag{3.60}$$

Put

$$P \triangleq 1 - F_0G_{cl,0} \tag{3.61}$$

Then

$$\begin{aligned}\mathbb{E}[\hat{\tilde{G}}_{cl}] &= \frac{\tilde{T}}{T_0}(-\frac{1}{F_0}+\frac{1}{F_0 P}\frac{P}{2\pi}\int_0^{\infty}\int_{-\pi}^{\pi}\frac{1}{P-F_0\sigma r(\cos\theta+j\sin\theta)}e^{(-\frac{r^2}{2})}rd\theta dr) \\ &= \frac{\tilde{T}}{T_0}(-\frac{1}{F_0}+\frac{1}{F_0 P}\int_0^{\infty} I(r)e^{(-\frac{r^2}{2})}rdr)\end{aligned} \tag{3.62}$$

with

$$I(r) \triangleq \frac{P}{2\pi}\int_{-\pi}^{\pi}\frac{d\theta}{P-F_0\sigma r(\cos\theta+j\sin\theta)} \tag{3.63}$$

Put

$$\breve{z} = \cos\theta + jsin\theta = e^{j\theta} \tag{3.64}$$

where $\breve{z}$ runs along the unit circle in the complex plane, given by the curve C, and

$$\begin{aligned}\frac{d\breve{z}}{d\theta} &= je^{j\theta} = j\breve{z} \\ d\theta &= \frac{d\breve{z}}{j\breve{z}}\end{aligned} \tag{3.65}$$

Then

$$\begin{aligned}I(r) &= \frac{P}{2\pi}\oint_C \frac{1}{P-F_0\sigma r\breve{z}}\frac{1}{j\breve{z}}d\breve{z} \\ &= \frac{Pj}{2\pi j^2}\oint_C \frac{1}{(P-F_0\sigma r\breve{z})\breve{z}}d\breve{z} \\ &= \frac{Pj}{2\pi}\oint_C \frac{1}{(F_0\sigma r\breve{z}-P)\breve{z}}d\breve{z} \\ &= \frac{Pj}{2\pi}\oint_C \frac{\frac{1}{F_0\sigma r}}{(\breve{z}-\frac{P}{F_0\sigma r})\breve{z}}d\breve{z} \\ &= \frac{Pj}{2\pi}\oint_C \Psi(r,\breve{z})d\breve{z}\end{aligned} \tag{3.66}$$

For a fixed r, $\Psi(\breve{z})$ has two poles at

$$\begin{aligned}\breve{z}_1 &= 0 \\ \breve{z}_2 &= \frac{P}{F_0\sigma r}\end{aligned} \tag{3.67}$$

The contour integral in Equation (3.66), can be evaluated using Cauchy's residue theorem [Pou18, p. 833]. The residues of $\Psi(\breve{z})$ are

$$\begin{aligned}Res_1(\Psi) &= \lim_{\breve{z}\to\breve{z}_1}(\breve{z}-\breve{z}_1)\frac{1/(F_0\sigma r)}{(\breve{z}-\breve{z}_1)(\breve{z}-\breve{z}_2)} = -\frac{1}{P} \\ Res_2(\Psi) &= \lim_{\breve{z}\to\breve{z}_2}(\breve{z}-\breve{z}_2)\frac{1/(F_0\sigma r)}{(\breve{z}-\breve{z}_1)(\breve{z}-\breve{z}_2)} = \frac{1}{P}\end{aligned} \tag{3.68}$$

The pole $\breve{z}_1$ lies within the unit circle, while the pole $\breve{z}_2$ is only inside the unit circle, i.e. $|\breve{z}_2| < 1$, for $r > r_0$, with

$$r_0 = |\frac{P}{F_0}|\frac{1}{\sigma} \tag{3.69}$$

which can be directly seen by inspecting the square of the magnitude of z_2, which is given by

$$|\breve{z}_2|^2 = \breve{z}_2\breve{z}_2^* = \frac{|\frac{P}{F_0}|^2\frac{1}{\sigma^2}}{r^2} \tag{3.70}$$

Hence, for $r > r_0$, $I(r)$ is given by

$$I(r) = \frac{Pj}{2\pi}(2\pi j\sum_{s=1}^{2} Res_s(\Psi)) = 0 \tag{3.71}$$

For $r < r_0$, $I(r)$ is given by

$$I(r) = \frac{Pj}{2\pi}(2\pi j Res_1(\Psi)) = 1 \tag{3.72}$$

Because of (3.71), and (3.72), Equation (3.62) is reduced to

$$\begin{aligned}\mathbb{E}[\hat{\tilde{G}}_{cl}] &= \frac{\tilde{T}}{T_0}(-\frac{1}{F_0} + \frac{1}{F_0 P}\int_0^\infty I(r)e^{(-\frac{r^2}{2})}rdr) \\ &= \frac{\tilde{T}}{T_0}(-\frac{1}{F_0} + \frac{1}{F_0 P}\alpha)\end{aligned} \tag{3.73}$$

with

$$\begin{aligned}\alpha &\triangleq \int_0^{r_0} I(r)e^{(-\frac{r^2}{2})}rdr + \int_{r_0}^\infty I(r)e^{(-\frac{r^2}{2})}rdr \\ &= \int_0^{r_0} e^{(-\frac{r^2}{2})}rdr \\ &= 1 - \exp\left(-\frac{{r_0}^2}{2}\right) \\ &= 1 - \exp\left(-\frac{1}{2\sigma^2}\left|\frac{P}{F_0}\right|^2\right) \\ &= 1 - \exp\left(-\frac{1}{2\sigma^2}\left|\frac{1 - F_0 G_{cl,0}}{F_0}\right|^2\right).\end{aligned} \tag{3.74}$$

Using the definition of F_0 and $\tilde{F}$, given by Equation (3.50), the following relation is obtained

$$\frac{\tilde{T}}{T_0}\frac{1}{F_0} = \frac{\tilde{T}}{T_0}\frac{T_0}{C_0 - \tilde{C}} = \frac{1}{\tilde{F}} \tag{3.75}$$

Inserting this relation into Equation (3.73) results in

$$\begin{aligned}\mathbb{E}[\hat{\tilde{G}}_{cl}] &= \frac{\tilde{T}}{T_0}(-\frac{1}{F_0}+\frac{1}{F_0 P}\alpha) \\ &= (-\frac{1}{\tilde{F}}+\frac{1}{\tilde{F}P}\alpha)\end{aligned} \tag{3.76}$$

Using $P = 1 - F_0 G_{cl,0}$ as defined in (3.61) and

$$\frac{F_0}{\tilde{F}} = \frac{\frac{C_0-\tilde{C}}{T_0}}{\frac{C_0-\tilde{C}}{\tilde{T}}} = \frac{\tilde{T}}{T_0} \tag{3.77}$$

we obtain the relation

$$\begin{aligned}\frac{1}{\tilde{F}P} &= \frac{1}{\tilde{F}}\frac{1}{1-F_0G_{cl,0}} = \frac{1}{\tilde{F}}\frac{F_0G_{cl,0}+1-F_0G_{cl,0}}{1-F_0G_{cl,0}} \\ &= \frac{1}{\tilde{F}}(\frac{F_0G_{cl,0}}{1-F_0G_{cl,0}}+1) = \frac{F_0}{\tilde{F}}\frac{G_{cl,0}}{1-F_0G_{cl,0}}+\frac{1}{\tilde{F}} = \frac{\tilde{T}}{T_0}\frac{G_{cl,0}}{1-F_0G_{cl,0}}+\frac{1}{\tilde{F}} \\ &= \tilde{G}_{cl}+\frac{1}{\tilde{F}}\end{aligned} \tag{3.78}$$

with $\tilde{G}_{cl}$ given by Equation (3.35). Inserting relation (3.78) in Equation (3.76) results in

$$\begin{aligned}\mathbb{E}[\hat{\tilde{G}}_{cl}] &= -\frac{1}{\tilde{F}}+(\tilde{G}_{cl}+\frac{1}{\tilde{F}})\alpha \\ &= \alpha\tilde{G}_{cl}+(1-\alpha)(-\frac{1}{\tilde{F}})\end{aligned} \tag{3.79}$$

which completes the proof of (3.43) in Lemma 3.6.1. □

It is seen that the resulting expected value of the anticipated updated closed-loop resembles in structure the expected value of the non-parametric, indirect plant estimate [Hea01b]. In (3.79) it can be seen that

1. The bias is reduced when the variance σ^2 of ϵ_k is reduced, as α, given by (3.74), tends to 1

2. The expected value $\mathbb{E}[\hat{\tilde{G}}_{cl}]$ tends to $-1/\tilde{F}$ when the variance σ^2 of ϵ_k is increased, as α, given by (3.74), tends to 0

3. The limit of the bias goes to zero when the initial feed-forward H_0 goes to infinity, see Lemma 3.6.2. This is not surprising, since increasing the feed-forward will turn the estimate towards an open-loop problem.

4. The limit of the bias goes to zero when the controller change goes to zero, i.e. $\tilde{C}$ goes to C_0, see Lemma 3.6.3

Lemma 3.6.2. *Given the expected value according to Lemma 3.6.1, the following limit holds with $H_0 \in \mathbb{C}$:*

$$\lim_{H_0 \to \infty} \mathbb{E}[\hat{\tilde{G}}_{cl}] = \tilde{G}_{cl} \tag{3.80}$$

Proof. The expected value $\mathbb{E}[\hat{\tilde{G}}_{cl}]$ is given by (3.43). Since $\tilde{F} = \frac{C_0 - \tilde{C}}{\tilde{T}}$, (3.45), with $\tilde{T} = \tilde{H} + \tilde{C}$, (3.38), is independent of $H_0 = r_H e^{j\theta_H}$, the limit in (3.80) is shown by showing that:

$$\lim_{H_0 \to \infty} \alpha = \lim_{r_H \to \infty} \alpha = 1 \tag{3.81}$$

where according to Equation (3.44),

$$\begin{aligned}
\alpha =& 1 - \exp\left(-\frac{1}{2\sigma^2}\left|\frac{1 - F_0 G_{cl,0}}{F_0}\right|^2\right) \\
=& 1 - \exp(-\frac{1}{2\sigma^2}|\frac{1 - \frac{C_0 - \tilde{C}}{H_0 + C_0} G_{cl,0}}{\frac{C_0 - \tilde{C}}{H_0 + C_0}}|^2) \\
=& 1 - \exp\left(-\frac{1}{2\sigma^2}|\frac{H_0}{C_0 - \tilde{C}} + \frac{C_0 - \left(C_0 - \tilde{C}\right) G_{cl,0}}{C_0 - \tilde{C}}|^2\right) \\
=& 1 - \exp\left(-\frac{1}{2\sigma^2}|H_0 k_1 + k_2|^2\right) \\
=& 1 - \exp\left(-\frac{1}{2\sigma^2}|r_H e^{j\theta_H} r_{k_1} e^{j\theta_{k_1}} + r_{k_2} e^{j\theta_{k_2}}|^2\right) \\
=& 1 - \exp\left(-\frac{1}{2\sigma^2}|r_H r_{k_1} e^{j(\theta_H + \theta_{k_1})} + r_{k_2} e^{j\theta_{k_2}}|^2\right)
\end{aligned} \tag{3.82}$$

with $k_1 = r_{k_1} e^{j\theta_{k_1}} = \frac{1}{C_0 - \tilde{C}}$ and $k_2 = r_{k_2} e^{j\theta_{k_2}} = \frac{C_0 - (C_0 - \tilde{C}) G_{cl,0}}{C_0 - \tilde{C}}$. Because

$$\begin{aligned}
&\lim_{r_H \to \infty} |r_H r_{k_1} e^{j(\theta_H + \theta_{k_1})} e^{j\theta_{k_1}} + r_{k_2} e^{j\theta_{k_2}}|^2 \\
&= \lim_{r_H \to \infty} |r_H r_{k_1} \left(\cos(\theta_H + \theta_{k_1}) + j \sin(\theta_H + \theta_{k_1})\right) + r_{k_2} \left(\cos(\theta_{k_2}) + j \sin(\theta_{k_2})\right)|^2 \\
&= \lim_{r_H \to \infty} [(r_H r_{k_1} \cos(\theta_H + \theta_{k_1}) + r_{k_2} \cos(\theta_{k_2}))^2 + (r_H r_{k_1} \sin(\theta_H + \theta_{k_1}) + r_{k_2} \sin(\theta_{k_2}))^2] \\
&= \lim_{r_H \to \infty} [(r_H^2 r_{k_1}^2 (\cos^2(\theta_H + \theta_{k_1}) + \sin^2(\theta_H + \theta_{k_1})) + r_{k_2}^2 (\cos^2(\theta_{k_2}) + \sin^2(\theta_{k_2})) \\
&+ 2 r_H r_{k_1} r_{k_2} \left(\cos(\theta_H + \theta_{k_1}) \cos(\theta_{k_2}) + \sin(\theta_H + \theta_{k_1}) \sin(\theta_{k_2})\right)] \\
&= \lim_{r_H \to \infty} r_H^2 r_{k_1}^2 + r_{k_2}^2 + 2 r_H r_{k_1} r_{k_2} \left(\cos(\theta_H + \theta_{k_1}) \cos(\theta_{k_2}) + \sin(\theta_H + \theta_{k_1}) \sin(\theta_{k_2})\right) \\
&= \infty
\end{aligned} \tag{3.83}$$

then the limit in (3.81) is 1. Note, that the exponential function is continuous everywhere. Therefore, the limit can be applied to the inner part of the exponential function. □

Lemma 3.6.3. *Given the expected value according to Lemma 3.6.1, the following limit holds:*

$$\lim_{\tilde{C}\to C_0} \mathbb{E}[\hat{\tilde{G}}_{cl}] = \tilde{G}_{cl} \tag{3.84}$$

Proof. The expected value $\mathbb{E}[\hat{\tilde{G}}_{cl}]$ is given by (3.43). Since α and $\tilde{F} = \frac{C_0-\tilde{C}}{\tilde{H}-\tilde{C}}$, both depend on $\Delta C = C_0 - \tilde{C}$, see Equation (3.44) and Equation (3.45), respectively, the limit in Equation (3.84) is shown by showing that:

1.
$$\lim_{\tilde{C}\to C_0} \alpha = 1 \tag{3.85}$$

2.
$$\lim_{\tilde{C}\to C_0} (1-\alpha)(-\frac{1}{\tilde{F}}) = 0 \tag{3.86}$$

Proof. (1) Equation (3.84) can be shown similarly as Lemma 3.6.2. First α is reformulated as follows

$$\begin{aligned}
\alpha =& 1 - \exp\left(-\frac{1}{2\sigma^2}\left|\frac{1-F_0 G_{cl,0}}{F_0}\right|^2\right) \\
=& 1 - \exp(-\frac{1}{2\sigma^2}|\frac{1-\frac{C_0-\tilde{C}}{H_0+C_0}G_{cl,0}}{\frac{C_0-\tilde{C}}{H_0+C_0}}|^2) \\
=& 1 - \exp(-\frac{1}{2\sigma^2}|\frac{H_0+C_0-\left(C_0-\tilde{C}\right)G_{cl,0}}{C_0-\tilde{C}}|^2) \\
=& 1 - \exp(-\frac{1}{2\sigma^2}|\frac{H_0+C_0}{C_0-\tilde{C}} - G_{cl,0}|^2) \\
=& 1 - \exp(-\frac{1}{2\sigma^2}|\frac{H_0+C_0}{\Delta C} - G_{cl,0}|^2) \\
=& 1 - \exp(-\frac{1}{2\sigma^2}|\frac{k_3}{\Delta C} - k_4|^2) \\
=& \alpha_{\Delta C}
\end{aligned} \tag{3.87}$$

where $\tilde{C} = C_0 - \Delta C$ was substituted in and where $\Delta C = C_0 - \tilde{C} = r_{\Delta C} e^{j\theta_{\Delta C}}$, $k_3 = H_0 + C_0 = r_{k_3} e^{j\theta_{k_3}}$ and $k_4 = G_{cl,0} = r_{k_4} e^{j\theta_{k_4}}$.
Now $\tilde{C} \to C_0$ implies that $\Delta C \to 0$ or $r_{\Delta C} \to 0$ such that we need to show that

$$\lim_{\Delta C\to 0} \alpha_{\Delta C} = \lim_{r_{\Delta C}\to 0} \alpha_{\Delta C} = 1 \tag{3.88}$$

Because

$$
\begin{aligned}
&\lim_{r_{\Delta C}\to 0} |\frac{1}{r_{\Delta C}} e^{-j\theta_{\Delta C}} r_{k_3} e^{j\theta_{k_3}} - r_{k_4} e^{j\theta_{k_4}}|^2 \\
&= \lim_{r_{\Delta C}\to 0} [(\frac{r_{k_3}}{r_{\Delta C}} \cos(\theta_{k_3} - \theta_{\Delta C}) - r_{k_4} \cos(\theta_{k_4}))^2 + (\frac{r_{k_3}}{r_{\Delta C}} \sin(\theta_{k_3} - \theta_{\Delta C}) - r_{k_4} \sin(\theta_{k_4}))^2] \\
&= \lim_{r_{\Delta C}\to 0} [\frac{r_{k_3}^2}{r_{\Delta C}^2} + {r_{k_4}}^2 - 2\frac{r_{k_3}}{r_{\Delta C}} r_{k_4} (\cos(\theta_{k_3} - \theta_{\Delta C}) \cos(\theta_{k_4}) + \sin(\theta_{k_3} - \theta_{\Delta C}) \sin(\theta_{k_4}))] \\
&= \infty
\end{aligned}
\tag{3.89}
$$

then the limit in (3.88) and hence the limit in (3.85) is 1. Note, that the exponential function is continuous everywhere. Therefore, the limit can be applied to the inner part of the exponential function. Hence, result (1). □

Proof. (2) The limit in Equation (3.86) can be shown as follows. First, using $\alpha_{\Delta C}$ defined by Equation (3.87) and $\tilde{F}$ defined by Equation (3.45), we reformulate:

$$\begin{aligned}(1-\alpha)(-\frac{1}{\tilde{F}}) &= \left(1-[1-exp(-\frac{1}{2\sigma^2}|\frac{k_3}{\Delta C}-k_4|^2)]\right)(-\frac{\tilde{H}+\tilde{C}}{C_0-\tilde{C}}) \\ &= exp(-\frac{1}{2\sigma^2}|\frac{k_3}{\Delta C}-k_4|^2)(-\frac{\tilde{H}-\left(C_0-\tilde{C}\right)+C_0}{C_0-\tilde{C}}) \\ &= \exp(-\frac{1}{2\sigma^2}|\frac{k_3}{C_0-\tilde{C}}-k_4|^2)(-\frac{\tilde{H}+C_0}{C_0-\tilde{C}}+1) \\ &= \exp(-\frac{1}{2\sigma^2}|\frac{k_3}{\Delta C}-k_4|^2)(-\frac{k_5}{\Delta C}+1) \\ &= f_{\Delta C}\end{aligned} \tag{3.90}$$

with $k_3 = H_0 + C_0 = r_{k_3}e^{j\theta_{k_3}}$, $k_4 = G_{cl,0} = r_{k_4}e^{j\theta_{k_4}}$, $k_5 = \tilde{H} + C_0 = r_{k_5}e^{j\theta_{k_5}}$ and $\Delta C = C_0 - \tilde{C} = r_{\Delta C}e^{j\theta_{\Delta C}}$. For the magnitude of $f_{\Delta C}$ we obtain:

$$\begin{aligned}f_{\Delta C}\overline{f_{\Delta C}} &= |\exp(-\frac{1}{2\sigma^2}|\frac{k_3}{\Delta C}-k_4|^2)(-\frac{k_5}{\Delta C}+1)|^2 \\ &= |\exp(-\frac{1}{2\sigma^2}|\frac{k_3}{\Delta C}-k_4|^2)|^2|(-\frac{k_5}{\Delta C}+1)|^2 \\ &= (\exp(-\frac{1}{2\sigma^2}|\frac{k_3}{\Delta C}-k_4|^2))^2|(-\frac{k_5}{\Delta C}+1)|^2 \\ &= \exp(-\frac{1}{\sigma^2}|\frac{k_3}{\Delta C}-k_4|^2)|(-\frac{k_5}{\Delta C}-1)|^2 \\ &= \exp(-\frac{1}{\sigma^2}|\frac{r_{k_3}}{r_{\Delta C}}e^{j(\theta_{k_3}-\theta_{\Delta C})}-r_{k_4}e^{j\theta_{k_4}}|^2)|(-\frac{r_{k_5}}{r_{\Delta C}}e^{j(\theta_{k5}-\theta_{\Delta C})}-1)|^2 \\ &= \exp(-\frac{1}{\sigma^2}[\frac{{r_{k_3}}^2}{r_{\Delta C}^2}+{r_{k_4}}^2-2\frac{r_{k_3}}{r_{\Delta C}}r_{k_4}(\cos(\theta_{k_3}-\theta_{\Delta C})\cos(\theta_{k_4})+\sin(\theta_{k_3}-\theta_{\Delta C})\sin(\theta_{k_4}))]) \\ &([-\frac{r_{k_5}}{r_{\Delta C}}\cos(\theta_{k_5}-\theta_{\Delta C})-1]^2+[-\frac{r_{k_5}}{r_{\Delta C}}\sin(\theta_{k_5}-\theta_{\Delta C})]^2) \\ &= \exp(-\frac{1}{\sigma^2}[\frac{{r_{k_3}}^2}{r_{\Delta C}^2}+{r_{k_4}}^2-2\frac{r_{k_3}}{r_{\Delta C}}r_{k_4}(\cos(\theta_{k_3}-\theta_{\Delta C})\cos(\theta_{k_4})+\sin(\theta_{k_3}-\theta_{\Delta C})\sin(\theta_{k_4}))]) \\ &(1+\frac{r_{k_5}^2}{r_{\Delta C}^2}+2\frac{r_{k_5}}{r_{\Delta C}}\cos(\theta_{k5}-\theta_{\Delta C})) \\ &= \exp(-(\frac{|a|}{r_{\Delta C}^2}+|b|+\frac{c}{r_{\Delta C}}))(1+\frac{|d|}{r_{\Delta C}^2}+\frac{e}{r_{\Delta C}}) \\ &= f_{r_{\Delta C}}\overline{f_{r_{\Delta C}}}\end{aligned} \tag{3.91}$$

where $a, b, c, d, e \in \mathbb{R}$. Hence,

$$\lim_{\Delta C\to 0} f_{\Delta C}\overline{f_{\Delta C}} = \lim_{r_{\Delta C}\to 0} f_{r_{\Delta C}}\overline{f_{r_{\Delta C}}} = 0 \tag{3.92}$$

Since the limit of the magnitude of the function $f(\Delta C)$ is zero, also the limit of the function is zero, i.e.

$$\begin{aligned} &\lim |f_{\Delta C}|^2 = 0 \Rightarrow \\ &\lim |f_{\Delta C}| = 0 \Rightarrow \\ &\lim |f_{\Delta C}| e^{j \arg(f_{\Delta C})} = \lim f_{\Delta C} = 0 \end{aligned} \tag{3.93}$$

Hence, result (2). □

□

3.6.3 Variance of Anticipated Updated Closed-loop

Lemma 3.6.4. *Under the same conditions as in Lemma 3.6.1:*

1. *We can express the second moment of $\hat{\tilde{G}}_{cl}$ about $\tilde{G}_{cl}$ as:*

$$\mathbb{E}[|\hat{\tilde{G}}_{cl} - \tilde{G}_{cl}|^2] = |\frac{\tilde{T}}{T_0}|^2 \mathbb{E}[|\frac{1}{P} \frac{\varepsilon_k}{(P - \varepsilon_k F_0)}|^2] \tag{3.94}$$

   with P given by (3.61).

2. *The expected value above is infinite.*

Proof. (1) The absolute squared error between $\hat{\tilde{G}}_{cl}$ and $\tilde{G}_{cl}$ is given by

$$\begin{aligned} |\hat{\tilde{G}}_{cl} - \tilde{G}_{cl}|^2 &= |\frac{\tilde{T}}{T_0} \frac{\hat{G}_{cl,0}}{1 - \hat{G}_{cl,0} F_0} - \frac{\tilde{T}}{T_0} \frac{G_{cl,0}}{1 - G_{cl,0} F_0}|^2 \\ &= |\frac{\tilde{T}}{T_0} \frac{G_{cl,0} + \varepsilon_k}{1 - \left(G_{cl,0} + \varepsilon_k\right) F_0} - \frac{\tilde{T}}{T_0} \frac{G_{cl,0}}{1 - G_{cl,0} F_0}|^2 \\ &= |\frac{\tilde{T}}{T_0} \frac{G_{cl,0} + \varepsilon_k}{P - \varepsilon_k F_0} - \frac{\tilde{T}}{T_0} \frac{G_{cl,0}}{P}|^2 \\ &= |\frac{\tilde{T}}{T_0} (\frac{(G_{cl,0} + \varepsilon_k) P}{(P - \varepsilon_k F_0) P} - \frac{G_{cl,0}(P - \varepsilon_k F_0)}{(P - \varepsilon_k F_0) P})|^2 \\ &= |\frac{\tilde{T}}{T_0} (\frac{\varepsilon_k P + \varepsilon_k F_0 G_{cl,0}}{(P - \varepsilon_k F_0) P})|^2 \\ &= |\frac{\tilde{T}}{T_0} (\frac{\varepsilon_k (1 - G_{cl,0} F_0) + \varepsilon_k F_0 G_{cl,0}}{(P - \varepsilon_k F_0) P})|^2 \\ &= |\frac{\tilde{T}}{T_0}|^2 |\frac{1}{P} \frac{\varepsilon_k}{(P - \varepsilon_k F_0)}|^2 \end{aligned} \tag{3.95}$$

Hence, result (1). □

Proof. (2) Since the probability density function $f_{\epsilon_k}(z)$ of ϵ_k is radially symmetric, i.e. it depends only on the magnitude $|z|$, [Hea01b], and additionally $f_{\epsilon_k}(z)$ is non-zero for all $z \in \mathbb{C}$, then by using result (4) in [Hea01b] it follows that $\mathbb{E}[|\frac{1}{P} \frac{\varepsilon_k}{(P - \varepsilon_k F_0)}|^2]$ is infinite. Hence, result (2). □

This means, that such an estimate suffers the same drawbacks as a classical indirect or direct plant estimate under closed-loop conditions [Hea01b], [GKP96b], as described in Section 2.3.2 and 2.3.1.

Example 3.2. ***Sample Properties of Anticipated Updated Closed-loop***
In this example we are concerned with the anticipated updated closed-loop $\hat{\tilde{G}}_{cl}$*, of the system described in Section 3.2. The anticipated updated closed-loop frequency response is obtained as described in Section 3.6, based on the initial closed-loop frequency response estimates presented in Example 3.1 and assuming that the new controller parameters, given in Table 3.5 were determined.*

First we investigate the influence of the signal-to-noise ratio on the expected value of the anticipated, updated closed-loop estimate, $\mathbb{E}[\hat{\tilde{G}}_{cl}]$*. We verify the derived analytical expression for the expected value of* $\hat{\tilde{G}}_{cl}$ *given by Equation* (3.43)*, by comparing it to the sample mean of the estimates of* $\tilde{G}_{cl}$*, since the sample mean is an estimator of the expected value. The estimates* $\hat{\tilde{G}}_{cl}$ *are obtained by the proposed estimation, Equation* (3.36)*, based on Monte Carlo simulation data. Figure 3.11 to 3.13 compare the theoretical value for the expected value of the anticipated updated closed-loop frequency response* $\mathbb{E}[\hat{\tilde{G}}_{cl}]$*, given by Lemma 3.6.1, with the true updated closed-loop frequency response* $\tilde{G}_{cl}$*, and with the sample mean*

$$\bar{\hat{\tilde{G}}}_{cl} = \frac{1}{M} \sum_{m=1}^{M} \hat{\tilde{G}}_{cl}^{[m]} \tag{3.96}$$

for $M = 10000$ *simulations. Thereby, Figure 3.11 to 3.13 reveal the results for a signal-to-noise ratio*

$$SNR = \left| \frac{R_{DFT}}{\sigma_n} \right| \tag{3.97}$$

of 1*,* 0.1 *and* 0.03*, respectively. For a high SNR of* 1*, Figure 3.11, almost no difference between the true closed-loop frequency response with updated controller parameters* $\tilde{G}_{cl}$ *and the expected value of its estimate is noticeable for this example system. For a medium SNR of* 0.1*, Figure 3.12, there is a bias at low frequencies. At a low SNR of* 0.03*, Figure 3.13, the expected value of the estimate is biased for almost all the considered frequencies,*

Parameter	Value
k	-0.27
k_I	-0.26
h	-1.44

Table 3.5: *Updated controller parameters.*

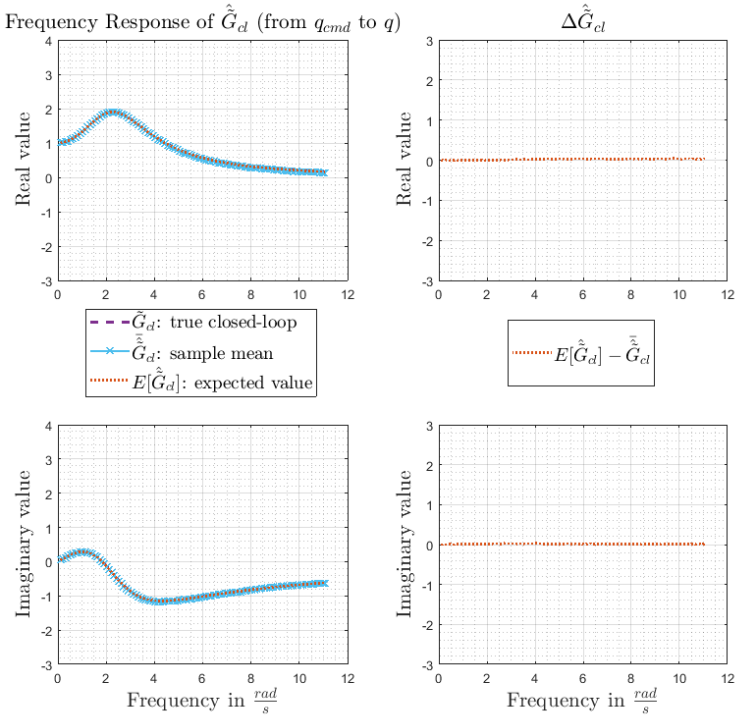

Figure 3.11: *Closed-loop estimate for SNR=1.*

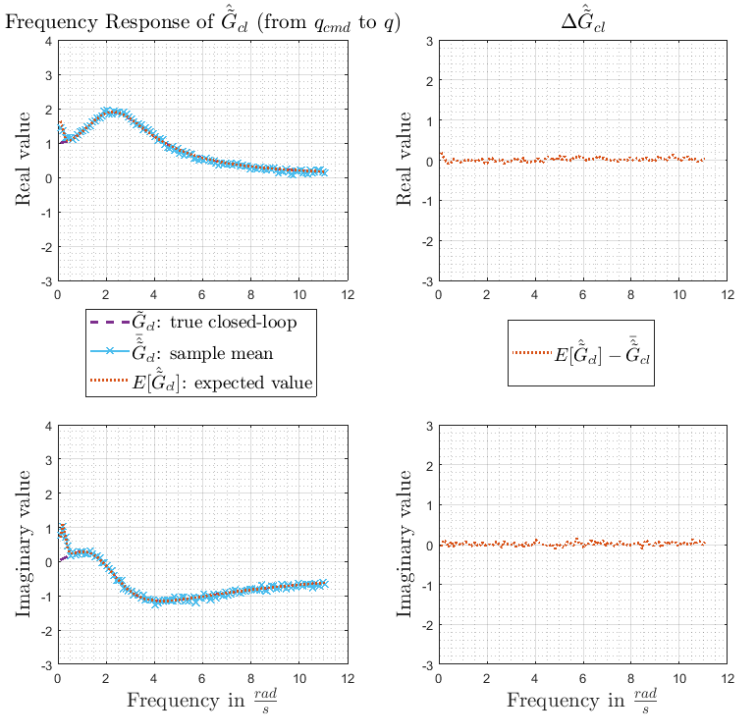

Figure 3.12: *Closed-loop estimate for SNR=0.1.*

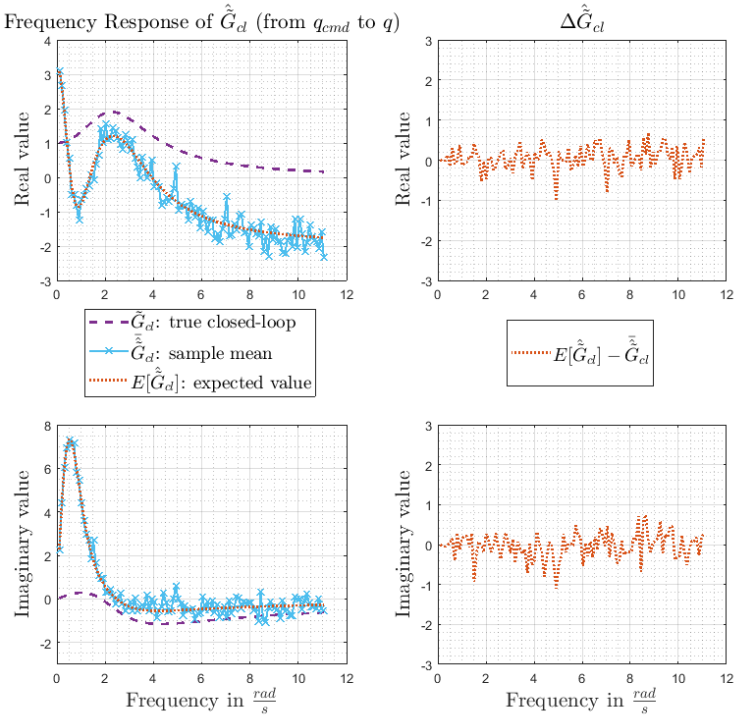

Figure 3.13: *Closed-loop estimate for SNR=0.03.*

meaning that the expected value of the anticipated closed-loop estimate deviates from the true closed-loop with updated controller parameters. Hence, as claimed, the deviation between $\tilde{G}_{cl}$ *and* $\mathbb{E}[\hat{\tilde{G}}_{cl}]$ *tends to* 0 *with increasing signal-to-noise ratio.*

We see also that for all cases the derived theoretical expected value $\mathbb{E}[\hat{\tilde{G}}_{cl}]$ *from Lemma 3.6.1, is centered around the sample mean, which verifies the derived analytical expression.*

Next the influence of the initial feed-forward gain, H_0*, on the deviation between the theoretical expected value given by Lemma 3.6.1,* $\mathbb{E}[\hat{\tilde{G}}_{cl}]$*, and the true value of the updated closed-loop,* $\tilde{G}_{cl}$*, is investigated. Figure 3.14 compares the theoretical expected value,* $\mathbb{E}[\hat{\tilde{G}}_{cl}]$*, with the true value of the updated closed-loop,* $\tilde{G}_{cl}$*, for a SNR of* 0.03*. Thereby, three different initial closed-loop systems were assumed, differing in the value of the feed-forward gain,* H_0*, only. The expected values of the estimate* $\hat{\tilde{G}}_{cl}$ *were calculated, based on*

1. *an initial feed forward gain of zero*

2. *an initial feed forward gain with value given in Table 3.3*

3. *half of the initial feed forward gain in Table 3.3.*

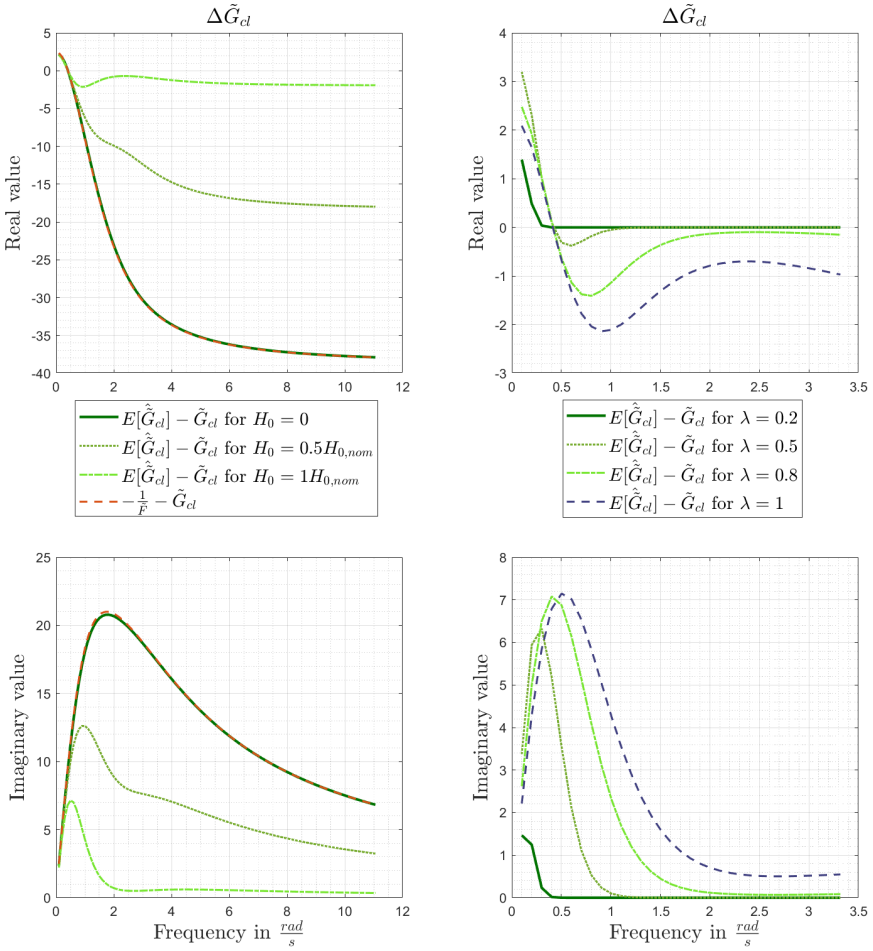

Figure 3.14: *Variation of feed-forward and controller parameters.*

The feedback and integral gain were kept at their initial value given in Table 3.3 and were not changed. As was shown in Lemma 3.6.2, $\mathbb{E}[\hat{\tilde{G}}_{cl}]$ *converges towards* $\tilde{G}_{cl}$ *when the initial feed forward,* H_0*, goes to infinity. We see now in Figure 3.14, that indeed the difference between the expected value of the anticipated closed-loop and its true value decreases with increasing initial feed forward gain.*

Another interesting point to note from Figure 3.14, is that for the considered very low SNR of 0.03 *in combination with a feed forward gain of zero (both have a decreasing effect on* α*, Equation* (3.44)*), the expected value of the estimate* $\mathbb{E}[\hat{\tilde{G}}_{cl}]$ *corresponds to* $-\frac{1}{\tilde{F}}$*, as expected for low values of* α*, see Equation* (3.43)*.*

Next, the influence of $\Delta C = C_0 - \tilde{C}$ *on the deviation between* $\mathbb{E}[\hat{\tilde{G}}_{cl}]$ *and* $\tilde{G}_{cl}$ *is investigated. According to Lemma 3.6.3 the expected value of the estimate converges towards the true value when* ΔC*, meaning the controller update, goes to zero. Figure 3.14 shows*

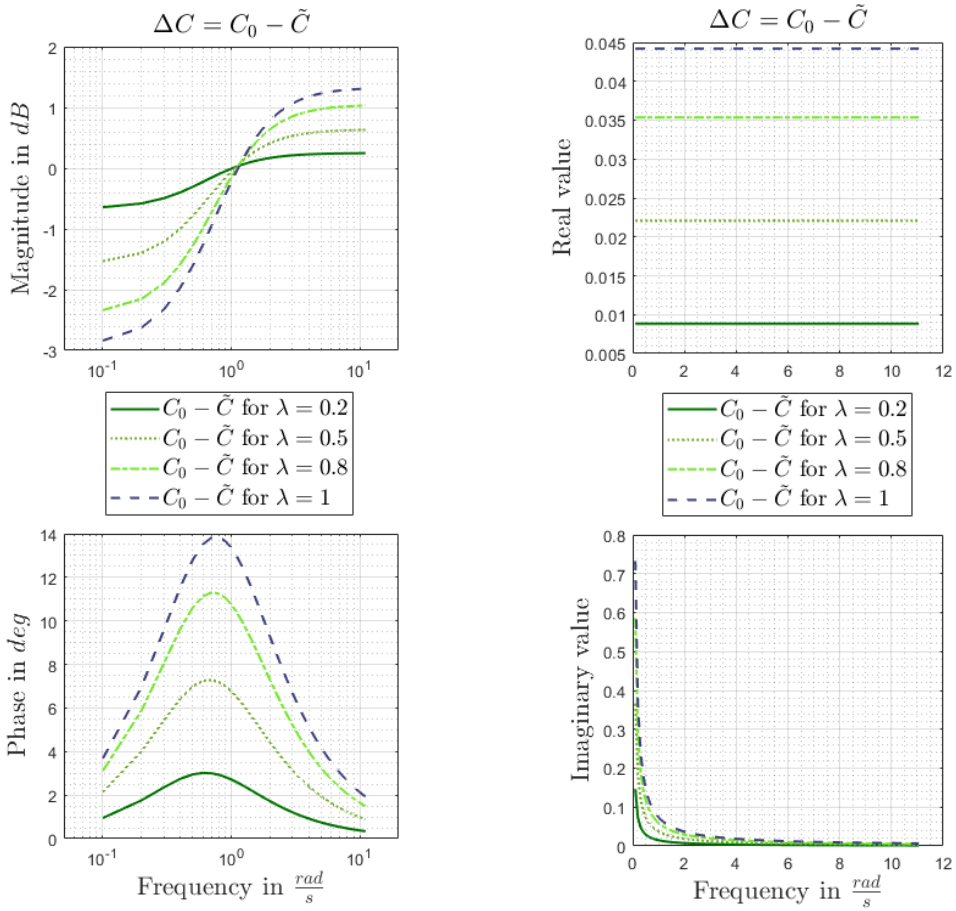

Figure 3.15: *Influence of λ on controller frequency responses.*

the difference between the expected value of the estimate $\mathbb{E}[\hat{\tilde{G}}_{cl}]$ and its true value $\tilde{G}_{cl}$, where the estimates were calculated based on the same initial closed-loop responses, but for different updated feedback and integral gain values, which were varied linearly according to

$$\tilde{p}_\lambda = \lambda(\tilde{p} - p_0) + p_0 \tag{3.98}$$

where p_0 is the respective initial controller parameter and $\tilde{p}$ is the respective updated parameter, both given in Table 3.3 and 3.5. The updated feed forward gain was kept constant at the value specified in Table 3.5. In Figure 3.15 the resulting frequency response $\Delta C(j\omega_k) = C_0(j\omega_k) - \tilde{C}(j\omega_k)$ is shown in terms of magnitude and phase as well as in terms of real and imaginary part for different values of λ. We see that for smaller values of λ, $\tilde{C}$ goes to C_0 monotonically for a fixed frequency, both in terms of magnitude and phase but also in terms of real and imaginary part. Meaning that with decreasing λ, the resulting ΔC is also decreasing. Further we see in Figure 3.14 that for sufficiently small λ the difference between $\mathbb{E}[\hat{\tilde{G}}_{cl}]$ and $\tilde{G}_{cl}$ becomes small as λ is decreased over all frequencies. But we also see, that the bias is not linear with the difference between C_0 and $\tilde{C}$,

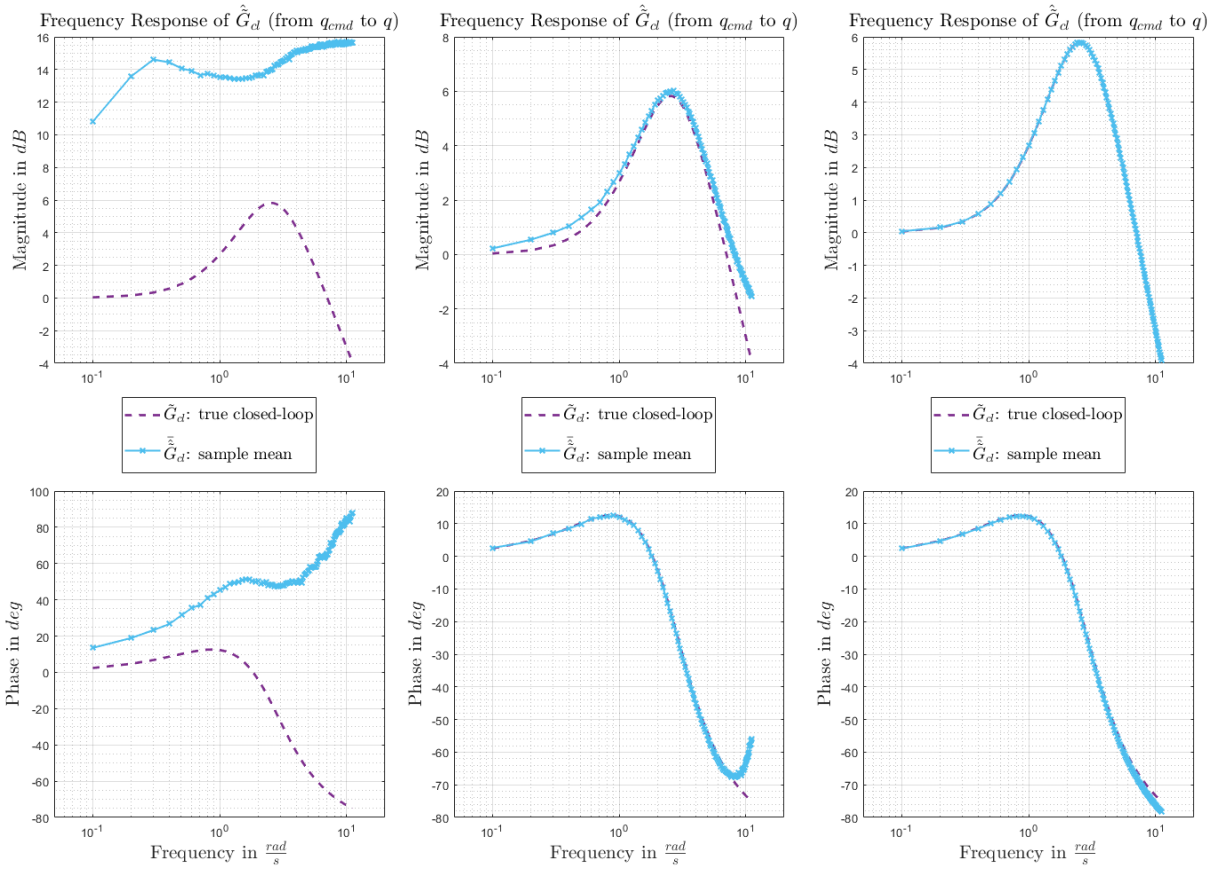

SNR of 0.1 SNR of 1 SNR of 10

Figure 3.16: *Magnitude and phase of closed-loop estimate, Left: SNR of 0.1; Middle: SNR of 1; Right: SNR of 10.*

i.e. the bias is not necessarily monotonically decreasing with decreasing difference between C_0 *and* $\tilde{C}$*. For low frequencies for example the bias in the real value is the largest for* $\lambda = 0.5$ *and decreases with increasing values of* λ*, while for a value of* $\lambda = 0.2$ *the bias is the smallest. Hence, from Lemma 3.6.3, it cannot be concluded that by reducing the controller update* (ΔC) *the bias is always reduced for all frequencies. This holds only for a sufficient decrease of* ΔC*.*

Finally, Figure 3.16 compares, for the considered example, the sample mean of the magnitude and phase of the closed-loop estimate (3.36)*, i.e.*

$$\begin{aligned} \overline{|\hat{\tilde{G}}_{cl}|} &= \frac{1}{M}\sum_{m=1}^{M} |\hat{\tilde{G}}_{cl}^{[m]}| \\ \overline{\hat{\tilde{\Phi}}_{cl}} &= \frac{1}{M}\sum_{m=1}^{M} arg(\hat{\tilde{G}}_{cl}^{[m]}) \end{aligned} \tag{3.99}$$

with its true values for SNR's of $0.1, 1$ *and* 10*. We see, that the bias decreases with increasing SNR."] [end of quotation from my manuscript [SSH]]*

In this section we derived an analytical expression for the bias of the anticipated, updated closed-loop frequency response estimate and showed that it is similar in structure to the indirect non-parametric plant estimate. Based on the derived theoretical expression for the expected value of the updated anticipated closed-loop frequency response estimate, $\mathbb{E}[\hat{\tilde{G}}_{cl}]$, the following relations were shown and verified via simulation:

1. The bias is reduced with increasing signal-to-noise ratio or by increasing the number of maneuver repetitions (with regard to the estimation of the initial closed-loop frequency response). The reason is, that with increasing signal-to-noise ratio the variance of the initial closed-loop estimate σ^2 is reduced, which is used for calculation of the anticipated closed-loop estimate. As was shown this variance directly influences the parameter α, Equation (3.44), such that α tends to 1 with decreasing σ^2, and the expected value, $\mathbb{E}[\hat{\tilde{G}}_{cl}]$, tends towards its true value $\tilde{G}_{cl}$. The conclusion for the test-based gain retuning is hence, that the experiments for estimating the initial closed-loop frequency response shall be designed such that the SNR is maximized. Because of nonlinearities (like actuator constraints for example) and drift away from the trim point the amplitudes of the excitation and consequently the SNR is however restricted.

2. The bias is reduced with increasing initial feed forward term, H_0, as was shown via simulation. In Lemma 3.6.2 it was shown that $\mathbb{E}[\hat{\tilde{G}}_{cl}]$ goes to $\tilde{G}_{cl}$, when the initial feed forward gain, H_0, goes to infinity. The conclusion for the test-based retuning procedure is that controller structures with a feed forward term lead to better results than structures without feed forward, because the bias between $\mathbb{E}[\hat{\tilde{G}}_{cl}]$ and $\tilde{G}_{cl}$ is lower.

3. The bias tends to zero when the controller update $\Delta C = C_0 - \tilde{C}$ is significantly reduced. In Lemma 3.6.3 it was shown that $\mathbb{E}[\hat{\tilde{G}}_{cl}]$ goes to $\tilde{G}_{cl}$, when ΔC goes to zero. However, not any reduction of the controller update ΔC, might lead to a decrease of the bias over all frequencies as simulation results showed. The conclusion for the test-based retuning procedure is that very large changes in the controller parameters shall be considered with caution as the anticipated closed-loop estimate based on which these controller updates might be determined, might be biased.

4. At last, it was shown that the variance is theoretically infinite, which is similar to the indirect and direct plant estimate under closed-loop conditions. This result is not intuitive when inspecting the simulation results, as we will see in the next sections, where the variance of the anticipated closed-loop estimates seems very small for high SNRs. The conclusion for the test-based retuning procedure is, that the estimates of the anticipated updated closed-loop shall be considered with caution and be checked for outliers. Based on the similarities with the indirect plant estimate, there is future basis for investigation of other variation measures and exclusion methods to better characterize and improve the statistical properties of the estimate.

Additional theoretical work is also to be undertaken to extend the results to multiple-input-multiple-output systems.
The anticipated closed-loop frequency response for a controller parameter set that differs from the initial gains used within the experiment, that was discussed in this section, will be used in the context of the retuning procedure within an optimization. The objective of the optimization is to determine a new gain set, such that the difference between desired and anticipated closed-loop response is minimized under some constraints. The optimization will be discussed in detail in Section 3.8. The considered constraints use an estimate of the stability margins in terms of gain and phase margins. These are discussed in the next section.

3.7 Anticipated Stability Margins for Updated Controller

In the previous section we investigated the anticipated closed-loop estimate for an updated set of controller parameters. This predicted closed-loop behavior is used as we will see in Section 3.8 to determine new controller parameters. The optimization problem that is formulated for this purpose incorporates constraints on the phase and gain margins to enforce the required stability criteria on the obtained new system with updated controller parameters. This section addresses the calculation of the anticipated margins for new controller parameters. Similar to the anticipated updated closed-loop frequency response, the anticipated margins are calculated based on the non-parametric closed-loop frequency response estimate obtained from experiments with initial controller parameters, as presented in Section 3.5.

The anticipated stability margins are calculated in terms of gain and phase margin, A_m and Φ_m, for the open-loop estimate $\tilde{C}(j\omega_k)\hat{G}(j\omega_k)$, where $\tilde{C}(j\omega_k)$ is the updated controller and $\hat{G}(j\omega_k)$ is obtained as the indirect non-parametric plant estimate calculated by (3.34), i.e.

$$\hat{G}(j\omega_k) = \frac{\hat{G}_{cl,0}(j\omega_k)}{T_0(j\omega_k) - C_0(j\omega_k)\hat{G}_{cl,0}(j\omega_k)} \tag{3.100}$$

with the initial controller $C_0(j\omega_k)$, $T_0(j\omega_k)$ given in (3.38), and the initial closed-loop estimate $\hat{G}_{cl,0}(j\omega_k)$ discussed in Section 3.5. The bias and variance of the anticipated open-loop estimate can be calculated with the same approach as presented in Section 3.6 for the anticipated updated closed-loop and as presented in [Hea01b] for a indirect plant estimate for a slightly different controller structure, noting that for high signal-to-noise ratio the bias will be approximately zero.

However, for calculation of the margins, the magnitude and phase of $\tilde{C}(j\omega_k)\hat{G}(j\omega_k)$ have to be calculated, for which an analytical closed-form of the bias and variance is not known to the author. Monte Carlo simulations, presented in Example 3.3 show that for a high signal-to-noise ratio the bias is almost zero for the considered system.

Example 3.3. ***Sample Properties of Anticipated Gain and Phase Margins***
In this example we are concerned with the anticipated gain and phase margins A_m, Φ_m, of the system described in Section 3.2. The anticipated margins are calculated as described in Section 3.7, based on the initial closed-loop frequency response estimates presented in Example 3.1.

We assume, that the new controller parameters, given in Table 3.5 were determined. In the following we investigate the magnitude and phase of the resulting open-loop frequency response $\tilde{C}(j\omega_k)G(j\omega_k)$ and its estimates, as well as the resulting margins and the corresponding estimates.

Figure 3.17 compares the magnitude and phase of the true updated open-loop frequency response $\tilde{C}(j\omega_k)G(j\omega_k)$ with magnitude and phase of the sample mean

$$\overline{\tilde{C}\hat{G}} = \frac{1}{M}\sum_{m=1}^{M}\tilde{C}\hat{G}^{[m]} \tag{3.101}$$

for $M = 10000$ simulations. Thereby, Figure 3.17 reveals the results for a signal-to-noise ratio

$$SNR = \left|\frac{R_{DFT}}{\sigma_n}\right| \tag{3.102}$$

of 1 and 10, respectively. We see that for a high signal-to-noise ratio the sample mean of the magnitude and phase of the anticipated open-loop frequency response match the true values. Since the phase is not crossing -180 degrees, we can only calculate the phase margin. Figure 3.18 shows the histograms of the respective SNR cases for all M samples of the calculated phase margins of $\tilde{C}\hat{G}^{[m]}$. We see that for a high SNR the phase margin sample values are close to the real value, i.e. $\Phi_m = 106.68°$. The sample mean of the estimated phase margins Φ_m for a SNR of 1 is $\bar{\hat{\Phi}}_m = 105.25°$ and for a SNR of 10 it is $\bar{\hat{\Phi}}_m = 106.71°$.

We saw in this section and the previous section how the anticipated closed-loop frequency response for a new gain set and the corresponding anticipated margins can be calculated. For high SNR we observed that for the considered system the estimated phase margins are close to the true phase margin. We noted also that, at least for the considered system, the magnitude and phase of the open-loop estimate with updated controller parameters, need to be considered with caution for low SNR's. However, for a large SNR they accurately reflect the true values. The next section presents how the derived estimates are incorporated into an optimization that determines a new set of controller parameters. The objective is to minimize the difference between the desired closed-loop frequency response and the closed-loop frequency response for an updated controller parameter set.

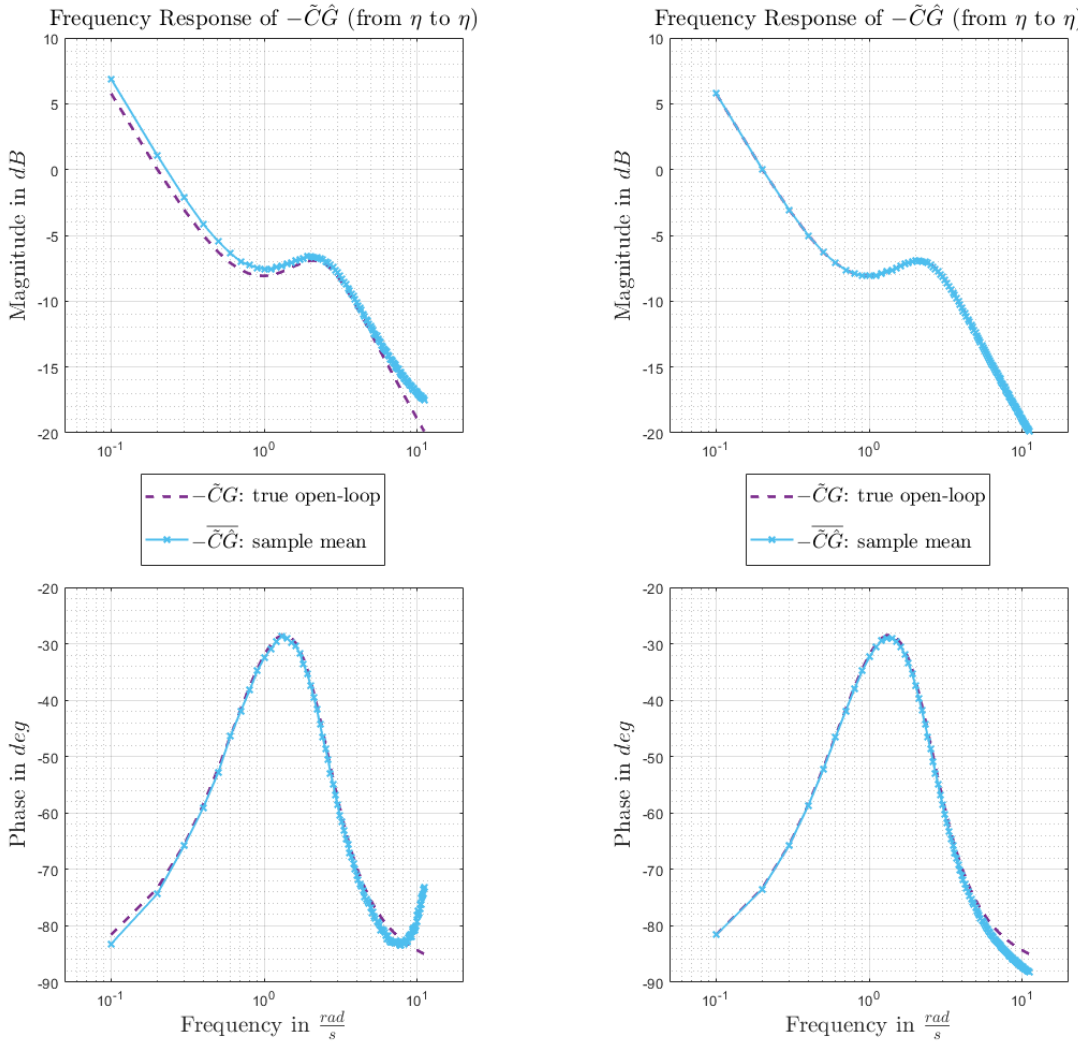

Figure 3.17: *Open-loop estimate, Left: SNR of 1; Right: SNR of 10.*

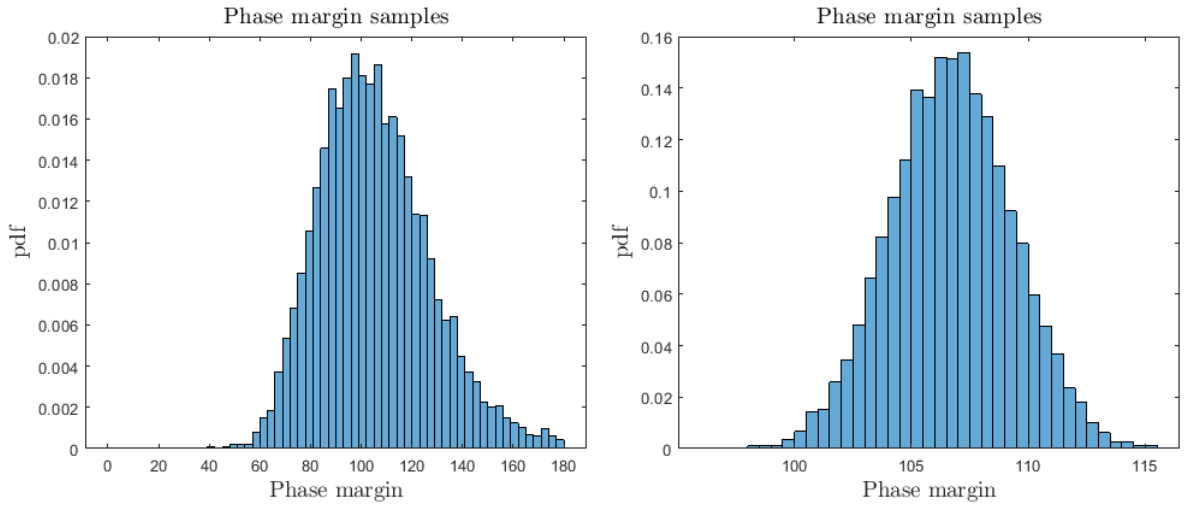

Figure 3.18: *Phase margin of open-loop estimate, Left: SNR of 1; Right: SNR of 10.*

3.8 Optimization Problem Formulation

This section presents the optimization problem that is formulated in order to determine new controller parameters (C2), such that the closed-loop frequency response with these updated controller parameters will be closer to the desired response than the closed-loop frequency response with the initial controller parameters. The following optimization problem addresses SISO controller structures. In my publication [GHSM21] and in section 4.4.3.5 the same optimization method is presented for a SIMO system.

The quadratic cost function to be minimized with respect to the controller parameter vector $\boldsymbol{p}$ is given by $J(\boldsymbol{p})$ in Equation (3.103). The objective is to minimize the deviation between the retuned closed-loop frequency response and the desired one. The deviation is quantified by a metric considering a weighted squared error in magnitude and phase of the respective frequency responses. The proposed deviation metric was already used successfully in the context of low order equivalent system (LOES) identification by [RT06]. In that context the deviation between the measured frequency response and the frequency response of a LOES is minimized with respect to the parameters of the LOES. The idea in the context of this thesis is to use a similar cost function structure to minimize the deviation between a desired closed-loop frequency response and an anticipated, updated closed-loop frequency response, with respect to the controller parameters. Furthermore, a regularization is proposed by adding a penalization term, keeping the tuned gains within reasonable bounds around the initial controller parameters. Finally, stability criteria are enforced by supplementary constraints. The cost function is given by:

$$J\left(\boldsymbol{p}\right) = \{\, \frac{20}{n_\omega} \sum_{k=1}^{n_\omega} (\mathrm{w}_\gamma\left(\omega_k\right) \left[\mathrm{w}_A \Delta_{|G_{cl}|}(j\omega_k, \boldsymbol{p}) + \mathrm{w}_\phi \Delta_{\angle G_{cl}}(j\omega_k, \boldsymbol{p})\right])\} + \left(\boldsymbol{p} - \boldsymbol{p}_0\right) \boldsymbol{Q} \left(\boldsymbol{p} - \boldsymbol{p}_0\right)^T \tag{3.103}$$

with

$$\begin{aligned} \Delta_{|G_{cl}|}(j\omega_k, \boldsymbol{p}) &= (\left|\hat{\tilde{G}}_{cl}\left(j\omega_k, \boldsymbol{p}\right)\right| - \left|G_{cl,des}\left(j\omega_k\right)\right|)^2 \\ \Delta_{\angle G_{cl}}(j\omega_k, \boldsymbol{p}) &= (\angle\hat{\tilde{G}}_{cl}\left(j\omega_k, \boldsymbol{p}\right) - \angle G_{cl,des}\left(j\omega_k\right))^2 \end{aligned} \tag{3.104}$$

where

$|\cdot|$ is the magnitude in dB at each frequency $\omega_k,\ \ k = 1, \ldots n_\omega$.

$\angle$ is the phase in degrees at each frequency $\omega_k,\ \ k = 1, \ldots n_\omega$.

ω_k are the selected, harmonically related frequencies $\omega_k = \frac{2\pi l_k}{T},\ l_k \in \mathbb{S},\ \ \mathbb{S} \subset \mathbb{N}, k = 1, ...n_\omega$, see Section 3.4

$\boldsymbol{Q}$ is a weighting matrix, penalizing the distance between the controller parameter vector $\boldsymbol{p}$ and initial controller parameter vector $\boldsymbol{p}_0$.

$\mathrm{w}_\gamma(\omega_k)$ is the frequency dependent relative weight.

w_A, w_ϕ are the relative weights for magnitude and phase squared-errors.

The anticipated closed-loop frequency response for the controller parameters $\boldsymbol{p}$, i.e. $\hat{\tilde{G}}_{cl}(j\omega_k, \boldsymbol{p})$, is calculated as described in Section 3.6. In the case that initial controller parameters were derived based on a model, the desired closed-loop frequency response $G_{cl,des}$ could be for example the nominal closed-loop response of plant model with initial controller as described in Section 3.2.2. [RT06] recommends choosing the relative weights for magnitude and phase squared-errors to $\mathrm{w}_A = 1$ and $\mathrm{w}_\phi = 0.01745$. This choice of weighting sets a $-1dB$ magnitude error comparable to $7.57°$ phase error and is equivalent to equal weighting of the real and imaginary parts of the transfer function error [RT06]. The cost function, Equation (3.103), is minimized with respect to $\boldsymbol{p}$ using the off-the-shelf solver *fmincon* from MATLAB. Upper and lower bounds are given for the parameter vector $\boldsymbol{p}$. The optimization problem is given by:

$$\begin{aligned} &\min_{\boldsymbol{p}} .\ J(\boldsymbol{p}) \\ &st. \\ &c_1(\boldsymbol{p}) = A_m - \hat{A}_m(\boldsymbol{p}) \leq 0 \\ &c_2(\boldsymbol{p}) = \Phi_m - \hat{\Phi}_m(\boldsymbol{p}) \leq 0 \end{aligned} \tag{3.105}$$

where

A_m is the adequate gain margin.

$\hat{A}_m(\boldsymbol{p})$ is the anticipated gain margin for the controller parameter vector $\boldsymbol{p}$.

Φ_m is the adequate phase margin.

$\hat{\Phi}_m(\boldsymbol{p})$ is the anticipated phase margin for the controller parameter vector $\boldsymbol{p}$.

The anticipated margins are calculated as described in Section 3.7. The constraints ensure that the resulting controller parameters lead to anticipated phase and gain margins larger or equal to the adequate margins. The posed optimization problem is not convex. Further, no formal proof yet was made to show that this optimization will converge or reveal the global minimum. However, by inspecting the anticipated updated closed-loop frequency response, it can be evaluated if the new solution is better that the initial guess. It is shown by Monte Carlo simulation, that for sufficiently high signal-to-noise ratios, the problem at hand converged to a solution which is better than the initial guess. Furthermore, the

Parameter	Value
Z_α	-1.147
Z_q	-0.022
M_α	-4.536
M_q	-2.049
M_η	-1.569

Table 3.6: *True plant parameters.*

problem at hand is not computational complex and with an usual desktop pc it can be solved within a few minutes. However, as the problem is solved off-line, there exist no demanding time constraints.

Example 3.4. ***Evaluation of Controller Parameter Retuning - Comparison of different Cost Function Formulations***

In this example we are concerned with the controller parameter tuning for the system described in Section 3.2. We will compare the tuning results for two different cost functions: The proposed cost function given by (3.103)*, which is formulated in terms of squared errors of magnitude and phase, and a cost function formulated in terms squared errors of real and imaginary parts given by*

$$J\left(\boldsymbol{p}\right) = \{\frac{20}{n_\omega}\sum_{k=1}^{n_\omega}(w_\gamma\left(\omega_k\right)\left[\Delta_{\Re(G_{cl})}(j\omega_k,\boldsymbol{p}) + \Delta_{\Im(G_{cl})}(j\omega_k,\boldsymbol{p})\right])\} + \left(\boldsymbol{p}-\boldsymbol{p}_0\right)\boldsymbol{Q}\left(\boldsymbol{p}-\boldsymbol{p}_0\right)^T \tag{3.106}$$

with

$$\begin{aligned}\Delta_{\Re(G_{cl})}(j\omega_k,\boldsymbol{p}) &= \left(\Re\left(\hat{\hat{G}}_{cl}(j\omega_k,\boldsymbol{p}) - G_{cl,des}(j\omega_k,\boldsymbol{p})\right)\right)^2\\ \Delta_{\Im(G_{cl})}(j\omega_k,\boldsymbol{p}) &= \left(\Im\left(\hat{\hat{G}}_{cl}(j\omega_k,\boldsymbol{p}) - G_{cl,des}(j\omega_k,\boldsymbol{p})\right)\right)^2\end{aligned} \tag{3.107}$$

The tuning results for both cases will be compared for different SNR's. The optimization uses the anticipated closed-loop frequency response for the parameter vector $\boldsymbol{p}$*. It was calculated as described in Section 3.6, based on the initial closed-loop estimate obtained from closed-loop simulation data of the true plant with the initial controller as described in Section 3.5. The parameters of the considered true plant are given in Table 3.6. The considered uncertainties correspond to an* 7% *increase in* Z_α*, an* 9% *increase in* M_α*, an* 21% *increase in* M_q *and a* 60% *decrease in* M_η*, compared to the nominal plant model parameters given in Table 3.2. The initial controller parameters are given in Table 3.3. The desired closed-loop frequency response is described in Section 3.2.2 and given by Equation* (3.14)*. The tuning was performed for* $M = 500$ *simulations and in each simulation only one repetition, i.e. R=1, of the maneuver with* $N = 6250$ *samples were used for the DFT.*

The quadratic cost functions are parametrized as follows. The weighting matrix $\boldsymbol{Q}$ *is chosen as unity matrix such that the penalty for changes is equal for all gains. The frequency dependent weight* $w_\gamma(\omega_k)$ *is chosen such that the most important frequency range, where the bounds from the outer-loop are most tight, is weighted stronger, in order to achieve a good matching with the desired dynamics in this frequency range, see Table 3.7. The frequency range where the closed-loop dynamics are already well attenuated is weighted very weakly. The remaining parameters are* $w_A = 1,\ w_\phi = 0.01745$ *as described in Section 3.8. The adequate values for the gain and Phase margin were given as* $A_m = 6dB,\ \Phi_m = 45°$.

$\omega_k[\frac{rad}{s}]$	< 0.05	0.05-4	4-10.5	> 10.5
$\mathrm{w}_\gamma(\omega_k)$	10	30	10	1

Table 3.7: *Frequency dependent relative weight.*

High SNR *First we consider a SNR of 10. Figure 3.19 shows the tuning result for the cost function given in Equation* (3.103) *in terms of magnitude and phase. We see the magnitude and phase for the anticipated tuned closed-loop frequency response as well as the true frequency responses of the untuned and tuned system. Furthermore, the error between the desired frequency response and the tuned frequency response as well as the error between the untuned and desired response is revealed together with the MUAD bounds. The MUAD bounds, which can serve for piloted flight control laws as an evaluation criterion, are described in Section 3.9. Figure 3.20 reveals the true frequency responses of the tuned and untuned closed-loop system for the case that cost function given in Equation* (3.106) *was used. Additionally, for the latter case the imaginary and real values of the anticipated tuned closed-loop response are shown in Figure 3.21. We see that for both cost functions similar results are obtained, where the tuned response is centered around the desired response accurately and is much closer to the desired response than the initial, untuned response.*
Figure 3.22 to 3.24 show the histogram of the controller parameters that were determined for each simulation. Depending on the choice of the cost function the result converges to different controller parameters. For both cases the phase margins of the true tuned open-loop, $\tilde{C}G$ *are not violated as they are above* 60 *degrees as Figure 3.25 shows. Since the Phase of* $\tilde{C}G$ *did not cross* -180 *degrees only the phase margin is revealed.*

Low SNR *Here a SNR of 3 is considered. Figure 3.26 shows the results for the cost function in Equation* (3.103) *and Figure 3.27 for the cost function in Equation* (3.106). *Both variants reveal similar deficiencies. The tuned responses clearly deviate from the desired response. However, the tuned responses are closer to the desired response than the untuned response. For both cases the phase margin of the tuned system is above its*

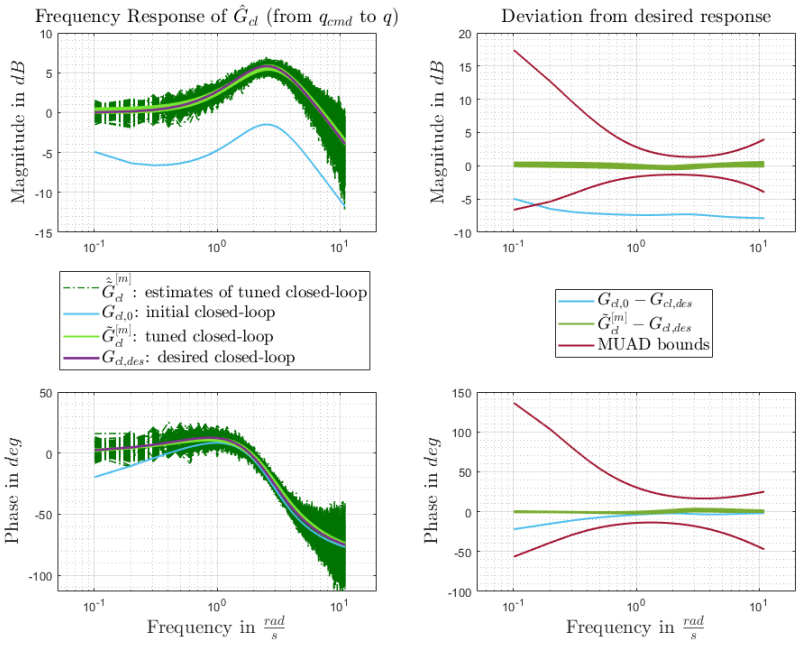

Figure 3.19: *Tuning result for magnitude and phase formulation of cost function for SNR=10.*

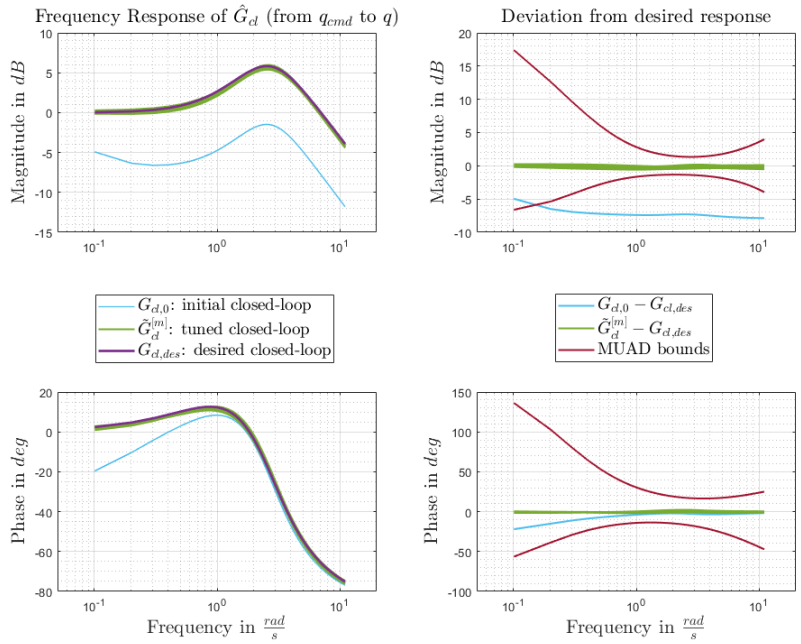

Figure 3.20: *Tuning result for real and imaginary part formulation of cost function for SNR=10, visualization of magnitude and phase.*

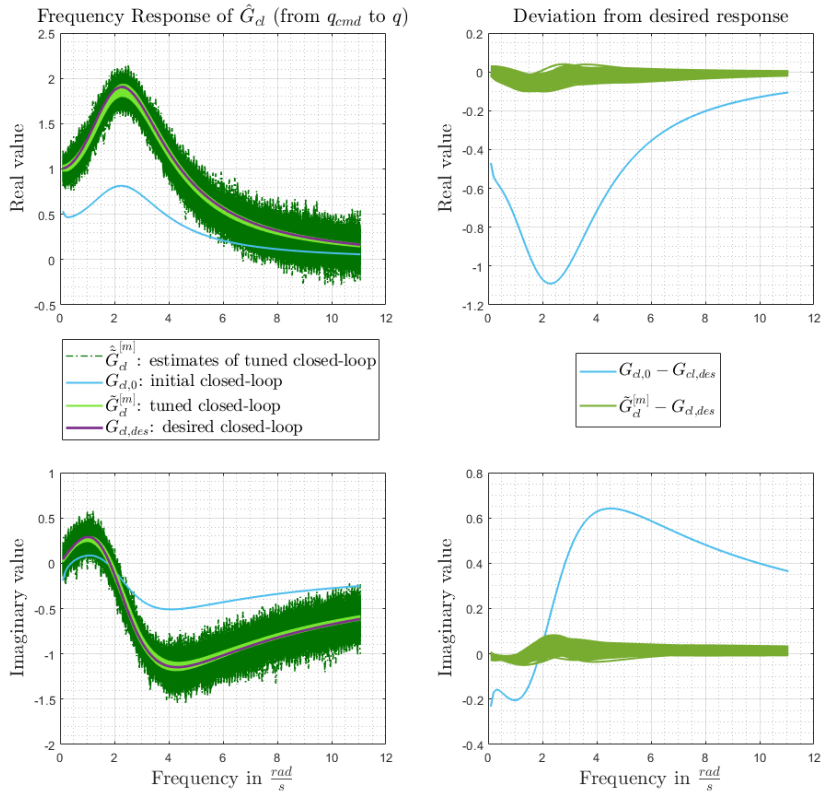

Figure 3.21: *Tuning result for real and imaginary part formulation of cost function for SNR=10, visualization of real and imaginary part.*

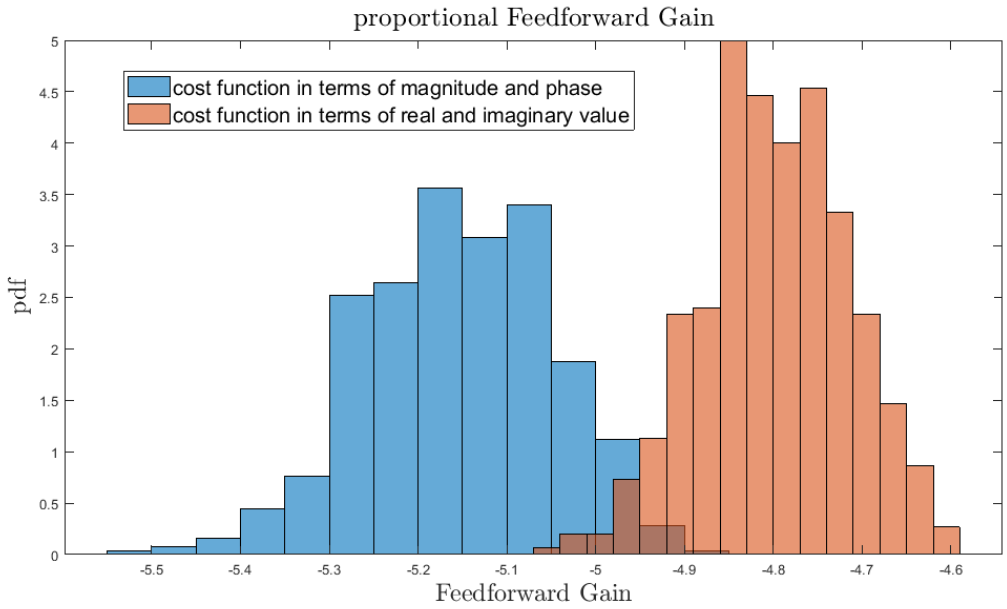

Figure 3.22: *Tuned Feedforward Gain for SNR=10, comparison of cost function in terms of magnitude and phase and cost function in terms of real and imaginary part.*

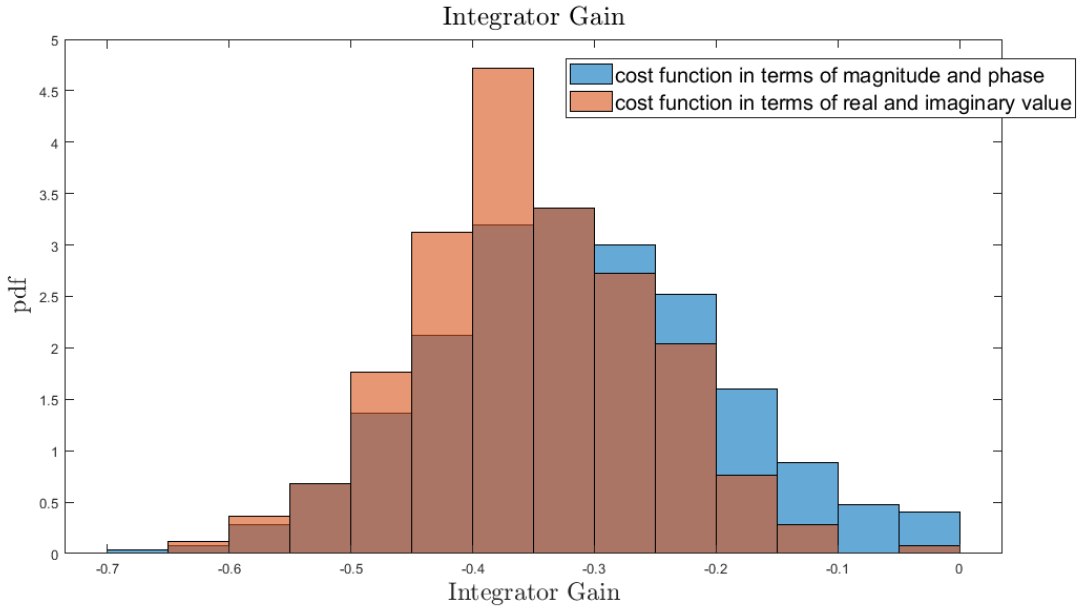

Figure 3.23: *Tuned Integrator Gain for SNR=10, comparison of cost function in terms of magnitude and phase and cost function in terms of real and imaginary part.*

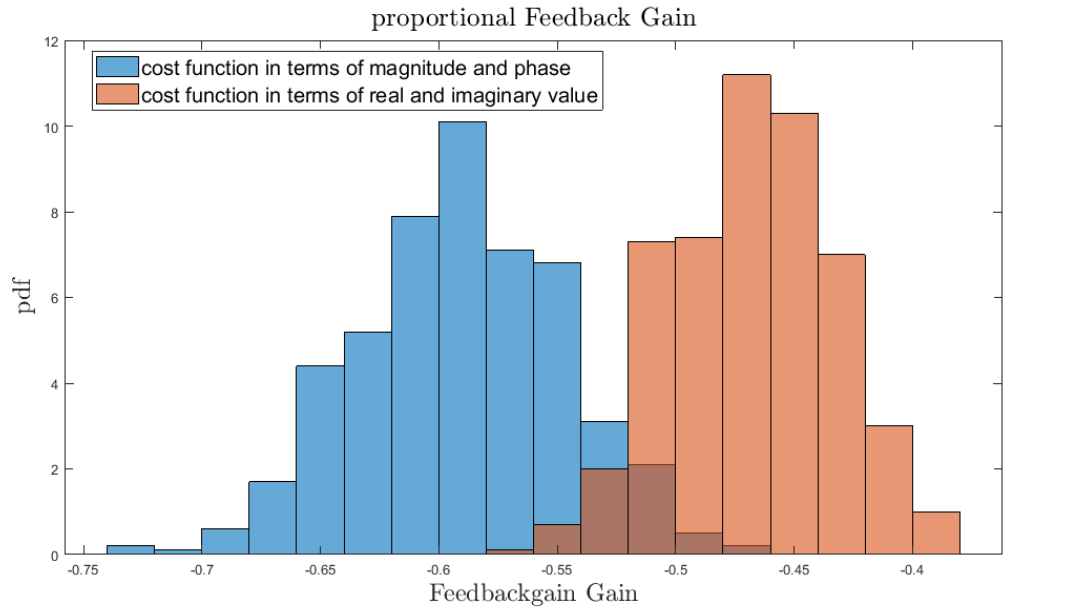

Figure 3.24: *Tuned Feedback Gain for SNR=10, comparison of cost function in terms of magnitude and phase and cost function in terms of real and imaginary part.*

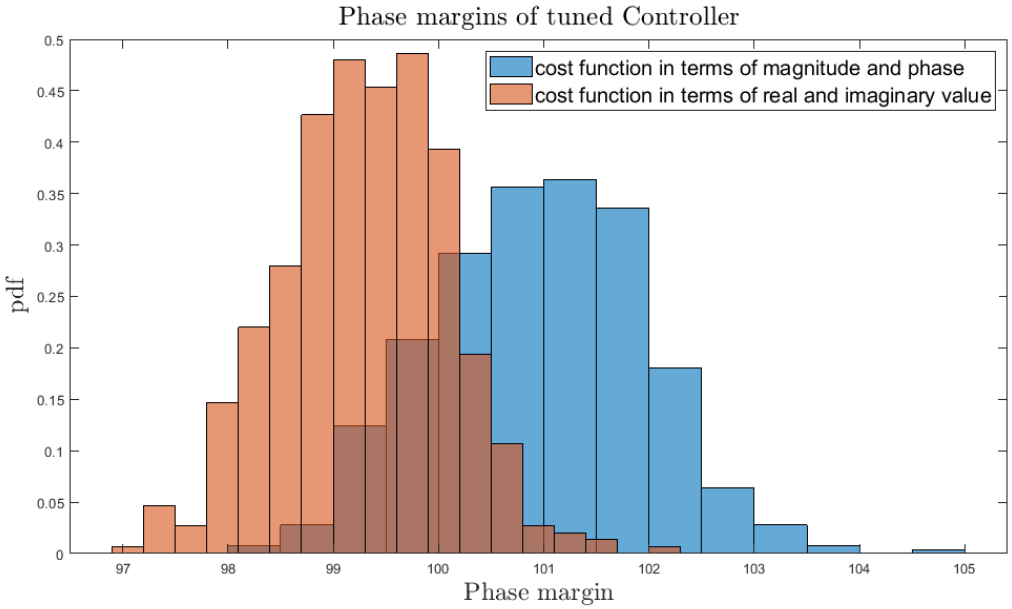

Figure 3.25: *Phase margin for SNR=10, comparison of cost function in terms of magnitude and phase and cost function in terms of real and imaginary part.*

adequate value as revealed in Figure 3.28. Since both methods, at least for the considered example, give similar results the formulation of the cost function in Equation (3.103) *is further investigated in the following, because interpretations are more straight forward in terms of a bode diagram rather than real and imaginary part of a transfer function. In order to improve the tuning result, in the case of not sufficiently large signal-to-noise ratio, more repetitions of the maneuver can be used in conjunction with an averaged ETFE for estimation of the initial closed-loop response as discussed in Section 2.2.5. As Figure 3.29 shows, the results for a SNR of* 3 *are improved significantly for* $R = 10$ *repetitions, compared to* $R = 1$.

Example 3.5. ***Evaluation of Controller Parameter Retuning - Monte Carlo Simulations for Uncertain Plant Parameters***

In this example Monte Carlo simulations are performed with varying uncertainties. The respective tuning results are revealed. The settings are the same as in Example 3.4, except if otherwise stated. A SNR of 10 was considered for all simulations. The maneuver was repeated twice, but only the second sequence was used in the DFT, to allow transients to die out, i.e. $R = 1$. *The cost function given in Equation* (3.103) *was used in the optimization. Uncertainties were only considered in the moment dynamics. The parameters* M_q *and* M_η *were varied with a normal distribution with a variance of 25% on the nominal values, given in Table 3.2. Due to the structure of the controller, i.e. a pure pitch rate feedback, mainly the damping of the system and variations in the control effectiveness can be adapted by the tuning. The damping is mainly influenced by the parameter* M_q *and the control effectiveness by* M_η. *The parameter* M_α, *influences mainly the eigenfrequency of the system and was varied with a normal distribution with variance of only 3%. Of course*

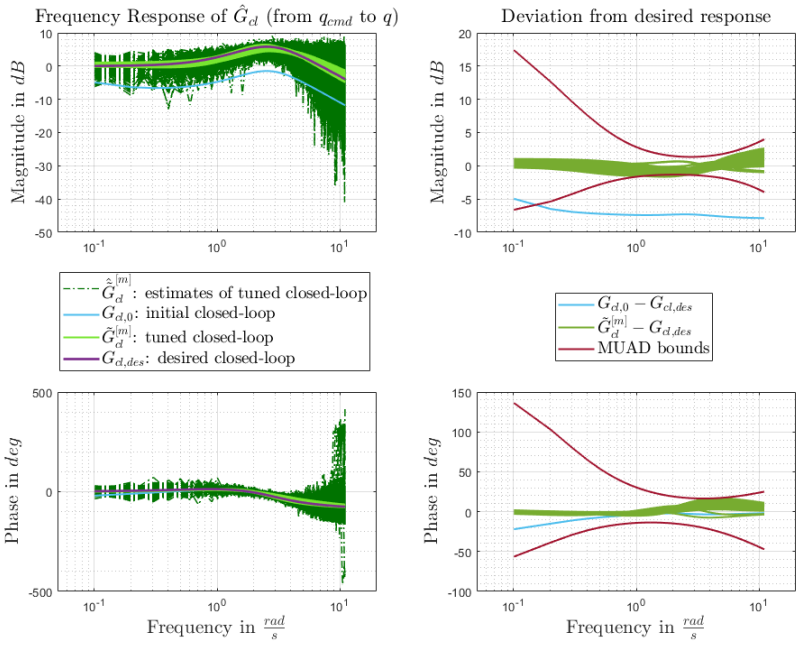

Figure 3.26: *Tuning result for magnitude and phase formulation of cost function for SNR=3.*

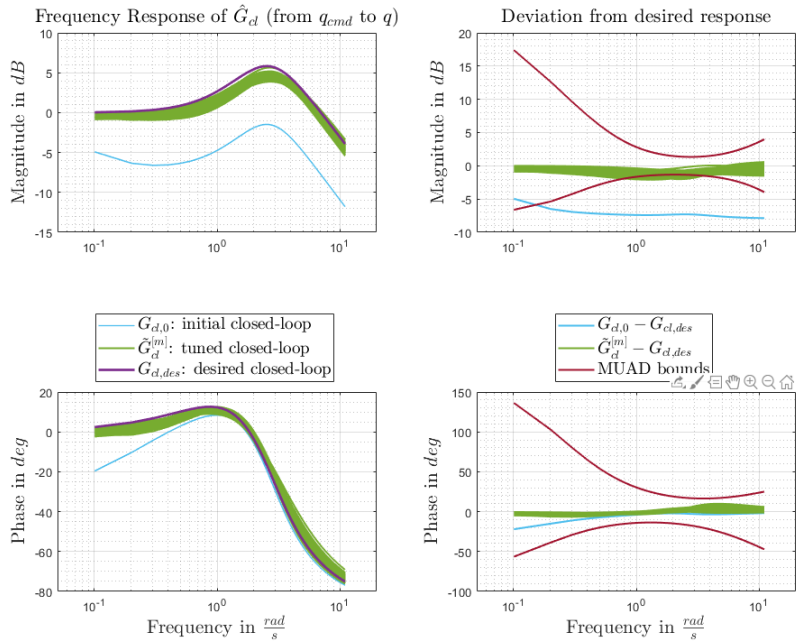

Figure 3.27: *Tuning result for real and imaginary part formulation of cost function for SNR=3.*

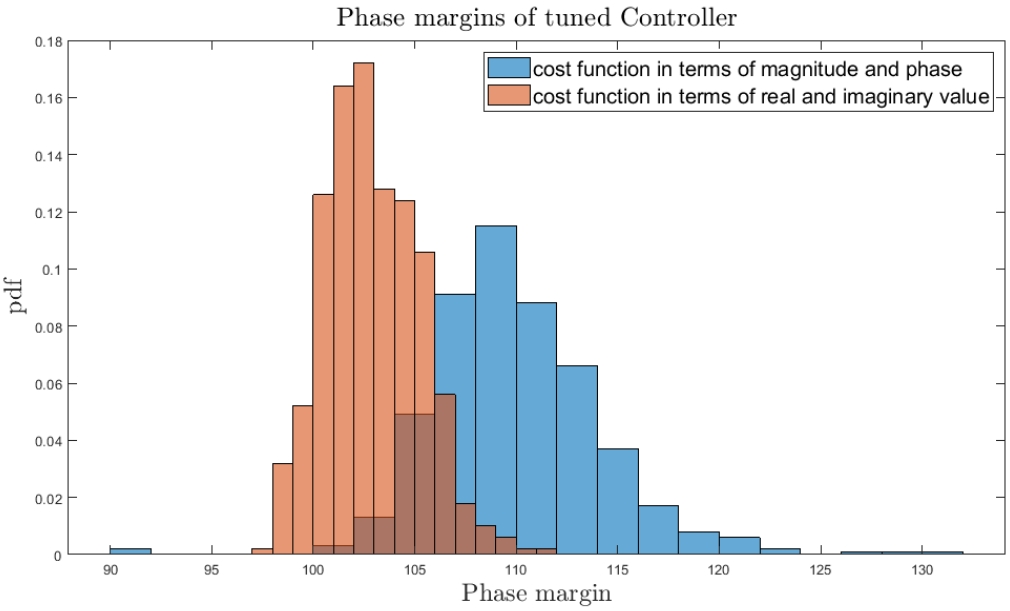

Figure 3.28: *Phase margin for SNR=3, comparison of cost function in terms of magnitude and phase and cost function in terms of real and imaginary part.*

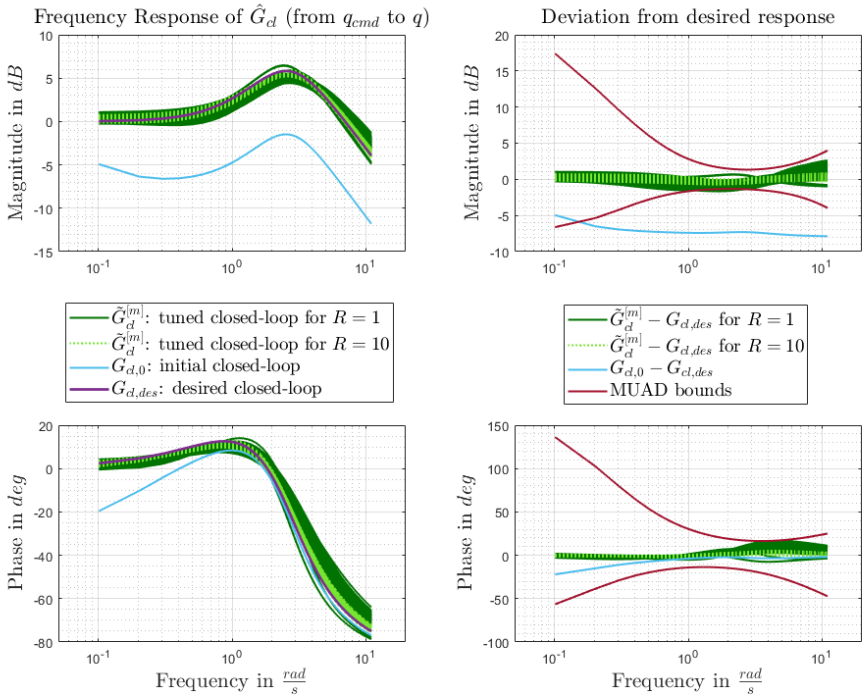

Figure 3.29: *Influence of number of repetitions of maneuver on tuning result for magnitude and phase formulation of cost function for SNR=3.*

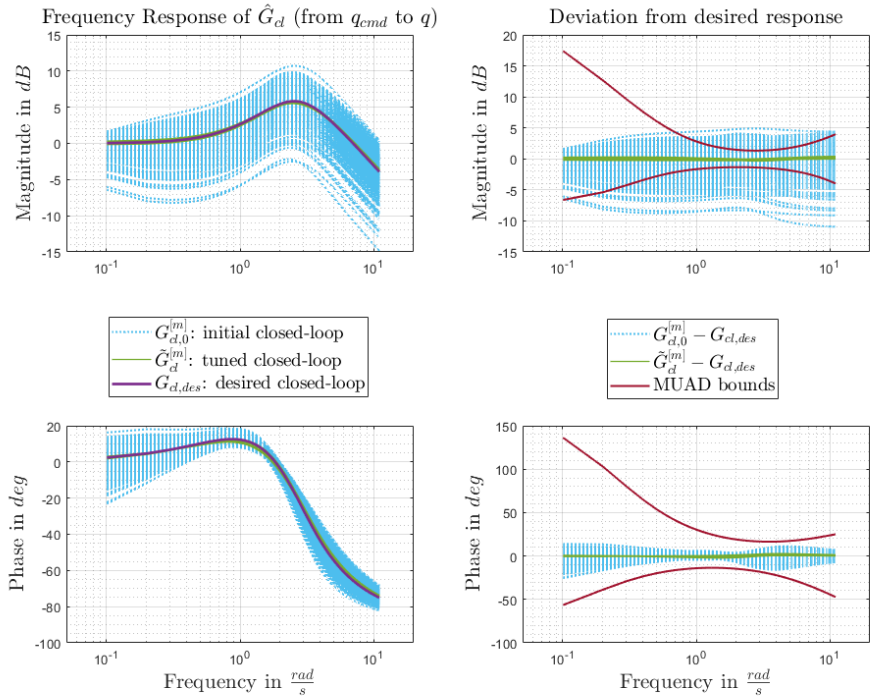

Figure 3.30: *Tuning results for Monte Carlo simulations with varying plant parameters.*

the controller tuning for a fixed controller structure is restricted, in how close the tuned response can approach the desired response depending on the uncertainties and required gain and phase margins. Figure 3.30 shows the tuning results for $M = 500$ *simulations, where one outlier was removed resulting from an unfeasible* M_η*. It can be seen that significant improvement can be achieved by the proposed retuning of the controller parameters. It is revealed that in contrast to the untuned response, the error between the desired frequency response and the tuned frequency response, is always within the MUAD bounds, described in Section 3.9, which can serve for piloted flight control laws as an evaluation criterion.*

The resulting margins were checked for satisfying their adequate values, which was always the case.

Example 3.6. ***Evaluation of Controller Parameter Retuning - Monte Carlo Simulations for Varying Initial Controller Parameters***

In this example Monte Carlo simulations are performed with varying initial controller parameters. The respective tuning results are revealed. The settings are the same as in Example 3.4, except if otherwise stated. A SNR of 10 was considered for all simulations. The maneuver was repeated twice, but only the second sequence was used in the DFT, to allow transients to die out, i.e. $R = 1$*. The cost function given in Equation* (3.103) *was used in the optimization. The considered uncertainties correspond to an* 11% *increase in*

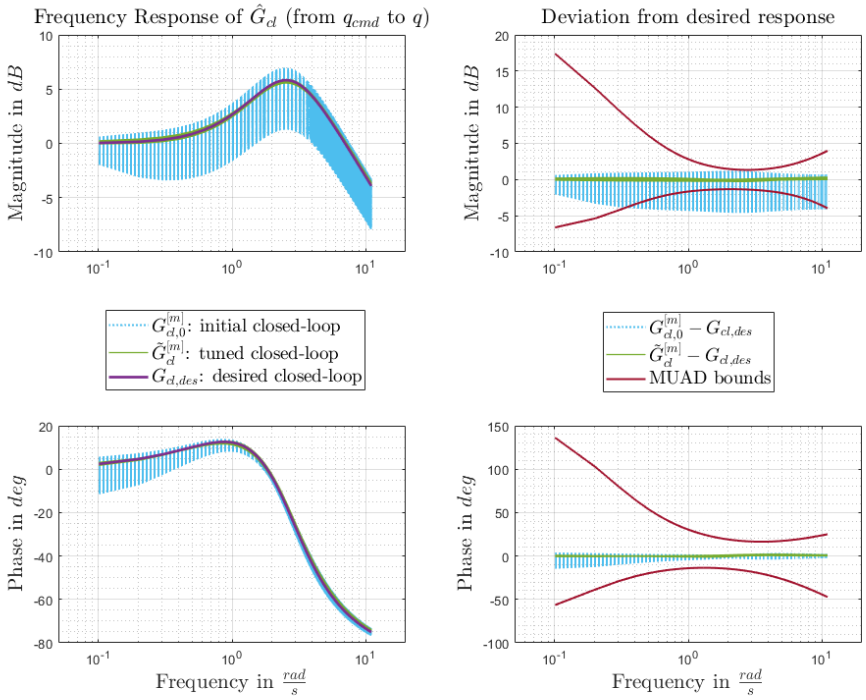

Figure 3.31: *Tuning results for varying initial controller parameters.*

M_q and a 15% decrease in M_η, compared to the nominal plant model parameters given in Table 3.2. The initial controller parameters, were uniformly varied with a spread of 25% around their nominal value given in Table 3.3. $M = 500$ simulations were performed.

Figure 3.31 shows the tuning results. It can be seen that significant improvement can be achieved by the proposed retuning of the controller parameters. It is revealed that in contrast to the untuned response, the error between the desired frequency response and the tuned frequency response, is always within the MUAD bounds, described in Section 3.9, which can serve for piloted flight control laws as an evaluation criterion. Figure 3.32 and 3.33 show the histograms of the tuned controller parameters. The margins were checked for fulfilment of the adequate values.

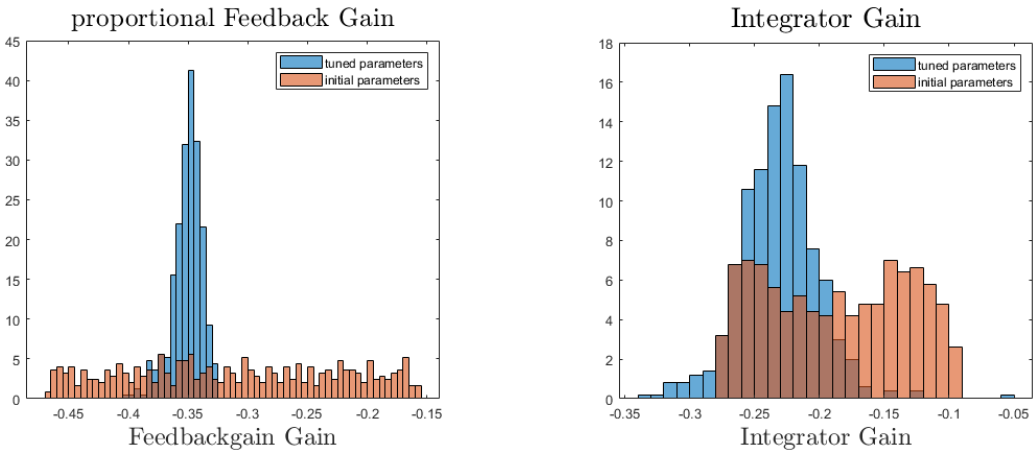

Figure 3.32: *Proportional feedback and integral controller parameters.*

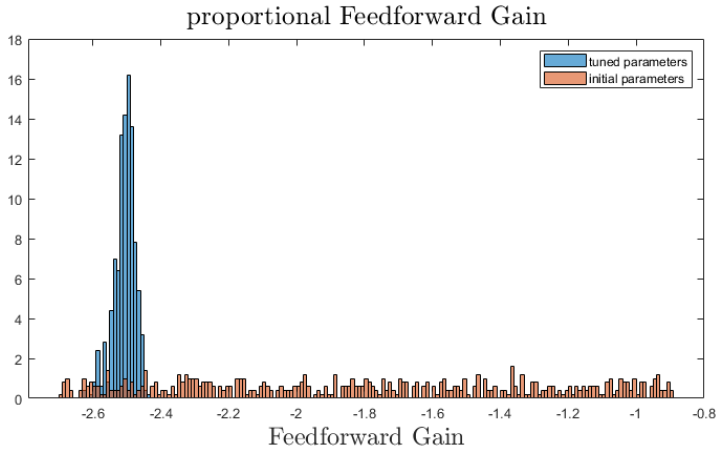

Figure 3.33: *Proportional feedforward controller parameters.*

3.9 Evaluation Criteria

Often the performance requirements imposed on a controller can be translated into a desired closed-loop behavior in the frequency domain.
For example, for a baseline flight controller, that is part of a cascaded autopilot system, requirements are specified in the AS94900, [SAE07], which is the SAE standard for flight control system design. These requirements define for example limits on the bandwidth, overshoot and stability margins. In case that the inner-loop is controlled by a human pilot, requirements are for example specified by the handbook of flying qualities of piloted aircraft, [US 97].
In both cases the requirements can be translated into a desired closed-loop behavior of the inner-loop in the frequency domain and specific bounds in some frequency regions. For example a model-based control design that ensures that all requirements are satisfied by the nominal closed-loop, could provide a desired behavior. But the desired inner-loop behavior could be also influenced by outer control loops like an autopilot for example. The outer-loop, being it an autopilot or a human, also needs to satisfy several requirements. These could be translated into a desired closed-loop behavior of the inner-loop and specific bounds in some frequency regions, such that it is ensured that the outer-loop satisfies its requirements if the actual inner-loop response stays within these boundaries. These boundaries can be used as an evaluation criterion to assess whether the tuned closed-loop frequency response is "close enough" to the desired behavior, or as constraints in the optimization problem.
In case of a human pilot, these bounds are the MUAD (Maximum Unnoticeable Added Dynamics) bounds, from the handbook of flying qualities of piloted aircraft, [US 97]. The MUAD bounds can be interpreted as the boundaries of the Maximum Unnoticeable Added Dynamics between two systems from the pilots point of view. If the difference between two systems remains within these bounds the pilot will not be able to distinguish between the dynamics of either system, i.e. the pilot will give it the same rating. The MUAD bounds originate from a NT-33 landing approach simulation tackling the question of mismatch, [Moo85]. In a simulator test campaign, pilots performed the same maneuvers on high-order systems and their low-order equivalents. By examining pilot rating differences between these systems, frequency response envelopes were derived, which are an approximate measure of maximum unnoticeable added dynamics. The original idea of the MUAD bounds is hence the definition of mismatch envelopes to assess the quality or fidelity of low order equivalent systems obtained by system identification methods compared to the corresponding high order systems, e.g. frequency responses obtained within flight test [RT06, p. 190]. The mismatch is defined in terms of magnitude and phase in the frequency domain as

$$\begin{aligned} \Delta_{|G|} &= |G_{HOS}| - |G_{LOES}| \\ \Delta_{\angle G} &= \angle G_{HOS} - \angle G_{LOES} \end{aligned} \tag{3.108}$$

Envelope	**Laplace function**
Upper Gain Envelope	$G_{UGE}(s) = \frac{3.16s^2+31.61s+22.79}{s^2+27.14s+1.84}$
Lower Gain Envelope	$G_{LGE}(s) = \frac{0.095s^2+9.92s+2.15}{s^2+11.6s+4.95}$
Upper Phase Envelope	$G_{UPE}(s) = \frac{68.89s^2+1100.12s+275.22}{s^2+39.94s+9.99}e^{0.006s}$
Lower Phase Envelope	$G_{LPE}(s) = \frac{475.32s^2+184100.12s-29460}{s^2+11.66s+0.039}e^{-0.0072s}$

Table 3.8: *MUAD bounds. [US 97]*

where $|G|$ is the magnitude in dB and $\angle G$ is the phase in radians. The indices HOS and $LOES$ denote the **h**igh **o**rder **s**ystem and **l**ow **o**rder **e**quivalent **s**ystem, respectively. $\Delta_{|G|}$ and $\Delta_{\angle G}$ are calculated at discrete frequencies and shall lie within the envelopes defined by the MUAD bounds. These envelopes are defined as functions of the Laplace variable s and given in Table 3.8. In the context of the proposed test-based controller parameter retuning for a baseline flight controller, the idea is to use the MUAD bounds to asses the mismatch between the desired and tuned closed-loop frequency response, i.e

$$\begin{aligned} |G_{LGE}| \leq (|\tilde{G}_{cl}| - |G_{cl,des}|) \leq |G_{UGE}| \\ \angle G_{LPE} \leq (\angle \tilde{G}_{cl} - \angle G_{cl,des}) \leq \angle G_{UPE} \end{aligned} \tag{3.109}$$

In case of the autopilot, the designer could give similar bounds that ensure, for some assumptions on the order and structure of the inner-loop closed-loop system, that all requirements for the autopilot will be satisfied, if the inner-loop response stays within these boundaries.

3.10 Outlook on Further Applications and Adaptations

The retuning procedure presented in the previous sections for SISO closed-loop systems is to be understood as the core concept. As will be shown in Chapter 4, by the two addressed applications, it can be adapted for retuning of SIMO and MIMO closed-loop systems.

Via the constraints in the optimization problem further objectives, besides the anticipated margins, can be addressed. For example if a higher level of safety is desired, it can be additionally incorporated into the constraints that the margins with the new controller parameters shall be also satisfied on the nominal plant model that was used for the initial controller design. Since showing that the initial controller parameters satisfy the adequate margins based on the model gives enough confidence to test them in flight, showing that the new parameters still satisfy the margins on the model eases their clearance. Of course such a design might lead to a resulting tuned closed-loop frequency response that is not as close to the desired response as it could otherwise be, due to the additional restriction. Meaning that the resulting controller parameters are more conservative.

Usually controller parameters for high performance aircraft are scheduled over indicated airspeed. In case of a failure of the airdata system, a low bandwidth emergency controller with a fixed- gain set takes over. Another application of the retuning concept could be to derive a fixed- gain set for varying plant dynamics due to varying operational conditions, based on flight test at different indicated airspeeds for example.

Another scenario, where the retuning concept could be applied and adapted to is for example to robustify initial controller parameters against variations in the plant dynamics due to different load cases for example, by performing flight tests at the same operational envelope point for the different load cases.

In both scenarios the optimization problem can be adapted similarly. Let $\hat{\tilde{G}}_{cl,i}(j\omega_k, \boldsymbol{p})$ describe the anticipated closed-loop frequency response, obtained as described in Section 3.6, based on an experiment i. These experiments could be for example

- at different velocities V_i
- at different load cases, but at the same envelope point
- or just repeated experiments under same conditions

Then the optimization problem in Section 3.8 can be adapted to

$$J(\boldsymbol{p}) = \sum_{i=1}^{n_E} J_i(\boldsymbol{p}) + (\boldsymbol{p} - \boldsymbol{p}_0)\, \boldsymbol{Q} (\boldsymbol{p} - \boldsymbol{p}_0)^T \tag{3.110}$$

where n_E is the number of experiments and where

$$J_i(\boldsymbol{p}) = \frac{20}{n_\omega}\sum_{k=1}^{n_\omega}(\mathrm{w}_{\gamma,i}(\omega_k)\left[\mathrm{w}_A\Delta_{|G_{cl,i}|}(j\omega_k,\boldsymbol{p}) + \mathrm{w}_\phi\Delta_{\angle G_{cl,i}}(j\omega_k,\boldsymbol{p})\right]) \tag{3.111}$$

with

$$\begin{aligned}\Delta_{|G_{cl,i}|}(j\omega_k,\boldsymbol{p}) &= (\left|\hat{\tilde{G}}_{cl,i}(j\omega_k,\boldsymbol{p})\right| - \left|G_{cl,des,i}(j\omega_k)\right|)^2\\ \Delta_{\angle G_{cl,i}}(j\omega_k,\boldsymbol{p}) &= (\angle\hat{\tilde{G}}_{cl,i}(j\omega_k,\boldsymbol{p}) - \angle G_{cl,des,i}(j\omega_k))^2\end{aligned} \tag{3.112}$$

The desired closed-loop frequency responses $\hat{\tilde{G}}_{cl,des,i}(j\omega_k)$, can be either chosen to be the same for all i (for example for different load cases or repeated experiments under same conditions), or to vary with i (for example for experiments at different airspeeds, where for a fixed-gain controller the desired dynamics will vary with airspeed). The optimization problem is given by:

$$\begin{aligned}&\min_{\boldsymbol{p}}.\ J(\boldsymbol{p})\\ &st.\\ &c_{1,i}(\boldsymbol{p}) = A_m - \hat{A}_{m,i}(\boldsymbol{p}) \le 0\\ &c_{2,i}(\boldsymbol{p}) = \Phi_m - \hat{\Phi}_{m,i}(\boldsymbol{p}) \le 0\\ &\text{for } i = 1\ldots n_E\end{aligned} \tag{3.113}$$

where $\hat{A}_{m,i}(\boldsymbol{p})$ and $\hat{\Phi}_{m,i}(\boldsymbol{p})$ are the anticipated margins for the new parameter set $\boldsymbol{p}$, based on the experiment data i, as described in Section 3.7.

Example 3.7. ***Evaluation of Controller Parameter Retuning - For a fixed Gain Controller based on Experiments at different Indicated Airspeeds*** *We consider the example system described in Section 3.2. Assume that the desired closed-loop dynamics, $\hat{\tilde{G}}_{cl,des,i}(j\omega_k)$, are given at low velocity, medium velocity and high velocity. Here, these desired dynamics are obtained as the nominal closed-loop dynamics, Equation* (3.4)*, based on the nominal linear plant models at the respective envelope points, and an initial fixed-gain controller with structure described in Section 3.2 and initial gains given in Table 3.3. The considered uncertainties correspond to a* 30% *decrease in M_q, an* 10% *increase in M_η and a* 2% *decrease in M_α, compared to the nominal plant parameters at the respective envelope points. The experiment was simulated on the closed-loop systems, composed of the true plant dynamics and initial controller at the respective velocities, with a signal-to-noise ratio of $SNR = 10$. The maneuver was repeated twice, but only the second sequence was used in the DFT, to allow transients to die out, i.e. $R = 1$. $N = 6250$ samples were used in the DFT. The cost function given in Equation* (3.110) *to* (3.113) *was used in the optimization, with parameters $\boldsymbol{Q}$, w_A, w_Φ, A_m and Φ_m, chosen as described in Example 3.4. The frequency dependent weights $w_{\gamma,i}(\omega_k)$ were chosen to be*

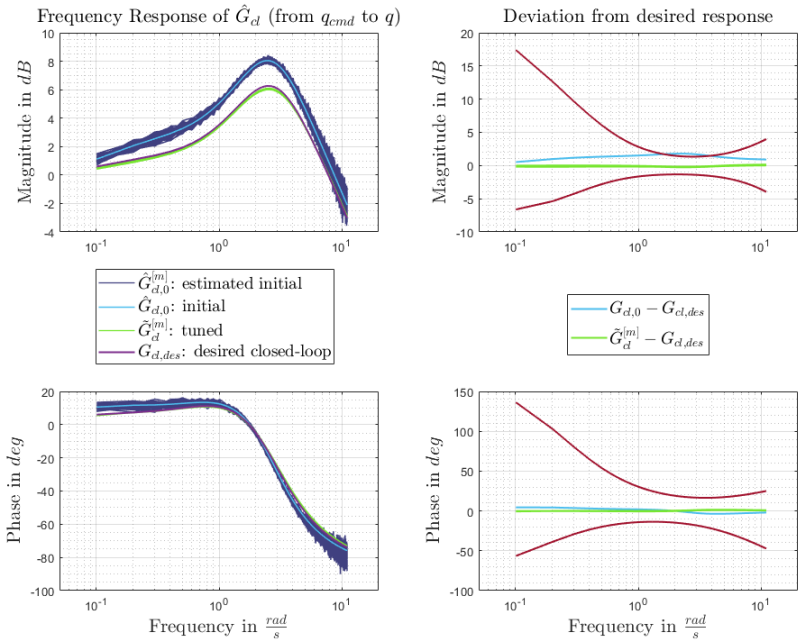

Figure 3.34: *Tuning result for high velocity.*

equal for each velocity i and are given in Table 3.7. Figure 3.34 to 3.36 show the tuning results for $M = 100$ simulations. We see that with the tuned fixed gain set, the closed-loop dynamics at all three velocities, $\tilde{G}_{cl,i}^{[m]}$, depicted in green, are closer to the respective desired dynamics than the initial untuned closed-loop responses, depicted in light blue.

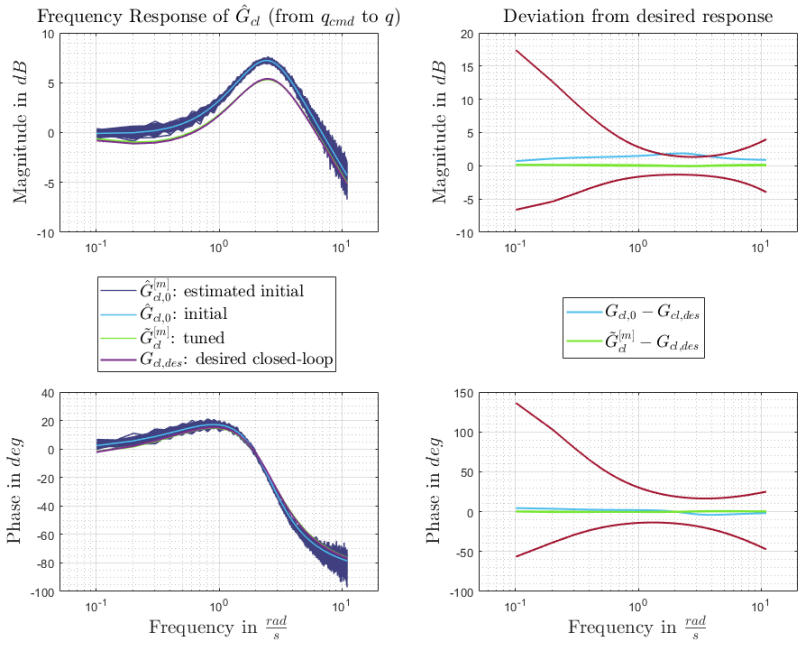

Figure 3.35: *Tuning result for medium velocity.*

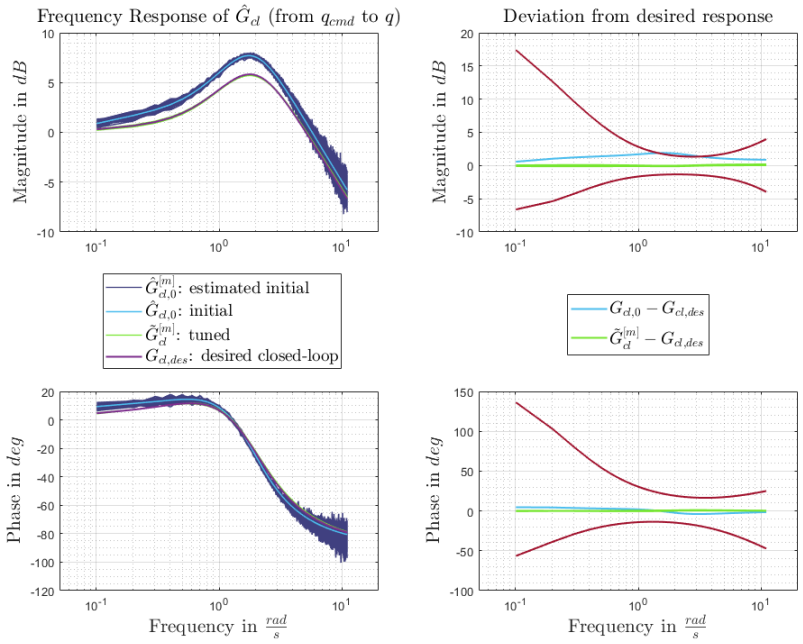

Figure 3.36: *Tuning result for low velocity.*

Chapter 4

Application

The test-based controller retuning concept is applied to an inner-loop controller of a modular, cascaded flight guidance and control system for optionally piloted general aviation (CS-23) aircraft and unmanned systems, that was developed at the institute of Flight System Dynamics at TUM (C5). The modular flight control system (FCS) was successfully tested in several flight test campaigns, [KSB+16], [SSK+16], [SPS+16b], for different platforms:

- DA42 M-NG flying test bed
- Dornier Do228 D-CODE
- Grob G-520T medium/high altitude long endurance (HALE/MALE) manned reconnaissance aircraft
- a very-light all-electric OPV demonstrator platform ELIAS.

The inner-loop controller was designed and assessed based on models for all platforms. The controller is divided into a longitudinal and lateral control law. The longitudinal inner-loop is a single-input-multiple output (SIMO) control law. The lateral control law is a multiple-input-multiple-output (MIMO) control law. As the most inner part of the flight control system the inner-loop controller performance relies on the discrepancy between the true aircraft dynamics and the model used during its gain design. These differences might result in a closed-loop response with the true aircraft that does not correspond to the desired behavior. Since the outer-loop control laws use the nominal inner-loop closed-loop dynamics for their design, it is desired that the true inner-loop closed-loop dynamics are as close as possible to the nominal inner-loop dynamics. This can be achieved with the proposed test-based gain retuning procedure. In this chapter the test-based gain retuning concept will be demonstrated for both, the lateral and the longitudinal inner-loop control laws to show its applicability to different controller structures. Since the considered controllers are a part of a complex flight control system, which is applied and tested on real aircraft, the demonstration of the concept for this application shows its capabilities in an

real application and not only on an academic simplified controller structure. Furthermore, the test-based retuning procedure was tested in simulation for all four platforms (Da42, Do228, G-520T, ELIAS), demonstrating its applicability also to different systems. The very-light all-electric OPV demonstrator platform ELIAS, however, showed in simulation a larger drift tendency away from the trim condition than the other platforms. Therefore, the number of maneuver repetitions had to be reduced, making the retuning more sensitive against the signal-to-noise ratio, compared to the other investigated aircraft. For the other platforms, similar simulation results were obtained, demonstrating that the proposed procedure is feasible. In the following, simulation results will be presented for the Do228 and flight test results for the G520.

First Section 4.1 briefly presents the demonstration platforms for which the FCS was developed and demonstrated on. Section 4.2 briefly introduces the Controller environment, i.e the FCS and the simulation framework in Section 4.3. Section 4.4 and 4.5 focus on the longitudinal and lateral inner-loop, respectively. Each of the both sections presents the controller structure, the test-based retuning concept and simulation and flight test results.

4.1 Demonstration Platforms

4.1.1 DA42 M-NG Flying Testbed

The Institute of Flight System Dynamics at Technical University of Munich (TUM-FSD) owns the research aircraft OE-FSD, depicted in Figure 4.1. This flying test-bed is a modified Diamond Aircraft Industries DA42 NG aircraft. It has been adapted with a fly-by-wire system that is mechanically connected to the existing flight control system via electrical and overload clutches, such that the platform can serve as an Optionally Piloted Vehicle (OPV). A safety system, enables the pilot to disable the automatic flight control system by either opening the clutches if a sufficiently large stick force is applied or by pushing a disengage button. The test-bed allows TUM-FSD to test modern flight control and flight management algorithms.

4.1.2 Dornier Do228 D-CODE

The Dornier Do228-101 D-CODE, shown in Figure 4.2, is an airborne research platform used by the German Aerospace Center (DLR). The Dornier Do228 D-CODE is a twin-engined turboprop CS-23 aircraft with 5.98t maximum take off weight (MTOW). In co-operation between TUM-FSD, RUAG, Aircraft Electronics Engineering, and Wittenstein A & S, a digital Automatic Flight Control System (AFCS) based on a modular avionics platform was developed, including electromechanical actuators and actuator control electronics, a flight control computer, data buses, data concentrator units etc.. Besides a system concept, architecture and safety concept, functional algorithms for an experi-

Figure 4.1: *DA42 M-NG flying testbed. [KH18]*

Figure 4.2: *Dornier Do228-101 D-CODE. [Kra20]*

mental autopilot were developed together with a generic mode control and monitoring Human Machine Interface (HMI). The developed safety concept ensures a safe transition between an active and passive autopilot system. The system integration was performed under Supplemental Type Certificates (STC) and the operation of the autopilot under a permit to fly. The experimental autopilot was developed by TUM-FSD as a part of the institute's modular flight guidance and control system.

4.1.3 Grob G-520T

The Grob G-520T, depicted in Figure 4.3, is a medium/high altitude long endurance (HALE/MALE) manned reconnaissance aircraft with short runway capabilities, a reconfigurable payload installation and a full approval for all-weather operations. The G-520T is a CS-23 single engine turboprop aircraft with a wingspan of 33 m, a maximum take-off weight (MTOW) of 4700 kg and a maximum altitude of 50000 ft. The aircraft was mod-

Figure 4.3: *Grob G-520T. © H3 Mission Systems*

ified within several research projects in cooperation with Silver Atena and Grob Aircraft to an OPV platform. The modifications include electromechanical actuators and actuator control electronics with safety clutches for the ailerons, elevator and rudder, a flight control computer, data buses, data concentrator units, a safety relay box, sensors for air and inertial reference data, etc.. TUM-FSD contributed with the development of a fail-passive system architecture, the development of a mode control and monitoring display and the development of functional algorithms for a full envelope mission autopilot as a part of the institute's modular flight guidance and control system.

4.1.4 Very-light all-electric OPV Demonstrator Platform ELIAS

ELIAS is based on the ultralight aircraft PC-Aero Electra-One. It was modified to a very-light, electrically- powered OPV demonstrator platform and is depicted in Figure 4.4. The adaptations include electromechanical, dual complex actuators with safety clutches for all surfaces, split ailerons, an electrical duplex engine with a fixed pitch / constant speed propeller and an electrically retractable landing gear. With an MTOW of 320 kg and a wing span of 11 m, the range is around 150 km. It was developed in cooperation with Acentiss, IABG, TUM-FSD, Silver Atena and others. TUM-FSD contributed in several projects with automatic flight control functions, trajectory control and automatic take-off and landing, which are parts of the institute's modular flight guidance and control system.

Figure 4.4: *Very-light all-electric OPV demonstrator platform ELIAS. [Kra20]*

4.2 Inner-loop Environment - Flight Control System

The addressed inner-loop controller was developed as a part of a modular cascaded flight guidance and control system for optionally piloted general aviation (CS-23) aircraft and unmanned systems. The developed flight control system is depicted in Figure 4.5. It is capable of full automatic flight from take off to landing and provides the full range of typical and beyond state-of-the art automated flight control functionalities as

- an automated waypoint navigation and flying, voice commanded flight management and a trajectory generation system [SPS+16a], [Sch18b]
- an automatic trajectory controller [Sch18a], [SSK+16]
- a flight path controller, including an automatic thrust controller and autopilot functions such as attitude control, speed control and flightpath control, [KSB+18], [KSB+16], [KGSH16], [KBD+18]
- automatic take off [ZMW+17] and landing [MH17], [KMH+19]
- ground control for centerline tracking [MZS+17]
- a central system automation module which handles the operating modes and activates applicable flight control loops [KH18], [Kra20]
- a inner-loop baseline controller [DBAG+16], [SGGH18], [GGS20], [GSG18]
- a maneuver injection tool [KGH18]

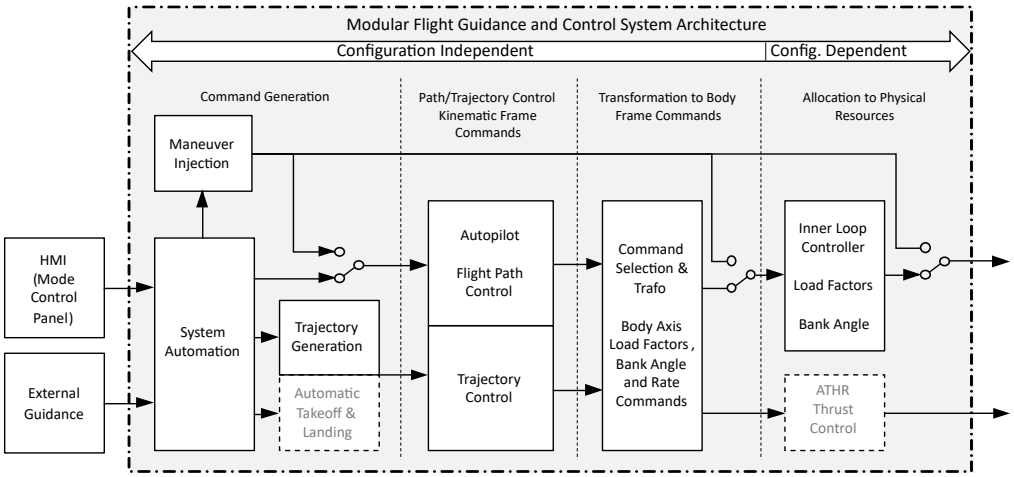

Figure 4.5: *Modular flight guidance and control system architecture, adapted for G-520T. [SSG+]*

The system includes and accounts for most of the real-world requirements and was already successfully parametrized, tested and applied in flight test experiments for the (CS-23) platforms, introduced in Section 4.1. The modularity and configurability of the developed generic architecture provides an easy adjustment and adaptation to new aircraft configurations and projects depending on their needs. For example in the G-520T project, as indicated in Figure 4.5, the automatic take-off and landing module was deactivated, since this component was not part of the project. Also, the thrust control functionality was disengaged, because the required auto thrust actuation system has not yet been installed.

4.3 Simulation Environment and Tool Chain

The simulations were performed using a high fidelity 6 degrees of freedom (DoF) nonlinear simulation model of the Do228 as example platform. The used modular model-in-the-Loop Simulation framework is presented in detail in [ZSMH18] for the DA42. It includes as core components the flight control computer model, actuation models, a flight dynamics model, a Dryden Turbulence model compliant to the disturbance model accepted and published by EASA in CS – AWO and sensor models. Additionally, structural modes are included, modelled as low damped second order transfer functions, to represent the effects on rate and specific force measurements. The simulation framework was set up in a modular and generic way to allow adaptation to the different aircraft configurations such that it could be used for simulation and assessment of all platforms introduced in Section 4.1. Additionally, a tool chain was build up that allows trimming and linearization, as well as verification and analysis of the linear models. These linear models were used in the initial model-based controller synthesis and analysis. The developed tool chain allows the baseline controller design and assessment to be easily adjusted and adapted to new aircraft configurations.

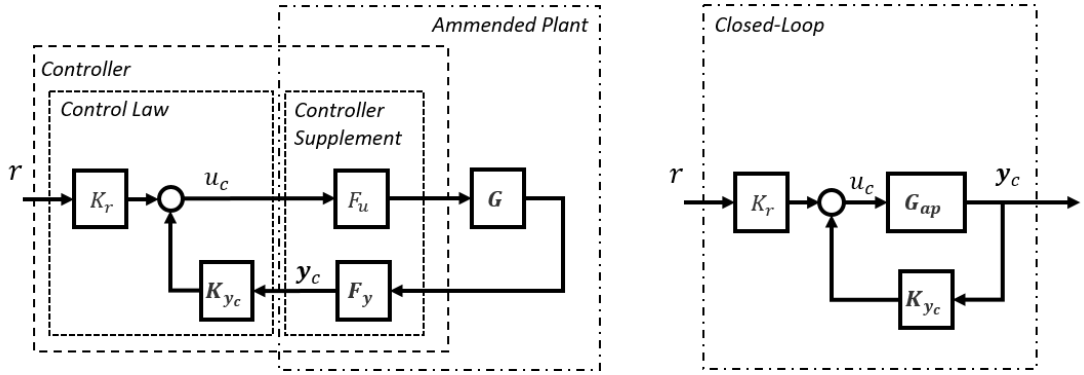

Figure 4.6: *Longitudinal inner-loop controller structure. [SSG+]*

4.4 Longitudinal Inner-loop

The following section describes the longitudinal inner-loop controller, which controls the aircraft's longitudinal motion. In Section 4.4.1 the control law is presented and in Section 4.4.2 several closed-loop and open-loop relations are presented, that are used in the test based gain retuning to estimate the margins, the amended plant and the anticipated closed-loop. Note, that main parts of Section 4.4 are extracted from my publications [GHSM21] and [SSG+]. Only minor changes have been made to parts of the notation to adapt to this thesis and additional explanations or intermediate steps have been included where necessary.

4.4.1 Control law and Controller Structure

The controller structure of the longitudinal inner-loop is depicted in Figure 4.6. It is described in detail in [GHSM21]. It is composed of the control law and another component denoted as controller supplement, which consists of structural filters and roll off filters, turn compensation and a mapping from the control law output to actuator commands, which is scheduled over indicated airspeed. The linear control law can be expressed by continuous linear time-invariant (LTI) models in Laplace domain by, [GHSM21],

$$u_c(s) = \begin{bmatrix} K_r(s, \boldsymbol{p}) & \boldsymbol{K}_{y_c}(s, \boldsymbol{p}) \end{bmatrix} \begin{bmatrix} r(s) \\ \boldsymbol{y}_c(s) \end{bmatrix} \tag{4.1}$$

where $r(s)$, $\boldsymbol{y}_c(s)$, $u_c(s)$ denote the Laplace-transforms of the following time-dependent signals:

- $r(s)$: is the reference input $r(t) = \Delta f_{z,B,cmd}(t)/g$. It is the normal specific force command, normalized with respect to the gravitational acceleration g in the z-axis direction of the body fixed frame. The delta refers to increments with respect to the turn compensation value $\frac{\cos\Theta}{\cos\Phi}$

- $\boldsymbol{y}_c(s)$: is a vector with the feedback signals used within the control law, i.e. $\boldsymbol{y}_c(t) = \begin{pmatrix} \Delta f_{z,B}(t)/g & \Delta q(t) \end{pmatrix}^T$. It is an output of the controller supplement subsystem, with the processed specific force measurement $\Delta f_{z,B}(t)/g$ and pitch rate $\Delta q(t)$, where the delta refers to increments with respect to the turn value $q_{turn} = \dot{\Psi} \sin \Phi \cos \Theta$ with $\dot{\Psi} = g/V \tan \Phi$.

- $u_c(s)$: is the output of the control law and corresponds to a pitch rate acceleration command, $u_c(t) = \dot{q}_{\mathrm{cmd}}(t)$.

The plant input is the desired elevator drivetrain command $\eta_{dt,cmd}$, which is mapped within the controller supplement component F_u from the pitch rate acceleration command provided by the control law.

The control law corresponds to a classical linear PI-type controller with integral action on the tracking error in normal specific force, feedback of normal specific force and pitch rate and a feed forward of the specific force command, providing an additional degree of freedom. The transfer function $K_r(s, \boldsymbol{p})$ in Equation (4.1) describes the behavior from the reference input to the control law output and is given by [GHSM21]

$$K_r(s, \boldsymbol{p}) = p_1 + p_2/s. \tag{4.2}$$

The Transfer function matrix (TFM) $\boldsymbol{K}_{y_c}(s, \boldsymbol{p})$ defines the response from feedback signals to the control law output. It is given by [GHSM21]

$$\boldsymbol{K}_{y_c}(s, \boldsymbol{p}) = \begin{pmatrix} p_3 - p_2/s & p_4 \end{pmatrix}. \tag{4.3}$$

The 4- dimensional parameter vector $\boldsymbol{p}$ comprises the feed-forward gain p_1, the integrator gain p_2 and the feedback gains p_3 and p_4.

$$\boldsymbol{p} = [p_1, p_2, p_3, p_4] \tag{4.4}$$

In the following sections, the dependence of Laplace operator s and time t is omitted, whenever the context is clear.

4.4.2 Closed-loop and Open-loop Relations

The Transfer function matrix (TFM) from the control law output u_c to the feedback signals $\boldsymbol{y}_c$ in open-loop is denoted as the amended plant with representation in the Laplace domain, given by

$$\boldsymbol{y}_c(s) = \boldsymbol{G}_{\mathrm{ap}}(s) u_c(s). \tag{4.5}$$

where

$$\boldsymbol{G}_{\mathrm{ap}}(s) = \boldsymbol{F}_y(s)\, \boldsymbol{G}(s)\, F_u(s) \tag{4.6}$$

The closed-loop LTI system is represented by the **closed-loop TFM** $\boldsymbol{G}_{\mathrm{cl}}(s,\boldsymbol{p})$ from the reference input r to the feedback signal vector $\boldsymbol{y}_c$

$$\boldsymbol{y}_c(s) = \boldsymbol{G}_{\mathrm{cl}}(s,\boldsymbol{p})r(s) \tag{4.7}$$

where $\boldsymbol{G}_{\mathrm{cl}}(s,\boldsymbol{p})$ is given by

$$\boldsymbol{G}_{\mathrm{cl}}(s,\boldsymbol{p}) = \Big[\boldsymbol{I} - \boldsymbol{G}_{\mathrm{ap}}(s)\,\boldsymbol{K}_{y_c}(s,\boldsymbol{p})\Big]^{-1}\boldsymbol{G}_{\mathrm{ap}}(s)\,K_r(s,\boldsymbol{p}) \tag{4.8}$$

This relation can be deduced from the block diagram in Fig. 4.6, [GHSM21], as follows. First, the control law u_c given by (4.1) in (4.5) results in

$$\boldsymbol{y}_c(s) = \boldsymbol{G}_{\mathrm{ap}}(s)\Big(K_r(s,\boldsymbol{p})r(s) + \boldsymbol{K}_{y_c}(s,\boldsymbol{p})\boldsymbol{y}_c(s)\Big) \tag{4.9}$$

By solving Equation (4.9) for $\boldsymbol{y}_c$ finally the relation in (4.8) and (4.7) is obtained:

$$\boldsymbol{y}_c(s) = \Big[\boldsymbol{I} - \boldsymbol{G}_{\mathrm{ap}}(s)\,\boldsymbol{K}_{y_c}(s,\boldsymbol{p})\Big]^{-1}\boldsymbol{G}_{\mathrm{ap}}(s)\,K_r(s,\boldsymbol{p})r(s) \tag{4.10}$$

Hence, the result.

The **amended plant TFM** can be expressed as a function of the closed-loop TFM and the controller according to, [GHSM21]

$$\boldsymbol{G}_{\mathrm{ap}}(s) = \boldsymbol{G}_{\mathrm{cl}}(s,\boldsymbol{p})\left[K_r(s,\boldsymbol{p}) + \boldsymbol{K}_{y_c}(s,\boldsymbol{p})\boldsymbol{G}_{\mathrm{cl}}(s,\boldsymbol{p})\right]^{-1} \tag{4.11}$$

This relation can be deduced by solving Equation (4.8) for $\boldsymbol{G}_{\mathrm{ap}}$: First multiply (4.8) with $\Big[\boldsymbol{I} - \boldsymbol{G}_{\mathrm{ap}}(s)\,\boldsymbol{K}_{y_c}(s,\boldsymbol{p})\Big]$ from the left:

$$\begin{aligned}\Big[\boldsymbol{I} - \boldsymbol{G}_{\mathrm{ap}}(s)\,\boldsymbol{K}_{y_c}(s,\boldsymbol{p})\Big]\,\boldsymbol{G}_{\mathrm{cl}}(s,\boldsymbol{p}) &= \boldsymbol{G}_{\mathrm{ap}}(s)\,K_r(s,\boldsymbol{p})\\ \boldsymbol{G}_{\mathrm{cl}}(s,\boldsymbol{p}) - \boldsymbol{G}_{\mathrm{ap}}(s)\,\boldsymbol{K}_{y_c}(s,\boldsymbol{p})\,\boldsymbol{G}_{\mathrm{cl}}(s,\boldsymbol{p}) &= \boldsymbol{G}_{\mathrm{ap}}(s)\,K_r(s,\boldsymbol{p})\end{aligned} \tag{4.12}$$

Then add $\boldsymbol{G}_{\mathrm{ap}}(s)\,\boldsymbol{K}_{y_c}(s,\boldsymbol{p})\boldsymbol{G}_{\mathrm{cl}}(s,\boldsymbol{p})$:

$$\begin{aligned}\boldsymbol{G}_{\mathrm{cl}}(s,\boldsymbol{p}) &= \boldsymbol{G}_{\mathrm{ap}}(s)\,K_r(s,\boldsymbol{p}) + \boldsymbol{G}_{\mathrm{ap}}(s)\,\boldsymbol{K}_{y_c}(s,\boldsymbol{p})\,\boldsymbol{G}_{\mathrm{cl}}(s,\boldsymbol{p})\\ \boldsymbol{G}_{\mathrm{cl}}(s,\boldsymbol{p}) &= \boldsymbol{G}_{\mathrm{ap}}(s)\,\Big[K_r(s,\boldsymbol{p}) + \boldsymbol{K}_{y_c}(s,\boldsymbol{p})\,\boldsymbol{G}_{\mathrm{cl}}(s,\boldsymbol{p})\Big]\end{aligned} \tag{4.13}$$

Finally, multiplication from the right with the inverse of $\Big[K_r(s,\boldsymbol{p}) + \boldsymbol{K}_{y_c}(s,\boldsymbol{p})\,\boldsymbol{G}_{\mathrm{cl}}(s,\boldsymbol{p})\Big]$ results in Equation (4.11). Hence, the result.

The stability margins at the actuator position are calculated based on the open-loop system

$$G_{cut}(s) = F_u(s)\,\boldsymbol{K}_{y_c}(s)\,\boldsymbol{F}_y(s)\,\boldsymbol{G}(s) \tag{4.14}$$

which represents the transfer function from actuator command to actuator command with a loop cut at this position. Since F_u is scalar, $G_{cut}(s)$ can be calculated by

$$G_{cut}(s) = \boldsymbol{K}_{y_c}(s)\,\boldsymbol{F}_y(s)\,\boldsymbol{G}(s)\,F_u(s) \;= \boldsymbol{K}_{y_c}(s)\,\boldsymbol{G}_{\mathrm{ap}}(s) \tag{4.15}$$

4.4.3 Testbased Gain Retuning for Longitudial Inner-loop

4.4.3.1 Desired Closed-loop

The linear nominal closed-loop system, denoted as $\boldsymbol{G}_{\mathrm{cl,nom}}(s, \boldsymbol{p}_0)$, that is composed of the initial longitudinal inner-loop controller, $K_r(s, \boldsymbol{p}_0)$, $\boldsymbol{K}_{y_c}(s, \boldsymbol{p}_0)$, and the nominal linear longitudinal amended plant model $\boldsymbol{G}_{\mathrm{ap,nom}}(s)$, is used as design model for the synthesis of the longitudinal autopilot control laws. Therefore, it is desired that the closed-loop frequency response of retuned controller and true plant corresponds to $\boldsymbol{G}_{\mathrm{cl,nom}}(s, \boldsymbol{p}_0)$. Hence, the desired closed-loop frequency response is the frequency response of $\boldsymbol{G}_{\mathrm{cl,nom}}(s, \boldsymbol{p}_0)$.

The initial controller was designed based on the linear longitudinal amended plant model including phugoid and short period dynamics. The linear longitudinal amended plant model was obtained based on the high fidelity 6DoF nonlinear model of the aircraft, using the developed tool chain. First the nonlinear flight dynamics model was trimmed for horizontal wings-level flight. Using these trim results the high fidelity 6DoF nonlinear model was linearized from u_c to $\boldsymbol{y}_c$, see Figure 4.6, including the following components

- phugoid and short period dynamics
- an actuator model, modelled as second order system according to

  $$G_{act}(s) = \frac{\omega_{act}^2}{s^2 + 2\zeta_{act}\omega_{act}s + \omega_{act}^2} \tag{4.16}$$

  where the parameters ω_{act} and ζ_{act} were obtained from ground tests with the actuation
- a mapping from elevator deflection commands to actuator position commands obtained from ground tests with the actuation
- a mapping from actuator position to surface deflections, obtained from ground tests with the actuation
- aeroelastic modes modelled as low damped second order filters according to

  $$G_{mode}(s) = \frac{\omega_{mode}^2}{s^2 + 2\zeta_{mode}\omega_{mode}s + \omega_{mode}^2} \tag{4.17}$$

where ω_{mode} and ζ_{mode} were obtained from flutter data provided by the air manufacturer for the first aeroelastic bending mode. The pitch rate and specific force of the nonlinear flight dynamics model were filtered by $G_{mode}(s)$ before they were fed into the controller.

- roll-off filters for all measurement signals, modelled as second order system according to

$$G_{fil}(s) = \frac{\omega_{fil}^2}{s^2 + 2\zeta_{fil}\omega_{fil}s + \omega_{fil}^2} \tag{4.18}$$

with ω_{fil} and ζ_{fil} chosen to obtain sufficient noise attenuation.

- notch filters modelled according to

$$G_{mode}(s) = \frac{s^2 + 2\zeta_{num}\omega_{num}s + \omega_{num}^2}{s^2 + 2\zeta_{den}\omega_{den}s + \omega_{den}^2} \tag{4.19}$$

where the parameters were chosen to prevent excitation of the modes by the controller and to realize sufficient attenuation of the open-loop frequency response at frequencies around the first aeroelastic bending mode frequency

- a mapping from control law output u_c to elevator deflection command, scheduled over dynamic pressure.

The resulting longitudinal linear model, i.e the amended plant depicted in Figure 4.6, was used for the synthesis of the longitudinal control law. Initial controller parameters were obtained using LQR for output feedback [LW13] or the MATLAB gain design routine *systune* from the *Control Design Toolbox*.

The resulting closed-loop response was assessed against requirements for the inner-loop controller. The requirements were given by adequate and desired values for the stability margins of the open-loop system as specified in the AS94900, [SAE07]. Other requirements defined limits on the bandwidth and overshoot and were defined by the outer-loops. Desired values were chosen to give better performance and robustness, while the adequate values are given as the minimum that needs to be satisfied.

4.4.3.2 Initial Closed-loop ETFE

The initial closed-loop estimate is obtained as an averaged ETFE as described in Section 3.5, by injecting the multi-sinusoidal excitation signal, described in Section 3.4, and measuring the feedback signals given in $\boldsymbol{y}_c$. The estimate of the non-parametric closed-loop frequency response $\hat{\boldsymbol{G}}_{cl,0}(j\omega_k)$, is calculated by Equation (3.18) at the discrete frequencies ω_k, defined by the parametrization of the multi-sine signal.

4.4.3.3 Amended Plant Estimate

Based on the estimated closed-loop frequency response $\hat{\boldsymbol{G}}_{\mathrm{cl},0}(j\omega_k)$, described above, the frequency response of the indirect non-parametric frequency response estimate of the amended plant $\hat{\boldsymbol{G}}_{\mathrm{ap}}(j\omega_k)$ can be calculated. This is possible because the controller parameters $\boldsymbol{p}_0$ that were applied in the flight tests for estimating $\hat{\boldsymbol{G}}_{cl,0}(j\omega_k)$, and thus the controller frequency responses $K_r(j\omega, \boldsymbol{p}_0)$ and $\boldsymbol{K}_{y_c}(j\omega, \boldsymbol{p}_0)$ are exactly known and because the control law is linear. The frequency response of the amended plant is estimated, using relation 4.11, by

$$\hat{\boldsymbol{G}}_{\mathrm{ap}}(j\omega_k) = \hat{\boldsymbol{G}}_{\mathrm{cl},0}(j\omega_k)\left[K_r(j\omega_k, \boldsymbol{p}_0) + \boldsymbol{K}_{y_c}(j\omega_k, \boldsymbol{p}_0)\hat{\boldsymbol{G}}_{\mathrm{cl},0}(j\omega_k)\right]^{-1} \tag{4.20}$$

4.4.3.4 Anticipated Closed-loop Estimate and Margins

The anticipated closed-loop estimate for a parameter set $\boldsymbol{p}$ is calculated based on the amended plant estimate $\hat{\boldsymbol{G}}_{\mathrm{ap}}(j\omega_k)$, described above, and the controller frequency responses $K_r(j\omega, \boldsymbol{p})$ and $\boldsymbol{K}_{y_c}(j\omega, \boldsymbol{p})$. Using the relation given by Equation (4.8), it is calculated by

$$\hat{\boldsymbol{G}}_{\mathrm{cl}}(j\omega_k, \boldsymbol{p}) = \left[\boldsymbol{I} - \hat{\boldsymbol{G}}_{\mathrm{ap}}(j\omega_k)\,\boldsymbol{K}_{y_c}(j\omega_k, \boldsymbol{p})\right]^{-1}\hat{\boldsymbol{G}}_{\mathrm{ap}}(j\omega_k)\,K_r(j\omega_k, \boldsymbol{p}) \tag{4.21}$$

An estimate of the anticipated stability margins for a parameter set $\boldsymbol{p}$ is obtained by calculating the gain and phase margins of the open-loop estimate $\hat{G}_{\mathrm{cut}}(j\omega_k, \boldsymbol{p})$. This estimate is calculated, using relation (4.15), by

$$\hat{G}_{cut}(j\omega_k, \boldsymbol{p}) = \boldsymbol{K}_{y_c}(j\omega_k, \boldsymbol{p})\,\hat{\boldsymbol{G}}_{\mathrm{ap}}(j\omega_k) \tag{4.22}$$

4.4.3.5 Optimization Problem

The optimization problem is described in detail in Section 3.8 for a SISO closed-loop system. Because the considered application is a SIMO system, with two outputs, $n_y = 2$, the cost function is adapted as follows [GHSM21]

$$J(\boldsymbol{p}) = \sum_{i=1}^{2}\{\frac{20}{n_\omega}\sum_{k=1}^{n_\omega}(\mathrm{w}_{\gamma,i}(\omega_k)\left[\mathrm{w}_A\Delta_{|G_{cl,y_i}|} + \mathrm{w}_\phi\Delta_{\angle G_{cl,y_i}}\right])\} + (\boldsymbol{p}-\boldsymbol{p}_0)\,\boldsymbol{Q}\,(\boldsymbol{p}-\boldsymbol{p}_0)^T \tag{4.23}$$

with

$$\begin{aligned}\Delta_{|G_{cl,y_i}|} &= (\left|\hat{G}_{cl,y_i}(j\omega_k, \boldsymbol{p})\right| - \left|G_{cl,des,y_i}(j\omega_k)\right|)^2\\ \Delta_{\angle G_{cl,y_i}} &= (\angle\hat{G}_{cl,y_i}(j\omega_k, \boldsymbol{p}) - \angle G_{cl,des,y_i}(j\omega_k))^2\end{aligned} \tag{4.24}$$

where $G_{\mathrm{cl,des},y_i}(j\omega_k)$ in Equation (4.24) represents the desired closed-loop frequency response at frequency ω_k from the reference input r to each of the outputs y_i, $i = 1, 2$ given in $\boldsymbol{y}_c$. In Equation (4.24), $\hat{G}_{\mathrm{cl},y_i}(j\omega_k, \boldsymbol{p})$ represents the anticipated closed-loop response, for the gain set $\boldsymbol{p}$. It is represented by the rows of $\hat{\boldsymbol{G}}_{\mathrm{cl}}(j\omega_k, \boldsymbol{p})$, which is computed according to Equation (4.21) utilizing the estimate of the amended plant $\hat{\boldsymbol{G}}_{\mathrm{ap}}(j\omega_k)$ given by Equation (4.20). Note, that though the overall objective is to improve the tracking, i.e. the response from r to y_1, the cost function also accounts for the response from r to y_2. With this strategy empirically better results could be obtained compared to using only the response from r to y_1 in the cost function. The remaining parameters and symbols in (4.24) and (4.23) are as defined in Section 3.8. The optimization problem is given by [GHSM21]:

$$\begin{aligned} &\min_{\boldsymbol{p}} .\ J(\boldsymbol{p}) \\ &st. \\ &c_1(\boldsymbol{p}) = A_m - \hat{A}_m(\boldsymbol{p}) \leq 0 \\ &c_2(\boldsymbol{p}) = \Phi_m - \hat{\Phi}_m(\boldsymbol{p}) \leq 0 \end{aligned} \tag{4.25}$$

where

A_m is the adequate gain margin

$\hat{A}_m(\boldsymbol{p})$ is the anticipated gain margin for the controller parameters $\boldsymbol{p}$

Φ_m is the adequate phase margin

$\hat{\Phi}_m(\boldsymbol{p})$ is the anticipated phase margin for the controller parameters $\boldsymbol{p}$.

The cost function $J(\boldsymbol{p})$ is minimized with respect to the controller parameters $\boldsymbol{p}$ using the off-the-shelf solver *fmincon* from MATLAB. Upper and lower bounds are given for the parameter vector $\boldsymbol{p}$. "The constraints ensure that the resulting gains lead to anticipated phase and gain margins larger or equal to the adequate margins. The posed optimization problem is not convex. Further, no formal proof yet was made to show that this optimization will converge or reveal the global minimum. However, it can be verified by comparing the resulting anticipated and the initial closed-loop response if the new parameters are better than the initial parameters. It is shown by Monte Carlo simulation in the following sections that the problem at hand converged to a solution which is better than the initial guess. Furthermore, the problem at hand is not computational complex and with an usual desktop pc it can be solved within a few minutes. However, as the problem is solved off-line, there exist no demanding time constraints."[GHSM21]

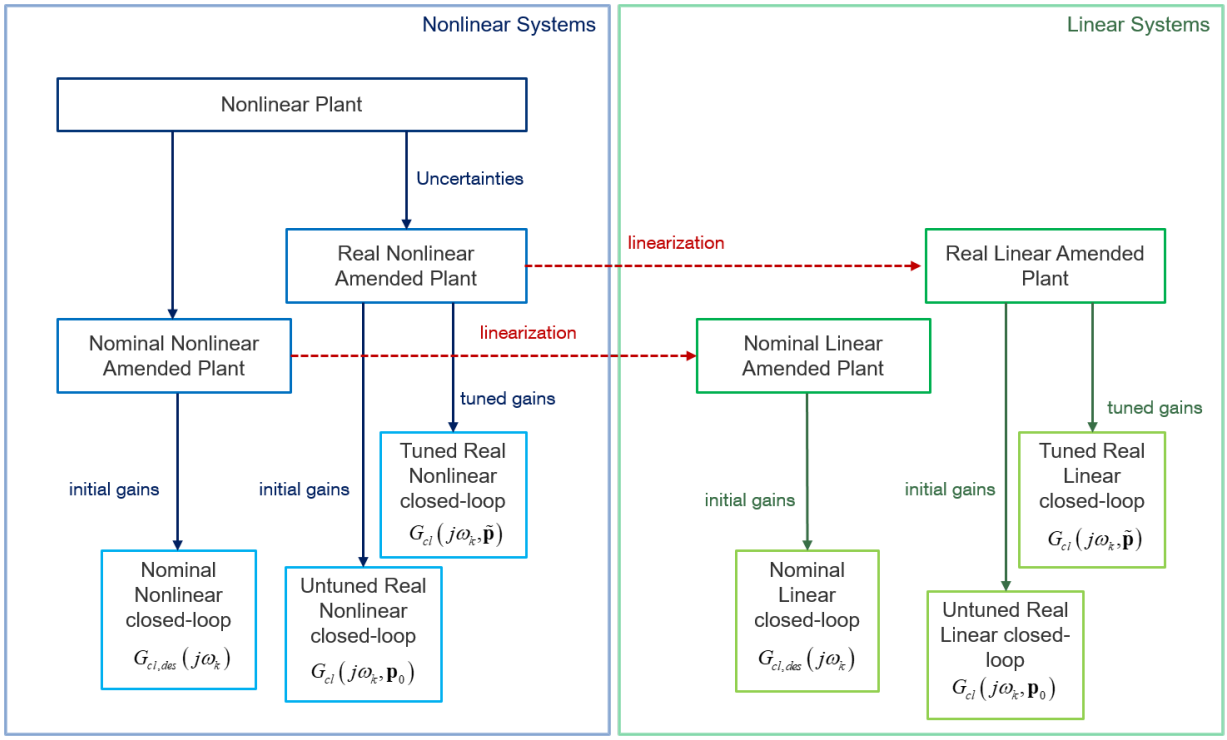

Figure 4.7: *Schematic of simulation setup and nomenclature. [GHSM21]*

4.4.4 Simulation Results

"The following section presents the simulation results of the proposed controller retuning based on a full 6DoF nonlinear simulation model. Figure 4.7 shows the setup and nomenclature of the simulations. First, we distinguish between the nonlinear (*nl*) and linear (*lin*) systems. The expression *nl* refers to data from the high fidelity non-linear Model-In-the-Loop Simulation framework, described in Section 4.3. The notation *lin* refers to data obtained with linear state space models. Furthermore, we distinguish between nominal and real systems. Based on the nominal *lin* amended plant, which is obtained via linearization of the nominal *nl* amended plant, model-based gain design is performed a priori the flight test. The resulting controller parameters are denoted as initial gains $\boldsymbol{p}_0$. Application of these gains to the nominal *lin* amended plant, results in the nominal *lin* closed-loop system, which constitutes the desired closed-loop response $\boldsymbol{G}_{\mathrm{cl,des}}(j\omega_k)$ for the gain retuning process. The expression real denotes the systems, which are obtained based on the plant subjected to aerodynamic uncertainties and/or a backlash element applied to the elevator deflection after the actuator dynamics. The linearization of the real *nl* plant results in the real *lin* plant and application of the initial gains leads to the untuned real *nl/lin* closed-loop $\boldsymbol{G}_{\mathrm{cl}}(j\omega_k, \boldsymbol{p}_0)$. The expression tuned, in contrast, describes the closed-loop system $\boldsymbol{G}_{\mathrm{cl}}(j\omega_k, \tilde{\boldsymbol{p}})$, obtained by application of the retuned gains, which are obtained through the proposed gain retuning process."[GHSM21]

In the following simulation results are shown for the Do228, see Section 4.1.2. Similar results were obtained in simulation for the other aircraft configurations presented in Section 4.1. However, here we present the results only for Do228 which were also published in [GHSM21]. It is worth to note, that for ELIAS and the G-520T, during the multi-sine maneuver, an increased drift away from the trim point was encountered. To keep the drift within acceptable bounds, only a decreased number of repetitions could be realized. Because the sensitivity of the estimates, with regard to disturbances and noise, is reduced with increasing number of repetitions by the averaged ETFE, in these cases instead of reducing the maneuver length, an additional altitude hold control was introduced to keep the aircraft at the operational point during the maneuver. This strategy will be explained in Section 4.4.5, where the flight tests for the G-520T are discussed.

4.4.4.1 General Settings - Uncertainties

For the following analysis, the aerodynamic uncertainties were considered to be multiplicative on the following aerodynamic derivatives [GHSM21]:

$C_{m\alpha}$ Pitch moment coefficient due to angle of attack (α).

C_{mq} Pitch moment coefficient due to pitch rate (q).

$C_{m\eta}$ Pitch moment coefficient due to elevator deflection (η).

$C_{L\alpha}$ Lift coefficient slope wrt. angle of attack (α).

$C_{L\eta}$ Lift coefficient slope wrt. elevator deflection (η).

For simulations where one uncertainty set was considered, 10% uncertainty was applied to all coefficients. For the Monte Carlo simulations with regard to aerodynamic uncertainties, a uniform distribution with a spread of 20% on the same coefficients were used. Additionally, the influence of a backlash element, that was applied at the elevator, was investigated. The backlash was varied within simulations between $0 - 1.2$ degrees.

4.4.4.2 General Settings - Reference Excitation Input Signal

The applied multi-sinusoidal excitation signal, injected at the reference input r is given by Equation (3.16). Its parametrization is summarized in Table 4.1. The considered frequency range lies between $\omega_1 \approx 0.42\frac{rad}{s}$ and $\omega_{n_\omega} \approx 20\frac{rad}{s}$. The parametrization is chosen such, that during the maneuver neither the actuator position limits nor the actuator rate limits are exceeded. Furthermore, the acceptable maneuver length is determined by simulations such that the drift from the test envelope point, given in terms of indicated airspeed and static pressure, remains within acceptable boundaries. These objectives

are determined as a compromise with ensuring an adequate signal-to-noise, by choosing an adequate number of repetitions, an adequate excitation amplitude and an adequate frequency resolution of the estimates.

	Symbol	**Value**
Amplitude	A	0.2g
Window length	T	15s
Frequency set (excited harmonics)	$\mathbb{S}$	1,3,5,...,47
Number of periods (repetitions of maneuver)	N	10

Table 4.1: *Maneuver injection input signal parameters.*

4.4.4.3 General Settings - Optimization

The parametrization of the quadratic cost function in Equation (4.23) is chosen as follows [GHSM21]. The weighting matrix $\boldsymbol{Q}$ is chosen as a diagonal matrix with values such that the penalty for changes in the integral gain is of one order of magnitude higher than the penalty for changes in the other gains. The frequency dependent weights for each output y_i, are chosen equal: $\mathrm{w}_{\gamma,1}(\omega_k) = \mathrm{w}_{\gamma,2}(\omega_k) = \mathrm{w}_{\gamma}(\omega_k)$, with $\mathrm{w}_{\gamma}(\omega_k)$ given in Table 4.2. The frequency dependent weights are chosen to achieve a good matching with the desired dynamics in the frequency range, where the bounds from the outer-loop are most tight. Frequencies, where the closed-loop dynamics are already well attenuated are weighted weakly. The remaining parameters are $\mathrm{w}_A = 1,\ \mathrm{w}_{\phi} = 0.01745$ as described in Section 3.8 and $A_m = 6dB,\ \Phi_m = 45°$.

$\omega_k[\frac{rad}{s}]$	< 0.5	0.5-4	4-6	> 6
$\mathrm{w}_{\gamma}(\omega_k)$	10	20	10	1

Table 4.2: *Frequency depending relative weight. [GHSM21]*

4.4.4.4 Simulation Results for Calm Atmosphere

To quantify the influence of aerodynamic uncertainties on the retuning results, Monte Carlo Simulations (100 simulations in total) in calm atmosphere were carried out. The applied uncertainties on the aerodynamic parameters were described in Section 4.4.4.1. The multi-sine was parametrized as specified in Section 4.4.4.2 and the optimization parameters are given in Section 4.4.4.3.

Figure 4.8 shows the deviation between the desired closed-loop frequency response and the tuned closed-loop frequency response, as well as the deviation between the desired and the initial (untuned) response. The depicted tuned and untuned responses are obtained

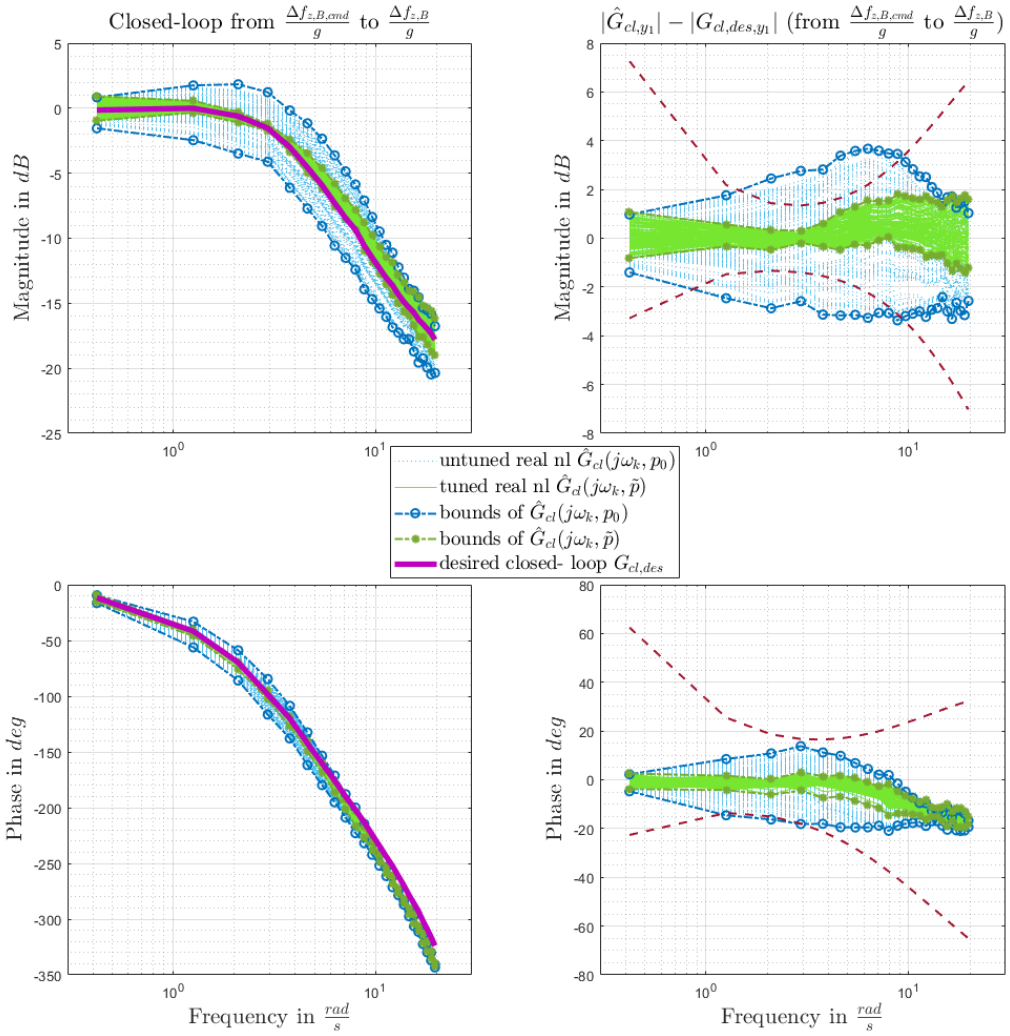

Figure 4.8: *Closed-loop frequency response with initial gains, retuned gains, and desired response, for varying uncertainties under calm air conditions. [GHSM21]*

as an averaged ETFE, based on simulation results of the controlled nonlinear plant model with the retuned and initial controller parameters, respectively. It can be seen that the tuned closed-loop responses are significantly closer to the desired response. Though the MUAD bounds, described in Section 3.9, are applicable to piloted cases and the considered controller constitutes the inner-loop for an autopilot, Figure 4.8 additionally depicts the MUAD bounds in dashed red lines in order to qualitatively quantify the improvement. We see, that all tuned responses are within the MUAD bounds. Hence, the proposed retuning procedure achieves an improvement.

Figure 4.9 additionally shows the anticipated tuned closed-loop response in orange. It can be seen that the anticipated tuned response lies almost exactly on top of the closed-loop response that is obtained from simulation with the tuned controller parameters. The achieved margins with the tuned gains were checked for satisfaction of their adequate

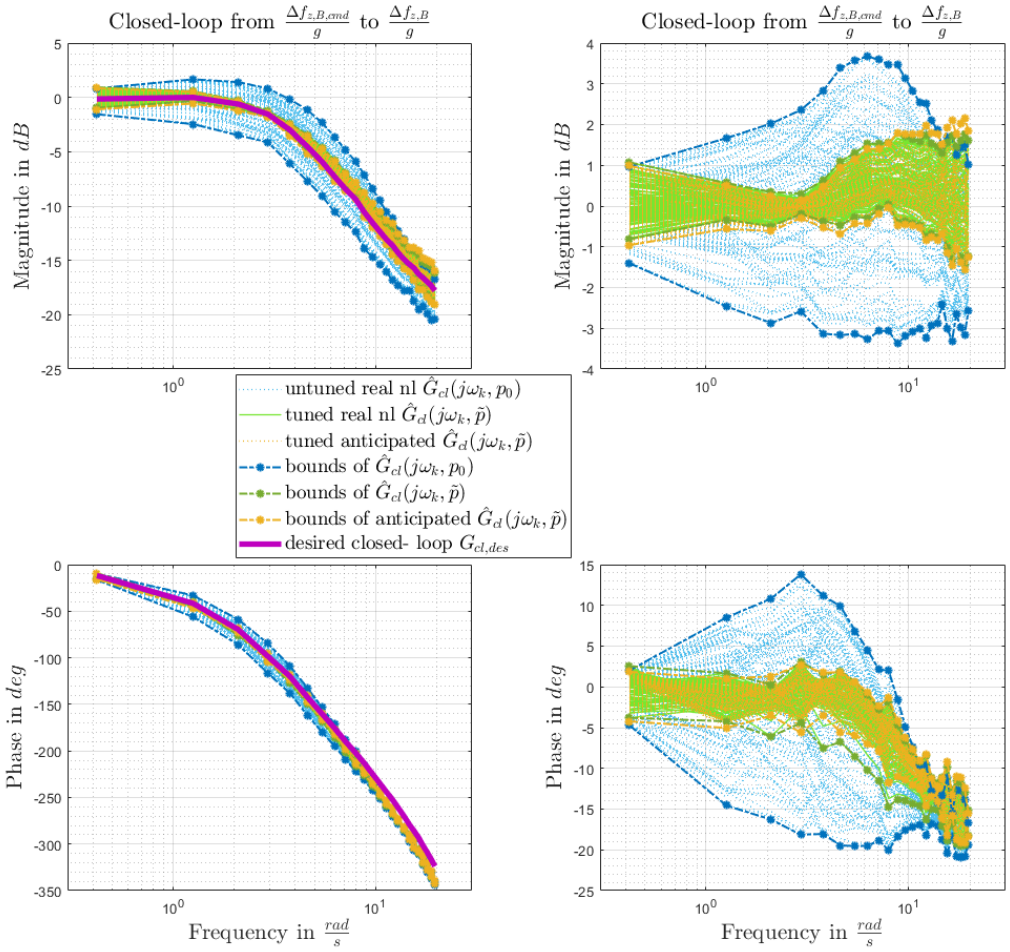

Figure 4.9: *Anticipated tuned closed-loop frequency response, desired response, closed-loop response with initial gains and with retuned gains for varying uncertainties under calm air conditions.*

values via interpolation of the corresponding frequency response $\hat{G}_{cut}(j\omega_k, \boldsymbol{p})\acute{}$, which was calculated as described in Section 4.4.3.4.

Figure 4.10 compares the desired closed-loop response to a step input, in $\Delta f_{z,B,cmd}(t)/g$ with an amplitude of 0.5, with the step responses of the closed-loop systems with tuned and initial (untuned) gains for one specific uncertainty set, which is described in Section 4.4.4.1. The desired step response with the optimized gains is reproduced much better.

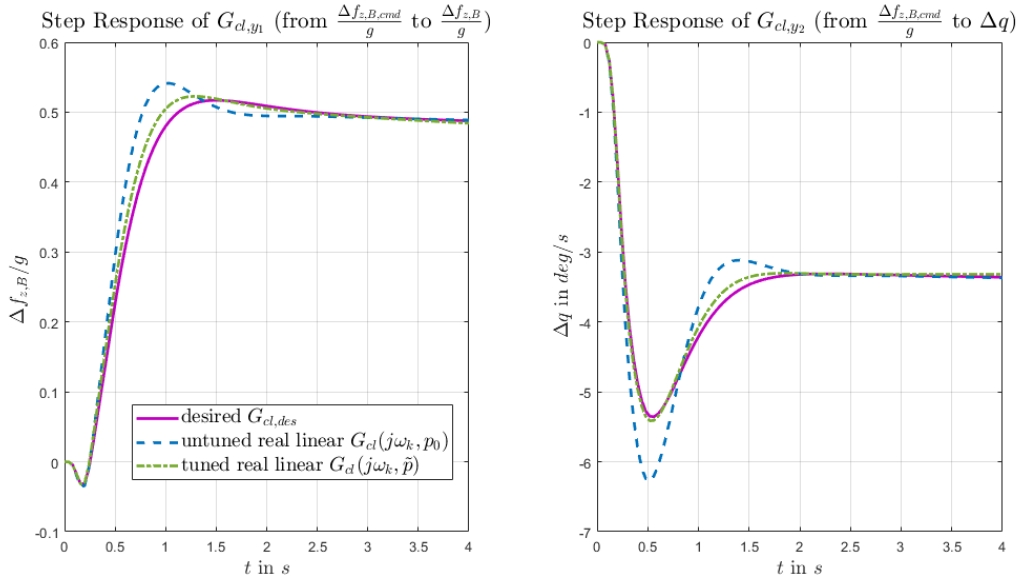

Figure 4.10: *Step response of control law with initial gains, retuned gains, and desired response. [GHSM21]*

4.4.4.5 Simulation Results for Light Turbulence

The following section investigates the effect of performing the tuning in light turbulence based on simulated flight tests as presented in [GHSM21]. The turbulence will distort the closed-loop frequency response estimate compared to an estimate from a calm air flight test. This is revealed in Figure 4.11 by the dashed blue lines. The light blue line shows the ETFE of the closed-loop frequency response obtained with data from simulation in calm atmosphere with the initial (untuned) controller parameters. The dark blue line is the same estimate obtained with data from simulation in light turbulence, and is thus deteriorated. Consequently, the optimized controller parameters obtained from this estimate will differ slightly from the parameters tuned based on flight in calm air. Figure 4.11 shows how much the tuned closed-loop responses by using the parameters obtained from turbulent or calm air flight test data, differ. This is revealed by the green dashed lines, which compare the closed-loop frequency responses obtained as ETFE's from simulation with the two sets of tuned gains in calm air. The simulations were performed based on one specific set of uncertainties, which is described in Section 4.4.4.1.

The following two observations can be made: First, the parameters tuned from a flight in calm air or in light turbulent air, both result in a closed-loop frequency response that is very close to the desired frequency response. Further quantification is made later through Monte Carlo simulations. Second, the estimated frequency response in turbulent conditions is more noisy. However, it seems to be more or the less centered around the estimated response from calm air conditions, and provides controller parameters that retrieve the desired frequency response. The variance of the estimated frequency response in turbulence depends on the signal-to-noise ratio and hence also on the intensity of the turbulence and the number of repetitions of the maneuver. It is a trade-off between the maneuver length T of one repetition which determines the frequency resolution ω_k of the estimated frequency response, the drift away from the considered operational envelope point and the amplitude of the excitation signal.

To quantify the influence of data collected in turbulent atmosphere on the tuning results, Monte Carlo Simulations (30 simulations in total) in light turbulence were carried out with one specific uncertainty set, which is described in Section 4.4.4.1. Figure 4.12 shows the deviation between the desired frequency response and the one obtained with the tuned controller parameters computed as an ETFE obtained from a simulated experiment in light turbulence, depicted as the light green dashed line. The deviation between the desired response and the response from tuning in calm air is also shown as the dark green line. Figure 4.12 reveals, that significant improvement can be achieved even in turbulent conditions. However, the best match will occur when updating the gains based on experiments in calm atmosphere. The achieved margins with the tuned controller parameters were checked for satisfaction of their adequate values as described before.

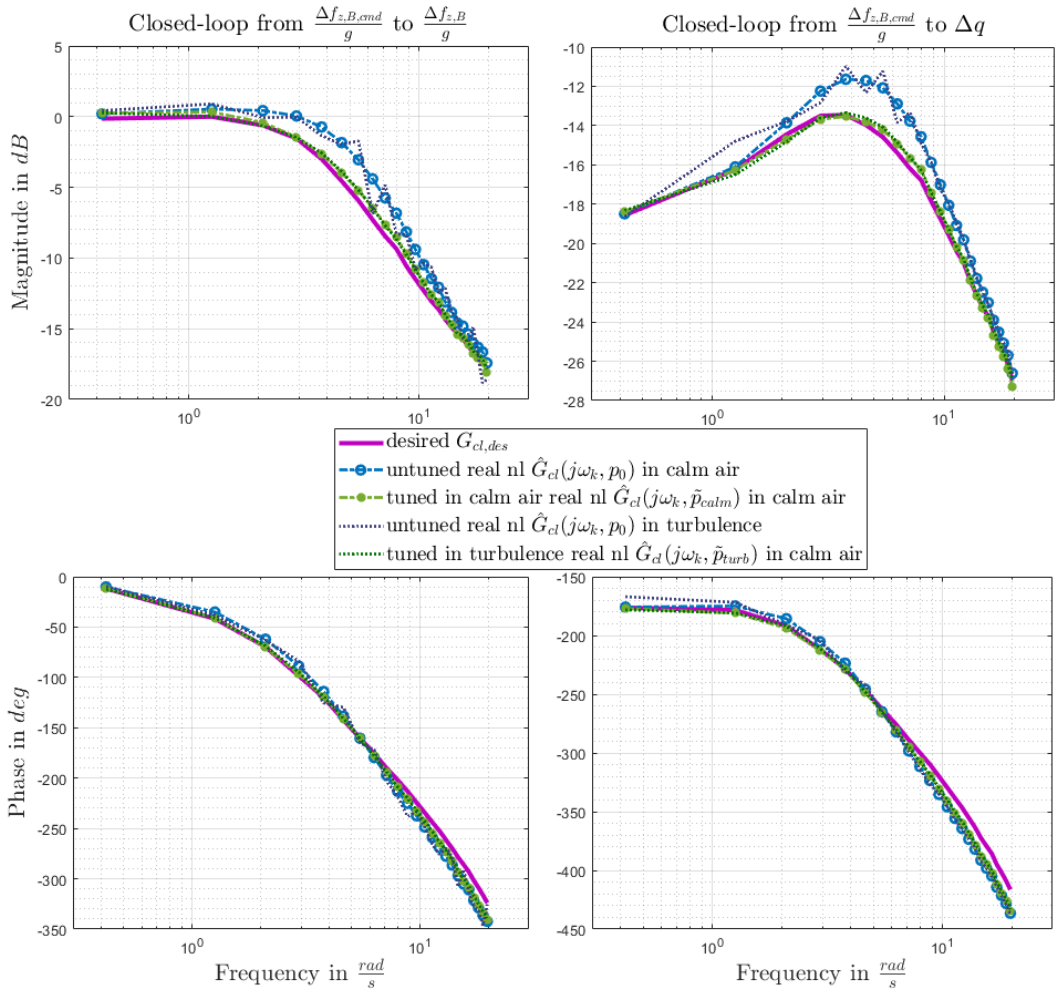

Figure 4.11: *Estimates of untuned closed-loop frequency responses with uncertain plant in calm air and turbulent conditions, compared to the respective tuned responses in calm air. [GHSM21]*

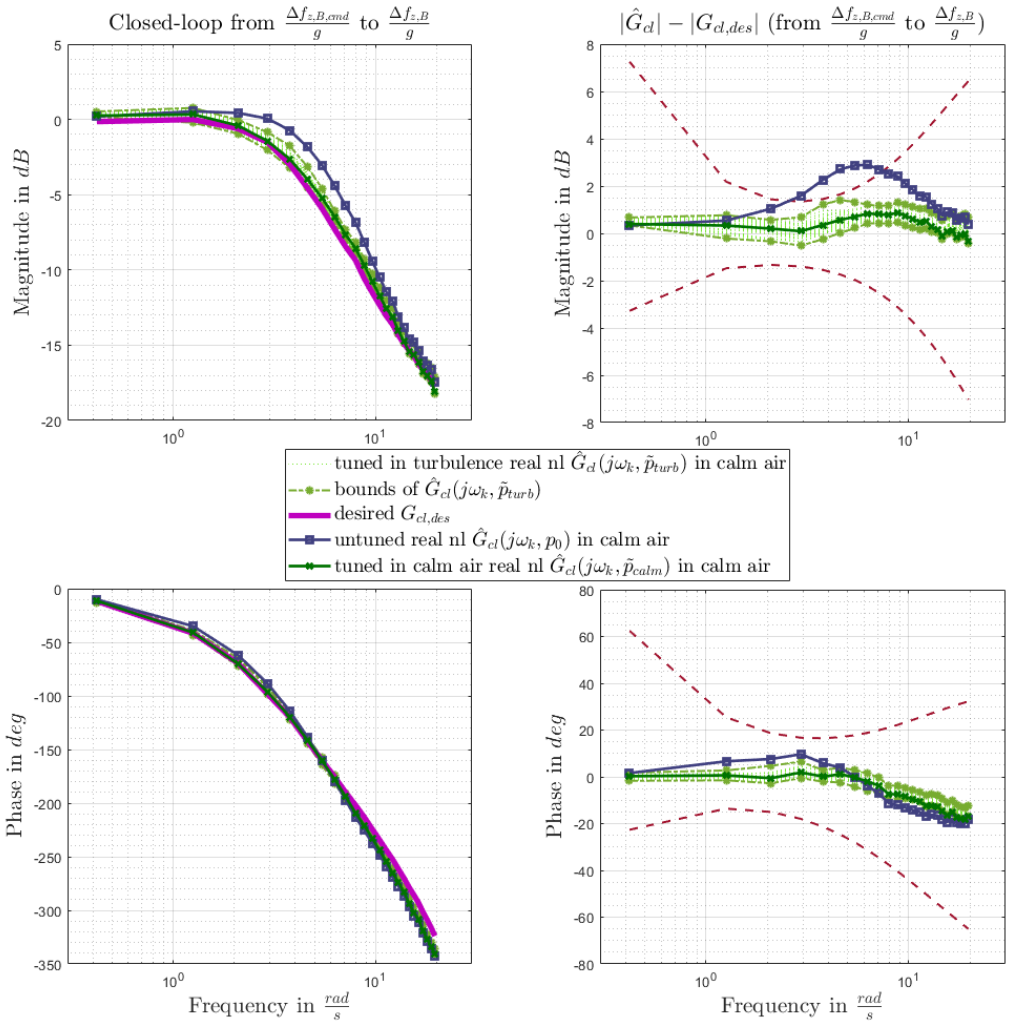

Figure 4.12: *Comparison of calm air frequency responses with gains tuned in calm air or turbulent air by Monte Carlo simulations. [GHSM21]*

4.4.4.6 Simulation Results with Backlash

The following section investigates the effect of backlash in the elevator deflections on the tuning results based on simulated flight tests. The simulations were performed based on one specific set of uncertainties with a varying backlash element. The backlash was evenly varied from 0 to 0.7 degrees. 7 simulations were performed in total in calm air with the different values for the backlash. Figure 4.13 and 4.14 show in blue the ETFE's of the initial (untuned) closed-loop response for each simulation, where the nominal aerodynamic coefficients were increased by 10% in Figure 4.13 and decreased by 10% in Figure 4.14.

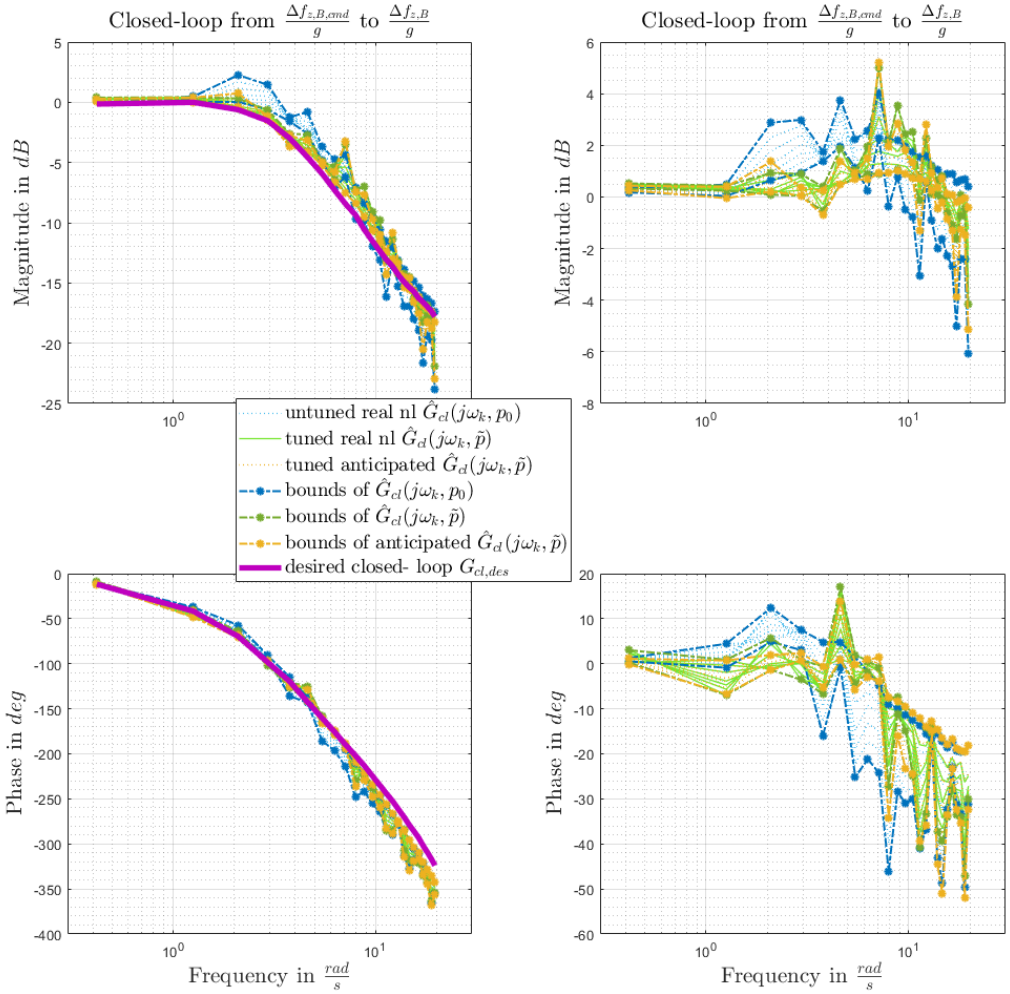

Figure 4.13: *Comparison of closed-loop frequency responses with varying backlash element* $(0 - 0.7$ *degrees) and aerodynamic coefficients increased by 10%.*

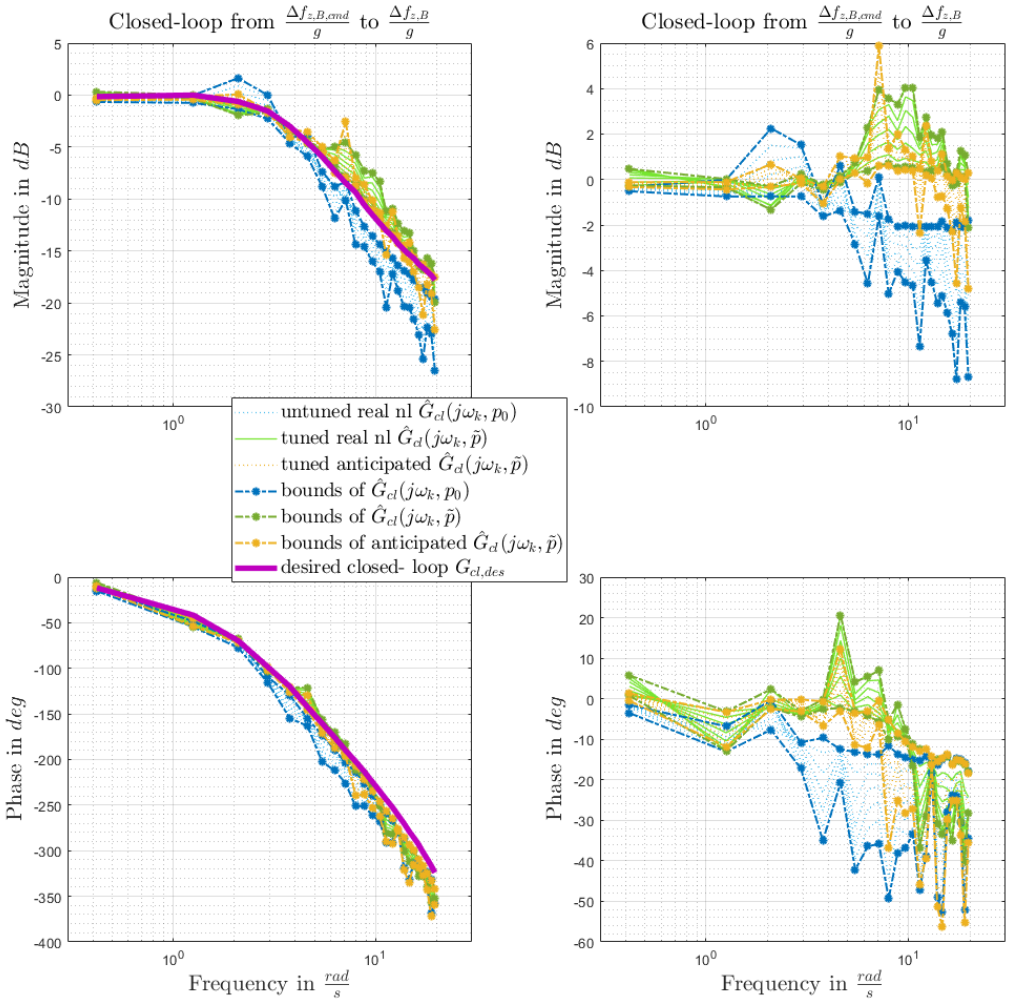

Figure 4.14: *Comparison of closed-loop frequency responses with varying backlash element* $(0 - 0.7$ *degrees) and aerodynamic coefficients decreased by 10%.*

Based on the respective initial closed-loop estimates the controller retuning was performed, where the penalties in the matrix $\boldsymbol{Q}$ were increased by one order of magnitude and two orders of magnitude for the integrator gain and specific force feedback gain, respectively, compared to the values given in Section 4.4.4.3. The simulations were repeated with the new controller parameters. Based on the respective simulation data, the ETFE's of the tuned closed-loop response, depicted in green, was calculated. We see that the tuned responses are closer to the desired response than the initial responses. Figure 4.15 shows the resulting step responses in specific force. The tuned closed-loop responses reveal an increasing steady state error with increasing backlash. Hence, the tuning shall be considered with care if large nonlinearities like backlash is expected. With increasing backlash the tuned frequency responses will additionally deviate from the anticipated closed-loop frequency responses, which are depicted in yellow in Figure 4.14. This effect is even better visible in Figure 4.16 where the backlash was varied from 0.8 up to 1.2

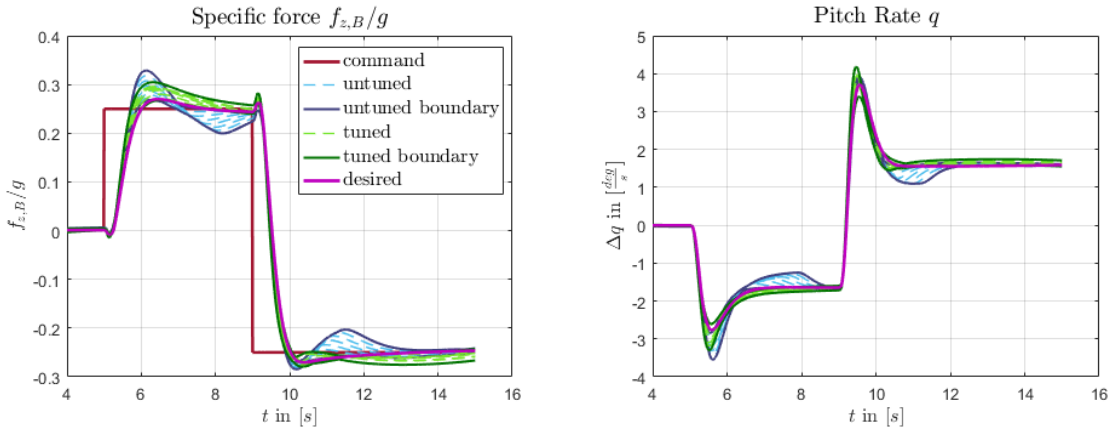

Figure 4.15: *Comparison of closed-loop step responses with varying backlash element* $(0 - 0.7$ *degrees) and aerodynamic coefficients decreased by 10%.*

degrees with aerodynamic coefficients decreased by 10%. In this case also the margins for the tuned controller parameter obtained from simulation were not satisfied, while the anticipated margins were satisfied.

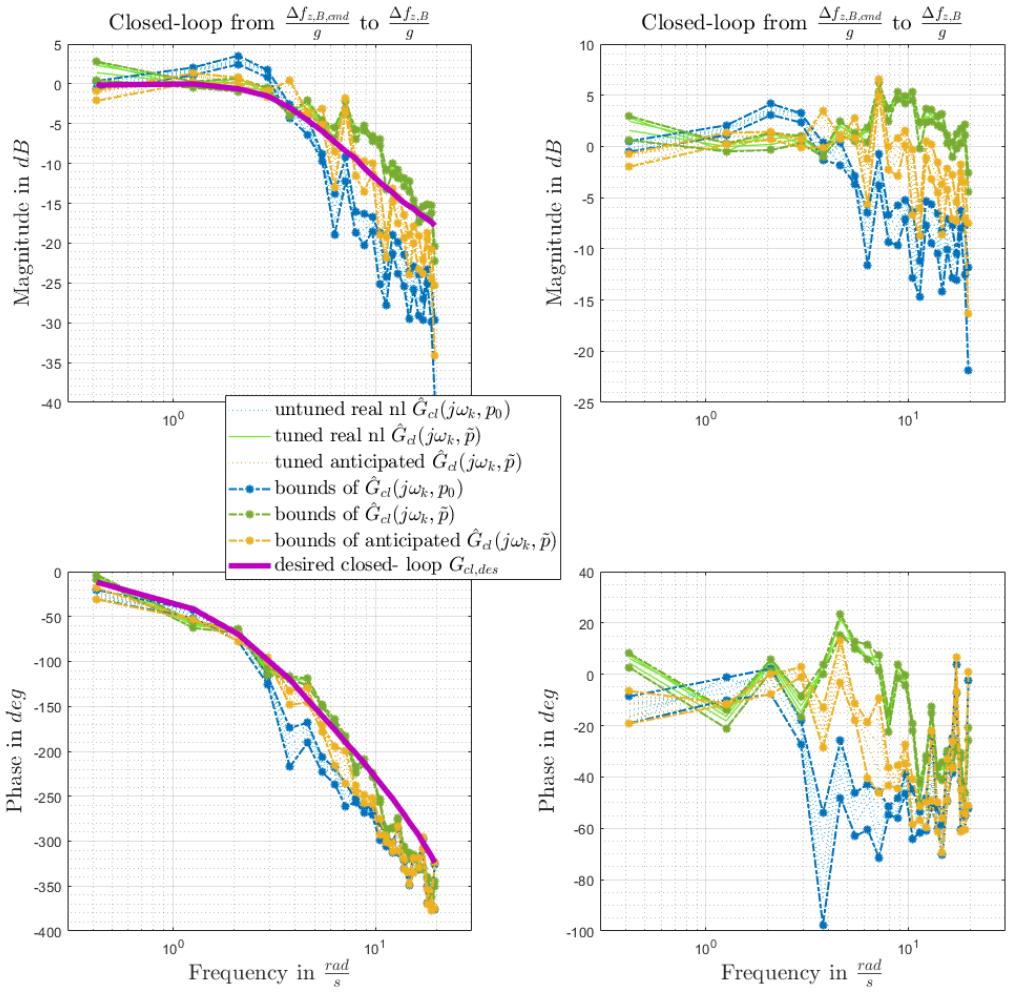

Figure 4.16: *Comparison of closed-loop frequency responses with varying backlash element* $(0.8 - 1.2$ *degrees) and aerodynamic coefficients decreased by 10%.*

4.4.5 Flight Test Results

In the following sections, the data of two flights of the G-520T testbed are considered, which took place near the airport EDMN close to Mindelheim, Germany. Note, that the entire section 4.4.5 is extracted from my manuscript [SSG+] for AIAA Scitech 2022 Forum. ["All flight tests presented in the following were performed at an envelope point defined by indicated airspeed and pressure altitude of

$$V_A = 115 \pm 5\,\text{KIAS} \quad \text{and} \quad h = 7500 \pm 700\,\text{ft} \tag{4.26}$$

see Figure 4.20.

The considered flight test maneuvers were executed with retracted landing gear and flaps in upright position. The flight tests were observed and instructed from a ground control station. A datalink allowed for live monitoring of telemetry data from the aircraft and to set flight test parameters from the ground control station. During the test flights, sensor data and FCC internal controller data were recorded directly on the FCC with a sample rate of 100Hz which equals the clock speed of the FCC.

Before each test maneuver, the aircraft was brought in steady state horizontal level flight with autopilot active in altitude and heading hold mode. As no auto thrust system was available yet, the pilot was instructed to maintain the trim airspeed by manually adjusting the power lever. Flight test maneuvers for the FTMI module were selected from ground control station based on a maneuver list index and confirmed via received status data from the aircraft. The activation of the selected maneuver was either done by the pilot via the mode control panel in the cockpit or from the ground control station after receiving clearance from the pilot. After execution of an injected maneuver, the autopilot modes roll and pitch angle hold were automatically activated.

During injection of $\Delta f_{z,B,cmd}(t)/g$ maneuvers, a low bandwidth altitude hold control loop was active to keep the aircraft close to the trim altitude, while not interfering with the flight test maneuver. This altitude control loop is particularly relevant for the longer-lasting multi-sine maneuvers during which the aircraft would otherwise drift away from the trim point without control of the aircraft flight path such that the assumption of linearity of the closed-loop dynamics would be no longer justified. Besides the $\Delta f_{z,B,cmd}(t)/g$ command, the maneuver sequences also include a bank angle command of $\Phi_{cmd}(t) = 0°$ and a lateral specific force command $f_{y,B,cmd}(t)/g = 0$ to keep the wings level and maintain coordinated flight.

4.4.5.1 General Settings - Reference Excitation Input Signal

The applied multi-sine signals are described in Section 3.4, Equation (3.16). Thereby, two differently parametrized multi-sinusoidal excitation signals, injected at the reference input r were tested within the flight tests.

The respective parametrization is summarized in Table 4.3. The main difference of the tested multi-sines is the window length T and consequently the frequency spacing of the closed-loop estimates which is an integer multiple of $\omega_{min} = 2\pi/T$. The considered frequency range lies between $\omega_1 \approx 0.31\frac{rad}{s}$ and $\omega_{n_\omega} \approx 8.17\frac{rad}{s}$ and between $\omega_1 \approx 0.42\frac{rad}{s}$ and $\omega_{n_\omega} \approx 6.2\frac{rad}{s}$, respectively. For both multi-sines, $N = 10$ repetitions of the maneuver were observed, such that the total length of the maneuver was in one case $150s$ and in the other case $200s$. The latter one gives a finer frequency resolution, but it was unclear in advance if the resulting drift from the trim point, due to the longer maneuver duration, would be within acceptable bounds. It turned out that both multi-sines provided acceptable and similar results as will be shown later.

	Symbol	**Maneuver ID 166**	**Maneuver ID 168**
Amplitude	A	0.2g	0.2g
Window length	T	15s	20s
Frequency set (excited harmonics)	$\mathbb{S}$	1,2,3,...,26	1,2,3,...,15
Number of periods (repetitions of maneuver)	N	10	10

Table 4.3: *Maneuver injection input signal parameters.*

The multi-sines 166 and 168 were repeated each three times in calm air under closed-loop conditions, with the initial and tuned controller parameters. In turbulent air conditions, multi-sines 166 and 168 were repeated each three times with the initial controller only.

4.4.5.2 General Settings - Initial Controller Parameters

The initial controller parameters $\boldsymbol{p}_0$ were calculated using classical gain design techniques based on a linear model of the amended plant $\boldsymbol{G}_{\text{ap,nom}}$ as described in Section 4.4.3.1. The initial controller parameters that were tested in flight are given in Table 4.4.

Parameter	**Name**	**Initial value**	**Tuned value**
p_1	feedforward	-0.16	-0.02
p_2	integrator	-1.19	-2.08
p_3	$\Delta f_z/g$ feedback	-0.17	-0.48
p_4	q feedback	1.07	4.43

Table 4.4: *Controller parameter values.*

4.4.5.3 General Settings - Optimization

The quadratic cost in Equation (3.103) is parametrized as follows. The weighting matrix $\boldsymbol{Q}$ is diagonal with values penalizing changes in the integral gain with one order of magnitude higher than changes in the feedforward gain and with two order of magnitude higher than the feedback gains. The weights $\mathrm{w}_\gamma(\omega_k)$ specify in which frequency range the difference between the desired and optimized response should be emphasized. It is chosen to prioritize frequencies where the bounds from the outer-loop is most tight. The respective values are given in Table 4.5. The frequency range where the closed-loop dynamics are already well attenuated is weighted very weakly. The weights for the relative influence of errors in magnitude and phase are chosen to $\mathrm{w}_A = 1$ and $\mathrm{w}_\phi = 0.01745$, as recommended by [RT06]. The adequate margins used for the constraints are selected as $A_m = 6dB,\ \Phi_m = 45°$ according to [SAE07]. The initial controller parameter values are

$\omega_k[\frac{rad}{s}]$	< 0.5	0.5-4	4-6	> 6
$\mathrm{w}_\gamma(\omega_k)$	50	50	10	1

Table 4.5: *Frequency depending relative weight.*

summarized in Table 4.4.

4.4.5.4 Initial Closed-loop ETFE: Transients and Steady State Assumption

It is known from [dv95] that for accurate estimation of the closed-loop frequency response, the transients from the beginning of the experiment should have died out, otherwise spectral leakage will occur in the Discrete Fourier Transform, and hence deteriorate the ETFE estimate. To verify the assumption that discarding the first period is sufficient for the transients to disappear, the first four periods of one experiment in calm air are shown in Figure 4.17. It can be seen that the first period differs from the following three, which are almost identical. Therefore, it is reasonable to assume that discarding the first period suffices to overcome the adverse effects of the transients.

4.4.5.5 Initial Closed-loop ETFE: Calm Air versus Turbulent Air

It is known from [dv95] that the variance of the ETFE increases with the noise on the data and reduces with the number of repetitions. In [GHSM21] simulation results showed this effect. This effect is also shown by the following flight test results. In Figure 4.18 the closed-loop frequency response estimates of the initial untuned control law for six experiments in calm air and six experiments in turbulent air are shown. The tests were performed with three repetitions of the multi-sine maneuver 166 and three repetitions of the multi-sine maneuver 168, defined in Table 4.3. It can be seen that the spread of the estimates is significantly larger for the data collected in turbulence. In Figure 4.19 the time domain data for the pitch rate and specific force per g for two particular experiments

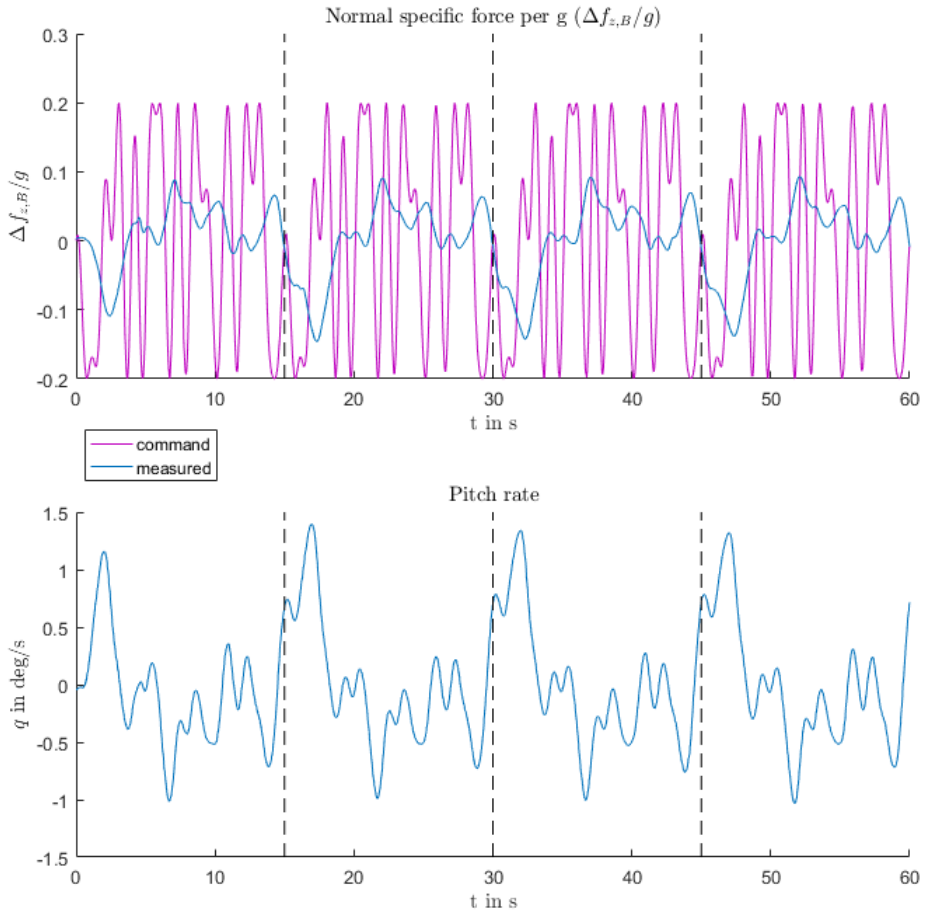

Figure 4.17: *First four periods of the multi-sine signal - visualization of transient response.*

is shown. The data shows four periods of the multi-sine maneuver with initial, untuned gains in calm air and turbulent air. In Figure 4.20 the corresponding values for lateral specific force per g, bank angle, pressure altitude and indicated airspeed is shown. By inspecting both figures the influence of the turbulence can be seen. It can be seen for the data sequence obtained in turbulence that a large disturbance at time $134s$ in both the and normal and lateral specific force per g causes deviations in normal specific force per g and pitch rate compared to the calm air sequence. Additionally, it is revealed that fluctuations in the airspeed at time $90s - 112s$ caused by disturbances also translates to a deviation compared to the calm air data. It is these fluctuations that cause the greater variance of the ETFE in turbulent flight as expected.

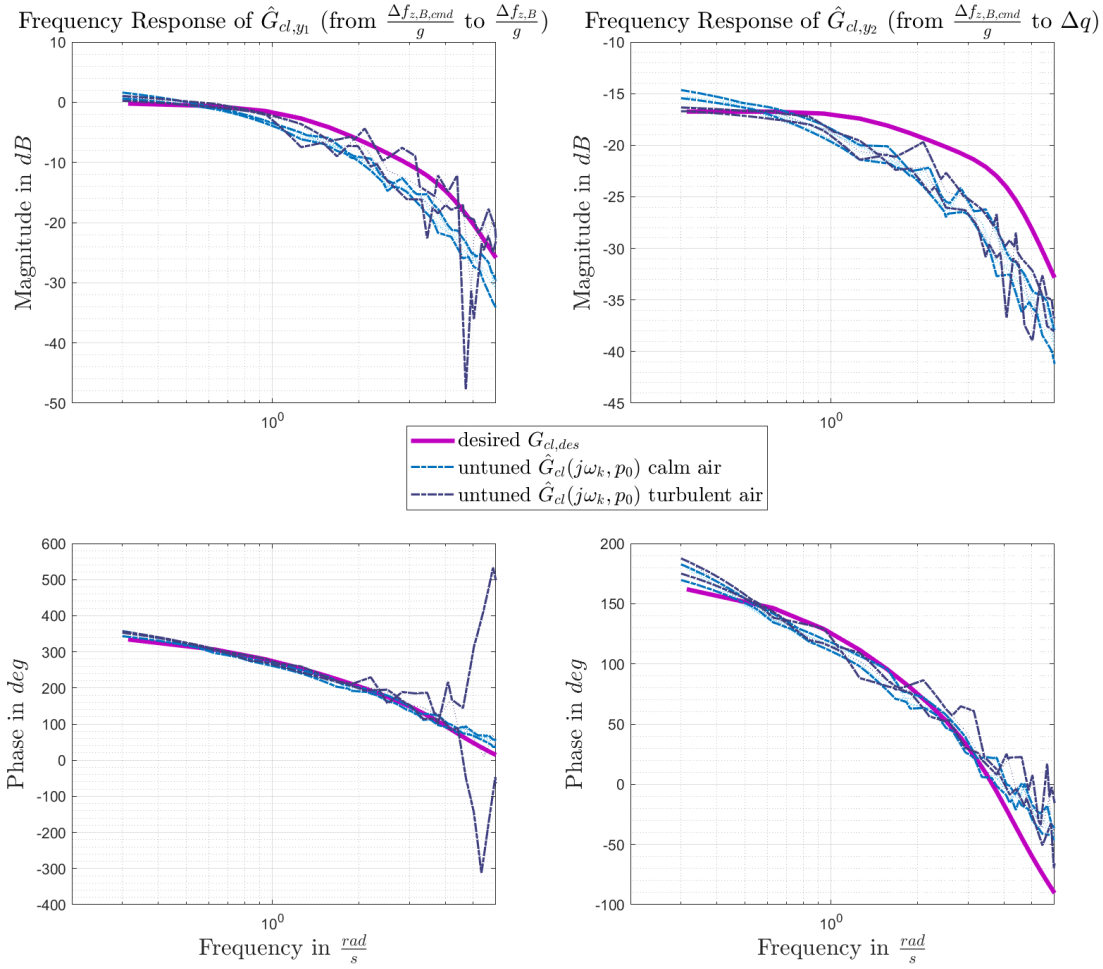

Figure 4.18: *Untuned closed-loop ETFE in calm and turbulent air.*

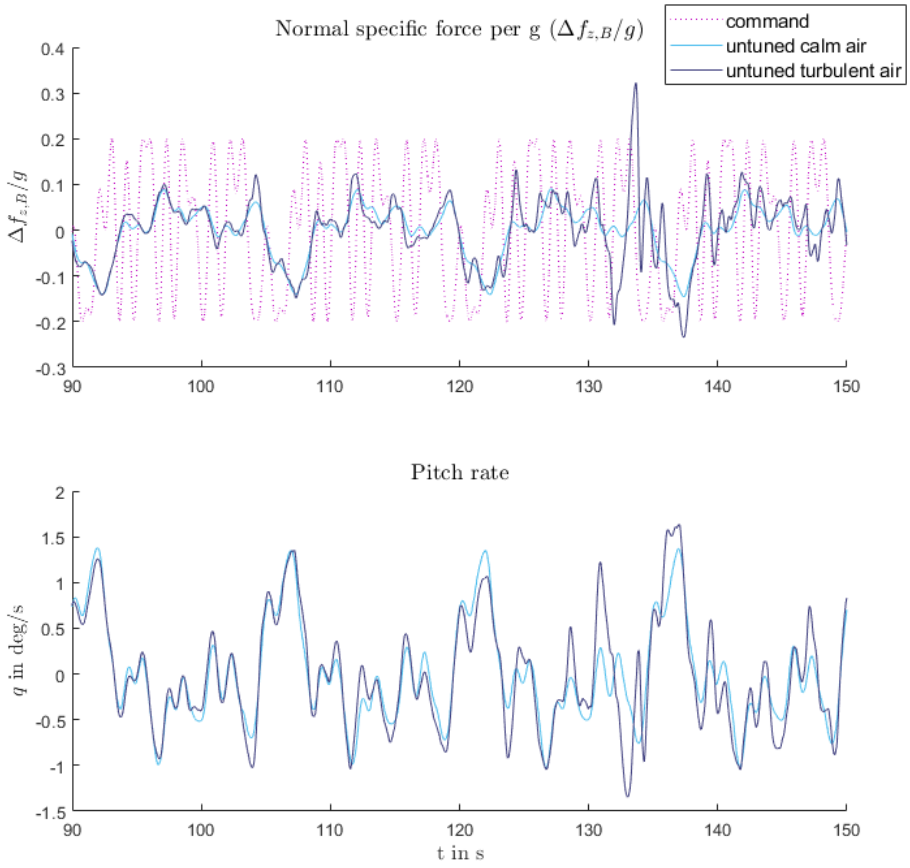

Figure 4.19: *Longitudinal time domain closed-loop responses in calm and turbulent air.*

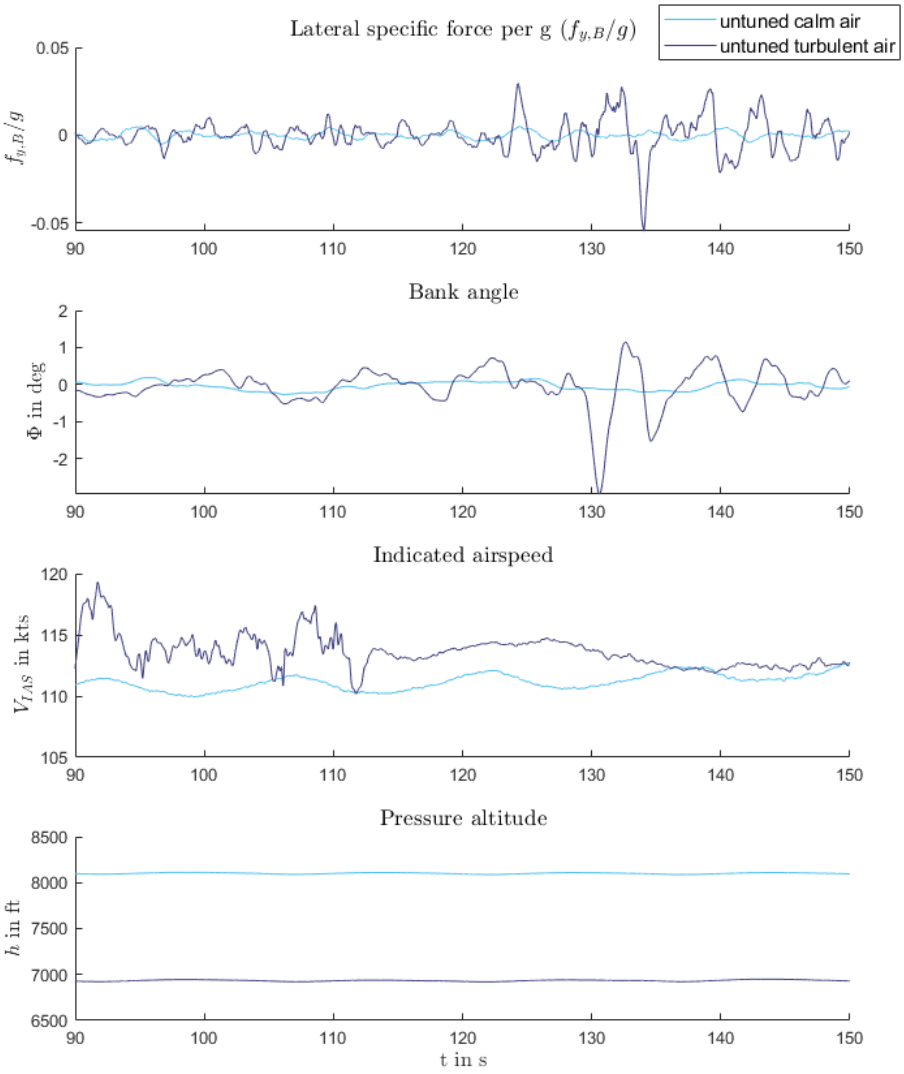

Figure 4.20: *Lateral time domain closed-loop responses, indicated airspeed and altitude in calm and turbulent air.*

4.4.5.6 Retuning Result

After the retuning, where the optimization was set-up as described in Section 4.4.5.3, several repeated flight test experiments were performed with the updated tuned controller parameters to determine how the updated closed-loop response compares to the desired design response and the anticipated, tuned closed-loop response. The tuned controller parameters are shown in Table 4.4. Figure 4.21 compares the initial closed-loop response, obtained from flight test with the initial gains, to the anticipated closed-loop response with tuned gains, and the actual tuned closed-loop response, obtained from flight test with the tuned controller parameters. Six flight test experiments (three with multi-sine 166 and three with multisine 168) were carried out providing six estimates of the initial closed-loop. One closed-loop estimate was chosen to optimize the controller parameters. The anticipated closed-loop estimates in Figure 4.21 were calculated based on the tuned controller parameters and the six initial closed-loop estimates. The same flight test experiments were carried out to estimate the closed-loop response with the updated, tuned gains.

Figure 4.21 shows that the controller parameters are optimized such, that the anticipated tuned closed-loop response is placed on top of the desired response. More importantly, Figure 4.21 shows that the actual ETFE's of the tuned closed-loop responses are on top of both the anticipated and the desired one. This demonstrates the capabilities of this flight test-based gain retuning approach."][end of quotation from my manuscript [SSG$^+$]]

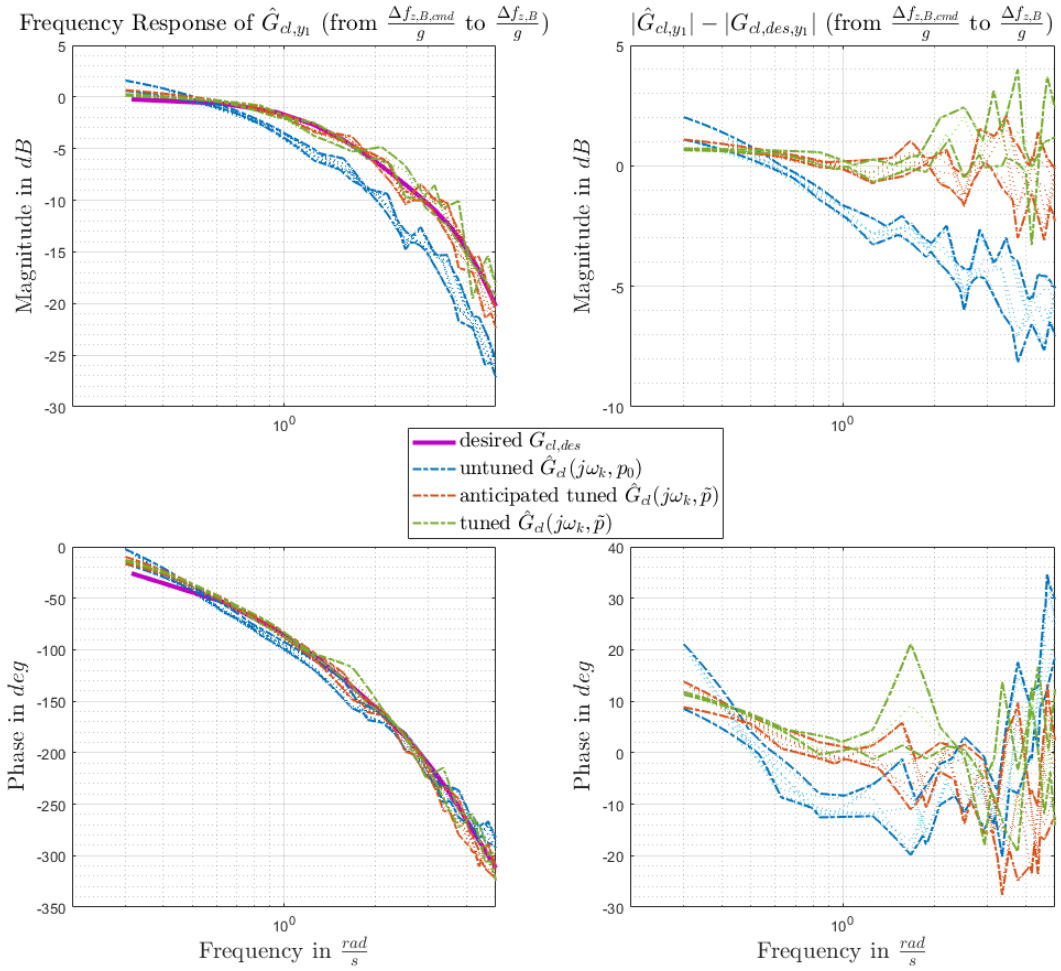

Figure 4.21: *Untuned closed-loop ETFE versus tuned ETFE and anticipated tuned closed-loop frequency response.*

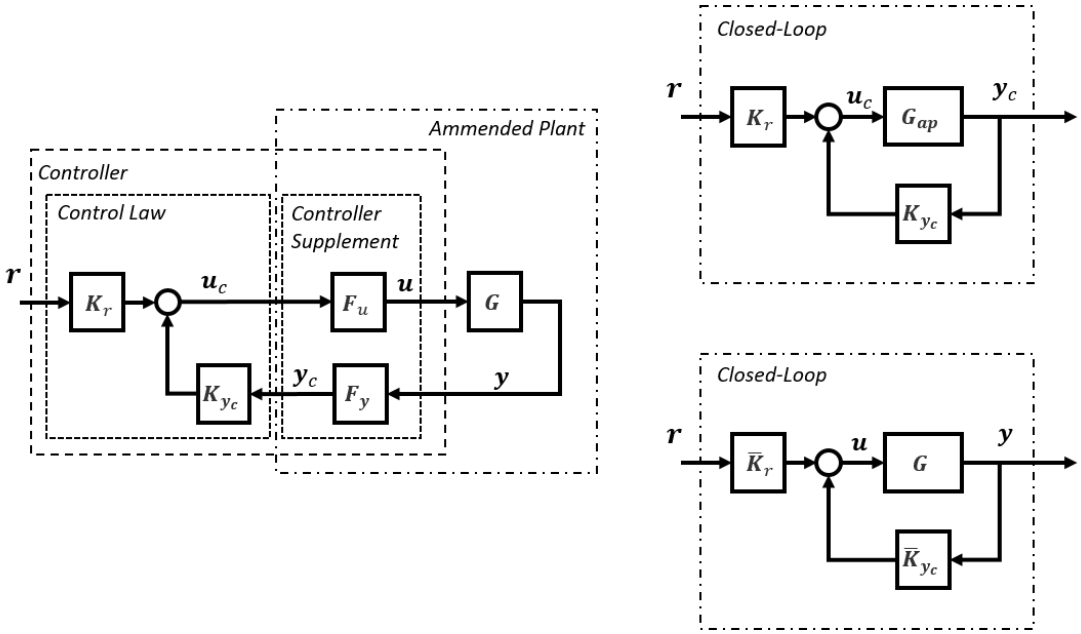

Figure 4.22: *Lateral inner-loop controller structure and closed-loop representations.*

4.5 Lateral Inner-loop

The following section describes the lateral inner-loop controller, which controls the aircraft's lateral motion. In Section 4.5.1 the control law is presented and in Section 4.5.2 several closed-loop and open-loop relations are presented, that are used within the test based gain retuning to estimate the anticipated margins, the amended plant and the anticipated closed-loop response.

4.5.1 Control Law and Controller Structure

The controller structure of the lateral inner-loop is depicted in the left picture in Figure 4.22. The closed-loop representations in the pictures on the right-hand side in Figure 4.22, expressed in terms of amended plant with control law (upper picture) and plant with amended controller (lower picture), will be explained in Section 4.5.2. The controller is composed, as can be seen in the left picture in Figure 4.22, of the control law and another component denoted as controller supplement, which consists of structural filters and roll off filters, turn compensation and a mapping from the control law output to actuator commands, which is scheduled over indicated airspeed. The linear control law can be expressed by continuous linear time-invariant (LTI) models in Laplace domain by

$$\boldsymbol{u}_c(s) = \begin{bmatrix} \boldsymbol{K}_r(s,\boldsymbol{p}) & \boldsymbol{K}_{y_c}(s,\boldsymbol{p}) \end{bmatrix} \begin{bmatrix} \boldsymbol{r}(s) \\ \boldsymbol{y}_c(s) \end{bmatrix} \tag{4.27}$$

where $\boldsymbol{r}(s)$, $\boldsymbol{y}_c(s)$, $\boldsymbol{u}_c(s)$ denote the Laplace-transforms of the following time-dependent signals:

- $\boldsymbol{r}(s)$: is a vector with the reference inputs, i.e. a bank angle command and a specific force command in the y-axis direction of the body fixed frame, normalized with respect to the gravitational acceleration g: $\boldsymbol{r}(t) = \begin{pmatrix} \Phi_{cmd}(t) & f_{y,B,cmd}(t)/g \end{pmatrix}^T$.
- $\boldsymbol{y}_c(s)$: is a vector with the feedback signals used within the control law, i.e. $\boldsymbol{y}_c(t) = \begin{pmatrix} \Phi(t) & \Delta p(t) & \Delta r(t) & f_{y,B}(t)/g \end{pmatrix}^T$. It is an output of the controller supplement subsystem, with the processed bank angle Φ, roll and yaw rate Δp and Δr, and processed specific force measurement $f_{y,B}/g$. The delta in the rates refers to increments with respect to the turn values $p_{turn} = -\dot{\Psi}\sin\Theta$ and $r_{turn} = \dot{\Psi}\cos\Phi\cos\Theta$ with $\dot{\Psi} = g/V\tan\Phi$.
- $\boldsymbol{u}_c(s)$: is the output of the control law and corresponds to a roll and yaw rate acceleration command, $\boldsymbol{u}_c(t) = \begin{pmatrix} \dot{p}_{cmd}(t) & \dot{r}_{cmd}(t) \end{pmatrix}^T$.

The plant input is the desired aileron and rudder drivetrain commands $\begin{pmatrix} \xi_{dt,cmd}(t) & \zeta_{dt,cmd}(t) \end{pmatrix}^T$, which is mapped within the controller supplement component $\boldsymbol{F}_u$ from the roll and yaw rate acceleration commands provided by the control law.

The control law corresponds to a classical linear PI-type controller with integral action on the tracking error in bank angle and lateral specific force, feedback of bank angle, roll and yaw rate and lateral specific force and a feed forward of the specific force command and bank angle command, providing additional degrees of freedom. The transfer function $\boldsymbol{K}_r(s, \boldsymbol{p})$ in Equation (4.27) describes the behavior from the reference input to the control law output and is given by

$$\boldsymbol{K}_r(s, \boldsymbol{p}) = \begin{bmatrix} (p_{\dot{p}\phi_c} + \frac{p_{I,\dot{p}\phi}}{s}) & p_{\dot{p}f_{y,c}} \\ p_{\dot{r}\phi_c} & (p_{\dot{r}f_{y,c}} + \frac{p_{I,\dot{r}f_y}}{s}) \end{bmatrix} \tag{4.28}$$

The Transfer function matrix (TFM) $\boldsymbol{K}_{y_c}(s, \boldsymbol{p})$ defines the response from feedback signals to the control law output. It is given by

$$\boldsymbol{K}_{y_c}(s, \boldsymbol{p}) = \begin{bmatrix} (p_{\dot{p}\phi} - \frac{p_{I,\dot{p}\phi}}{s}) & p_{\dot{p}p} & p_{\dot{p}r} & p_{\dot{p}f_y} \\ p_{\dot{r}\phi} & p_{\dot{r}p} & p_{\dot{r}r} & (p_{\dot{r}f_y} - \frac{p_{I,\dot{r}f_y}}{s}) \end{bmatrix}. \tag{4.29}$$

The parameter vector

$$\boldsymbol{p} = [\boldsymbol{p}_H, \boldsymbol{p}_I, \boldsymbol{p}_K] \tag{4.30}$$

comprises the feed-forward gains

$$\boldsymbol{p}_H = \begin{bmatrix} p_{\dot{p}\phi_c} & p_{\dot{p}f_{y,c}} & p_{\dot{r}\phi_c} & p_{\dot{r}f_{y,c}} \end{bmatrix}, \tag{4.31}$$

the integrator gains

$$\boldsymbol{p}_I = \begin{bmatrix} p_{I,\dot{p}\phi} & p_{I,\dot{r}f_y} \end{bmatrix} \tag{4.32}$$

and the feedback gains

$$\boldsymbol{p}_K = \begin{bmatrix} p_{\dot{p}\phi} & p_{\dot{p}p} & p_{\dot{p}r} & p_{\dot{p}f_y} & p_{\dot{r}\phi} & p_{\dot{r}p} & p_{\dot{r}r} & p_{\dot{r}f_y} \end{bmatrix} \tag{4.33}$$

In the following sections, the dependence of Laplace operator s and time t is omitted, whenever the context is clear.

4.5.2 Closed-loop and Open-loop Relations

The Transfer function matrix (TFM) from the control law output signals $\boldsymbol{u}_c$ to the feedback signals $\boldsymbol{y}_c$ in open-loop is denoted as the amended plant with representation in the Laplace domain, given by

$$\boldsymbol{y}_c(s) = \boldsymbol{G}_{\text{ap}}(s)\boldsymbol{u}_c(s). \tag{4.34}$$

where

$$\boldsymbol{G}_{\text{ap}}(s) = \boldsymbol{F}_y(s)\,\boldsymbol{G}(s)\,\boldsymbol{F}_u(s) \tag{4.35}$$

see Figure 4.22. The closed-loop LTI system is represented by the **closed-loop TFM** $\boldsymbol{G}_{\text{cl}}(s,\boldsymbol{p})$ from the reference input signal vector $\boldsymbol{r}$ to the feedback signal vector $\boldsymbol{y}_c$

$$\boldsymbol{y}_c(s) = \boldsymbol{G}_{\text{cl}}(s,\boldsymbol{p})\boldsymbol{r}(s) \tag{4.36}$$

where $\boldsymbol{G}_{\text{cl}}(s,\boldsymbol{p})$ is given by

$$\boldsymbol{G}_{\text{cl}}(s,\boldsymbol{p}) = \Big[\boldsymbol{I} - \boldsymbol{G}_{\text{ap}}(s)\,\boldsymbol{K}_{y_c}(s,\boldsymbol{p})\Big]^{-1}\boldsymbol{G}_{\text{ap}}(s)\,\boldsymbol{K}_r(s,\boldsymbol{p}) \tag{4.37}$$

This relation can be deduced from the block diagram in Fig. 4.22, as follows. First, the control law $\boldsymbol{u}_c$ given by (4.27) in (4.34) results in

$$\boldsymbol{y}_c(s) = \boldsymbol{G}_{\text{ap}}(s)\Big(\boldsymbol{K}_r(s,\boldsymbol{p})\boldsymbol{r}(s) + \boldsymbol{K}_{y_c}(s,\boldsymbol{p})\boldsymbol{y}_c(s)\Big) \tag{4.38}$$

By solving Equation (4.38) for $\boldsymbol{y}_c$ finally the relation in (4.37) and (4.36), which we wanted to show, is obtained:

$$\boldsymbol{y}_c(s) = \Big[\boldsymbol{I} - \boldsymbol{G}_{\text{ap}}(s)\,\boldsymbol{K}_{y_c}(s,\boldsymbol{p})\Big]^{-1}\boldsymbol{G}_{\text{ap}}(s)\,\boldsymbol{K}_r(s,\boldsymbol{p})\boldsymbol{r}(s) \tag{4.39}$$

Hence, the result.
Alternatively, the closed-loop TFM $\boldsymbol{G}_{\text{cl}}(s,\boldsymbol{p})$ can be expressed by

$$\boldsymbol{G}_{\text{cl}}(s,\boldsymbol{p}) = \Big[\boldsymbol{I} - \boldsymbol{G}(s)\,\bar{\boldsymbol{K}}_{y_c}(s,\boldsymbol{p})\Big]^{-1}\boldsymbol{G}(s)\,\bar{\boldsymbol{K}}_r(s,\boldsymbol{p}) \tag{4.40}$$

where

$$\begin{aligned}\bar{\boldsymbol{K}}_{y_c}(s,\boldsymbol{p}) &= \boldsymbol{F}_u(s)\boldsymbol{K}_{y_c}(s,\boldsymbol{p})\boldsymbol{F}_y(s)\\ \bar{\boldsymbol{K}}_r(s,\boldsymbol{p}) &= \boldsymbol{F}_u(s)\boldsymbol{K}_r(s,\boldsymbol{p})\end{aligned} \tag{4.41}$$

see Figure 4.22.

The **amended plant TFM** can be expressed as a function of the closed-loop TFM and the controller according to

$$\boldsymbol{G}_{\mathrm{ap}}(s) = \boldsymbol{G}_{\mathrm{cl}}(s,\boldsymbol{p})\left[\boldsymbol{K}_r(s,\boldsymbol{p}) + \boldsymbol{K}_{y_c}(s,\boldsymbol{p})\boldsymbol{G}_{\mathrm{cl}}(s,\boldsymbol{p})\right]^{-1} \tag{4.42}$$

This relation can be deduced by solving Equation (4.37) for $\boldsymbol{G}_{\mathrm{ap}}$: First multiply (4.37) with $\left[\boldsymbol{I} - \boldsymbol{G}_{\mathrm{ap}}(s)\,\boldsymbol{K}_{y_c}(s,\boldsymbol{p})\right]$ from the left:

$$\begin{aligned}\left[\boldsymbol{I} - \boldsymbol{G}_{\mathrm{ap}}(s)\,\boldsymbol{K}_{y_c}(s,\boldsymbol{p})\right]\boldsymbol{G}_{\mathrm{cl}}(s,\boldsymbol{p}) &= \boldsymbol{G}_{\mathrm{ap}}(s)\,\boldsymbol{K}_r(s,\boldsymbol{p})\\ \boldsymbol{G}_{\mathrm{cl}}(s,\boldsymbol{p}) - \boldsymbol{G}_{\mathrm{ap}}(s)\,\boldsymbol{K}_{y_c}(s,\boldsymbol{p})\,\boldsymbol{G}_{\mathrm{cl}}(s,\boldsymbol{p}) &= \boldsymbol{G}_{\mathrm{ap}}(s)\,\boldsymbol{K}_r(s,\boldsymbol{p})\end{aligned} \tag{4.43}$$

Then add $\boldsymbol{G}_{\mathrm{ap}}(s)\,\boldsymbol{K}_{y_c}(s,\boldsymbol{p})\boldsymbol{G}_{\mathrm{cl}}(s,\boldsymbol{p})$:

$$\begin{aligned}\boldsymbol{G}_{\mathrm{cl}}(s,\boldsymbol{p}) &= \boldsymbol{G}_{\mathrm{ap}}(s)\,\boldsymbol{K}_r(s,\boldsymbol{p}) + \boldsymbol{G}_{\mathrm{ap}}(s)\,\boldsymbol{K}_{y_c}(s,\boldsymbol{p})\,\boldsymbol{G}_{\mathrm{cl}}(s,\boldsymbol{p})\\ \boldsymbol{G}_{\mathrm{cl}}(s,\boldsymbol{p}) &= \boldsymbol{G}_{\mathrm{ap}}(s)\left[\boldsymbol{K}_r(s,\boldsymbol{p}) + \boldsymbol{K}_{y_c}(s,\boldsymbol{p})\,\boldsymbol{G}_{\mathrm{cl}}(s,\boldsymbol{p})\right]\end{aligned} \tag{4.44}$$

Finally, multiplication from the right with the inverse of $\left[\boldsymbol{K}_r(s,\boldsymbol{p}) + \boldsymbol{K}_{y_c}(s,\boldsymbol{p})\,\boldsymbol{G}_{\mathrm{cl}}(s,\boldsymbol{p})\right]$ results in Equation (4.42). Hence the result.

Similarly, the **plant TFM** can be expressed as a function of the closed-loop TFM and the amended controller, Equation (4.41), according to

$$\boldsymbol{G}(s) = \boldsymbol{G}_{\mathrm{cl}}(s,\boldsymbol{p})\left[\bar{\boldsymbol{K}}_r(s,\boldsymbol{p}) + \bar{\boldsymbol{K}}_{y_c}(s,\boldsymbol{p})\boldsymbol{G}_{\mathrm{cl}}(s,\boldsymbol{p})\right]^{-1} \tag{4.45}$$

The **stability margins** are calculated at the actuator positions, as depicted in Figure 4.23, based on the loop-cut $G_{\xi,cut}$ at the aileron u_1 and the loop cut $G_{\zeta,cut}$ at the rudder u_2, respectively. These actuator cuts can be calculated by

$$\begin{aligned}G_{\xi,\mathrm{cut}} &= \frac{L_{11}(1-L_{22}) + L_{12}L_{21}}{(1-L_{22})}\\ G_{\zeta,\mathrm{cut}} &= \frac{L_{22}(1-L_{11}) + L_{12}L_{21}}{(1-L_{11})}\end{aligned} \tag{4.46}$$

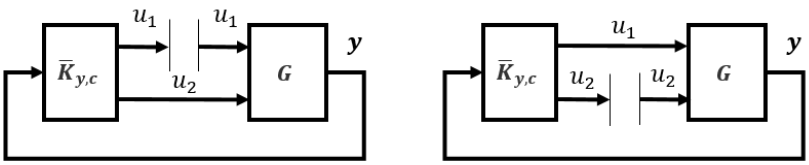

Figure 4.23: *Actuator cuts for calculation of stability margins.*

where

$$\boldsymbol{L} = \begin{bmatrix} L_{11} & L_{12} \\ L_{21} & L_{22} \end{bmatrix} = \bar{\boldsymbol{K}}_{y_c}\boldsymbol{G} \tag{4.47}$$

Note, that the dependency on the Laplace operator and the parameter vector was omitted here for better readability. These relations for $G_{\xi,cut}$ and $G_{\zeta,cut}$ can be deduced from Figure 4.23 as follows. Based on the relation

$$\begin{bmatrix} u_1 \\ u_2 \end{bmatrix} = \bar{\boldsymbol{K}}_{y_c}\boldsymbol{G}\begin{bmatrix} u_1 \\ u_2 \end{bmatrix} = \begin{bmatrix} L_{11} & L_{12} \\ L_{21} & L_{22} \end{bmatrix}\begin{bmatrix} u_1 \\ u_2 \end{bmatrix} \tag{4.48}$$

the closed-loop relation for the rudder u_2 is obtained by solving

$$u_2 = L_{21}u_1 + L_{22}u_2 \tag{4.49}$$

for u_2, which results in

$$u_2 = \frac{L_{21}}{(1 - L_{22})}u_1 \tag{4.50}$$

Relation (4.50) is substituted into

$$u_1 = L_{11}u_1 + L_{12}u_2 = L_{11}u_1 + L_{12}\frac{L_{21}}{(1 - L_{22})}u_1 = \frac{L_{11}(1 - L_{22}) + L_{12}L_{21}}{(1 - L_{22})}u_1 \tag{4.51}$$

Hence the result for the aileron cut $G_{\xi,cut}$. The rudder cut $G_{\zeta,cut}$ is obtained in similar manner.

4.5.3 Testbased Gain Retuning for Lateral Inner-loop

4.5.3.1 Desired Closed-loop

The linear nominal closed-loop system, denoted as $\boldsymbol{G}_{\mathrm{cl,nom}}(s, \boldsymbol{p}_0)$, that is composed of the initial lateral inner-loop controller, $\boldsymbol{K}_r(s, \boldsymbol{p}_0)$, $\boldsymbol{K}_{y_c}(s, \boldsymbol{p}_0)$, and the nominal linear lateral amended plant model $\boldsymbol{G}_{\mathrm{ap,nom}}(s)$, is used as design model for the synthesis of the lateral autopilot control laws. Therefore, it is desired that the closed-loop frequency response of retuned controller and true plant corresponds to $\boldsymbol{G}_{\mathrm{cl,nom}}(s, \boldsymbol{p}_0)$. Hence, the desired closed-loop frequency response is the frequency response of $\boldsymbol{G}_{\mathrm{cl,nom}}(s, \boldsymbol{p}_0)$.

The initial controller is designed using classical linear gain design methods, based on the linear lateral amended plant model including roll, spiral and dutch roll dynamics. This linear lateral amended plant model is obtained based on the high fidelity 6DoF nonlinear model of the aircraft, using the developed tool chain. First, the nonlinear flight dynamics model is trimmed for horizontal wings-level flight. Using these trim results the high fidelity 6DoF nonlinear model is linearized from $\boldsymbol{u}_c$ to $\boldsymbol{y}_c$, see Figure 4.22, including the following components

- roll, spiral and dutch roll dynamics
- actuator models for aileron and rudder, modelled as second order systems according to

$$G_{act,k}(s) = \frac{\omega_{act,k}^2}{s^2 + 2\zeta_{act,k}\omega_{act,k}s + \omega_{act,k}^2} \tag{4.52}$$

  for $k = \xi, \zeta$, where the parameters $\omega_{act,k}$ and $\zeta_{act,k}$ were obtained from ground tests with the actuation
- a mapping from aileron and rudder deflection commands to the respective actuator position commands obtained from ground tests with the actuation
- a mapping from actuator position to surface deflections, obtained from ground tests with the actuation
- aeroelastic modes modelled as low damped second order filters according to

$$G_{mode}(s) = \frac{\omega_{mode}^2}{s^2 + 2\zeta_{mode}\omega_{mode}s + \omega_{mode}^2} \tag{4.53}$$

  where ω_{mode} and ζ_{mode} were obtained from flutter data provided by the air manufacturer for the first aeroelastic bending mode. The rates and specific force of the nonlinear flight dynamics model were filtered by $G_{mode}(s)$ before they were fed into the controller.
- roll-off filters for all measurement signals, modelled as second order system according to

$$G_{fil}(s) = \frac{\omega_{fil}^2}{s^2 + 2\zeta_{fil}\omega_{fil}s + \omega_{fil}^2} \tag{4.54}$$

  with ω_{fil} and ζ_{fil} chosen to obtain sufficient noise attenuation.
- notch filters modelled according to

$$G_{mode}(s) = \frac{s^2 + 2\zeta_{num}\omega_{num}s + \omega_{num}^2}{s^2 + 2\zeta_{den}\omega_{den}s + \omega_{den}^2} \tag{4.55}$$

where the parameters where chosen to prevent excitation of the modes by the controller and to realize sufficient attenuation of the open-loop frequency response at frequencies around the first aeroelastic bending mode frequency

- a mapping from control law output $\boldsymbol{u}_c$ to aileron and rudder deflection commands, scheduled over indicated airspeed.

The resulting lateral linear model, i.e the amended plant depicted in Figure 4.22, was used for the synthesis of the lateral control law. Initial controller parameters were obtained using Eigenstructure Assignement.

The resulting closed-loop response was assessed against requirements for the inner-loop controller. The requirements were given by adequate and desired values for the stability margins of the open-loop system with loop-cuts at the actuators as specified in the AS94900, [SAE07], which is the SAE standard for flight control system design. Other requirements defined limits on the bandwidth and overshoot and were defined by the outer-loops. In addition, maximum lateral acceleration values were specified at steady bank angles as well as during roll. Desired values were chosen to give better performance and robustness, while the adequate values are given as the minimum that needs to be satisfied.

4.5.3.2 Initial Closed-loop ETFE

The initial closed-loop TFM estimate is obtained by averaged ETFE's as described in Section 3.5, by two separate experiments. In the first experiment a multi-sinusoidal excitation signal, described in Section 3.4, is injected for the bank angle command. In the second experiment a multi- sinusoidal excitation signal is injected for the lateral specific force command. For both experiments the feedback signals given in $\boldsymbol{y}_c$ are measured and the respective ETFE's from each reference signal to each output signal are calculated by Equation (3.18) at the discrete frequencies ω_k, defined by the parametrization of the multi-sine signal. The obtained ETFE's are then composed to the closed-loop frequency response TFM $\hat{\boldsymbol{G}}_{cl,0}(j\omega_k)$.

4.5.3.3 Amended Plant Estimate

Based on the estimated closed-loop frequency response $\hat{\boldsymbol{G}}_{\mathrm{cl},0}(j\omega_k)$, described above, the indirect non-parametric frequency response estimate of the amended plant $\hat{\boldsymbol{G}}_{\mathrm{ap}}(j\omega_k)$ can be calculated. This is possible, because the controller parameters $\boldsymbol{p}_0$ that were applied in the flight tests for estimating $\hat{\boldsymbol{G}}_{cl,0}(j\omega_k)$, and thus the controller frequency responses $\boldsymbol{K}_r(j\omega, \boldsymbol{p}_0)$ and $\boldsymbol{K}_{y_c}(j\omega, \boldsymbol{p}_0)$ are exactly known and because the control law is linear. The frequency response of the amended plant is estimated, using relation (4.42), by

$$\hat{\boldsymbol{G}}_{\mathrm{ap}}(j\omega_k) = \hat{\boldsymbol{G}}_{\mathrm{cl},0}(j\omega_k)\left[\boldsymbol{K}_r(j\omega_k, \boldsymbol{p}_0) + \boldsymbol{K}_{y_c}(j\omega_k, \boldsymbol{p}_0)\hat{\boldsymbol{G}}_{\mathrm{cl},0}(j\omega_k)\right]^{-1} \tag{4.56}$$

4.5.3.4 Plant Estimate

Based on the estimated closed-loop frequency response $\hat{\boldsymbol{G}}_{\mathrm{cl},0}(j\omega_k)$, described in Section 4.5.3.2, the indirect non-parametric frequency response estimate of the plant, $\hat{\boldsymbol{G}}(j\omega_k)$, can be calculated. This is possible because the controller parameters $\boldsymbol{p}_0$ that were applied in the flight tests for estimating $\hat{\boldsymbol{G}}_{cl,0}(j\omega_k)$, and thus the controller frequency responses $\boldsymbol{K}_r(j\omega, \boldsymbol{p}_0)$ and $\boldsymbol{K}_{y_c}(j\omega, \boldsymbol{p}_0)$, as well as $\boldsymbol{F}_u(j\omega)$ and $\boldsymbol{F}_y(j\omega)$ are exactly known. The frequency response of the plant is estimated, using relation (4.45), by

$$\hat{\boldsymbol{G}}(j\omega_k) = \hat{\boldsymbol{G}}_{\mathrm{cl},0}(j\omega_k) \left[\bar{\boldsymbol{K}}_r(j\omega_k, \boldsymbol{p}_0) + \bar{\boldsymbol{K}}_{y_c}(j\omega_k, \boldsymbol{p}_0)\hat{\boldsymbol{G}}_{\mathrm{cl},0}(j\omega_k)\right]^{-1} \tag{4.57}$$

with $\bar{\boldsymbol{K}}_{y_c}$ and $\bar{\boldsymbol{K}}_r$ given by Equation (4.41).

4.5.3.5 Anticipated Closed-loop Estimate

The anticipated closed-loop estimate for a parameter set $\boldsymbol{p}$ is calculated based on the amended plant estimate $\hat{\boldsymbol{G}}_{\mathrm{ap}}(j\omega_k)$, (4.56), and based on the controller frequency responses $\boldsymbol{K}_r(j\omega, \boldsymbol{p})$ and $\boldsymbol{K}_{y_c}(j\omega, \boldsymbol{p})$. It is calculated, using the relation given by Equation (4.37), by

$$\hat{\boldsymbol{G}}_{\mathrm{cl}}(j\omega_k, \boldsymbol{p}) = \left[\boldsymbol{I} - \hat{\boldsymbol{G}}_{\mathrm{ap}}(j\omega_k)\, \boldsymbol{K}_{y_c}(j\omega_k, \boldsymbol{p})\right]^{-1} \hat{\boldsymbol{G}}_{\mathrm{ap}}(j\omega_k)\, \boldsymbol{K}_r(j\omega_k, \boldsymbol{p}) \tag{4.58}$$

4.5.3.6 Anticipated Margins

An estimate of the anticipated stability margins for a parameter set $\boldsymbol{p}$ is obtained by calculating the gain and phase margins of the actuator cut frequency response estimates $\hat{G}_{\xi,\mathrm{cut}}(j\omega_k, \boldsymbol{p})$ and $\hat{G}_{\zeta,\mathrm{cut}}(j\omega_k, \boldsymbol{p})$. These estimates are calculated, using the relations given in Equation (4.46), by

$$\begin{aligned}
\hat{G}_{\xi,\mathrm{cut}}(j\omega_k, \boldsymbol{p}) &= \frac{\hat{L}_{11}(j\omega_k, \boldsymbol{p})(1 - \hat{L}_{22}(j\omega_k, \boldsymbol{p})) + \hat{L}_{12}(j\omega_k, \boldsymbol{p})\hat{L}_{21}(j\omega_k, \boldsymbol{p})}{(1 - \hat{L}_{22}(j\omega_k, \boldsymbol{p}))} \\
\hat{G}_{\zeta,\mathrm{cut}}(j\omega_k, \boldsymbol{p}) &= \frac{\hat{L}_{22}(j\omega_k, \boldsymbol{p})(1 - \hat{L}_{11}(j\omega_k, \boldsymbol{p})) + \hat{L}_{12}(j\omega_k, \boldsymbol{p})\hat{L}_{21}(j\omega_k, \boldsymbol{p})}{(1 - \hat{L}_{11}(j\omega_k, \boldsymbol{p}))}
\end{aligned} \tag{4.59}$$

where $\boldsymbol{L}$ is estimated by

$$\hat{\boldsymbol{L}}(j\omega_k, \boldsymbol{p}) = \begin{bmatrix} \hat{L}_{11}(j\omega_k, \boldsymbol{p}) & \hat{L}_{12}(j\omega_k, \boldsymbol{p}) \\ \hat{L}_{21}(j\omega_k, \boldsymbol{p}) & \hat{L}_{22}(j\omega_k, \boldsymbol{p}) \end{bmatrix} = \bar{\boldsymbol{K}}_{y_c}(j\omega_k, \boldsymbol{p})\hat{\boldsymbol{G}}(j\omega_k) \tag{4.60}$$

using the plant estimate, Equation (4.57), and the amended controller calculated by Equation (4.41).

4.5.3.7 Optimization Problem

The optimization problem is described in detail in Section 3.8 for a SISO closed-loop system. The lateral controller is a MIMO system, with two inputs and four outputs. The objective of the retuning is to improve the bank angle tracking. Therefore, the cost function is adapted as follows

$$J(\boldsymbol{p}) = \sum_{i=1}^{4}\{\frac{20}{n_\omega}\sum_{k=1}^{n_\omega}(\mathrm{w}_{\gamma,y_i}(\omega_k)\left[\mathrm{w}_A\Delta_{|G_{cl,y_i\Phi_c}|} + \mathrm{w}_\phi\Delta_{\angle G_{cl,y_i\Phi_c}}\right])\} + (\boldsymbol{p}-\boldsymbol{p}_0)\,\boldsymbol{Q}\,(\boldsymbol{p}-\boldsymbol{p}_0)^T \tag{4.61}$$

with

$$\begin{aligned}\Delta_{|G_{cl,y_i\Phi_c}|} &= (\left|\hat{G}_{cl,y_i\Phi_c}(j\omega_k,\boldsymbol{p})\right| - \left|G_{cl,des,y_i\Phi_c}(j\omega_k)\right|)^2\\ \Delta_{\angle G_{cl,y_i\Phi_c}} &= (\angle\hat{G}_{cl,y_i\Phi_c}(j\omega_k,\boldsymbol{p}) - \angle G_{cl,des,y_i\Phi_c}(j\omega_k))^2\end{aligned} \tag{4.62}$$

where $G_{\mathrm{cl,des},y_i\Phi_c}(j\omega_k)$ in Equation (4.62) represents the desired closed-loop frequency response at frequency ω_k from the reference input $r_1 = \Phi_c$ to each of the outputs y_i, $i = 1,2,3,4$ given in $\boldsymbol{y}_c$. $\hat{G}_{\mathrm{cl},y_i\Phi_c}(j\omega_k,\boldsymbol{p})$ represents the anticipated closed-loop response, for the gain set $\boldsymbol{p}$. It is represented by the elements of $\hat{\boldsymbol{G}}_{\mathrm{cl}}(j\omega_k,\boldsymbol{p})$, which is computed according to Equation (4.58) utilizing the estimate of the amended plant $\hat{\boldsymbol{G}}_{\mathrm{ap}}(j\omega_k)$ given by Equation (4.56). Note, that though the overall objective is to improve the tracking, i.e. the response from r_1 to y_1, the cost function also accounts for the responses from r_1 to the other feedback signals. With this strategy empirically better results could be obtained compared to using only the response from r to y_1 in the cost function. The remaining parameters and symbols in (4.62) and (4.61) are as defined in Section 3.8. The optimization problem is given by:

$$\begin{aligned}&\min_{\boldsymbol{p}}.\ J(\boldsymbol{p})\\ &st.\\ &c_{1,l}(\boldsymbol{p}) = A_m - \hat{A}_{m,l}(\boldsymbol{p}) \le 0\\ &c_{2,l}(\boldsymbol{p}) = \Phi_m - \hat{\Phi}_{m,l}(\boldsymbol{p}) \le 0\\ &\text{for } l = 1,2\end{aligned} \tag{4.63}$$

where $\hat{A}_{m,l}(\boldsymbol{p})$ and $\hat{\Phi}_{m,l}(\boldsymbol{p})$ are the anticipated margins for the aileron and rudder cut for the new parameter set $\boldsymbol{p}$, respectively, as described in Section 4.5.3.6, and A_m and Φ_m are the adequate margin values.

The cost function $J(\boldsymbol{p})$ is minimized with respect to the controller parameters $\boldsymbol{p}$ using the off-the-shelf solver *fmincon* from MATLAB. Upper and lower bounds are given for the parameter vector $\boldsymbol{p}$. The constraints ensure that the resulting gains lead to anticipated phase and gain margins larger or equal to the adequate margins. The posed optimization

problem is not convex. Further, no formal proof yet was made to show that this optimization will converge or reveal the global minimum. However, it can be verified by inspecting the resulting anticipated and the initial closed-loop response if the new parameters are better than the initial parameters. It is shown by Monte Carlo simulation in the following sections that the problem at hand converged to a solution which is better than the initial guess. Furthermore, the problem at hand is not computational complex and with a usual desktop pc it can be solved within a few minutes. However, as the problem is solved off-line, there exist no demanding time constraints.

4.5.4 Simulation Results

The following section presents the simulation results of the proposed controller retuning based on a full 6DoF nonlinear simulation model. Figure 4.7 shows the setup and nomenclature of the simulations, which are explained in detail in Section 4.4.4. In the following simulation results are shown for the G-520T testbed, see Section 4.1.3.

4.5.4.1 General Settings - Uncertainties

For the following analysis, the aerodynamic uncertainties were considered to be multiplicative on the following aerodynamic derivatives:

C_{lp} Roll moment coefficient due to roll rate (p).

C_{lr} Roll moment coefficient due to yaw rate (r).

$C_{l\xi}$ Roll moment coefficient due to aileron deflection (ξ).

$C_{l\zeta}$ Roll moment coefficient due to rudder deflection (ζ).

C_{nr} Yaw moment coefficient due to yaw rate (r).

$C_{n\beta}$ Yaw moment coefficient due to sideslip angle (β).

$C_{n\xi}$ Yaw moment coefficient due to aileron deflection (ξ).

$C_{n\zeta}$ Yaw moment coefficient due to rudder deflection (ζ).

For simulations where one uncertainty set was considered, Table 4.6 summarizes the values of the multiplicative factors that were applied to all coefficients. For the Monte Carlo simulations with regard to aerodynamic uncertainties, the multiplicative factors were uniformly distributed in the range given in Table 4.7. The uncertainty range is chosen to be spread around the parameter value, as expected from initial flight tests, and not around the nominal value used within the model and initial controller design. Additionally, the influence of a backlash element, that was applied at the aileron and rudder, was investigated. The backlash was varied within simulations between $0 - 1.2$ degrees.

Parameter	Uncertainty factor
C_{lp}	1.5
C_{lr}	1.02
$C_{l\xi}$	1.05
$C_{l\zeta}$	1.02
C_{nr}	1.02
$C_{n\beta}$	0.98
$C_{n\xi}$	0.98
$C_{n\zeta}$	1.0

Table 4.6: *Multiplicative factors on aerodynamic coefficients.*

Parameter	Uncertainty factor range
C_{lp}	1.6-2.4
C_{lr}	1.0-1.1
$C_{l\xi}$	0.8-1.2
$C_{l\zeta}$	1.0-1.3
C_{nr}	1.0-1.1
$C_{n\beta}$	0.9-1.0
$C_{n\xi}$	0.7-1.0
$C_{n\zeta}$	1.0

Table 4.7: *Range of multiplicative factors on aerodynamic coefficients within Monte Carlo simulations.*

4.5.4.2 General Settings - Reference Excitation Input Signal

The applied multi-sinusoidal excitation signal, injected at the reference input $\boldsymbol{r}$ is given by Equation (3.16). Its parametrization is summarized in Table 4.8, for each reference input (Φ_{cmd} and $f_{y,B,cmd}/g$), respectively. During each maneuver the other reference input was commanding a value of zero.

The considered frequency range is the same for both maneuvers and lies between $\omega_1 \approx 0.21\frac{rad}{s}$ and $\omega_{n_\omega} \approx 6.28\frac{rad}{s}$. The parametrization is chosen such that during the maneuver neither the actuator position limits nor the actuator rate limits are exceeded. Furthermore, the maneuver length is determined by simulations such that the drift from the test envelope point, given in terms of indicated airspeed and static pressure, remains within acceptable boundaries. These objectives are determined as a compromise with ensuring an adequate signal-to-noise by an adequate number of repetitions, an adequate excitation amplitude and an adequate frequency resolution of the estimates.

	Symbol	Φ_{cmd}	$f_{y,cmd}$
Amplitude	A	4 deg	0.01 g
Window length	T	30s	30s
Frequency set (excited harmonics)	$\mathbb{S}$	1,2,3,...,30	1,2,3,...,30
Number of periods (repetitions of maneuver)	N	7	5

Table 4.8: *Maneuver injection input signal parameters.*

4.5.4.3 General Settings - Optimization

The parametrization of the quadratic cost function in Equation (4.61) is chosen follows. The weighting matrix $\boldsymbol{Q}$ is chosen as a diagonal matrix with penalty values set to one for all controller parameters given in Equation (4.31), (4.32) and (4.33), except the weights for the feed forward gain $p_{\dot{p}\Phi_c}$, and the integral gains $p_{I,\dot{p}\Phi}$ and $p_{I,\dot{p}f_y}$ which were all set to 100. The weight for the feed forward gain $p_{\dot{r}f_y}$ was set to 1000.

For $y_1 = \Phi$ and $y_2 = \Delta p$ the same frequency dependent weights are chosen. They are given in Table 4.9. For $y_3 = \Delta r$ and $y_4 = f_y/g$ the frequency dependent weights in Table 4.10 are selected. The frequency dependent weights are chosen to achieve a good matching with the desired dynamics in the frequency range, where the bounds from the outer-loop are most tight. Frequencies, where the closed-loop dynamics are already well attenuated are weighted weakly. The remaining parameters are $\mathrm{w}_A = 1,\ \mathrm{w}_\phi = 0.01745$ as described in Section 3.8 and $A_m = 6dB,\ \Phi_m = 45°$.

$\omega_k[\frac{rad}{s}]$	< 0.05	$0.05 - 1$	$1 - 3$	> 3
$\mathrm{w}_{\gamma,y_1}(\omega_k) = \mathrm{w}_{\gamma,y_2}(\omega_k)$	0	100	1	0.1

Table 4.9: *Frequency dependent relative weights for frequency responses from bank angle command to bank angle and roll rate.*

$\omega_k[\frac{rad}{s}]$	< 0.1	$0.1 - 0.5$	$0.5 - 2$	$2 - 6$	> 6
$\mathrm{w}_{\gamma,y_3}(\omega_k) = \mathrm{w}_{\gamma,y_4}(\omega_k)$	10	20	30	20	0.1

Table 4.10: *Frequency dependent relative weights for frequency responses from bank angle command to lateral specific force and yaw rate.*

4.5.4.4 Simulation Results for Calm Atmosphere

To quantify the influence of aerodynamic uncertainties on the retuning results, Monte Carlo Simulations (100 simulations in total) in calm atmosphere were carried out. The applied uncertainties on the aerodynamic parameters were described in Section 4.5.4.1. Figure 4.24 shows the deviation between the desired closed-loop frequency response and the tuned closed-loop frequency response, as well as the deviation between the desired and the initial (untuned) response. The depicted tuned and untuned responses are obtained as an averaged ETFE, based on simulation results of the controlled nonlinear plant model with the retuned and initial controller parameters, respectively. It can be seen that the tuned closed-loop responses are closer to the desired response. Hence, the proposed retuning procedure achieves an improvement.

The achieved margins with the tuned gains were checked for satisfaction of their adequate values via interpolation of the corresponding anticipated frequency response estimates $\hat{G}_{cut}(j\omega_k, \boldsymbol{p})$. It turned out that the anticipated margins, which were all satisfied by the constraints of the optimization, give a poor estimate for the aileron actuator cut phase margins, which were not satisfied and slightly below the required 45 degrees on the true plant.

Figure 4.25 compares the desired response to a step input, in Φ_{cmd} with an amplitude of 5 degrees, with the step responses of the closed-loop systems with tuned and initial (untuned) gains. The desired step response with the optimized gains is reproduced much better.

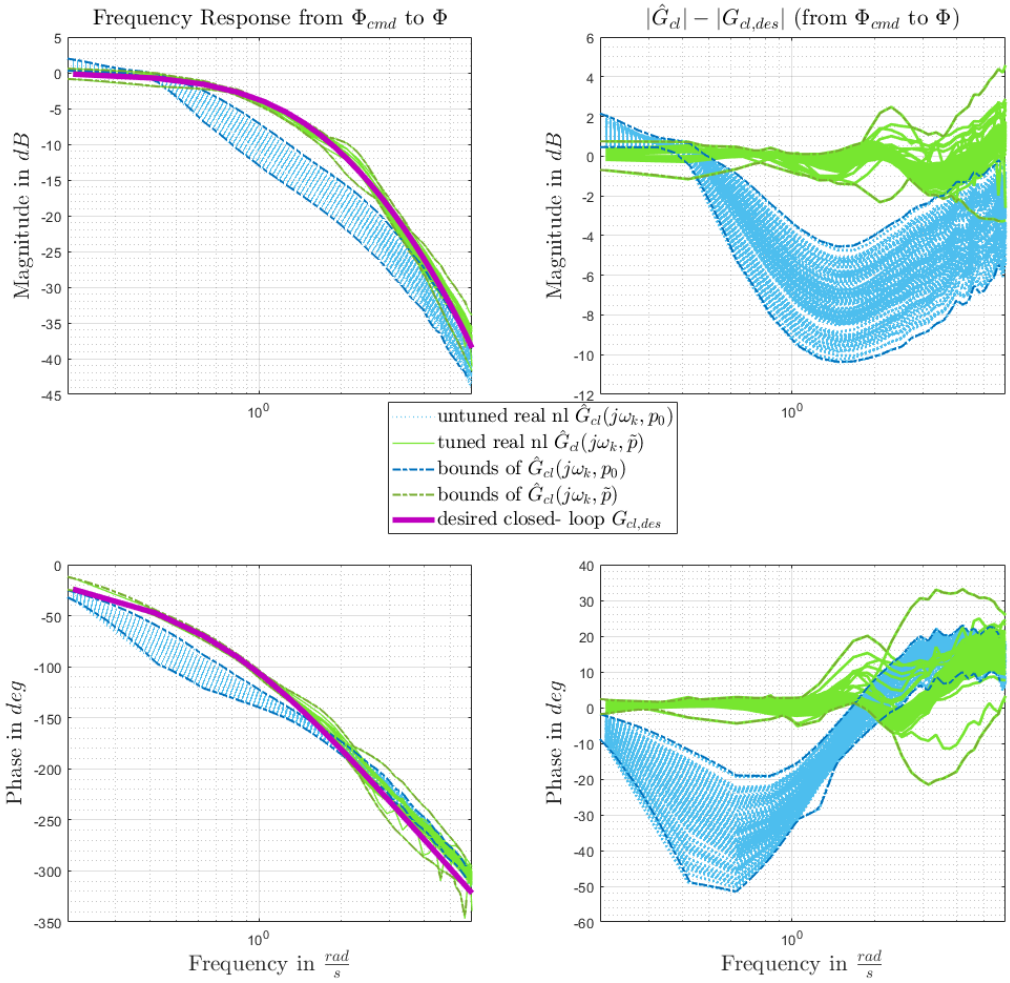

Figure 4.24: *Closed-loop frequency response with initial gains, retuned gains, and desired response, for varying uncertainties under calm air conditions.*

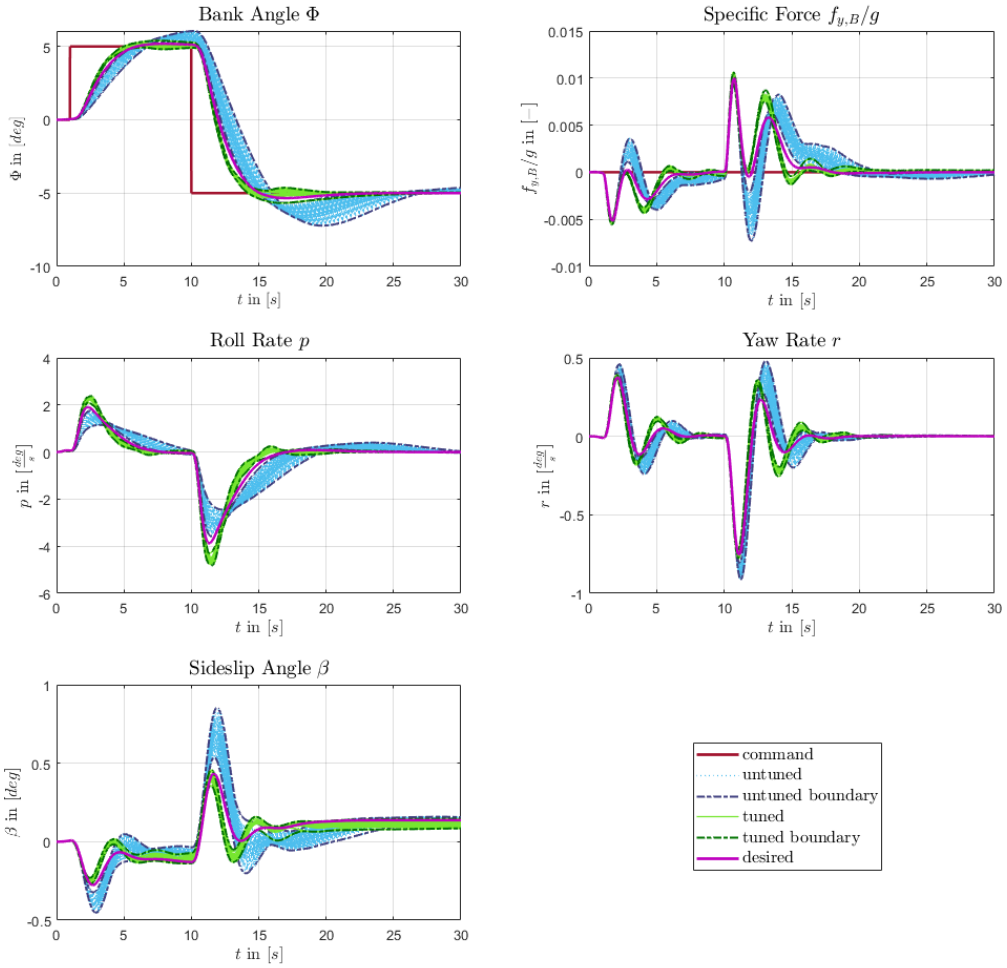

Figure 4.25: *Step response of closed-loop systems with initial gains, retuned gains, and desired closed-loop step response.*

4.5.4.5 Simulation Results for Light Turbulence

The following section investigates the effect of performing the tuning in light turbulence based on Monte Carlo simulations (30 simulations in total) in light turbulence. The turbulence will distort the closed-loop frequency response estimate compared to an estimate from a calm air flight test. This is revealed in Figure 4.26 by the light blue lines. The

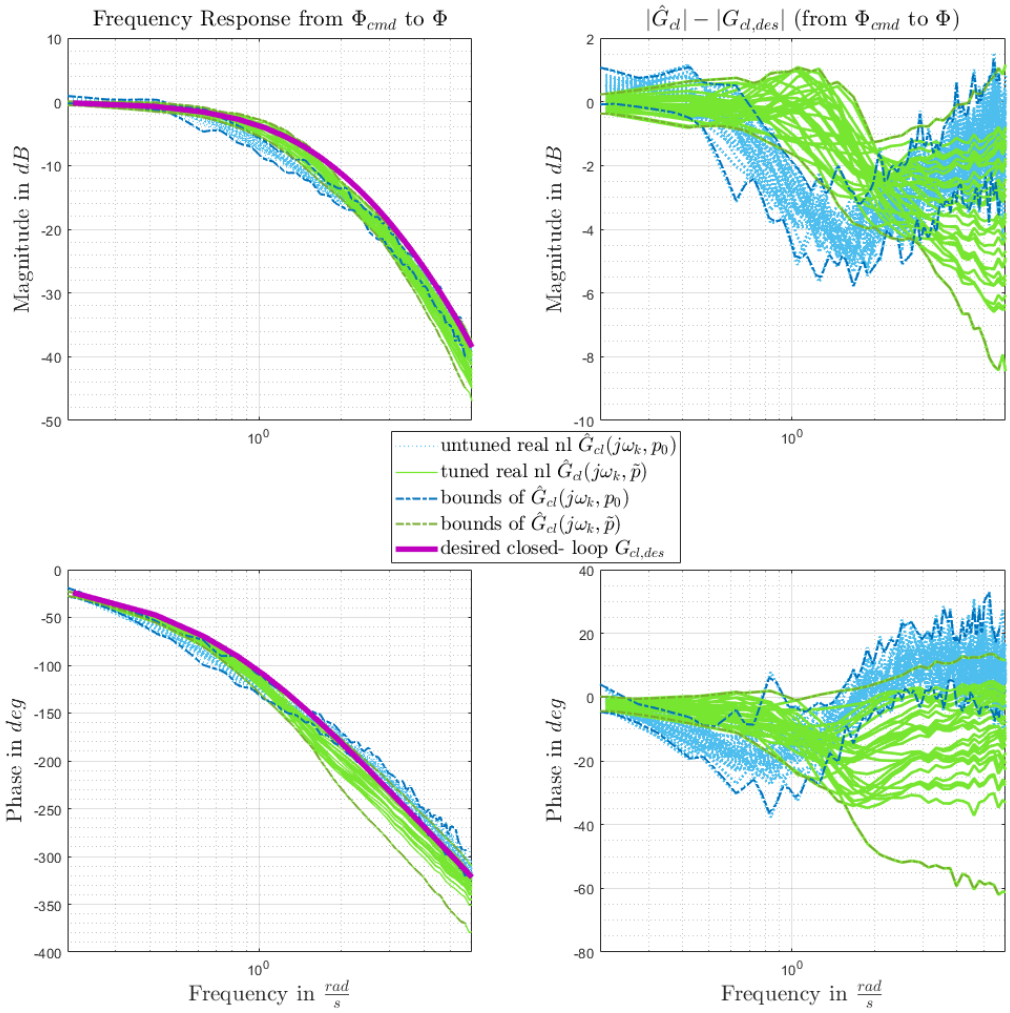

Figure 4.26: *Tuning results for initial closed-loop frequency responses obtained in turbulent air by Monte Carlo simulations.*

light blue lines are the closed-loop frequency response estimates obtained from simulation in light turbulence with the initial controller parameters and one specific uncertainty set as described in Section 4.5.4.1. This uncertainty set mainly considers uncertainties in the roll motion. The penalties for the controller parameters given by the diagonal entries of the matrix $\boldsymbol{Q}$ are adapted compared to Section 4.5.4.3 such that the controller parameters related to the roll motion are penalized less and are mainly tuned by the optimization. This is done by increasing the penalties to 1000 for all gains except the feed forward gain

$p_{\dot{p}\Phi_c}$, the integral gain $p_{I,\dot{p}\Phi}$ and the feedback gains $p_{\dot{p}\Phi}$ and $p_{\dot{p}p}$, which remain at the same values as described in Section 4.5.4.3. Furthermore, more emphasis is given to the bank angle tracking by decreasing the corresponding frequency dependent weights for the specific force and yaw rate given in Table 4.10 by a factor of 10. The frequency responses from bank angle command to lateral specific force are weighted that low also because the signal-to-noise ratio of $f_{y,B}$ is low in turbulence. The reason is that in coordinated turns the lateral specific force is regulated to zero. For the bank angle and roll rate the same frequency dependent weights, as given by Table 4.9, are selected.

Figure 4.26 shows in green the resulting tuned closed-loop responses, obtained as averaged ETFE from simulation in calm atmosphere with the tuned parameters set. The parameters tuned from a flight in light turbulent air, result, in this example, in a closed-loop frequency response that is close to the desired frequency response. Figure 4.27 compares the desired response to a step input, in Φ_{cmd} with an amplitude of 5 degrees, with the step responses of the closed-loop systems with tuned and initial (untuned) gains. As can be seen, the desired step response with the optimized gains is not reproduced satisfactory in all cases. Especially, the tuned response of the lateral specific force is deteriorated compared to the untuned response, due to the low weighting of the corresponding frequency response in the optimization in order to account for the respective low signal-to-noise in turbulence. Hence, especially for this considered controller and objectives calm air conditions are of immense importance for the retuning. Furthermore, a large variation in the tuned controller parameters was observed between the simulations. Hence, flight tests shall be performed under calm air conditions.

As we also saw for the longitudinal controller, the estimated initial frequency response in turbulent conditions is more noisy than in calm air. As a consequence the anticipated closed-loop response might differ from the actual tuned response. The variance of the estimated frequency response in turbulence depends on the signal-to-noise ratio and hence also on the intensity of the turbulence and the number of repetitions of the maneuver. It is a trade-off between the maneuver length T of one repetition which determines the frequency resolution ω_k of the estimated frequency response, the drift away from the considered operational envelope point and the amplitude of the excitation signal.

Due to the coupling effects of the MIMO control structure the optimization result in turbulence seemed to be sensitive towards the uncertainties, the choice of parameter penalties and frequency dependent weights.

The achieved margins with the tuned controller parameters were checked for satisfaction of their adequate values as described before. Again the anticipated margins all satisfied by the constraints of the optimization their adequate values while the aileron actuator cut phase margin on the true system was slightly below the required 45 degrees.

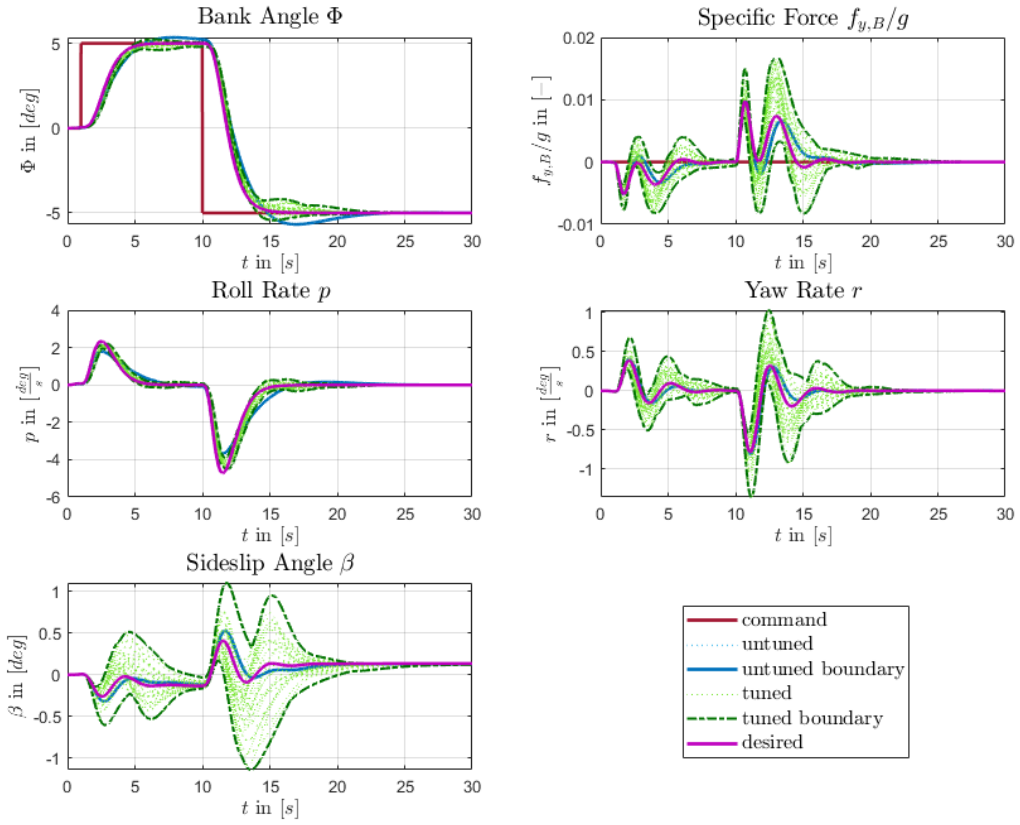

Figure 4.27: *Tuning results for initial frequency responses obtained in turbulent air by Monte Carlo Simulations.*

4.5.4.6 Simulation Results with Backlash

The following section investigates the effect of backlash in the aileron deflections on the tuning results based on simulated flight tests. The simulations were performed based on one specific set of uncertainties described in Section 4.5.4.1, with an varying backlash element on the aileron. Figure 4.28 shows the tuning results for a case where the backlash was evenly varied from 0 to 0.6 degrees. 7 simulations were performed in total in calm air with different values for the backlash. Based on the respective initial closed-loop estimates the controller retuning was performed, where the same penalty $\boldsymbol{Q}$ as in Section 4.5.4.5 was used. The frequency dependent weights are selected as given by Table 4.9 and 4.10. The simulations were repeated with the new controller parameters. Based on the respective simulation data the ETFE's of the tuned closed-loop response, depicted in green, was calculated. The anticipated tuned closed-loop response, which is not depicted here, matched this tuned closed-loop response closely. We further see, that the tuned responses are closer to the desired response than the initial responses. With increasing backlash the tuning result though deteriorates, as can be seen in Figure 4.29, which depicts the step responses to a bank angle command of 5 degrees. With increasing backlash the steady state error increases.

Again the anticipated margins all satisfied by the constraints of the optimization their adequate values while the aileron actuator cut phase margin on the true system was slightly below the required 45 degrees.

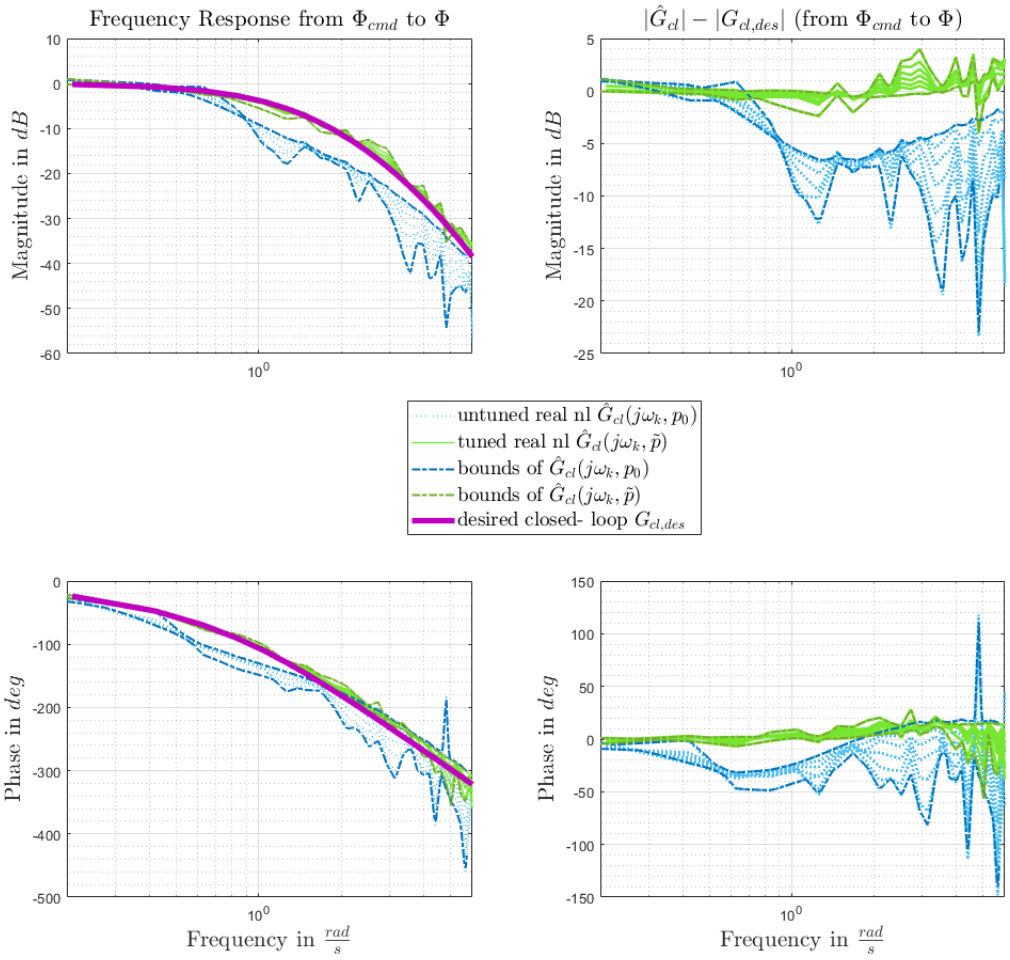

Figure 4.28: *Comparison of closed-loop frequency responses with varying backlash element* $(0 - 0.6$ *degrees).*

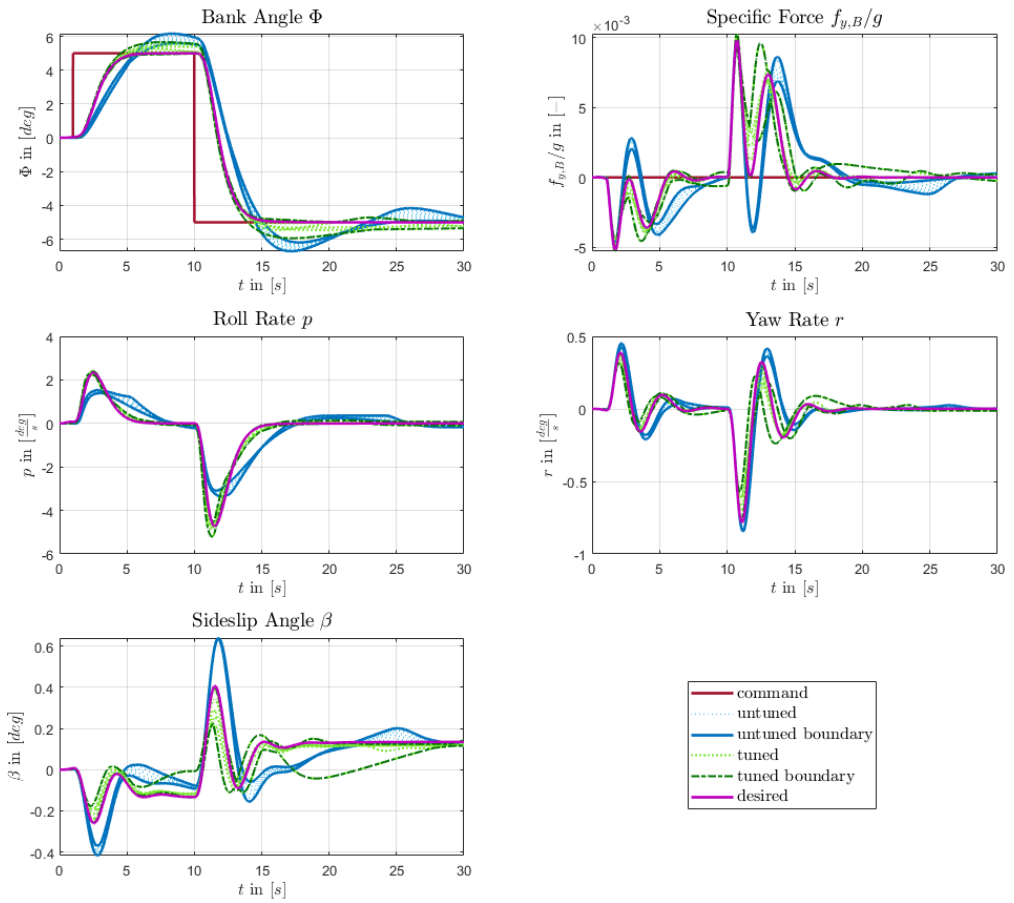

Figure 4.29: *Comparison of closed-loop step responses with varying backlash element* $(0 - 0.6$ *degrees).*

Like for the longitudinal controller, the retuning shall be considered with care if large nonlinearities like backlash are expected, because the tuned response will deviate from the anticipated closed-loop response. This effect is visible in Figure 4.30 where the backlash was varied from 0.7 up to 1.0 and where the anticipated closed-loop response is depicted in orange. The resulting tuned step responses, depicted in Figure 4.31, are significantly deteriorated in this case.

The retuning showed furthermore a high sensitivity towards the gain penalties and frequency dependent weights. In Figure 4.32 the penalty matrix $\boldsymbol{Q}$ was changed to the values described in Section 4.5.4.3. Additionally, the weights for the specific force and yaw rate were decreased by a factor of 10 like in Section 4.5.4.5. While the anticipated closed-loop frequency response is close to the desired, the actual tuned response differs significantly.

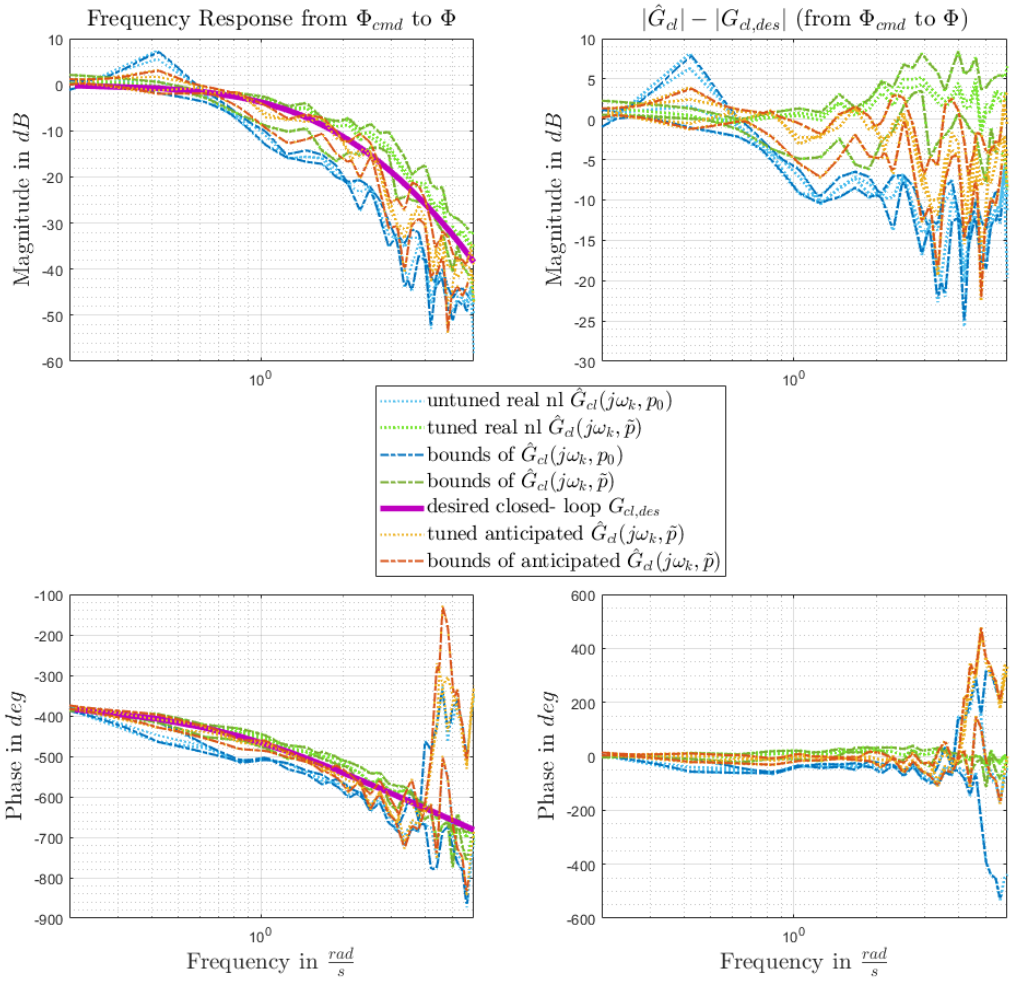

Figure 4.30: *Comparison of closed-loop frequency responses with varying backlash element* $(0.7 - 1$ *degrees).*

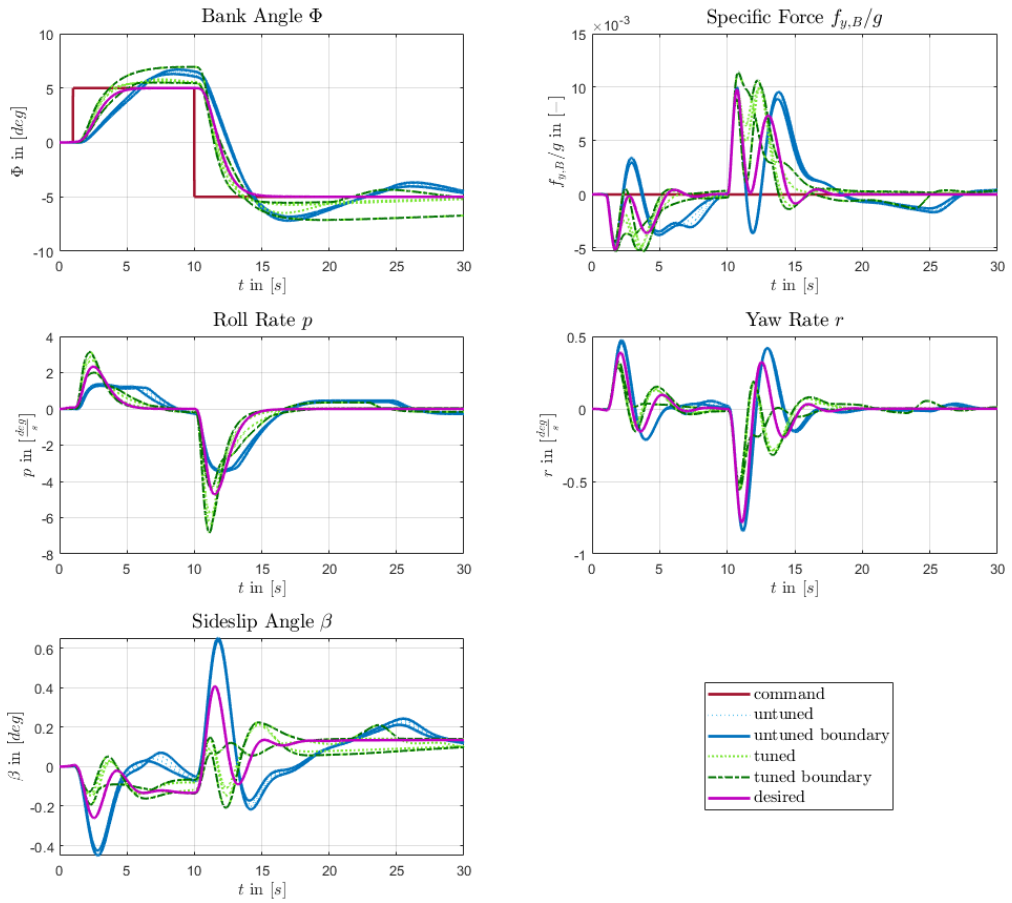

Figure 4.31: *Comparison of closed-loop step responses with varying backlash element* $(0.7 - 1$ *degrees).*

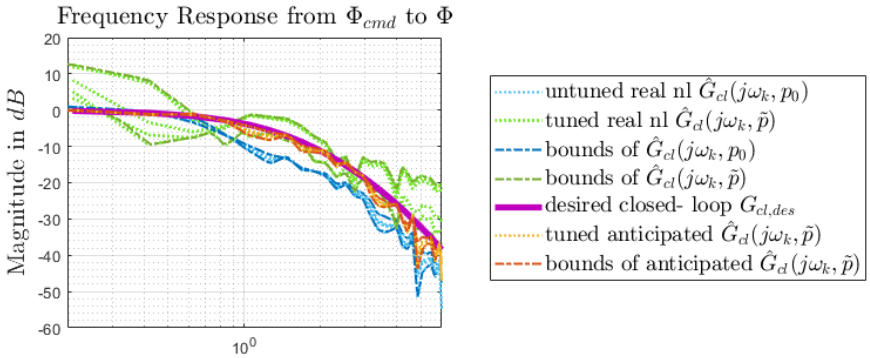

Figure 4.32: *Comparison of closed-loop step responses with varying backlash element* $(0 - 0.4$ *degrees) for a different optimization setting.*

4.5.5 Flight Test Results

In the following sections the data of two flights of the G-520T testbed are considered, which took place near the airport EDMN close to Mindelheim, Germany. All flight tests presented in the following were performed at an envelope point defined by indicated airspeed and pressure altitude of

$$V_A = 115 \pm 5\,\text{KIAS} \quad \text{and} \quad h = 9100 \pm 200\,\text{ft} \tag{4.64}$$

see Figure 4.33.

The considered flight test maneuvers were executed with retracted landing gear and flaps in upright position. The flight test procedure was the same as for the longitudinal controller and is described in detail in Section 4.4.5. During the test flights, sensor data and FCC internal controller data were recorded directly on the FCC with a sample rate of 100Hz which equals the clock speed of the FCC.

For the retuning procedure for the lateral controller two multi-sine maneuvers have been performed: A Φ multi-sine command, where the lateral specific force $f_{y,B}/g$ command was kept to zero and a $f_{y,B}/g$ multi-sine command, where the Φ command was kept at zero. During the maneuvers the longitudinal controller was also active. To keep the aircraft at the trim envelope point, the normal specific force command corresponded to the trim value. In the next section the parametrization of the multi-sines is summarized.

4.5.5.1 General Settings - Reference Excitation Input Signal

The applied multi-sine signals are described in Section 3.4, Equation (3.16). Thereby, the two differently parametrized multi-sinusoidal excitation signals, which were already introduced in Section 4.5.4.2, Table 4.8, were injected within the flight tests at the reference input $r_1 = \Phi_{cmd}$ and $r_2 = f_{y,B,cmd}/g$, respectively.

The multi-sine maneuvers were repeated each three times under closed-loop conditions, with the initial controller parameters. Unfortunately, no multi-sine flight tests with the tuned controller parameters are yet available.

4.5.5.2 General Settings - Initial Controller Parameters

The initial controller parameters $\boldsymbol{p}_0$ are calculated using classical gain design techniques based on a linear model of the amended plant $\boldsymbol{G}_{\text{ap,nom}}$ as described in Section 4.5.3.1. The initial controller parameters that were tested in flight are given in Table 4.11.

Type	Parameter	Tuned value	Initial value	Tuned value
$feedforward$ $\boldsymbol{p}_H$	$p_{\dot{p}\Phi_c}$	5.52	6.07	-
	$p_{\dot{p}f_{y,c}}$	-12.73	-12.73	-
	$p_{\dot{r}\Phi_c}$	0.64	0.98	-
	$p_{\dot{r}f_{y,c}}$	7.31	7.31	-
$integrator$ $\boldsymbol{p}_I$	$p_{I,\dot{p}\Phi}$	0.13	0.30	-
	$p_{I,\dot{p}f_y}$	0	0	-
	$p_{I,\dot{r}\Phi}$	-	0	0.61
	$p_{I,\dot{r}f_y}$	1.88	3.20	-
$feedback$ $\boldsymbol{p}_K$	$p_{\dot{p}\Phi}$	5.77	6.35	-
	$p_{\dot{p}p}$	-	0	0.45
	$p_{\dot{p}r}$	-	-4.52	-4.57
	$p_{\dot{p}f_y}$	0	0	-
	$p_{\dot{r}\Phi}$	-	0.87	1.33
	$p_{\dot{r}p}$	-	0	-0.44
	$p_{\dot{r}r}$	2.19	2.53	-
	$p_{\dot{r}f_y}$	-	-0.04	-0.14

Table 4.11: *Controller parameter values.*

4.5.5.3 General Settings - Optimization

The parametrization of the quadratic cost function in Equation (4.61) is chosen as follows. The weighting matrix $\boldsymbol{Q}$ is chosen as a diagonal matrix with penalty values chosen as 500 for all controller parameters given in Equation (4.31), (4.32) and (4.33), except the weights for the integral gains $p_{I,\dot{p}f_y}$ and $p_{I,\dot{r}\Phi}$, which were chosen as 10.000 and the feedforward and feedback gains $p_{\dot{p}\Phi_c}$, $p_{\dot{p}p}$ and $p_{\dot{p}\Phi}$, which were set to 1.

For $y_1 = \Phi$ and $y_2 = \Delta p$ the same frequency dependent weights are chosen. They are given in Table 4.12. For $y_3 = \Delta r$ and $y_4 = f_y/g$ the weights are selected constant over all frequencies with a value of $\mathrm{w}_{\gamma,y_3,\Phi_c}(\omega_k) = \mathrm{w}_{\gamma,y_3,\Phi_c}(\omega_k) = 0.1$. The frequency dependent weights are chosen to achieve a good matching with the desired dynamics in the frequency range, where the bounds from the outer-loop are most tight. Frequencies, where the closed-loop dynamics are already well attenuated are weighted weakly. The remaining parameters are $\mathrm{w}_A = 1,\ \mathrm{w}_\phi = 0.01745$ as described in Section 3.8 and $A_m = 6dB,\ \Phi_m = 45°$.

$\omega_k\left[\frac{rad}{s}\right]$	< 0.5	$0.5 - 0.7$	$0.7 - 1.3$	$1.3 - 3$	> 3
$\mathrm{w}_{\gamma,y_1,\Phi_c}(\omega_k) = \mathrm{w}_{\gamma,y_2,\Phi_c}(\omega_k)$	0	1000	100	1	0.1

Table 4.12: *Frequency dependent relative weights for frequency responses from bank angle command to output signals.*

4.5.5.4 Evaluation of Multi-sine Maneuvers with Initial Closed-loop

The bank angle command multi-sine and specific force multi-sine tests described in Section 4.5.5.1 were repeated each three times. Figure 4.33 shows the indicated speed, pressure altitude and normal specific force measurements during the bank angle maneuver. Figure

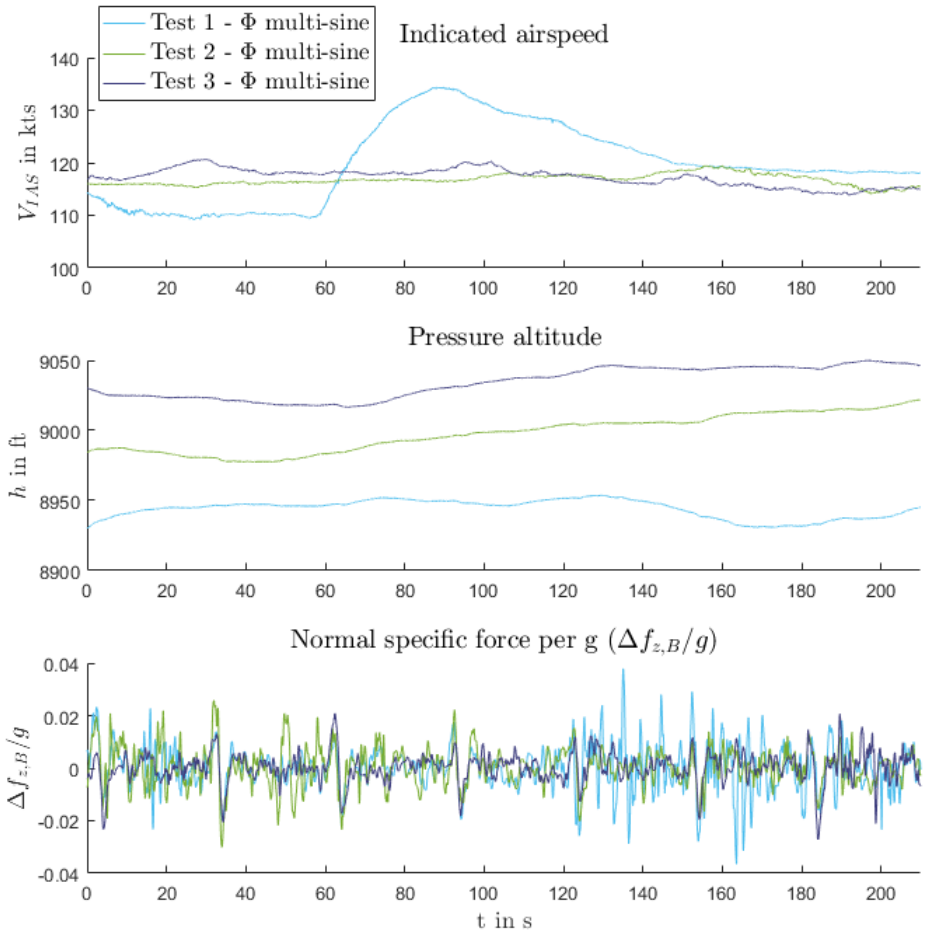

Figure 4.33: *Bank angle command multi-sine measurements.*

4.34 shows the respective measurements during the lateral specific force maneuver. It can be seen in the velocity measurement in Figure 4.33, that the first bank angle test was disturbed and in the normal specific force measurement in Figure 4.34 it can be seen that the third test was disturbed. Therefore, only the second and third bank angle tests and the first and second specific force tests are used for identification of the initial closed-loop system and retuning.

Figure 4.35 and 4.36 show the measured output signals $\boldsymbol{y}_c$ for the first four periods of the multi-sine, for the selected bank angle maneuver and lateral specific force maneuver.

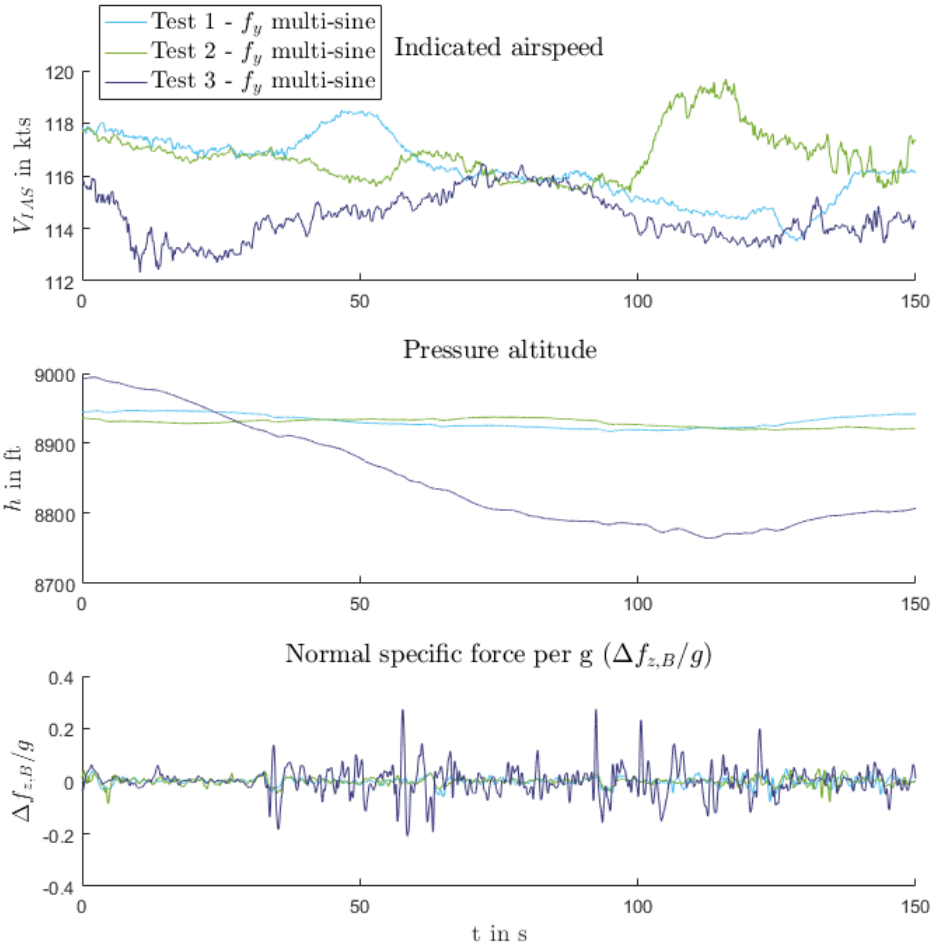

Figure 4.34: *Lateral specific force command multi-sine measurements.*

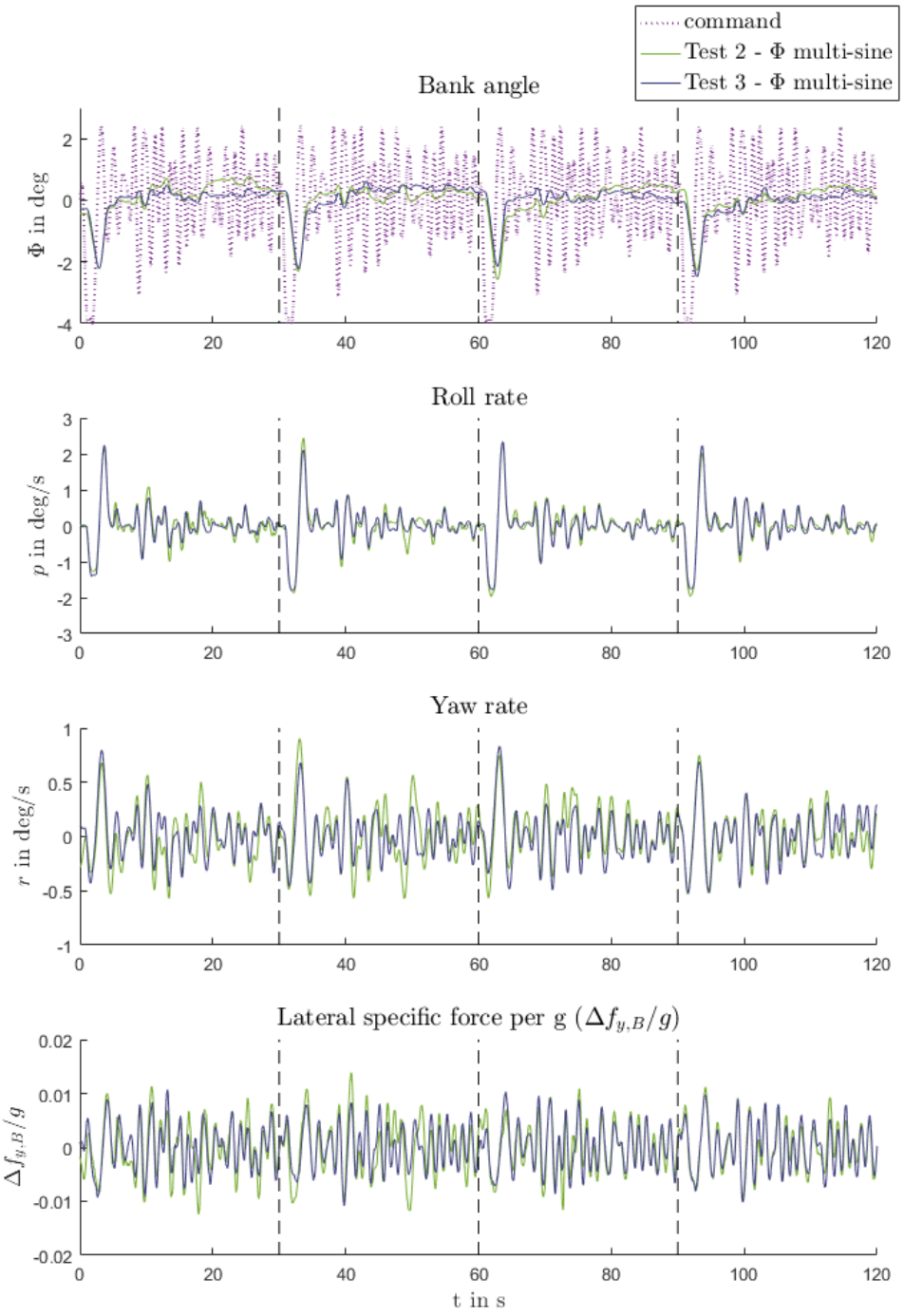

Figure 4.35: *Measurements of first four periods of the bank angle command multi-sine.*

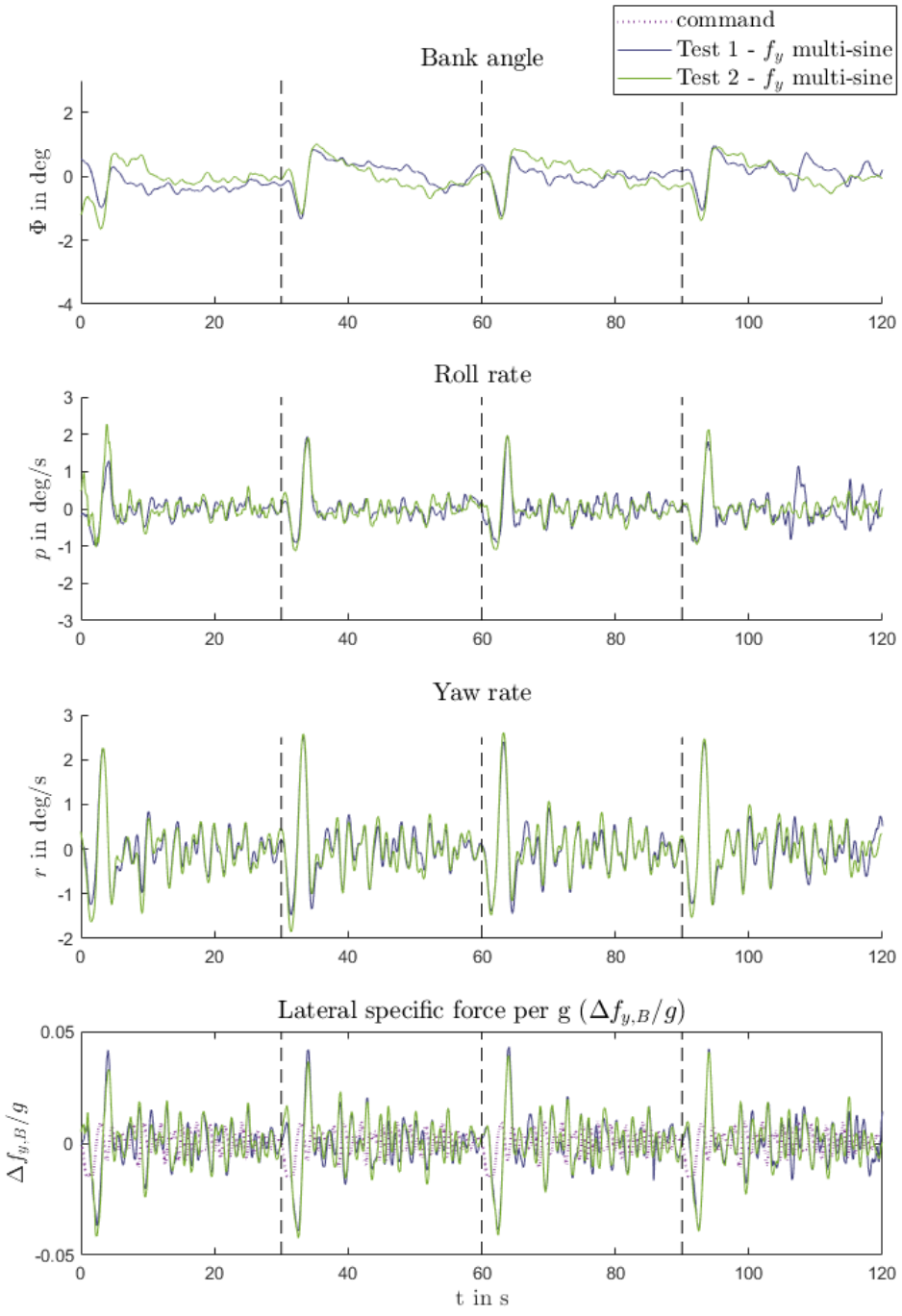

Figure 4.36: *Measurements of first four periods of the lateral specific force command multi-sine.*

4.5.5.5 Retuning Results

Based on the initial closed-loop estimates obtained from the selected multi-sine experiments described in Section 4.5.5.4 the retuning of the controller parameters was performed. The optimization was set up as described in Section 4.5.5.3. Unfortunately no multi-sine data of repeated flight test experiments with the updated tuned controller parameters is available yet for estimation of the updated closed-loop response. But instead doublets in the bank angle command with the tuned controller parameters have been already performed. Figure 4.37 shows first the desired closed-loop response, the estimate of the initial closed-loop and the anticipated tuned closed-loop frequency response. It shows that the initial untuned closed-loop response, depicted in blue, inherits magnitudes above $0dB$ at low frequencies. As revealed by Figure 4.38, which compares doublets in the bank angle with untuned and retuned controller parameters, the initial closed-loop is not steady state accurate and overshoots the commanded bank angle. The anticipated closed-loop frequency response is closer to the desired response (see Figure 4.37) and the tracking of the doublets in bank angle command is improved compared to the untuned response.

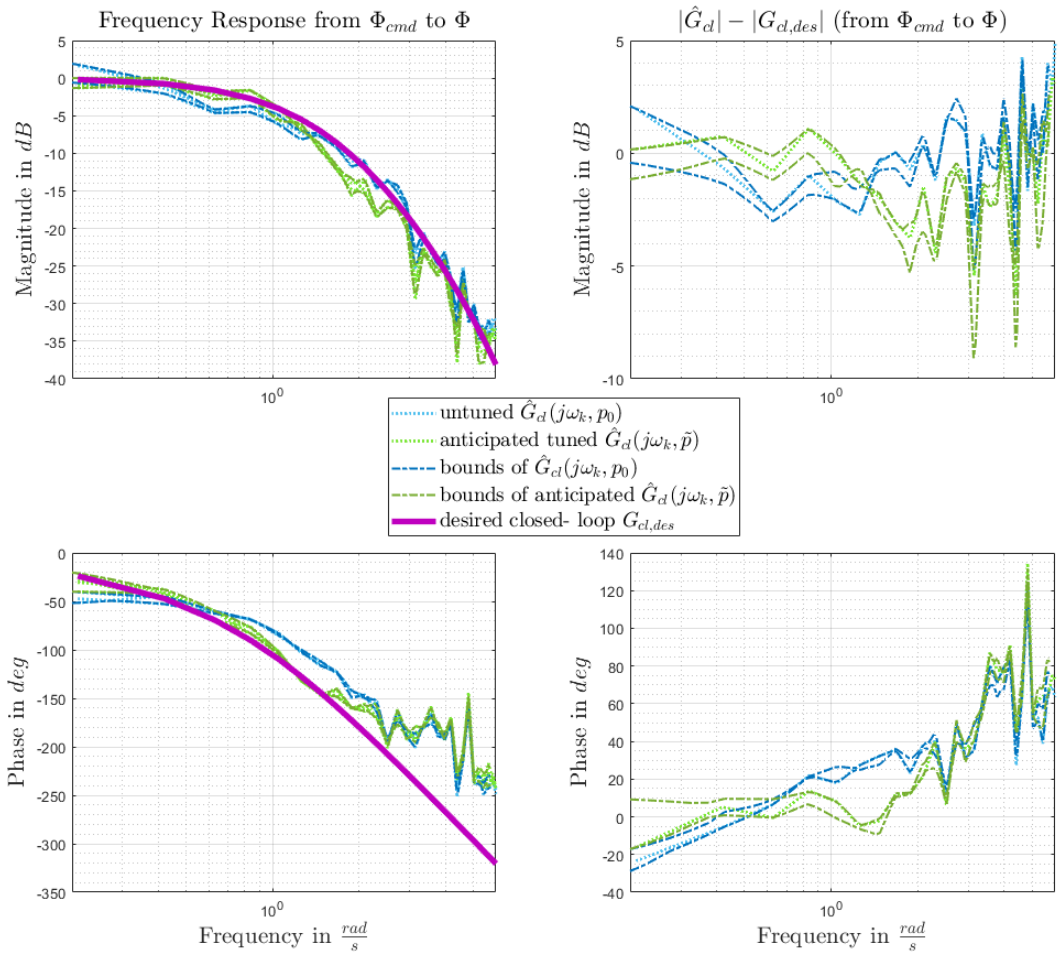

Figure 4.37: *Untuned closed-loop ETFE versus anticipated tuned closed-loop frequency response.*

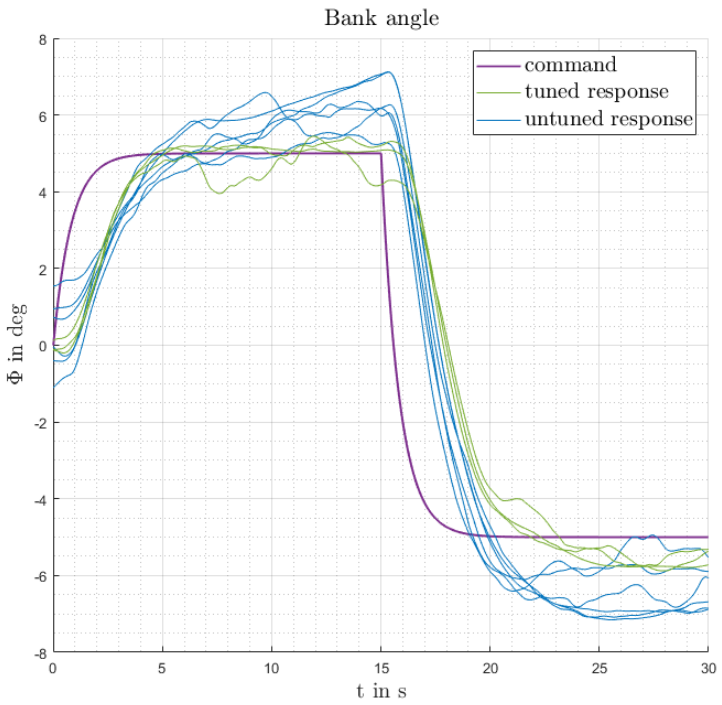

Figure 4.38: *Untuned closed-loop response versus tuned closed-loop response to a doublet command in bank angle.*

Chapter 5

Summary and Perspective

This section summarizes and reviews the contributions of this thesis. Based on the drawn conclusions an overview of possible future research and perspectives is given.

5.1 Contribution 1: Novel Test-based Gain Retuning Procedure for Linearizable Control laws

The main contribution of this thesis is a novel experiment based controller retuning method, presented in Section 3.1. The method is capable of improving existing underperforming controllers by retuning the controller parameters based on closed-loop experiment data.

Based on tests performed on the true system under closed-loop conditions with the initial controller parameters, the closed-loop and open-loop frequency response is estimated. Using these estimates, the anticipated closed-loop frequency response and stability margins for an updated set of controller parameters is calculated. This relationship is utilized within an optimization problem to adjust the controller parameters to obtain an improved closed-loop response. By minimizing the deviation between the anticipated tuned closed-loop response and a desired closed-loop frequency response sufficiently, the closed-loop performance on the true system is enhanced.

A beneficial characteristic of the developed concept is that the proposed method is non-parametric. The controller parameters are updated directly from closed-loop input–output data, without the intermediate step of a parametric plant-model identification. Since, the performance of model-based controllers is highly dependent on the model accuracy, one drawback of an intermediate model identification is a possible plant-model mismatch due to inaccuracy in identified model structure or parameters. This problem is mitigated in the developed concept by the fact that the closed-loop test data is directly exploited without resorting to a parametrized plant model. This allows to take into account the true order of the system in contrast to approaches based on a parametrized plant model which typically is a low order approximation of the system. Moreover, the demand for extensive, costly

flight test campaigns (to identify a very accurate model by full estimation of aerodynamic parameters, as performed in civil aviation) is mitigated. Hence, the method is suitable for the currently rapidly emerging market of novel small to medium sized Manned and Unmanned Aerial Vehicles as well as Optionally Piloted Vehicles and General aviation aircraft, which are very cost-sensitive compared to large transport aircraft.

The proposed retuning procedure was presented as an offline strategy: First an experiment is performed with the initial controller parameters. Based on the obtained data the controller gains are retuned offline. Then another flight test is performed with the tuned controller parameters to verify the result. Future work should focus on extending the concept to an online procedure, in order to reduce the costs of the on ground data processing tasks. Here the focus could be on measures like confidence regions and the theoretical framework to assure the safety of operation with the retuned controller parameters.

Future work should also investigate if besides the control law gains other controller parameters, for example notch filter characteristics, could be included into the retuning procedure. Since the non-parametric frequency responses will contain high order dynamics like structural modes, the notch filters might be optimized such that the resulting open-loop frequency response remain below the required attenuation, such that an excitation of the structural modes is prevented.

Another interesting aspect to be investigated is whether the retuning procedure, which is formulated to optimize the tracking behavior, given by the desired closed-loop frequency response, could be adapted to take desired disturbance rejection characteristics into account.

Future efforts could also direct towards investigating a retuning of more modern controller structures, like incremental dynamic inversion (INDI) controller schemes.

5.2 Contribution 2: Optimization Problem for Test-based Gain Retuning

In Section 3.8 an optimization problem is proposed for SISO systems, to retune the controller parameters such that the deviation between the desired and the anticipated closed-loop frequency response for the new controller parameter set is minimized. The deviation is quantified by a metric considering a frequency weighted squared error in magnitude and phase of the respective frequency responses. The proposed deviation metric was already used successfully in the context of low order equivalent system (LOES) identification by [RT06]. In that context the deviation between measured frequency response and LOES frequency response is minimized with respect to the plant parameters. In the context of this thesis a similar structure was used to minimize the deviation between a desired closed-loop frequency response and an anticipated closed-loop frequency response,

with respect to the controller parameters. Additionally, a regularization was proposed by adding a penalization term to keep the tuned gains within reasonable bounds around the initial gains and stability criteria were enforced by supplementary constraints.

In Section 3.10 the optimization problem formulation was adapted to cover additional retuning scenarios as for example

- a fixed gain controller at different operating points (e.g. different velocities)
- a fixed gain controller at different operating configurations (e.g load cases)

In Section 4.4.3.5 the optimization problem formulation was adapted for SIMO systems, based on the application example of a longitudinal baseline controller for fixed- wing aircraft and in Section 4.5.3.7 for a MIMO controller, based on the application example of a lateral baseline controller. Simulation results revealed that under some conditions the result of the retuning might be sensitive towards the choice of the penalization term and the frequency dependent weights, especially in the MIMO case where an increased number of controller parameters and cross couplings are expected. In future work further efforts could be undertaken to find formulations for a deterministic choice of the weights. For example metrics like MUAD bounds, discussed in Section 3.9, could be incorporated into the weighting measures, where applicable.

For the MIMO application example the optimization problem was formulated based on the condition that only the tracking of one reference signal was relevant (from bank angle command to measured bank angle). But in general it is expected that for MIMO controllers the tracking of all reference signals shall be improved at the same time. This topic is another perspective for future work.

5.3 Contribution 3: Calculation of the Non-parametric, Anticipated Closed-loop Frequency Response for an Updated Controller Parameter Set

In Section 3.6 a method to calculate the non-parametric, anticipated tuned closed-loop frequency response for an updated controller parameter set, based on closed-loop experiments with an initial controller was proposed. First, based on experimental data a non-parametric closed-loop frequency response estimate of the true plant with initial controller is calculated. Based on this estimate, the anticipated closed-loop frequency response for an updated set of controller parameters can be calculated, assuming that the controller, that was applied during the experiment is linear and exactly known.

As the simulation results of the applications in Section 4.4 and 4.5 have shown, the estimates and retuning results in turbulence are deteriorated compared to flight tests performed in calm air conditions. In Section 3.8 it was shown that the estimates can be improved under noisy conditions by increasing the number of repetitions of the maneuver.

However, more repetitions mean a higher maneuver duration and hence increase the costs. Future work could concentrate on developing other measures to improve the estimates in the presence of disturbances and providing confidence regions.

Further simulation results in Section 4.4.4.6 and 4.5.4.6 revealed the restriction of the retuning concept when nonlinearities, for example large backlash in the actuation, are expected. The anticipated tuned closed-loop estimate might in these cases deviate from the true tuned closed-loop frequency response. With regard to the estimation of frequency response functions, concepts dealing with the presence of nonlinear distortions are covered in the literature [SPRD01]. Future work could focus on how to deal with nonlinear distortions in the context of the retuning procedure and estimation of the anticipated tuned closed-loop frequency response.

5.4 Contribution 4: Analytic Expression for the Bias of the Anticipated Closed-loop Estimate

For a single-input-single-output closed-loop system with a linear controller with error feedback and feed-forward an analytical expression for the bias of the anticipated closed-loop frequency response has been derived in Section 3.6.2. It was shown that the bias is small for small changes in the feedback controller, large initial feed-forward or large signal-to-noise ratios and verified by simulation results. Future work could calculate similar expressions for the bias for a SIMO or MIMO case as considered in the application examples.

Furthermore, it was shown in Section 3.6.3 that the variance of the anticipated, tuned closed-loop frequency response estimate is theoretically infinite, similar to indirect non-parametric plant estimates [Hea01b]. This result was not intuitive when inspecting the simulation results, where the variance of the anticipated closed-loop estimates seemed small for high SNRs. It was concluded for the test-based retuning procedure, that the estimates of the anticipated updated closed-loop shall be considered with caution and be checked for outliers.

Based on the similarities with the indirect plant estimate, similar strategies could in future work be applied to the anticipated tuned closed-loop estimates to overcome this problem. For example exclusion zones [WG04], [WG02], could be introduced, nonlinear averaging techniques could be applied [GKP96b] or alternative measures for the variance [Hea02], for example the first moment of the distance of the estimate from the true value measured by the magnitude (MAD - mean absolute deviation), could be used.

5.5 Contribution 5: Practical Demonstration on different Aircraft including Flight Tests

In Section 4.4 the controller parameter retuning was demonstrated for a longitudinal baseline controller on different CS-23 aircraft. The longitudinal baseline controller is part of a modular flight control system and was flight tested on the platforms presented in Section 4.1. The controller entails all components that are necessary for real applications, e.g. roll off filters to attenuate noise, notch filters, control allocation, trim compensation etc.. The concept was analyzed for this application via Monte Carlo simulations on a high fidelity 6 Degrees of Freedom simulation environment including real world effects like noise, structural and aeroelastic modes, backlash and light turbulence. Finally, in Section 4.4.5 the concept was successfully demonstrated with real flight tests on a real flexible large fixed-wing aircraft.

In Section 4.5 the controller parameter retuning was demonstrated for a lateral baseline controller with MIMO structure. Simulations revealed promising results. However, with regard to coupling effects, disturbances and nonlinearities, MIMO structures could be investigated more thoroughly in future work. The retuning procedure was partly demonstrated by real flight tests. Multi-sine flight test results with the tuned parameters for verification are unfortunately missing.

However, simulation results and flight tests have demonstrated that the proposed concept is an interesting and promising, novel method in retuning controller parameters of an existing underperforming controller.

Appendix A

Dirac Impulse

Definition A.0.1. *The dirac impulse is a complicated mathematical construct. However, it can be used with the usual rules of calculus with the following definition [TZ95, p. 22]:*

$$\delta(t) = \begin{cases} 0 & \text{for } t \neq 0 \\ \infty & \text{for } t = 0 \end{cases} \tag{A.1}$$

Property A.0.1. *The sifting property of the dirac impulse is [TZ95, p. 22]*

$$\int_{t_1}^{t_2} x(t)\delta(t - t_0)dt = \begin{cases} x(t_0) & t_1 < t_0 < t_2 \\ 0 & \text{otherwise} \\ \text{undefined for} & t_0 = t_1 \text{ or } t_2 \end{cases} \tag{A.2}$$

which is of immense importance. For $x(t) = 1$ it follows that

$$\int_{t_1}^{t_2} \delta(t)dt = 1 \tag{A.3}$$

with $t_1 < 0 < t_2$ and

$$\int_{t_1}^{t_2} \delta(t - t_0)dt = 1 \tag{A.4}$$

for $t_1 < t_0 < t_2$.

Property A.0.2. *The scaling property of the Dirac impulse is given by*

$$\delta(af) = \frac{\delta(f)}{|a|} \tag{A.5}$$

with $a \in \mathbb{R}$, see [Bri88, p. 33].

Appendix B

Relation between Dirac Impulse and Integral of Complex Exponential Function

Lemma B.0.1. *The infinite integral of the complex exponential function* $e^{\pm j2\pi ft}$ *equals the dirac impulse:*

$$\int_{-\infty}^{\infty} e^{\pm j2\pi ft} dt = \delta(f) \tag{B.1}$$

Proof. The integral of $e^{\pm j2\pi ft}$ is

$$\int_{-a/2}^{a/2} e^{\pm j2\pi ft} dt = \frac{1}{\pm j2\pi f} e^{\pm j2\pi ft}\Big|_{-a/2}^{a/2} = \frac{1}{\pm j2\pi f}[e^{\pm j\pi fa} - e^{\mp j\pi fa}] \tag{B.2}$$

The complex exponential is given in terms of cosine and sine by

$$e^{\pm j\pi fa} = \cos(\pi fa) \pm j\sin(\pi fa) \tag{B.3}$$

and

$$e^{\mp j\pi fa} = \cos(\pi fa) \mp j\sin(\pi fa) \tag{B.4}$$

Inserting (B.3) and (B.4) into (B.2) results in

$$\begin{aligned} \int_{-a/2}^{a/2} e^{\pm j2\pi ft} dt &= \frac{1}{\pm j2\pi f}[\cos(\pi fa) \pm j\sin(\pi fa) - (\cos(\pi fa) \mp j\sin(\pi fa))] \\ &= \frac{1}{\pm j2\pi f}(\pm 2j\sin(\pi fa)) \\ &= \frac{\sin(\pi fa)}{\pi f} \end{aligned} \tag{B.5}$$

In literature it is commonly known that

$$\lim_{\omega\to\infty} \frac{\sin(\omega t)}{\pi t} = \lim_{f\to\infty} \frac{\sin(2\pi f t)}{\pi t} = \delta(t) \tag{B.6}$$

see [Pou18, p. 1-9] for example. The validity of this equality requires advanced math and constitutes a complicated problem. Therefore, the proof is omitted here, and the reader is referred to the corresponding literature. But using (B.6), (B.5) becomes

$$\lim_{a\to\infty} \int_{-a/2}^{a/2} e^{\pm j2\pi f t} dt = \lim_{a\to\infty} \frac{\sin(\pi a f)}{\pi f} = \delta(f) \tag{B.7}$$

Hence, the result. □

Appendix C

Relation between Discrete Time Fourier Transform and Fourier Transform

Lemma C.0.1. *The DTFT* (2.39) *of a sampled signal, i.e. the discrete sequence* $x[n] = x(nT_s)$ *equals the Fourier transform of the respective continuous signal* $x(t)$*, scaled by the sampling frequency* $f_s = 1/T_s$ *and periodically repeated with a distance of* kf_s (2.42)*. This relation is given by:*

$$X_{DTFT}(f) = \sum_{n=-\infty}^{\infty} x[n]e^{-j2\pi f(nT_s)} = \frac{1}{T_s}\sum_{k=-\infty}^{\infty} X_{FT}(f - kf_s) \tag{C.1}$$

Proof. First of all $q = f - kf_s$ is substituted into the right side of (C.1).

$$\frac{1}{T_s}\sum_{k=-\infty}^{\infty} X_{FT}(f - kf_s) = \frac{1}{T_s}\sum_{k=-\infty}^{\infty} X_{FT}(q(k)) \tag{C.2}$$

$X_{FT}(q)$ is the Fourier transform of the continuous signal $x(t)$ and is calculated according to (2.26). Equation (C.2) becomes

$$\frac{1}{T_s}\sum_{k=-\infty}^{\infty} X_{FT}(q(k)) = \frac{1}{T_s}\sum_{k=-\infty}^{\infty} \int_{-\infty}^{\infty} x(t)e^{-j2\pi q(k)t}dt \tag{C.3}$$

The position of the integral and sum can be exchanged and $q = f - kf_s$ is substituted back in

$$\begin{aligned}\frac{1}{T_s}\sum_{k=-\infty}^{\infty}\int_{-\infty}^{\infty}x(t)e^{-j2\pi q(k)t}dt &= \frac{1}{T_s}\int_{-\infty}^{\infty}\sum_{k=-\infty}^{\infty}x(t)e^{-j2\pi q(k)t}dt \\ &= \frac{1}{T_s}\int_{-\infty}^{\infty}\sum_{k=-\infty}^{\infty}x(t)e^{-j2\pi(f-kf_s)t}dt \\ &= \frac{1}{T_s}\int_{-\infty}^{\infty}(\sum_{k=-\infty}^{\infty}e^{j2\pi kf_st})x(t)e^{-j2\pi ft}dt\end{aligned} \tag{C.4}$$

For the infinite sum of the complex exponential function in (C.4), according to Lemma D.0.1, the following relation holds

$$\frac{1}{T_s}\sum_{k=-\infty}^{\infty}e^{j2\pi kf_st} = \sum_{n=-\infty}^{\infty}\delta(t-nT_s) \tag{C.5}$$

Hence, (C.4) becomes

$$\int_{-\infty}^{\infty}(\sum_{n=-\infty}^{\infty}\delta(t-nT_s))x(t)e^{-j2\pi ft}dt \tag{C.6}$$

Multiplication of the dirac comb $\mathrm{III}_{T_s} = \sum_{n=-\infty}^{\infty}\delta(t-nT_s)$ with the continuous time signal $x(t)$ will result in non-zero values only at time instances $t = nT_s$. Consequently, the product $\sum_{n=-\infty}^{\infty}\delta(t-nT_s)x(t)$ in (C.6) can be formulated as

$$\sum_{n=-\infty}^{\infty}\delta(t-nT_s)x(t) = \sum_{n=-\infty}^{\infty}\delta(t-nT_s)x(nT_s) \tag{C.7}$$

resulting in

$$\begin{aligned}\int_{-\infty}^{\infty}\left(\sum_{n=-\infty}^{\infty}\delta(t-nT_s)x(nT_s)\right)e^{-j2\pi ft}dt &= \sum_{n=-\infty}^{\infty}\left(x(nT_s)\int_{-\infty}^{\infty}\delta(t-nT_s)e^{-j2\pi ft}dt\right) \\ &= \sum_{n=-\infty}^{\infty}x(nT_s)\mathcal{F}\{\delta(t-nT_s)\}\end{aligned} \tag{C.8}$$

where the integral $\int_{-\infty}^{\infty}\delta(t-nT_s)e^{-j2\pi ft}dt$ constitutes the Fourier transform of $\delta(t-nT_s)$, according to its definition given in (2.26). According to Lemma E.0.1, the Fourier transform of $\delta(t-nT_s)$ is

$$\mathcal{F}\{\delta(t-nT_s)\} = e^{-j2\pi fnT_s} \tag{C.9}$$

Hence, (C.8) becomes

$$\sum_{n=-\infty}^{\infty}x(nT_s)e^{-j2\pi fnT_s} \tag{C.10}$$

Hence, the result. □

Appendix D

Relation between Dirac Comb and sum of Complex Exponential Functions

Lemma D.0.1. *Let $III_{T_s} = \sum_{n=-\infty}^{\infty} \delta(t - nT_s)$ be a dirac comb or impulse train. Then the relation of the dirac comb and the complex exponential function is given by*

$$\sum_{n=-\infty}^{\infty} \delta(t - nT_s) = \sum_{k=-\infty}^{\infty} \frac{1}{T_s} e^{j2\pi k f_s t} \tag{D.1}$$

Proof. The dirac comb III_{T_s} is periodic and therefore it can be expressed as a Fourier series according to (2.30), resulting in

$$\mathrm{III}_{T_s} = \sum_{n=-\infty}^{\infty} \delta(t - nT_s) = \sum_{k=-\infty}^{\infty} C_k e^{j\omega_s k t} \tag{D.2}$$

with $\omega_s = \frac{2\pi}{T_s}$ and with the constant coefficient C_k calculated according to (2.31) as

$$C_k = \frac{1}{T_s} \int_{-T_s/2}^{T_s/2} \mathrm{III}_{T_s}(t) e^{-j\omega_s k t} dt = \frac{1}{T_s} \int_{-T_s/2}^{T_s/2} (\sum_{n=-\infty}^{\infty} \delta(t - nT_s)) e^{-j\omega_s k t} dt \tag{D.3}$$

Since $\delta(t - nT_s)$ is only non-zero for $t = nT_s$, and the integral in (D.3) is from $-T_s/2$ to $T_s/2$, only $\delta(t - 0T_s)$ for $n = 0$ from the sum $\sum_{n=-\infty}^{\infty} \delta(t - nT_s)$ will contribute to the integral. Hence, we can write (D.3) as

$$C_k = \frac{1}{T_s} \int_{-T_s/2}^{T_s/2} \delta(t) e^{-j\omega_s k t} dt \tag{D.4}$$

The sifting property of the dirac impulse, Property A.0.1, is given by

$$\int_{t_1}^{t_2} x(t)\delta(t-t_0)dt = \begin{cases} x(t_0) & t_1 < t_0 < t_2 \\ 0 & \text{otherwise} \\ \text{undefined for} & t_0 = t_1 \text{ or } t_2 \end{cases} \tag{D.5}$$

It allows to use the dirac function with its non-zero value shifted to t_0 to "pick" or "sift" out a functions value at t_0. Using the sifting property of the dirac function with $t_0 = 0$ and $x(t) = e^{-j\omega_s kt}$, Equation (D.4) finally results in

$$C_k = \frac{1}{T_s} e^{-j\omega_s k0} = \frac{1}{T_s} \tag{D.6}$$

Substituting C_k (D.6), into (D.2) and using $\omega_s = 2\pi f_s$ finally gives the relation

$$\sum_{n=-\infty}^{\infty} \delta(t - nT_s) = \sum_{k=-\infty}^{\infty} \frac{1}{T_s} e^{j2\pi f_s kt} \tag{D.7}$$

Hence, the result. □

Appendix E

Fourier Transform of Shifted Dirac Impulse

Lemma E.0.1. *The Fourier transform of the shifted dirac impulse $\delta(t - nT_s)$ is*

$$\mathcal{F}\{\delta(t - nT_s)\} = e^{-j2\pi fnT_s} \tag{E.1}$$

Proof. The Fourier transform is calculated according to (2.26) by

$$\mathcal{F}\{\delta(t - nT_s)\} = \int_{-\infty}^{\infty} \delta(t - nT_s)e^{-j2\pi ft}dt \tag{E.2}$$

Using the sifting property of the dirac function, Property A.0.1, given by

$$\int_{t_1}^{t_2} x(t)\delta(t - t_0)dt = \begin{cases} x(t_0) & t_1 < t_0 < t_2 \\ 0 & \text{otherwise} \\ \text{undefined for} & t_0 = t_1 \text{ or } t_2 \end{cases} \tag{E.3}$$

with $t_0 = nT_s$ and $x(t) = e^{-j2\pi ft}$ in (E.2) results in

$$\int_{-\infty}^{\infty} \delta(t - nT_s)e^{-j2\pi ft}dt = e^{-j2\pi fnT_s} \tag{E.4}$$

Hence, the result. □

Appendix F

Relation between DTFT and FT for the Product of Impulse Train with Continuous Time Signal

Lemma F.0.1. *Let* $III_{T_s}(t) = \sum_{n=-\infty}^{\infty} \delta(t - nT_s)$ *be a dirac comb or impulse train. Then the Fourier transform of* $x(t)III_{T_s}(t)$*, equals the DTFT of the sequence* $x(nT_s)$*, i.e. [OBS01]*

$$\mathcal{F}\{x(t)III_{T_s}(t)\} = X_{DTFT}(f) \tag{F.1}$$

Note that the sampling of a continuous time signal is often modelled as a multiplication with a dirac comb $x(t)$ $III_{T_s}(t)$*. A dirac comb is an impulse train* $III_{T_s}(t) = \sum_{n=-\infty}^{\infty} \delta(t - nT_s)$*, where dirac impulses are periodically repeated with period* T_s*. It is important to emphasize that this is strictly a mathematical construct to investigate the properties of the DTFT/DFT, and it is not how the sampling operation would be implemented [OBS01].*

Proof. According to Lemma C.0.1 the DTFT of a signal $x(t)$ equals the FT of this signal, scaled by $1/T_s$ and periodically repeated with a distance of kf_s, i.e.

$$X_{DTFT}(f) = \frac{1}{T_s} \sum_{k=-\infty}^{\infty} X_{FT}(f - kf_s) \tag{F.2}$$

In the following we will show that

$$\mathcal{F}\{x(t)\mathrm{III}_{T_s}(t)\} = \frac{1}{T_s} \sum_{k=-\infty}^{\infty} X_{FT}(f - kf_s) \tag{F.3}$$

and consequently equals the DTFT. Since the Fourier transform is a special case of the Laplace transform, the FT inherits the computational rules for transforms from the Laplace transform. Consequently, the FT of the product of two signals equals the convolution of their respective FTs.

$$\mathcal{F}\{x(t)\mathrm{III}_{T_s}(t)\} = \mathcal{F}\{x(t)\} * \mathcal{F}\{\mathrm{III}_{T_s}(t)\} = X_{FT}(f) * \mathcal{F}\{\mathrm{III}_{T_s}(t)\} \tag{F.4}$$

According to Lemma G.0.1, the Fourier transform of $\mathrm{III}_{T_s}(t)$ is given by

$$\mathcal{F}\{\mathrm{III}_{T_s}(t)\} = \frac{1}{T_s}\sum_{k=-\infty}^{\infty}\delta(f-kf_s) = \frac{1}{T_s}\mathrm{III}_{f_s}(f) \tag{F.5}$$

The convolution in (F.4), hence, results in

$$\begin{aligned} X_{FT}(f) * \mathcal{F}\{\mathrm{III}_{T_s}(t)\} &= \frac{1}{T_s}X_{FT}(f) * \mathrm{III}_{f_s}(f) \\ &= \frac{1}{T_s}\int_{-\infty}^{\infty} X_{FT}(\tilde{f})\mathrm{III}_{f_s}(f-\tilde{f})d\tilde{f} \\ &= \frac{1}{T_s}\int_{-\infty}^{\infty} X_{FT}(\tilde{f})\sum_{k=-\infty}^{\infty}\delta(f-\tilde{f}-kf_s)d\tilde{f} \\ &= \frac{1}{T_s}\sum_{k=-\infty}^{\infty}\int_{-\infty}^{\infty} X_{FT}(\tilde{f})\delta(f-\tilde{f}-kf_s)d\tilde{f} \\ &= \frac{1}{T_s}\sum_{k=-\infty}^{\infty}\int_{-\infty}^{\infty} X_{FT}(\tilde{f})\delta(-(\tilde{f}-f+kf_s))d\tilde{f} \end{aligned} \tag{F.6}$$

Application of the scaling property of the dirac impulse, Property A.0.1, i.e.

$$\delta(af) = \frac{\delta(f)}{|a|} \tag{F.7}$$

to Equation (F.6) with $a=-1$ results in

$$\frac{1}{T_s}\sum_{k=-\infty}^{\infty}\int_{-\infty}^{\infty} X_{FT}(\tilde{f})\delta(-(\tilde{f}-f+kf_s))d\tilde{f} = \frac{1}{T_s}\sum_{k=-\infty}^{\infty}\int_{-\infty}^{\infty} X_{FT}(\tilde{f})\delta(\tilde{f}-f+kf_s)d\tilde{f} \tag{F.8}$$

Application of the sifting property of the dirac impulse, Property A.0.1, i.e.

$$\int_{t_1}^{t_2} x(t)\delta(t-t_0)dt = \begin{cases} x(t_0) & t_1 < t_0 < t_2 \\ 0 & \text{otherwise} \\ \text{undefined for} & t_0 = t_1 \text{ or } t_2 \end{cases} \tag{F.9}$$

to Equation (F.8) with $t=\tilde{f}$ and $t_0 = f-kf_s$ finally results in the relation

$$\begin{aligned} \mathcal{F}\{x(t)\mathrm{III}_{T_s}(t)\} &= \frac{1}{T_s}\sum_{k=-\infty}^{\infty}\int_{-\infty}^{\infty} X_{FT}(\tilde{f})\delta(\tilde{f}-f+kf_s)d\tilde{f} \\ &= \frac{1}{T_s}\sum_{k=-\infty}^{\infty} X_{FT}(f-kf_s) \end{aligned} \tag{F.10}$$

Hence, the result. □

Appendix G

Fourier Transform of Dirac Impulse Train (Dirac Comb)

Lemma G.0.1. *Let*

$$III_{T_s}(t) = \sum_{n=-\infty}^{\infty} \delta(t - nT_s) \tag{G.1}$$

be a dirac comb or dirac impulse train with impulse spacing T_s. The Fourier transform of $III_{T_s}(t)$ is again an impulse train, but with inverse impulse spacing, i.e. $f_s = 1/T_s$, and a scaling factor of $1/T_s$, i.e.

$$\mathcal{F}\{III_{T_s}(t)\} = \frac{1}{T_s} \sum_{k=-\infty}^{\infty} \delta(f - kf_s) = \frac{1}{T_s} III_{f_s}(f) \tag{G.2}$$

Proof. The impulse train (G.1) is periodic. Therefore, it can be expressed as a Fourier series according to (2.30) as

$$\mathrm{III}_{T_s}(t) = \sum_{k=-\infty}^{\infty} C_k e^{j2\pi f_s k t} \tag{G.3}$$

with the Fourier coefficients calculated according to (2.31) as

$$C_k = \frac{1}{T_s} \int_{-T_s/2}^{T_s/2} \mathrm{III}_{T_s}(t) e^{-j2\pi k t} dt = \frac{1}{T_s} \int_{-T_s/2}^{T_s/2} \sum_{n=-\infty}^{\infty} \delta(t - nT_s) e^{-j2\pi k t} dt \tag{G.4}$$

On the integration interval $[-T_s/2, T_s/2]$ the impulse train $\sum_{n=-\infty}^{\infty} \delta(t - nT_s)$ will be only non-zero for n=0. Therefore, (G.4) becomes (G.5). With the sifting property of the dirac impulse, Property A.0.1, C_k is finally calculated to have the constant value

$$C_k = \frac{1}{T_s} \int_{-T_s/2}^{T_s/2} \delta(t) e^{-j2\pi k t} dt = \frac{1}{T_s} e^{-j2\pi k 0} = \frac{1}{T_s} \tag{G.5}$$

The dirac comb is hence given by

$$\mathrm{III}_{T_s}(t) = \frac{1}{T_s} \sum_{k=-\infty}^{\infty} e^{j2\pi f_s k t} \tag{G.6}$$

where the calculated value of C_k was inserted into (G.3). According to (2.26) the Fourier transform of the dirac comb (G.6) is given by

$$\begin{aligned} \mathcal{F}\{\frac{1}{T_s} \sum_{k=-\infty}^{\infty} e^{j2\pi f_s k t}\} &= \frac{1}{T_s} \int_{-\infty}^{\infty} \sum_{k=-\infty}^{\infty} e^{j2\pi f_s k t} e^{-j2\pi f t} dt \\ &= \frac{1}{T_s} \sum_{k=-\infty}^{\infty} \int_{-\infty}^{\infty} e^{j2\pi f_s k t} e^{-j2\pi f t} dt \\ &= \frac{1}{T_s} \sum_{k=-\infty}^{\infty} \int_{-\infty}^{\infty} e^{-j2\pi (f - f_s k) t} dt \end{aligned} \tag{G.7}$$

By Lemma B.0.1 the integral of $e^{-j2\pi \bar{f} t}$ is given by

$$\int_{-\infty}^{\infty} e^{-j2\pi \bar{f} t} dt = \delta(\bar{f}) \tag{G.8}$$

With $\bar{f} = f - k f_s$ the relation (G.8) is substituted into (G.7) results in

$$\begin{aligned} \mathcal{F}\{\mathrm{III}_{T_s}(t)\} &= \frac{1}{T_s} \sum_{k=-\infty}^{\infty} \int_{-\infty}^{\infty} e^{-j2\pi (f - k f_s) t} dt \\ &= \frac{1}{T_s} \sum_{k=-\infty}^{\infty} \delta(f - k f_s) \\ &= \frac{1}{T_s} \mathrm{III}_{f_s}(f) \end{aligned} \tag{G.9}$$

which is an impulse train with spacing f_s, scaled with factor $1/T_s$. Hence, the result. □

Appendix H

Relation between DTFT and DFT

Lemma H.0.1. *Let $x(t)$ be a periodic signal with period $T_w = NT_s$. Then the following relation holds:*

$$X_{DTFT}(f_k) = \frac{1}{\sqrt{N}T_s}\delta(0)X_{DFT}[k] \tag{H.1}$$

with

$$X_{DFT}[k] = \frac{1}{\sqrt{N}}\sum_{n=0}^{N-1} x[n]e^{-\frac{j2\pi kn}{N}} \tag{H.2}$$

Hence, for a periodic signal $x(t)$ with period $T_w = NT_s$, only a finite time sequence of $T_w - T_s$, or N samples are necessary to exactly calculate the DTFT at the discrete frequencies $f_k = k\frac{1}{T_w} = kf_H$ with $k = 0, \dots N-1$.

Proof. In Section 2.2.2 the DTFT was introduced by Equation (2.39) as

$$X_{DTFT}(f) = \sum_{n=-\infty}^{\infty} x[n]e^{-j2\pi f(nT_s)} \tag{H.3}$$

with the discrete sequence $x[n] = x(nT_s)$ which is composed of the samples of $x(t)$ at sampling frequency $f_s = \frac{1}{T_s}$. The sum in (H.3) can be expressed as

$$\begin{aligned}
X_{DTFT}(f) = &\sum_{n=-\infty}^{-1} x[n]e^{-j2\pi f(nT_s)} + \sum_{n=0}^{N-1} x[n]e^{-j2\pi f(nT_s)} \\
&+ \sum_{n=N}^{2N-1} x[n]e^{-j2\pi f(nT_s)} + \sum_{n=2N}^{3N-1} x[n]e^{-j2\pi f(nT_s)} \\
&+ \sum_{n=3N}^{\infty} x[n]e^{-j2\pi f(nT_s)} \\
&= \sum_{n=-\infty}^{-1} x[n]e^{-j2\pi f(nT_s)} + \sum_{n=0}^{N-1} x[n]e^{-j2\pi f(nT_s)} \\
&+ \sum_{n=0}^{N-1} x[n+N]e^{-j2\pi f((n+N)T_s)} + \sum_{n=0}^{N-1} x[n+2N]e^{-j2\pi f((n+2N)T_s)} \\
&+ \sum_{n=3N}^{\infty} x[n]e^{-j2\pi f(nT_s)}
\end{aligned} \tag{H.4}$$

If the signal is periodic with period $T_w = NT_s$ then

$$\begin{aligned} x(t) &= x(t + mT_w) = x(t + mNT_s) \\ x(nT_s) &= x(nT_s + mT_w) = x((n + mN)T_s) \\ x[n] &= x[n + mN] \end{aligned} \tag{H.5}$$

with $m \in \mathbb{Z}$ holds, and the sum in (H.4) can be expressed as

$$\begin{aligned} X_{DTFT}(f) = &\sum_{n=-\infty}^{-1} x[n]e^{-j2\pi f(nT_s)} \\ &+ \sum_{n=0}^{N-1} x[n](e^{-j2\pi f(nT_s)} + e^{-j2\pi f((n+N)T_s)} + e^{-j2\pi f((n+2N)T_s)}) \\ &+ \sum_{n=3N}^{\infty} x[n]e^{-j2\pi f(nT_s)} \end{aligned} \tag{H.6}$$

This expression can be further simplified to

$$\begin{aligned} X_{DTFT}(f) = &\sum_{n=-\infty}^{-1} x[n]e^{-j2\pi f(nT_s)} \\ &+ \sum_{n=0}^{N-1} x[n]e^{-j2\pi f(nT_s)}(e^{-j2\pi f(0\cdot NT_s)} + e^{-j2\pi f(1\cdot NT_s)} + e^{-j2\pi f(2\cdot NT_s)}) \\ &+ \sum_{n=3N}^{\infty} x[n]e^{-j2\pi f(nT_s)} \\ = &\sum_{n=-\infty}^{-1} x[n]e^{-j2\pi f(nT_s)} \\ &+ (\sum_{n=0}^{N-1} x[n]e^{-j2\pi f(nT_s)})(\sum_{l=0}^{2} e^{-j2\pi f(l\cdot NT_s)}) \\ &+ \sum_{n=3N}^{\infty} x[n]e^{-j2\pi f(nT_s)} \end{aligned} \tag{H.7}$$

The first and last summand in (H.7) can be expressed the same way as the term in the middle, finally leading to

$$\begin{aligned} X_{DTFT}(f) &= \sum_{n=0}^{N-1} x[n]e^{-j2\pi f(nT_s)}(\sum_{l=-\infty}^{\infty} e^{-j2\pi f(l\cdot NT_s)}) \\ &= \sum_{n=0}^{N-1} x[n]e^{-j2\pi f(nT_s)}(\sum_{l=-\infty}^{\infty} e^{-j2\pi f(l\cdot T_w)}) \end{aligned} \tag{H.8}$$

where $T_w = NT_s$ was inserted. By Lemma I.0.1, the second sum in (H.8) equals a dirac impulse train with period $f_H = \frac{1}{T_w}$ and scaled with factor $\frac{1}{T_w}$, i.e.

$$\sum_{l=-\infty}^{\infty} e^{-j2\pi f(l\cdot T_w)} = \frac{1}{T_w} \sum_{m=-\infty}^{\infty} \delta(f - mf_H) \tag{H.9}$$

Relation (H.9) is inserted into (H.8) resulting in

$$X_{DTFT}(f) = \sum_{n=0}^{N-1} x[n] e^{-j2\pi f(nT_s)} \left(\frac{1}{T_w} \sum_{m=-\infty}^{\infty} \delta(f - mf_H) \right) \tag{H.10}$$

Since the dirac train in (H.10) is only non-zero for $f = mf_H = m\frac{1}{NT_s}$, $\sum_{n=0}^{N-1} x[n]e^{-j2\pi f(nT_s)}$ will be multiplied with zero except for these specific values of f. Hence, we can write, using $f_H = \frac{1}{T_w} = \frac{1}{NT_s}$:

$$\begin{aligned} X_{DTFT}(f) &= \frac{1}{T_w} \sum_{n=0}^{N-1} \left(x[n] \sum_{m=-\infty}^{\infty} e^{-j2\pi (mf_H)(nT_s)} \delta(f - mf_H) \right) \\ &= \frac{1}{T_w} \sum_{n=0}^{N-1} \left(x[n] \sum_{m=-\infty}^{\infty} e^{-j2\pi (m\frac{1}{NT_s})(nT_s)} \delta(f - mf_H) \right) \\ &= \frac{1}{T_w} \sum_{n=0}^{N-1} x[n] \sum_{m=-\infty}^{\infty} e^{-j2\pi \frac{mn}{N}} \delta(f - mf_H) \end{aligned} \tag{H.11}$$

If the DTFT is only considered at discrete frequencies

$$f_k = kf_H \tag{H.12}$$

with $k = 0, \ldots, N-1$, meaning that f_k is an integer multiple of the harmonic frequency $f_H = \frac{1}{T_w}$, where T_w was the period of the periodic signal $x(t)$, the following relation is obtained

$$X_{DTFT}(f = kf_H) = \frac{1}{T_w} \sum_{n=0}^{N-1} x[n] \sum_{m=-\infty}^{\infty} e^{-j2\pi \frac{mn}{N}} \delta(kf_H - mf_H) \tag{H.13}$$

In (H.13), $\delta(kf_H - mf_H)$ is 0 except for $m = k$. Hence, we can write

$$\begin{aligned} X_{DTFT}(kf_H) &= \frac{1}{T_w} \sum_{n=0}^{N-1} x[n] e^{-j2\pi \frac{kn}{N}} \delta(0) \\ &= \frac{1}{NT_s} \sum_{n=0}^{N-1} x[n] e^{-j2\pi \frac{kn}{N}} \delta(0) \end{aligned} \tag{H.14}$$

Equation (H.14) gives the relation between the DTFT and DFT as

$$X_{DTFT}(kf_H) = \frac{1}{\sqrt{N}T_s} \delta(0) X_{DFT}[k] \tag{H.15}$$

as can be directly seen by recalling that the DFT was defined in (2.9) by

$$X_{DFT}[k] = \frac{1}{\sqrt{N}} \sum_{n=0}^{N-1} x(nT_s) e^{-\frac{j2\pi kn}{N}}, k = 0, ...N-1 \tag{H.16}$$

Hence, the result. □

Appendix I

Relation between the Sum of Complex Exponential Functions and a Dirac Comb

Lemma I.0.1. *Let $T_w = NT_S$ and $f_H = \frac{1}{T_w}$, then the following relation holds*

$$\sum_{l=-\infty}^{\infty} e^{-j2\pi f(l\cdot T_w)} = \frac{1}{T_w} \sum_{m=-\infty}^{\infty} \delta(f - mf_H) \tag{I.1}$$

Proof. By Lemma D.0.1 the relation between the dirac comb and complex exponential function is given by

$$\mathrm{III}_{T_s}(t) = \sum_{m=-\infty}^{\infty} \delta(t - mT_s) = \frac{1}{T_s} \sum_{l=-\infty}^{\infty} e^{j2\pi \frac{1}{T_s} lt} \tag{I.2}$$

with $\frac{1}{T_s} = f_s$. Substitution of variables according to $T_s = f_H$ and $t = f$ results in

$$\mathrm{III}_{f_H}(f) = \sum_{m=-\infty}^{\infty} \delta(f - mf_H) = \frac{1}{f_H} \sum_{l=-\infty}^{\infty} e^{j2\pi \frac{1}{f_H} lf} \tag{I.3}$$

Multiplication with f_H and substitution of $f_H = \frac{1}{T_w}$ finally leads to

$$\frac{1}{T_w} \sum_{m=-\infty}^{\infty} \delta(f - mf_H) = \sum_{l=-\infty}^{\infty} e^{j2\pi T_w lf} \tag{I.4}$$

Hence, the result. □

Relation I.1 can also be shown similarly as in the proof of Lemma G.0.1, and is given in the following. The dirac comb $\mathrm{III}_{f_H}(f)$ is a periodic repetition of dirac impulses with period f_H and can be expressed as a Fourier Series (2.30) by

$$\mathrm{III}_{f_H}(f) = \sum_{m=-\infty}^{\infty} \delta(f - mf_H) = \sum_{p=-\infty}^{\infty} C_p e^{j2\pi \frac{1}{f_H} pf} \tag{I.5}$$

The coefficient C_p is calculated according to (2.31) by

$$C_p = \frac{1}{f_H} \int_{-f_H/2}^{f_H/2} (\sum_{m=-\infty}^{\infty} \delta(f - m f_H)) e^{-j2\pi \frac{1}{f_H} p f} df \tag{I.6}$$

Since the limits of the integral are $\pm \frac{f_H}{2}$ the impulse train $\sum_{m=-\infty}^{\infty} \delta(f - m f_H)$ will only contribute to the integral for $m = 0$. Hence, we can write

$$C_p = \frac{1}{f_H} \int_{-f_H/2}^{f_H/2} \delta(f) e^{-j2\pi \frac{1}{f_H} p f} df \tag{I.7}$$

Application of the sifting property, Property A.0.1, i.e.

$$\int_{t_1}^{t_2} x(t)\delta(t - t_0)dt = \begin{cases} x(t_0) & t_1 < t_0 < t_2 \\ 0 & \text{otherwise} \\ \text{undefined for} & t_0 = t_1 \text{ or } t_2 \end{cases} \tag{I.8}$$

to (I.7) with $t = f$ and $t_0 = 0$ leads to

$$C_p = \frac{1}{f_H} e^{-j2\pi \frac{1}{f_H} p \cdot 0} = \frac{1}{f_H} \tag{I.9}$$

This result is inserted for C_p into (I.5), resulting in

$$\sum_{m=-\infty}^{\infty} \delta(f - m f_H) = \frac{1}{f_H} \sum_{p=-\infty}^{\infty} e^{j2\pi \frac{1}{f_H} p f} \tag{I.10}$$

Multiplication of both sides with f_H leads to

$$f_H \sum_{m=-\infty}^{\infty} \delta(f - m f_H) = \sum_{p=-\infty}^{\infty} e^{j2\pi \frac{1}{f_H} p f} \tag{I.11}$$

With the following relation

$$\sum_{p=-\infty}^{\infty} e^{j2\pi \frac{1}{f_H} p f} = \sum_{l=-\infty}^{\infty} e^{-j2\pi \frac{1}{f_H} l f} \tag{I.12}$$

and with $f_H = \frac{1}{T_w} = \frac{1}{N T_s}$ finally the relation

$$\sum_{l=-\infty}^{\infty} e^{-j2\pi f (l T_w)} = \frac{1}{T_w} \sum_{m=-\infty}^{\infty} \delta(f - m f_H) \tag{I.13}$$

is derived. Hence, the result.

Appendix J

Relation between FT of a Continuous Time Mathematical Model of a Truncated Sampled Sequence of $x(t)$ and the DFT

Lemma J.0.1. *Let $x(t)$ be a continuous time signal and*

$$\tilde{x}(t) = III_{T_s}(t)x(t)w(t) \tag{J.1}$$

a mathematical model of the truncated sampled sequence of $x(t)$, where $w(t)$ is a rectangular window function as defined in (L.1)*, and $III_{T_s}(t) = \sum_{n=-\infty}^{\infty} \delta(t - nT_s)$ is a dirac comb. Then the Fourier transform of $\tilde{x}(t)$, will equal the DFT* (2.9) *of $x(nT_s)$, at the discrete frequencies $f = kf_H$, $k \in \mathbb{Z}$ and scaled with factor $\sqrt{N}$, i.e.*

$$\tilde{X}_{FT}(kf_H) = \mathcal{F}\{III_{T_s}(t)x(t)w(t)\} = \sqrt{N}X_{DFT}[k] \tag{J.2}$$

with

$$X_{DFT}[k] = \frac{1}{\sqrt{N}} \sum_{n=0}^{N-1} x(nT_s)e^{-\frac{j2\pi kn}{N}} \tag{J.3}$$

Proof. The Fourier transform of (J.1) is according to (2.26)

$$\begin{aligned} \tilde{X}_{FT}(f) &= \mathcal{F}\{\mathrm{III}_{T_s}(t)x(t)w(t)\} \\ &= \int_{-\infty}^{\infty} \mathrm{III}_{T_s}(t)x(t)w(t)e^{-j2\pi ft}dt \end{aligned} \tag{J.4}$$

Since the rectangular window function $w(t)$ is

$$w(t) = \begin{cases} 1 & \text{for } 0 \leq t < T_w \\ 0 & \text{otherwise} \end{cases} \tag{J.5}$$

(J.4) equals

$$\tilde{X}_{FT}(f) = \int_{t=0}^{t=T_w=NT_s} \mathrm{III}_{T_s}(t)x(t)e^{-j2\pi ft}dt \tag{J.6}$$

for the variable t the relation $t = mT_s$, $m \in \mathbb{R}$ is substituted, with $dt = T_s dm$ and $m = \frac{t}{T_s}$ resulting in

$$\begin{aligned}\tilde{X}_{FT}(f) &= T_s \int_{m=0}^{m=N} \mathrm{III}_{T_s}(mT_s)x(mT_s)e^{-j2\pi fmT_s}dm \\ &= T_s \int_{m=0}^{N} \sum_{n=-\infty}^{\infty} \delta(mT_s - nT_s)x(mT_s)e^{-j2\pi fmT_s}dm\end{aligned} \tag{J.7}$$

Since $\delta(mT_s - nT_s)$ is zero for $m \neq n$, $x(mTs)$ and $e^{-j2\pi fmT_s}$ will be multiplied with zero and only $x(nTs)$ and $e^{-j2\pi fnT_s}$ will contribute to the integral. Hence, (J.7) can be written as

$$\begin{aligned}\tilde{X}_{FT}(f) &= T_s \int_{m=0}^{N} \sum_{n=-\infty}^{\infty} \delta(mT_s - nT_s)x(nT_s)e^{-j2\pi fnT_s}dm \\ &= T_s \sum_{n=-\infty}^{\infty} \int_{m=0}^{N} \delta(mT_s - nT_s)x(nT_s)e^{-j2\pi fnT_s}dm\end{aligned} \tag{J.8}$$

In some cases it is important to specify whether the integration interval $\int_a^b$ contains the boundaries, i.e. $[a, b], (a, b), [a, b)$ or $(a, b]$, as this determines the integral when integrating over a dirac function. In the case at hand the dirac function is integrated over the interval $[0, T_w)$ or rather $[0, N)$.

$$\tilde{X}_{FT}(f) = T_s \sum_{n=-\infty}^{\infty} \int_{[0,N)} \delta(mT_s - nT_s)x(nT_s)e^{-j2\pi fnT_s}dm \tag{J.9}$$

Since $\delta(mT_s - nT_s)$ is zero for $m \neq n$, all values of n outside the integration range $[0, N)$ will not contribute to the integral. Thus, the infinite sum in (J.8) can be replaced by the finite sum from $n = 0$ to $n = N - 1$.

$$\begin{aligned}
\tilde{X}_{FT}(f) &= T_s \sum_{n=0}^{N-1} \int_{[0,N)} \delta(mT_s - nT_s) x(nT_s) e^{-j2\pi f n T_s} dm \\
&= T_s \sum_{n=0}^{N-1} \int_{[0,N)} \delta(T_s(m-n)) x(nT_s) e^{-j2\pi f n T_s} dm \\
&= \sum_{n=0}^{N-1} \int_{[0,N)} \delta(m-n) x(nT_s) e^{-j2\pi f n T_s} dm \\
&= \sum_{n=0}^{N-1} x(nT_s) e^{-j2\pi f n T_s} \int_{[0,N)} \delta(m-n) dm \\
&= \sum_{n=0}^{N-1} x(nT_s) e^{-j2\pi f n T_s}
\end{aligned} \tag{J.10}$$

In (J.10) the scaling property of the dirac impulse, Property A.0.2, i.e.

$$\delta(af) = \frac{\delta(f)}{|a|} \tag{J.11}$$

was applied with $a = T_s$ and the property (A.4) with $t = m$ and $t_0 = n$. Finally, at the discrete frequencies $f = kf_H = k\frac{1}{T_w} = \frac{k}{NT_s}$ the relation

$$\begin{aligned}
\tilde{X}_{FT}(kf_H) &= \sum_{n=0}^{N-1} x(nT_s) e^{-\frac{j2\pi kn}{N}} \\
&= \sqrt{N} X_{DTF}[k]
\end{aligned} \tag{J.12}$$

is obtained with

$$X_{DFT}[k] = \frac{1}{\sqrt{N}} \sum_{n=0}^{N-1} x(nT_s) e^{-\frac{j2\pi kn}{N}} \tag{J.13}$$

Hence, the result. □

Appendix K

Relation between DTFT and FT for the Product of a Continuous Time Signal with a Dirac Comb and a Rectangular Window Function

Lemma K.0.1. *Let $x(t)$ be a continuous signal, $w(t)$ a rectangular window function as defined in* (L.1)*, and $III_{T_s}(t) = \sum_{n=-\infty}^{\infty} \delta(t - nT_s)$ a dirac comb. Then the Fourier transform of the product of $x(t)$ with $III_{T_s}(t)$ and $w(t)$, is given by*

$$\begin{aligned} \tilde{X}_{FT}(f) &= \mathcal{F}\{\tilde{x}(t) = III_{T_s}(t)x(t)w(t)\} \\ &= \int_{-\infty}^{\infty} X_{DTFT}(\bar{f})T_w sinc(\pi(f-\bar{f})T_w)e^{-j\pi(f-\bar{f})T_w}d\bar{f} \end{aligned} \tag{K.1}$$

Proof. Since the FT of a product of two signals corresponds to the convolution of their respective FT, $\mathcal{F}\{\mathrm{III}_{T_s}(t)x(t)w(t)\}$ can be rewritten as

$$\mathcal{F}\{\mathrm{III}_{T_s}(t)x(t)w(t)\} = \mathcal{F}\{\mathrm{III}_{T_s}(t)x(t)\} * \mathcal{F}\{w(t)\} = \mathcal{F}\{\mathrm{III}_{T_s}(t)x(t)\} * W_{FT}(f) \tag{K.2}$$

By Lemma F.0.1 the FT of $\mathrm{III}_{T_s}(t)x(t)$ corresponds to the DTFT:

$$\mathcal{F}\{\mathrm{III}_{T_s}(t)x(t)\} = X_{DTFT}(f) \tag{K.3}$$

Consequently (K.2) corresponds to

$$\mathcal{F}\{\mathrm{III}_{T_s}(t)x(t)\} * W_{FT}(f) = X_{DTFT}(f) * W_{FT}(f) \tag{K.4}$$

By Lemma L.1.1, the FT of $w(t)$ is given by

$$W_{FT}(f) = T_w \text{sinc}(\pi f T_w) e^{-j\pi f T_w} \tag{K.5}$$

The convolution in (K.4) then finally results in

$$\begin{aligned} X_{DTFT}(f) * W_{FT}(f) &= \int_{-\infty}^{\infty} X_{DTFT}(\bar{f}) W_{FT}(f - \bar{f}) d\bar{f} \\ &= \int_{-\infty}^{\infty} X_{DTFT}(\bar{f}) T_w \text{sinc}(\pi(f - \bar{f}) T_w) e^{-j\pi(f-\bar{f})T_w} d\bar{f} \end{aligned} \tag{K.6}$$

Hence, the result. □

Appendix L

Fourier Transform and Rectangular Window Function

L.1 Fourier Transform of Rectangular Window Function

Lemma L.1.1. *The Fourier transform of the rectangular window function, given by*

$$w(t) = \begin{cases} 1 & \text{for } 0 \leq t < T_w \\ 0 & \text{otherwise} \end{cases} \tag{L.1}$$

is

$$\mathcal{F}\{w(t)\} = W_{FT}(f) = T_w sinc(\pi f T_w) e^{-j\pi f T_w} \tag{L.2}$$

Proof. According to Equation (2.26) the FT of $w(t)$ is calculated by

$$W_{FT}(f) = \int_{-\infty}^{\infty} w(t) e^{-j2\pi ft} dt \tag{L.3}$$

Since $w(t)$ is one for $0 \leq t < T_w$ and zero otherwise, (L.3) can be written as

$$\begin{aligned} W_{FT}(f) &= \int_0^{T_w} e^{-j2\pi ft} dt \\ &= -\frac{1}{j2\pi f}[e^{-j2\pi f T_w} - e^{-j2\pi f 0}] \\ &= -\frac{1}{j2\pi f}[e^{-j2\pi f T_w} - 1] \end{aligned} \tag{L.4}$$

According to Equation (2.17)

$$e^{-j2\pi f T_w} = \cos(2\pi f T_w) - j\sin(2\pi f T_w) \tag{L.5}$$

holds. Inserting (L.5) into (L.4) leads to

$$W_{FT}(f) = \frac{1}{2\pi f}\sin(2\pi f T_w) - \frac{1}{j2\pi f}[\cos(2\pi f T_w) - 1] \tag{L.6}$$

For the first term the trigonometric identity

$$\sin(2\Theta) = 2\sin(\Theta)\cos(\Theta) \tag{L.7}$$

is used. For the second term the trigonometric identity

$$\cos(2\Theta) = 1 - 2\sin^2(\Theta) \tag{L.8}$$

is applied, finally resulting in

$$\begin{aligned} W_{FT}(f) &= \frac{1}{2\pi f} 2\sin(\pi f T_w)\cos(\pi f T_w) - \frac{1}{j2\pi f}[-2sin^2(\pi f T_w)] \\ &= \frac{1}{\pi f}\sin(\pi f T_w)[\cos(\pi f T_w) + \frac{1}{j}\sin(\pi f T_w)] \\ &= \frac{1}{\pi f}\sin(\pi f T_w)[\cos(\pi f T_w) - j\sin(\pi f T_w)] \\ &= \frac{1}{\pi f}\sin(\pi f T_w)e^{-j\pi f T_w} \\ &= T_w\frac{1}{\pi f T_w}\sin(\pi f T_w)e^{-j\pi f T_w} \\ &= T_w\text{sinc}(\pi f T_w)e^{-j\pi f T_w} \end{aligned} \tag{L.9}$$

where $\text{sinc}(\pi f T_w)$ is the sinc function defined by

$$\text{sinc}(at) = \frac{\sin(at)}{at} \tag{L.10}$$

according to [Pou18, p. 7-15]. Hence, the result.

□

L.2 Fourier Transform of Centered Rectangular Window Function

Lemma L.2.1. *The Fourier transform of the rectangular window function, given by*

$$w(t) = \begin{cases} 1 & for\ -\frac{T_w}{2} \leq t < \frac{T_w}{2} \\ 0 & otherwise \end{cases} \tag{L.11}$$

is

$$\mathcal{F}\{w(t)\} = W_{FT}(f) = T_w sinc(\pi T_w f) \tag{L.12}$$

Proof. According to Equation (2.27) the FT of $w(t)$ is calculated by

$$W_{FT}(f) = \int_{-\infty}^{\infty} w(t) e^{-j2\pi ft} dt \tag{L.13}$$

Since $w(t)$ is one for $-\frac{T_w}{2} \leq t < \frac{T_w}{2}$ and zero otherwise, (L.13) can be written as

$$\begin{aligned} W_{FT}(f) &= \int_{-\frac{T_w}{2}}^{\frac{T_w}{2}} e^{-j2\pi ft} dt \\ &= -\frac{1}{j2\pi f}[e^{-j2\pi f\frac{T_w}{2}} - e^{j2\pi f\frac{T_w}{2}}] \\ &= \frac{1}{\pi f}[\sin(2\pi f\frac{T_w}{2})] \\ &= T_w \frac{\sin(\pi f T_w)}{\pi f T_w} \\ &= T_w \text{sinc}(\pi T_w f) \end{aligned} \tag{L.14}$$

where $\text{sinc}(\pi f T_w)$ is the sinc function defined by

$$\text{sinc}(at) = \frac{\sin(at)}{at} \tag{L.15}$$

according to [Pou18, p. 7-15]. Hence, the result. □

Appendix M

Statistics

M.0.1 Cumulative Distribution Function

Definition M.0.1. *The **cumulative distribution function** of a real-valued random variable X is defined as*

$$F_X(x) = P(X \leq x) \tag{M.1}$$

where $P(X \leq x)$ is the probability that X realizes a value less or equal to x, [PP18, p. 77].

Definition M.0.2. *The **joint cumulative distribution function** of two real-valued random variables X and Y is defined as*

$$F_{X,Y}(x, y) = P(X \leq x, Y \leq y) \tag{M.2}$$

*where $P(X \leq x, Y \leq y)$ is the probability that X realizes a value less or equal to x **and** Y realizes a value less or equal to y, [PP18, p. 89].*

M.0.2 Probability Density Function

Definition M.0.3. *The **probability density function** of a real-valued random variable X is defined as [PP18, p. 85]*

$$f_X(x) = \frac{d}{dx} F_X(x) \tag{M.3}$$

where $F_X(x)$ is the cumulative distribution function introduced in Definition M.0.1.

Definition M.0.4. *The **joint probability density function** of two real-valued random variables X and Y is defined as [PP18, p. 92]*

$$f_{X,Y}(x, y) = \frac{\partial^2}{\partial x \partial y} F_{X,Y}(x, y) \tag{M.4}$$

where $F_{X,Y}(x, y)$ is the joint cumulative distribution function introduced in Definition M.0.2.

Definition M.0.5. *The* ***marginal probability density functions*** *of two real-valued random variables X and Y are defined as [PP18, p. 94]*

$$\begin{aligned} f_X(x) &= \int_{-\infty}^{\infty} f_{X,Y}(x,y)dy \\ f_Y(y) &= \int_{-\infty}^{\infty} f_{X,Y}(x,y)dx \end{aligned} \tag{M.5}$$

where $f_{X,Y}(x,y)$ is the joint probability density function introduced in Definition M.0.4.

M.0.3 Expected Value Operator

Definition M.0.6. *The expected value of a real-valued random variable X is defined as [PP18, p. 110]*

$$\mathbb{E}[X] = \mu_x = \int_{-\infty}^{\infty} x f_X(x)dx \tag{M.6}$$

where $f_X(x)$ is the probability density function, introduced in Definition M.0.3, or the marginal probability density function of X, introduced in Definition M.0.5, in case two real valued random variables are considered with joint probability density function $f_{X,Y}(x,y)$, see Definition M.0.4.

Property M.0.1. *The expectation operator $\mathbb{E}[\cdot]$ is linear. Hence, the following relations hold [PP18, p. 113]*

$$\begin{aligned} \mathbb{E}[X_1 + X_2] &= \mathbb{E}[X_1] + \mathbb{E}[X_2] \\ \mathbb{E}[aX] &= a\mathbb{E}[X] \end{aligned} \tag{M.7}$$

where X_1, X_2 and X are real-valued random variables and $a \in \mathbb{R}$ is a constant.

Lemma M.0.1. *Let X_1 and X_2 be real-valued random variables then [PP18, p. 119]*

$$\mathbb{E}[X_1 X_2] = \mathbb{E}[X_1]\mathbb{E}[X_2] + cov[X_1, X_2] \tag{M.8}$$

where $cov[X_1, X_2]$ is the covariance, see Definition M.0.8.

Note Lemma M.0.5, if X_1 and X_2 are independent.

M.0.4 Variance

Definition M.0.7. *The variance of a real-valued random variable X is [PP18, p. 117]*

$$var[X] = \mathbb{E}[(X - \mu_x)^2] = cov[X, X] = \mathbb{E}[X^2] - \mathbb{E}[X]^2 \tag{M.9}$$

where μ_x is the expected value of X, see Appendix M.0.3 and $cov[X, X]$ is the covariance of X with itself, see Definition M.0.8 and Property M.0.3.

For the variance operator the following basic properties exist [PP18, p. 121]:

Property M.0.2.

$$var[X] \geq 0 \tag{M.10}$$

$$\begin{aligned} var[a] &= 0 \\ var[X + a] &= var[X] \\ var[aX] &= a^2 var[X] \end{aligned} \tag{M.11}$$

for all $a \in \mathbb{R}$.

$$\begin{aligned} var[aX_1 + bX_2] &= a^2 var[X_1] + b^2 var[X_2] + 2abcov[X_1, X_2] \\ var[aX_1 - bX_2] &= a^2 var[X_1] + b^2 var[X_2] - 2abcov[X_1, X_2] \end{aligned} \tag{M.12}$$

for all $a, b \in \mathbb{R}$.

Lemma M.0.2. *Let the real-valued random variables $X_1, X_2, \ldots, X_N$ be uncorrelated, meaning their covariance are zero, see Definition M.0.9, then the following relation holds [PP18, p. 124]*

$$var[\sum_{n=1}^{N} X_n] = \sum_{n=1}^{N} var[X_n] \tag{M.13}$$

Lemma M.0.3. *Let the two real-valued random variables X_1 and X_2 be independent, then the variance of their product can be calculated by [Goo60]*

$$var[X_1 X_2] = \mathbb{E}[X_1]^2 var[X_2] + \mathbb{E}[X_2]^2 var[X_1] + var[X_1] var[X_2] \tag{M.14}$$

M.0.5 Covariance

Definition M.0.8. *For two real-valued random variables X_1 and X_2 with expected values μ_{x_1} and μ_{x_2} and variance $\sigma_{x_1}^2$ and $\sigma_{x_2}^2$ the **covariance** is defined as [PP18, p. 119]*

$$cov[X_1, X_2] = \mathbb{E}[(X_1 - \mu_{x_1})(X_2 - \mu_{x_2})] \tag{M.15}$$

Often the following property is used:

Property M.0.3. *Let X_1 and X_2 be two real-valued random variables then [PP18, p. 119]*

$$cov[X_1, X_2] = \mathbb{E}[X_1 X_2] - \mathbb{E}[X_1]\mathbb{E}[X_2] \tag{M.16}$$

Proof. The relation (M.16) is obtained from (M.15) using the fact that the expectation operator is linear, see Property M.0.1

$$\begin{aligned}\mathbb{E}[(X_1 - \mu_{X_1})(X_2 - \mu_{x_2})] &= \mathbb{E}[X_1X_2 - \mu_{x_1}X_2 - \mu_{x_2}X_1 + \mu_{x_1}\mu_{x_2}] \\ &= \mathbb{E}[X_1X_2] - \mathbb{E}[\mu_{x_1}X_2] - \mathbb{E}[\mu_{x_2}X_1] + \mathbb{E}[\mu_{x_1}\mu_{x_2}] \\ &= \mathbb{E}[X_1X_2] - \mu_{x_1}\mathbb{E}[X_2] - \mu_{x_2}\mathbb{E}[X_1] + \mu_{x_1}\mu_{x_2}\end{aligned} \tag{M.17}$$

As $\mathbb{E}[X_1] = \mu_{x_1}$ and $\mathbb{E}[X_2] = \mu_{x_2}$ Equation (M.17) results in

$$cov[X_1, X_2] = \mathbb{E}[X_1X_2] - \mathbb{E}[X_1]E[X_2], \tag{M.18}$$

□

Property M.0.4. *The covariance is symmetric such that*

$$cov[X_1, X_2] = cov[X_2, X_1] \tag{M.19}$$

Definition M.0.9. *Two real-valued random variables X_1 and X_2 are said to be* ***uncorrelated*** *if $cov[X_1, X_2] = 0$, [PP18, p. 121] .*

Lemma M.0.4. *Let two real-valued random variables X_1 and X_2 be independent, see Appendix M.0.13, then their covariance will be zero [PP18, p. 123] .*

Proof. As X_1 and X_2 are independent, according to Lemma M.0.5

$$\mathbb{E}[X_1X_2] = \mathbb{E}[X_1]\mathbb{E}[X_2] \tag{M.20}$$

holds. Hence, the covariance is according to Equation (M.16) zero. □

Note, that if the covariance of two random variables is zero this does not imply that they are independent.

M.0.6 Correlation

Definition M.0.10. *For two random variables X_1 and X_2 with expected values μ_{x_1} and μ_{x_2} and variance $\sigma^2_{x_1}$ and $\sigma^2_{x_2}$ the* ***correlation*** *is defined as [PP18, p. 119]*

$$\rho_{x_1,x_2} = corr[X_1, X_2] = \frac{cov[X_1, X_2]}{\sigma_x\sigma_y} \tag{M.21}$$

where $cov[X_1, X_2]$ is the covariance, see Definition M.0.8.

Property M.0.5. *The correlation is symmetric such that*

$$corr[X_1, X_2] = corr[X_2, X_1] \tag{M.22}$$

M.0.7 Stationarity of a Sequence of Random Variables

Definition M.0.11. *A sequence of random variables*

$$X[1], X[2], \dots X[N] \tag{M.23}$$

is denoted as stationary if and only if its joint distribution is equal to the joint distribution of the shifted sequence

$$X[1+\tau], X[2+\tau], \dots X[N+\tau] \tag{M.24}$$

for any $\tau \in \mathbb{N}$, [Sta02, p. 326].

Property M.0.6. *All terms of a stationary sequence have the same distribution, i.e. $X[n]$ and $X[n+\tau]$ have the same distribution for any n and $\tau \in \mathbb{N}$. From this it follows, that since they have the same distribution, all terms of the sequence also have the same expected value and the same variance, [Sta02, p. 326].*

M.0.8 Independent and Identically Distributed Random Variables (i.i.d.)

Definition M.0.12. *A collection of random variables (for example a sequence of random variables) is denoted as* ***independent and identically distributed*** *if each random variable has the same probability distribution and if all random variables are mutually independent, see Definition M.0.13, from each other, [MC04, p. 289].*

M.0.9 Mutual Independence

Definition M.0.13. *A collection of random variables (for example a sequence of random variables) are denoted as mutually independent if the realization of each random variable does not affect the probability distribution of any combination of the other random variables in the collection.*

Lemma M.0.5. *Let two real-valued random variables X_1 and X_2 be independent, then the expected value of their product equals the product of the expected value of each random variable [PP18, p. 116]*

$$\mathbb{E}[X_1 X_2] = \mathbb{E}[X_1]\mathbb{E}[X_2] \tag{M.25}$$

and their covariance, see Definition M.0.8, is zero

$$cov[X_1, X_2] = 0 \tag{M.26}$$

meaning that they are uncorrelated, see Definition M.0.9.

Note, that if two random variables are uncorrelated (covariance of zero) they might not be independent.

Lemma M.0.6. *Let two real-valued random variables X_1 and X_2 be uncorrelated, see Definition M.0.9, and jointly normal, see Definition M.0.16, then X_1 and X_2 are independent, [PP18, p. 116].*

M.0.10 Normal Distribution / Gaussian Distribution

The one- dimensional (univariate) normal distribution, often also called Gaussian distribution, is characterized by the probability density function, [MC04, p. 72]

$$f(x) = \frac{1}{\sigma\sqrt{2\pi}} e^{-\frac{1}{2}(\frac{x-\mu}{\sigma})^2} \tag{M.27}$$

for the real-valued random variable X. The parameter μ is the expected value of X.

$$\mathbb{E}[X] = \mu \tag{M.28}$$

The parameter σ is the standard deviation of X. The variance of X is given by σ^2.

$$var[X] = \sigma^2 \tag{M.29}$$

Lemma M.0.7. *Let Y be a real-valued random variable with standard normal distribution, see Definition M.0.15, then [MC04, p. 73]*

$$X = \sigma Y + \mu \tag{M.30}$$

will be normally distributed with expected value μ and standard deviation σ.

Definition M.0.14. *A normally distributed real-valued random variable X with expected value μ and variance σ^2 is denoted as [MC04, p. 73]*

$$X \sim \mathcal{N}(\mu, \sigma^2) \tag{M.31}$$

M.0.11 Standard Normal Distribution

Definition M.0.15. *The standard normal distribution is a special case of the normal distribution, see Appendix M.0.10, where $\mu = 0$ and $\sigma = 1$, [MC04, p. 73].*

M.0.12 Joint Normality

Definition M.0.16. *Two normally distributed random variables X_1 and X_2, see Appendix M.0.10, are said to be **jointly normal** if for all $a, b \in \mathbb{R}$, [MC04, p. 254]*

$$Y = aX_1 + bX_2 \tag{M.32}$$

has a normal distribution.

Lemma M.0.8. *Let two real-valued random variables X_1 and X_2 be independent and normally distributed, then X_1 and X_2 are jointly normal, see Definition M.0.16, [MC04, p. 256], meaning that*

$$Y = aX_1 + bX_2 \tag{M.33}$$

is normally distributed for all $a, b \in \mathbb{R}$.

M.0.13 Joint Normal Distribution / Multivariate Normal Distribution / Multivariate Gaussian Distribution

The one-dimensional (univariate) normal distribution, see Appendix M.0.10, can be generalized to higher dimensions and is then denoted as **multivariate normal distribution**, where every linear combination of the elements of a real-valued random vector $\mathbf{X} = [X_1, X_2, \dots X_n]^T$ has a univariate normal distribution, meaning that they are jointly normal, see Definition M.0.16. In case that two random variables are considered, it is referred to as **bivariate normal distribution**.
The multivariate distribution of a n-dimensional random vector $\mathbf{X} = [X_1, X_2, \dots X_n]^T$ is denoted as

$$\mathbf{X} \sim \mathcal{N}(\mu, \mathbf{\Sigma}) \tag{M.34}$$

where μ is the n-dimensional expected value vector

$$\mu = \begin{bmatrix} \mu_1, & \mu_2, & \dots & \mu_n \end{bmatrix}^T = \begin{bmatrix} \mathbb{E}[X_1], & \mathbb{E}[X_2], & \dots & \mathbb{E}[X_n] \end{bmatrix}^T \tag{M.35}$$

and where $\mathbf{\Sigma}$ is the $n \times n$ dimensional covariance matrix

$$\mathbf{\Sigma} = \begin{bmatrix} cov[X_1, X_1] & \dots & cov[X_1, X_n] \\ \vdots & \ddots & \vdots \\ cov[X_n, X_1] & \dots & cov[X_n, X_n] \end{bmatrix} \tag{M.36}$$

with the respective covariances as elements. Note, that $\mathbf{\Sigma}$ is symmetric, because of Property M.0.4. The probability density function is [MC04, p. 250]

$$f_{\mathbf{x}}(\mathbf{x}) = \frac{1}{\sqrt{(2\pi)^n det(\mathbf{\Sigma})}} e^{-\frac{1}{2}(\mathbf{x}-\mu)^T \mathbf{\Sigma}^{-1}(\mathbf{x}-\mu)} \tag{M.37}$$

where $det(\mathbf{\Sigma})$ is the determinant of $\mathbf{\Sigma}$.

M.0.14 Complex Random Variable

The concept of a complex random variable is often a source of confusion [MC04]. A complex random variable is defined by $Z = X + jY$ where X and Y are real random variables.

M.0.15 Distribution of a Complex Random Variable

The distribution of a complex random variable $Z = X+jY$ is defined as the joint bivariate distribution of the real random variables X and Y.

$$F_Z(z) \widehat{=} P(X \leq x, Y \leq y) = F_{X,Y}(x, y) \tag{M.38}$$

The functions $F_Z(z)$ and $F_{X,Y}(x, y)$ are the **cumulative distribution function** of Z and the **joint distribution function** of the random variables X and Y, see Definitions M.0.1 and M.0.2. The **probability density function** is defined by

$$f_Z(z) \widehat{=} f_{X,Y}(x, y) = \frac{\partial^2}{\partial x \partial y} P(\leq x, Y \leq y) \tag{M.39}$$

and $f_Z(z)$ is a real-valued function $f : \mathbb{C} \to \mathbb{R}$.

M.0.16 Expected Value of a Complex Random Variable

Definition M.0.17. *The **expected value of a complex random variable** $Z = X + jY$ is [MC04, p. 220]*

$$\mathbb{E}[Z] = \int_{\mathbb{C}} z f_Z(z) dz \tag{M.40}$$

where the differential element dz is understood to be

$$dz = dxdy \tag{M.41}$$

and the integral should be understood as

$$\int_{\mathbb{C}} dz = \int_{-\infty}^{\infty} \int_{-\infty}^{\infty} dxdy \tag{M.42}$$

Note, that this notation denotes a multidimensional integral and should not be confused with a complex contour integral, where $dz = dx + jdy$.

Property M.0.7. *The expected value of a complex random variable $Z = X + jY$ corresponds to*

$$\mathbb{E}[Z] = \mathbb{E}[X + jY] = \mathbb{E}[X] + j\mathbb{E}[Y] \tag{M.43}$$

Proof. Let $Z = X + jY$ be a complex random variable. The expected value $\mathbb{E}[Z]$ is according to Definition M.0.17, and using the probability density function $f_Z(z)$ given by Equation (M.39):

$$\begin{aligned}\mathbb{E}[Z] &= \int_{\mathbb{C}} z f_Z(z) dz = \int_{-\infty}^{\infty}\int_{-\infty}^{\infty} (x+jy) f_{X,Y}(x,y) dxdy \\ &= \int_{-\infty}^{\infty}\int_{-\infty}^{\infty} x f_{X,Y}(x,y) dxdy + j\int_{-\infty}^{\infty}\int_{-\infty}^{\infty} y f_{X,Y}(x,y) dxdy\end{aligned} \tag{M.44}$$

In Equation (M.44) we can substitute the marginal probability density functions $f_X(x)$ and $f_Y(y)$, which are introduced in Definition (M.0.5) by

$$\begin{aligned}f_X(x) &= \int_{-\infty}^{\infty} f_{X,Y}(x,y) dy \\ f_Y(y) &= \int_{-\infty}^{\infty} f_{X,Y}(x,y) dx\end{aligned} \tag{M.45}$$

such that we obtain

$$\begin{aligned}\mathbb{E}[Z] &= \int_{-\infty}^{\infty} x f_X(x) dx + j\int_{-\infty}^{\infty} y f_Y(y) dy \\ &= \mathbb{E}[X] + j\mathbb{E}[Y]\end{aligned} \tag{M.46}$$

This corresponds to $\mathbb{E}[Z] = \mathbb{E}[X] + j\mathbb{E}[Y]$ according to the definition of the expected value, see Definition M.0.6. □

M.0.17 Covariance, Pseudo Covariance and Variance of Complex Random Variables

Definition M.0.18. *The covariance can be extended to complex random variables. The* ***covariance of two complex random variables*** *Z and W is defined as, [PP18, p. 119]*

$$K_{ZW} = cov[Z,W] = \mathbb{E}[(Z-\mu_z)\overline{(W-\mu_w)}] \tag{M.47}$$

Lemma M.0.9. *According to [PP18, p. 119]*

$$K_{ZW} = \mathbb{E}[Z\bar{W}] - \mathbb{E}[Z]\mathbb{E}[\bar{W}] \tag{M.48}$$

Definition M.0.19. *The* ***pseudo covariance of two complex random variables*** *Z and W is defined as [MC04, p. 221]*

$$C_{ZW} = cov[Z,\bar{W}] = \mathbb{E}[(Z-\mu_z)(W-\mu_w)] \tag{M.49}$$

Lemma M.0.10. *According to [PP18, p. 119]*

$$C_{ZW} = \mathbb{E}[ZW] - \mathbb{E}[Z]\mathbb{E}[W] \tag{M.50}$$

Definition M.0.20. *The **variance of a complex random variable** $Z = X + jY$ is*

$$K_{ZZ} = var[Z] = cov[Z, Z] = \mathbb{E}[(Z - \mu_z)\overline{(Z - \mu_z)}] \tag{M.51}$$

where the covariance for complex random variables was introduced in Definition M.0.18.

Lemma M.0.11. *The variance is a non-negative real number. Let $Z = X + jY$ be a complex random variable then the variance of Z is, [MC04, p. 220],*

$$K_{ZZ} = var[Z] = var[X] + var[Y] = \sigma_x^2 + \sigma_y^2 \tag{M.52}$$

Proof. The product of a complex number with its conjugate complex is according to Lemma M.0.21 its absolute value squared. Hence,

$$var[Z] = \mathbb{E}[(Z - \mu_z)\overline{(Z - \mu_z)}] = \mathbb{E}[|(Z - \mu_z)|^2] = \mathbb{E}[(X - \mu_x)^2 + (Y - \mu_y)^2] \tag{M.53}$$

Because of the linearity of the expected value operator, Property M.0.1,

$$var[Z] = \mathbb{E}[(X - \mu_x)^2] + \mathbb{E}[(Y - \mu_y)^2] \tag{M.54}$$

where the real part X and imaginary part Y of Z are real-valued random variables. According to the definition of the variance of real-valued random variables, see Definition M.0.7, we thus obtain:

$$var[Z] = var[X] + var[Y] \tag{M.55}$$

□

Definition M.0.21. *The **pseudo variance of a complex random variable** $Z = X + jY$ is [MC04, p. 221]*

$$C_{ZZ} = cov[Z, \bar{Z}] = \mathbb{E}[(Z - \mu_Z)^2] \tag{M.56}$$

Note, that the pseudo-covariance for complex random variables was introduced in Definition M.0.19.

Lemma M.0.12. *Let $Z = X + jY$ be a complex random variable, then the pseudo variance, Definition M.0.21, can be related to the entries of the covariance matrix* (M.69) *of the bivariate distribution of the real and imaginary part of the complex random variable $Z = X + jY$ via [MC04, p. 220]*

$$C_{ZZ} = cov[Z, \bar{Z}] = var[X] - var[Y] + 2jcov[X, Y] \tag{M.57}$$

Proof. Let $Z = X + jY$ be a complex random variable, then according to Definition M.0.21

$$\begin{aligned} C_{ZZ} &= cov[Z, \bar{z}] = \mathbb{E}[(Z - \mu_Z)^2] = \mathbb{E}[((X + jY) - (\mu_x + j\mu_y))^2] \\ &= \mathbb{E}[((X - \mu_x) + j(Y - \mu_y))^2] \\ &= \mathbb{E}[(X - \mu_x)^2 + j^2(Y - \mu_y)^2 + j(X - \mu_x)(Y - \mu_y) + j(Y - \mu_y)(X - \mu_x)] \end{aligned} \tag{M.58}$$

where μ_z was replaced using Property M.0.7 of the expected value of a complex random variable. Because of the linearity of the expected value, see Property M.0.1, we thus obtain

$$\begin{aligned} C_{ZZ} &= \mathbb{E}[(X - \mu_x)^2] + \mathbb{E}[j^2(Y - \mu_y)^2] + \mathbb{E}[j(X - \mu_x)(Y - \mu_y)] + \mathbb{E}[j(Y - \mu_y)(X - \mu_x)] \\ &= \mathbb{E}[(X - \mu_x)^2] - \mathbb{E}[(Y - \mu_y)^2] + j\mathbb{E}[(X - \mu_x)(Y - \mu_y)] + j\mathbb{E}[(Y - \mu_y)(X - \mu_x)] \\ &= var[X] - var[Y] + jcov[X, Y] + jcov[Y, X] \\ &= var[X] - var[Y] + 2jcov[X, Y] \end{aligned} \tag{M.59}$$

where the Definitions of the variance and covariance of a real valued random variable given in M.0.7 and M.0.8 were used, as well as the symmetry property of the covariance, see Property M.0.4. □

Lemma M.0.13. *Let $Z = X + jY$ be a complex random variable, then the variance of its real and imaginary part, X and Y, and their covariance can be related to the variance K_{ZZ} (Definition M.0.20) and pseudo variance C_{ZZ} (Definition M.0.21) of Z as follows.*

$$\begin{aligned} \sigma_x^2 = var[X] &= \mathbb{E}[(X - \mathbb{E}[X])(X - \mathbb{E}[X])] = \frac{1}{2}\Re(K_{ZZ} + C_{ZZ}) \\ \sigma_y^2 = var[Y] &= \mathbb{E}[(Y - \mathbb{E}[Y])(Y - \mathbb{E}[Y])] = \frac{1}{2}\Re(K_{ZZ} - C_{ZZ}) \\ cov[X, Y] &= \mathbb{E}[(X - \mathbb{E}[X])(Y - \mathbb{E}[Y])] = \frac{1}{2}\Im(-K_{ZZ} + C_{ZZ}) \\ cov[Y, X] &= \mathbb{E}[(Y - \mathbb{E}[Y])(X - \mathbb{E}[X])] = \frac{1}{2}\Im(K_{ZZ} + C_{ZZ}) \end{aligned} \tag{M.60}$$

Proof. By inserting the relation given in Lemma M.0.11 and Lemma M.0.12 for K_{ZZ} and C_{ZZ} into (M.60) the equalities can be directly seen. □

Definition M.0.22. *Let $Z = X + jY$ be a complex random variable, then its covariance matrix can be either expressed in terms of Z according to*

$$\Sigma_{ZZ} = \begin{bmatrix} K_{ZZ} & C_{ZZ} \\ \bar{C}_{ZZ} & \bar{K}_{ZZ} \end{bmatrix} \tag{M.61}$$

or in terms of its real and imaginary part, X and Y as follows

$$\Sigma_{XY} = \begin{bmatrix} \sigma_x^2 & cov[X,Y] \\ cov[Y,X] & \sigma_y^2 \end{bmatrix} \tag{M.62}$$

where K_{ZZ} is the variance of Z, Definition M.0.20, C_{ZZ} is the pseudo variance of Z, Definition M.0.21, σ_x^2, σ_y^2 are the variances of X and Y, Definition M.0.7, and $cov[X,Y]$ is the covariance of X and Y, Definition M.0.8. The elements of these matrices are thereby related to each other according to Lemma M.0.11, Lemma M.0.12 and Lemma M.0.13.

M.0.18 Proper Complex Random Variable

Definition M.0.23. *A complex random variable $Z = X + jY$ is called proper if its pseudo-variance, Definition M.0.21, vanishes, i.e. $C_{ZZ} = 0$. Otherwise, Z is called improper [SS10, p. 35].*

According to Lemma M.0.12, the pseudo-variance carries information about the variance mismatch $var[X] - var[Y]$ in its real part and about the correlation between X and Y i.e. $cov[X,Y]$ in its imaginary part. Hence, the pseudo-variance is zero if X and Y have identical variances, i.e. $var[X] - var[Y] = 0$, and are independent, because then $cov[X,Y] = 0$.

M.0.19 Complex Normal Distribution

The complex normal distribution of a complex random variable Z is defined as [SS10, p. 39]

$$f_z(z) = \frac{1}{\pi\sqrt{JK}} e^{-\frac{1}{2}\begin{bmatrix} \overline{(z-\mu_z)} \\ (z-\mu_z) \end{bmatrix}^T \Sigma_{ZZ}^{-1} \begin{bmatrix} (z-\mu_z) \\ \overline{(z-\mu_z)} \end{bmatrix}} \tag{M.63}$$

where $\overline{(z-\mu_z)}$ denotes the conjugate complex of $(z-\mu_z)$ and Σ_{ZZ} is the covariance matrix defined in Definition M.0.22 as [SS10, p. 34]

$$\Sigma_{ZZ} = \begin{bmatrix} K & C \\ \bar{C} & \bar{K} \end{bmatrix} \tag{M.64}$$

The variance and pseudo variance of Z are according to Lemma M.0.11 and Lemma M.0.12

$$\begin{aligned} K &= cov[Z,Z] = \sigma_x^2 + \sigma_y^2 \\ C &= cov[Z,\bar{Z}] = \sigma_x^2 - \sigma_y^2 + 2jcov[X,Y] \end{aligned} \tag{M.65}$$

Finally, J is defined as

$$J = \bar{K} - \bar{C}K^{-1}C \tag{M.66}$$

In order to improve readability in the following proofs the subindex $(*)_{ZZ}$ was omitted. The complex normal distribution is hence described by the three parameters μ_z, K, C and the complex normal random variable Z is denoted as

$$Z \sim \mathcal{N}_C(\mu_z, K, C) \tag{M.67}$$

Lemma M.0.14. *A complex normal distribution characterizes a complex random variable Z with bivariate normal distribution of its real and imaginary part. According to Appendix M.0.13 the probability function of the bivariate normal distribution of the random variables X, Y is of the form*

$$f_{x,y}(x,y) = \frac{1}{2\pi\sqrt{det(\mathbf{\Sigma_{XY}})}} e^{-\frac{1}{2}\begin{bmatrix}(x-\mu_x)\\(y-\mu_y)\end{bmatrix}^T \mathbf{\Sigma}_{XY}^{-1} \begin{bmatrix}(x-\mu_x)\\(y-\mu_y)\end{bmatrix}} \tag{M.68}$$

where the covariance matrix is

$$\mathbf{\Sigma_{XY}} = \begin{bmatrix}\sigma_x^2 & cov[X,Y]\\ cov[Y,X] & \sigma_y^2\end{bmatrix} \tag{M.69}$$

with the variances σ_x^2 and σ_y^2, Appendix M.0.7. Note that $\mathbf{\Sigma_{XY}}$ is symmetric as for the covariances $cov[X,Y] = cov[Y,X]$ holds, see Property M.0.4. In terms of the complex random variable Z we can thus write

$$f_z(z) = \frac{1}{2\pi\sqrt{det(\mathbf{\Sigma_{XY}})}} e^{-\frac{1}{2}\begin{bmatrix}\Re(z-\mu_z)\\ \Im(z-\mu_z)\end{bmatrix}^T \mathbf{\Sigma}_{XY}^{-1} \begin{bmatrix}\Re(z-\mu_z)\\ \Im(z-\mu_z)\end{bmatrix}} \tag{M.70}$$

where μ_z is the expected value of the complex random variable defined in M.0.16, and

$$\mathbf{\Sigma_{XY}} = \begin{bmatrix}\sigma_{\Re(Z)}^2 & cov[\Re(Z), \Im(Z)]\\ cov[\Im(Z), \Re(Z)] & \sigma_{\Im(Z)}^2\end{bmatrix} \tag{M.71}$$

Proof. Let the complex random variable Z be distributed according to (M.63). According to Lemma M.0.11 and M.0.12 the variance and pseudo variance can be related to the covariance matrix (M.69) of the bivariate distribution of the real and imaginary part of the complex random variable $Z = X + jY$ via

$$\begin{aligned} K &= cov[Z,Z] = \sigma_x^2 + \sigma_y^2\\ C &= cov[Z,\bar{Z}] = \sigma_x^2 - \sigma_y^2 + 2jcov[X,Y] \end{aligned} \tag{M.72}$$

where σ_x^2 and σ_y^2 are the variances of the real and imaginary part. Using the relation (M.65), J is calculated as

$$\begin{aligned} J = \bar{K} - \bar{C}K^{-1}C &= \sigma_x^2 + \sigma_y^2 - (\frac{(\sigma_x^2 - \sigma_y^2 - 2jcov[X,Y])(\sigma_x^2 - \sigma_y^2 + 2jcov[X,Y]))}{\sigma_x^2 + \sigma_y^2} \\ &= \sigma_x^2 + \sigma_y^2 - \frac{(\sigma_x^2 - \sigma_y^2)^2 + 4cov[X,Y]^2}{\sigma_x^2 + \sigma_y^2}. \end{aligned} \tag{M.73}$$

Multiplication with K results in

$$\begin{aligned} JK &= \sigma_x^2 + \sigma_y^2 - (\sigma_x^2 - \sigma_y^2)^2 - 4cov[X,Y]^2 \\ &= \sigma_x^4 + \sigma_y^4 + 2\sigma_y^2\sigma_x^2 - (\sigma_x^4 + \sigma_y^4 - 2\sigma_y^2\sigma_x^2) - 4cov[X,Y]^2 \\ &= 4\sigma_y^2\sigma_x^2 - 4cov[X,Y]^2. \end{aligned} \tag{M.74}$$

Inserting this result in $\frac{1}{\pi\sqrt{JK}}$, results in

$$\frac{1}{\pi\sqrt{JK}} = \frac{1}{2\pi\sqrt{\sigma_x^2\sigma_y^2 - cov[X,Y]^2}}. \tag{M.75}$$

For the exponent in Equation (M.63):

$$-\frac{1}{2}\begin{bmatrix}\overline{(z-\mu_z)} \\ (z-\mu_z)\end{bmatrix}^T \begin{bmatrix}K & C \\ \bar{C} & \bar{K}\end{bmatrix}^{-1} \begin{bmatrix}(z-\mu_z) \\ \overline{(z-\mu_z)}\end{bmatrix} \tag{M.76}$$

we calculate

$$\begin{bmatrix}K & C \\ \bar{C} & \bar{K}\end{bmatrix}^{-1} = \frac{1}{\bar{K}K - \bar{C}C}\begin{bmatrix}\bar{K} & -C \\ -\bar{C} & K\end{bmatrix} \tag{M.77}$$

Hence,

$$\begin{aligned} &-\frac{1}{2}\begin{bmatrix}\overline{(z-\mu_z)} \\ (z-\mu_z)\end{bmatrix}^T \begin{bmatrix}K & C \\ \bar{C} & \bar{K}\end{bmatrix}^{-1} \begin{bmatrix}(z-\mu_z) \\ \overline{(z-\mu_z)}\end{bmatrix} = \\ &-\frac{1}{2}\begin{bmatrix}\overline{(z-\mu_z)} \\ (z-\mu_z)\end{bmatrix}^T \frac{1}{\bar{K}K - \bar{C}C}\begin{bmatrix}\bar{K} & -C \\ -\bar{C} & K\end{bmatrix}\begin{bmatrix}(z-\mu_z) \\ \overline{(z-\mu_z)}\end{bmatrix} = \\ &\frac{1}{2}\frac{\overline{(z-\mu_z)}(z-\mu_z)\bar{K} - (z-\mu_z)^2\bar{C} - \overline{(z-\mu_z)}^2 C + (z-\mu_z)\overline{(z-\mu_z)}K}{\bar{K}K - \bar{C}C} \end{aligned} \tag{M.78}$$

Using the property $\overline{ab} = \bar{a}\bar{b}$, see M.0.23, and $\bar{\bar{a}} = a$ we obtain for Equation (M.78) the following expression

$$\begin{aligned}&\frac{1}{2}\frac{\overline{(z-\mu_z)}(z-\mu_z)\bar{K}-(z-\mu_z)^2\bar{C}-\overline{(z-\mu_z)^2\bar{C}}+(z-\mu_z)\overline{(z-\mu_z)}K}{\bar{K}K-\bar{C}C}=\\&\frac{1}{2}\frac{\overline{(z-\mu_z)}(z-\mu_z)(\bar{K}+K)-((z-\mu_z)^2\bar{C}+\overline{(z-\mu_z)^2\bar{C}})}{\bar{K}K-\bar{C}C}.\end{aligned}\tag{M.79}$$

Using the relation given in Lemma M.0.21 for the product of a complex number and its conjugate complex and the relation for the sum of a complex number and its conjugate, see Lemma M.0.22, we derive at

$$\frac{1}{2}\frac{[(x-\mu_x)^2+(y+\mu_y)^2]2\Re(K)-2\Re((z-\mu_z)^2\bar{C})}{\Re(K)^2+\Im(K)^2-\Re(C)^2-\Im(C)^2}.\tag{M.80}$$

Using

$$(z-\mu_z)^2=((x-\mu_x)+j(y-\mu_y))^2=(x-\mu_x)^2-(y-\mu_y)^2+2j(x-\mu_x)(y-\mu_y)\tag{M.81}$$

and

$$\bar{C}=\sigma_x^2-\sigma_y^2-2jcov[X,Y]\tag{M.82}$$

the following term becomes

$$\begin{aligned}&2\Re((z-\mu_z)^2\bar{C})=\\&2((\sigma_x^2-\sigma_y^2)[(x-\mu_x)^2-(y-\mu_y)^2]-(-1)2(x-\mu_x)(y-\mu_y)2cov[X,Y])=\\&2(\sigma_x^2-\sigma_y^2)[(x-\mu_x)^2-(y-\mu_y)^2]+8(x-\mu_x)(y-\mu_y)cov[X,Y].\end{aligned}\tag{M.83}$$

With K and C from Equation (M.65) we calculate the following terms:

$$[(x-\mu_x)^2+(y+\mu_y)^2]2\Re(K)=[(x-\mu_x)^2+(y+\mu_y)^2]2(\sigma_x^2+\sigma_y^2)\tag{M.84}$$

and

$$\begin{aligned}\Re(K)^2+\Im(K)^2-\Re(C)^2-\Im(C)^2&=(\sigma_x^2+\sigma_y^2)^2-(\sigma_x^2-\sigma_y^2)^2-4cov[X,Y]^2\\&=4\sigma_y^2\sigma_x^2-4cov[X,Y]^2\end{aligned}\tag{M.85}$$

where Equation (M.74) was additionally used. Inserting the results in Equation (M.83),(M.84) and (M.85) into Equation (M.80) finally results in

$$
\begin{aligned}
&\frac{1}{2}\frac{[(x-\mu_x)^2+(y+\mu_y)^2]2\Re(K)-2\Re((z-\mu_z)^2\bar{C})}{\Re(K)^2+\Im(K)^2-\Re(C)^2-\Im(C)^2}= \\
&\frac{1}{2}\frac{[(x-\mu_x)^2+(y+\mu_y)^2]2(\sigma_x^2+\sigma_y^2)-2(\sigma_x^2-\sigma_y^2)[(x-\mu_x)^2-(y-\mu_y)^2]}{4\sigma_y^2\sigma_x^2-4cov[X,Y]^2}- \\
&\frac{-8(x-\mu_x)(y-\mu_y)cov[X,Y]}{4\sigma_y^2\sigma_x^2-4cov[X,Y]^2}= \\
&\frac{1}{2}\frac{4\sigma_y^2(x-\mu_x)^2+4\sigma_x^2(y+\mu_y)^2-8(x-\mu_x)(y-\mu_y)cov[X,Y]}{4\sigma_y^2\sigma_x^2-4cov[X,Y]^2}= \\
&\frac{1}{2}\frac{\sigma_y^2(x-\mu_x)^2+\sigma_x^2(y+\mu_y)^2-2(x-\mu_x)(y-\mu_y)cov[X,Y]}{\sigma_y^2\sigma_x^2-cov[X,Y]^2}.
\end{aligned}
\tag{M.86}
$$

Inserting result (M.86) and (M.75) into (M.63) provides

$$
\begin{aligned}
f_z(z) &= \frac{1}{\pi\sqrt{JK}}e^{-\frac{1}{2}\begin{bmatrix}\overline{(z-\mu_z)}\\(z-\mu_z)\end{bmatrix}^T\begin{bmatrix}K & C\\ \bar{C} & \bar{K}\end{bmatrix}^{-1}\begin{bmatrix}(z-\mu_z)\\\overline{(z-\mu_z)}\end{bmatrix}} \\
&= \frac{1}{\pi\sqrt{JK}} = \frac{1}{2\pi\sqrt{\sigma_x^2\sigma_y^2-cov[X,Y]^2}}e^{\frac{1}{2}\frac{\sigma_y^2(x-\mu_x)^2+\sigma_x^2(y+\mu_y)^2-2(x-\mu_x)(y-\mu_y)cov[x,y]}{\sigma_y^2\sigma_x^2-cov[X,Y]^2}}
\end{aligned}
\tag{M.87}
$$

This corresponds to the bivariate normal distribution of the real and imaginary part of the complex random variable Z which is given in (M.68) as

$$
\begin{aligned}
f_{x,y}(x,y) &= \frac{1}{2\pi\sqrt{det(\mathbf{\Sigma})}}e^{-\frac{1}{2}\begin{bmatrix}(x-\mu_x)\\(y-\mu_y)\end{bmatrix}^T\frac{1}{det(\mathbf{\Sigma})}\begin{bmatrix}\sigma_y^2 & -cov[X,Y]\\ -cov[Y,X] & \sigma_x^2\end{bmatrix}\begin{bmatrix}(x-\mu_x)\\(y-\mu_y)\end{bmatrix}} \\
&= \frac{1}{2\pi\sqrt{det(\mathbf{\Sigma})}}e^{-\frac{1}{2}\frac{1}{det(\mathbf{\Sigma})}\begin{bmatrix}(x-\mu_x)\sigma_y^2-cov[Y,X](y-\mu_y)\\ -cov[Y,X](x-\mu_x)+(y-\mu_y)\sigma_x^2\end{bmatrix}^T\begin{bmatrix}(x-\mu_x)\\(y-\mu_y)\end{bmatrix}} \\
&= \frac{1}{2\pi\sqrt{\sigma_x^2\sigma_y^2-cov[X,Y]^2}}e^{\frac{1}{2}\frac{(x-\mu_x)^2\sigma_y^2-2cov[X,Y](y-\mu_y)(x-\mu_x)+(y-\mu_y)^2\sigma_x^2}{\sigma_x^2\sigma_y^2-cov[X,Y]^2}}.
\end{aligned}
\tag{M.88}
$$

□

M.0.20 Distribution of a Proper Complex Normal Random Variable

Lemma M.0.15. *Let $Z = X + jY$ be a complex normal random variable and let Z be proper, Definition M.0.23, then the probability density function of the complex normal distribution simplifies to*

$$f_z(z) = \frac{1}{2\pi\sigma^2} e^{-\frac{|z-\mu_z|^2}{2\sigma^2}} \tag{M.89}$$

Proof. The probability density function of the complex normal distribution, given in equation (M.63) is

$$f_z(z) = \frac{1}{\pi\sqrt{JK}} e^{-\frac{1}{2}\begin{bmatrix}\overline{(z-\mu_z)} \\ (z-\mu_z)\end{bmatrix}^T \begin{bmatrix}K & C \\ \bar{C} & \bar{K}\end{bmatrix}^{-1} \begin{bmatrix}(z-\mu_z) \\ \overline{(z-\mu_z)}\end{bmatrix}} \tag{M.90}$$

By Definition M.0.23 a proper complex random variable has zero pseudo-variance, i.e. $C = 0$ such that according to (M.66), $J = \bar{K}$. Furthermore, $C = 0$ implies by Equation (M.0.13), that the real part X and imaginary part Y have identical variances, i.e. $var[X] = var[Y] = \sigma^2$. The variance K of the proper complex normal random variable is hence given according to Lemma M.0.11 by $K = var[X] + var[Y] = 2\sigma^2$. Consequently, the distribution simplifies to

$$\begin{aligned}
f_z(z) &= \frac{1}{\pi\sqrt{\bar{K}K}} e^{-\frac{1}{2}\begin{bmatrix}\overline{(z-\mu_z)} \\ (z-\mu_z)\end{bmatrix}^T \begin{bmatrix}K & 0 \\ 0 & \bar{K}\end{bmatrix}^{-1} \begin{bmatrix}(z-\mu_z) \\ \overline{(z-\mu_z)}\end{bmatrix}} \\
&= \frac{1}{\pi\sqrt{\bar{K}K}} e^{-\frac{1}{2\bar{K}K}\begin{bmatrix}\overline{(z-\mu_z)} \\ (z-\mu_z)\end{bmatrix}^T \begin{bmatrix}\bar{K} & 0 \\ 0 & K\end{bmatrix} \begin{bmatrix}(z-\mu_z) \\ \overline{(z-\mu_z)}\end{bmatrix}} \\
&= \frac{1}{\pi 2\sigma^2} e^{-\frac{1}{2(2\sigma^2)^2}\begin{bmatrix}\overline{(z-\mu_z)}2\sigma^2 \\ (z-\mu_z)2\sigma^2\end{bmatrix}^T \begin{bmatrix}(z-\mu_z) \\ \overline{(z-\mu_z)}\end{bmatrix}} \\
&= \frac{1}{2\pi\sigma^2} e^{-\frac{\overline{(z-\mu_z)}2\sigma^2(z-\mu_z)+(z-\mu_z)2\sigma^2\overline{(z-\mu_z)}}{2(2\sigma^2)^2}} = \frac{1}{2\pi\sigma^2} e^{-\frac{2\overline{(z-\mu_z)}(z-\mu_z)}{2(2\sigma^2)}} = \frac{1}{2\pi\sigma^2} e^{-\frac{\overline{(z-\mu_z)}(z-\mu_z)}{2\sigma^2}} \\
&= \frac{1}{2\pi\sigma^2} e^{-\frac{|z-\mu_z|^2}{2\sigma^2}}
\end{aligned} \tag{M.91}$$

where Lemma M.0.21 for the product of a complex number with its conjugate complex was used. □

M.0.21 Distribution of Proper Complex Normal Random Variable in Polar-coordinates

A proper complex normal random variable $Z = X + jY$, where X and Y are two independent normal random variables with expected values $\mathbb{E}[X] = \mu_x$ and $\mathbb{E}[Y] = \mu_y$ and equal variances $var[X] = var[Y] = \sigma^2$, can be expressed in polar-coordinates as

$$Z = Re^{j\Theta} = R\cos\Theta + jR\sin\Theta \tag{M.92}$$

with amplitude $R = |Z| = \sqrt{X^2 + Y^2}$ and phase $\Theta = Arg(Z) \in [0, 2\pi)$. The expected value of Z is $\mu_z = \mu_x + j\mu_y = \nu e^{j\phi}$, where $\nu = |\mu_z| = \sqrt{\mu_x^2 + \mu_y^2}$ and $\phi = Arg(\mu_z)$. With $dz = dxdy = rdrd\theta$ it is possible to change the variables in the distribution of the proper complex normal random variable Z, given in Lemma M.0.15, to obtain the bivariate distribution in polar-coordinates, i.e. amplitude R and phase Θ as

$$f_{R,\Theta}(r, \theta) = \frac{r}{2\pi\sigma^2} e^{-\frac{|re^{j\theta} - \nu e^{j\phi}|^2}{2\sigma^2}} \tag{M.93}$$

M.0.22 Marginal Distribution of the Amplitude of a Proper Complex Normal Random Variable

The marginal distribution, see Definition M.0.5, of the amplitude of a proper complex normal random variable $Z = X + jY$ is calculated in [OM12]. It is derived by integrating the bivariate distribution (M.93) which is given in polar-coordinates, i.e. amplitude $R = |Z| = \sqrt{X^2 + Y^2}$ and phase $\Theta = Arg(Z) \in [0, 2\pi)$, over the interval $\theta = [0, 2\pi]$, resulting in

$$f_R(r) = \frac{r}{\sigma^2} e^{-\frac{r^2+\nu^2}{2\sigma^2}} I_0(\lambda) \tag{M.94}$$

which is the so called Rician distribution [Sim07, p. 11] (often also called Rice or Ricean distribution), with

$$\lambda = \frac{r\nu}{\sigma^2} \tag{M.95}$$

where $\nu = |\mu_z| = \sqrt{\mu_x^2 + \mu_y^2} = \sqrt{\mathbb{E}[X]^2 + \mathbb{E}[Y]^2}$, and where $\sigma^2 = var[X] = var[Y]$. In (M.94), $I_0(\lambda)$ is the modified Bessel function of the first kind, order 0 and argument λ. The modified Bessel function of first kind and order zero is calculated as the series [AS65, p. 375]

$$I_0(\lambda) = \sum_{k=0}^{\infty} \frac{(\frac{1}{4}\lambda^2)^k}{(k!)^2} \tag{M.96}$$

The expected value and variance of the Rician distribution are known to be [Yak19],[Par61]:

$$\begin{aligned} \mathbb{E}[R] &= \sigma\sqrt{\frac{\pi}{2}} L_{1/2}^{(0)}(-\frac{\nu^2}{2\sigma^2}) \\ var[R] &= 2\sigma^2 + \nu^2 - \sigma^2\frac{\pi}{2}(L_{1/2}^{(0)})^2(-\frac{\nu^2}{2\sigma^2}) \end{aligned} \tag{M.97}$$

where $L_k^{(0)}(x)$, with degree $k = 1/2$ being a non-integer, represents a Laguerre function of order 0 and shall be not confused with the Laguerre polynomial, which is defined only for integer values of the degree k. The Laguerre function of order 0 and non-integer degree k can be expressed in terms of the Kummer function according to [OMS10, p. 215] as

$$L_k^{(0)}(x) =_1 F_1(-k, 1, x) \tag{M.98}$$

The Kummer function ${}_1F_1(-k, c, x)$, which together with the Tricomi function is known as the confluent hypergeometric functions, is primarily defined over the Kummer's series by [OMS10, p. 486]

$${}_1F_1(k, c, x) = 1 + \frac{kx}{c1!} + \frac{k(k+1)x^2}{c(c+1)2!} + \frac{k(k+1)(k+2)x^3}{c(c+1)(c+2)3!} + \ldots = \sum_{j=0}^{\infty} \frac{(k)_j}{(c)_j(1)_j} x^j \tag{M.99}$$

The presence of the modified Bessel function in the Rician distribution, makes the mathematical treatment rather cumbersome. For example when calculating the sample mean of R, no closed-form expression is available for the resulting distribution of the sum of multiple Rician distributed variables [Lop09].

Note, that in case, that the real and imaginary values x and y are perturbed by normally distributed noise N with zero mean, we obtain the normal random variables $X = x+N$ and $Y = y+N$. Note also that then the undisturbed, true magnitude $\sqrt{x^2 + y^2}$ will correspond to $\nu = \sqrt{\mathbb{E}[X]^2 + \mathbb{E}[Y]^2}$, because $\mathbb{E}[N] = 0$ (since N has zero mean). It shall be noticed that in contrast the expected value of the amplitude $\mathbb{E}[R] = \mathbb{E}[\sqrt{X^2 + Y^2}]$, which is a Rician distributed random variable, does not coincide with the true magnitude ν according to (M.97). However, the Rician distribution is known to be connected with two other distributions: the Normal distribution and Rayleigh distribution [Yak19]. The Rician distribution is parametrized by the parameters ν and σ. The ratio of these Rician parameters characterizes the signal-to-noise ratio [Yak19]:

$$\kappa = \frac{\nu}{\sigma} \tag{M.100}$$

Depending on this signal-to-noise ratio, two limiting cases can be distinguished:

- In the first limiting case the signal-to-noise ratio is considered to be negligibly small, i.e. $\frac{\nu}{\sigma} \to 0$ (i.e $\mathbb{E}[X] = \mathbb{E}[Y] = 0$, such that $\nu = 0$). Then the Rician distribution is transformed into a Rayleigh distribution [Yak19].

- In the second limiting case the signal-to-noise ratio is considered to be very high, i.e. $\frac{\nu}{\sigma} \to \infty$ (i.e $\sigma^2 = 0$ or $\nu >> \sigma$). Then the Rician distribution is transformed into a normal distribution with mean ν and variance σ^2 [Yak19].

Since the second limiting case is of more interest for our application, the focus will be on large signal-to-noise ratios in the following.

Lemma M.0.16. *According to [GP95] the Rician distribution starts to approximate the normal distribution already for signal-to-noise ratios of $\nu/\sigma = 3$ and the pdf* (M.94) *can be approximated by [Ric44, p. 299],[Lat98, p. 499]*

$$p_R(r) \approx \frac{1}{\sqrt{(2\pi\sigma^2)}} e^{-\frac{(r-\nu)^2}{2\sigma^2}} \tag{M.101}$$

Hence, for high signal intensities the distribution of the magnitude R can be considered as normally distributed with mean $\mathbb{E}[R] = \nu$ and variance σ^2.

Proof. According to [Lat98, p. 499] it can be shown that for large SNR ($\nu >> \sigma$), [Ric44]

$$I_0(\frac{r\nu}{\sigma^2}) \approx \sqrt{\frac{\sigma^2}{2\pi r\nu}} e^{\frac{r\nu}{\sigma^2}} \tag{M.102}$$

such that the pdf (M.94) becomes

$$f_R(r) \approx \frac{r}{\sigma^2} e^{-\frac{r^2+\nu^2}{2\sigma^2}} \sqrt{\frac{\sigma^2}{2\pi r\nu}} e^{\frac{r\nu}{\sigma^2}} = \frac{r}{\sqrt{2\pi r\nu\sigma^2}} e^{-\frac{r^2+\nu^2-2r\nu}{2\sigma^2}} = \frac{\sqrt{r}}{\sqrt{2\pi\sigma^2}\sqrt{\nu}} e^{-\frac{(r-\nu)^2}{2\sigma^2}} \tag{M.103}$$

Because large SNR is considered, i.e. ($\nu >> \sigma$), $r \approx \nu$, such that

$$f_R(r) \approx \frac{1}{\sqrt{2\pi\sigma^2}} e^{-\frac{(r-\nu)^2}{2\sigma^2}} \tag{M.104}$$

□

M.0.23 Marginal Distribution of the Phase of a Proper Complex Normal Random Variable

The marginal distribution, see Definition M.0.5, of the phase of a proper complex normal random variable $Z = X + jY$ is given in [Lat98, p. 499]. It is obtained by integrating the bivariate pdf expressed in polar-coordinates, i.e. amplitude $R = |Z| = \sqrt{X^2 + Y^2}$ and phase $\Theta = Arg(Z) \in [0, 2\pi)$, given as $f_{R,\Theta}(r, \theta)$ in Equation (M.93), with respect to the amplitude:

$$f_\Theta(\theta) = \int_0^\infty f_{R,\Theta}(r, \theta) dr \tag{M.105}$$

The resulting marginal distribution for the phase is known to be [Lat98, p. 499],[HP08]

$$f_\Theta(\theta) = \frac{1}{2\pi} e^{-\frac{\nu^2}{2\sigma^2}} \{1 + \frac{\nu}{\sigma}\sqrt{2\pi}\cos\theta e^{\frac{\nu^2}{2\sigma^2}\cos^2\theta}[1 - Q(\frac{\nu\cos\theta}{\sigma})]\} \tag{M.106}$$

where $\nu = |\mu_z| = \sqrt{\mu_x^2 + \mu_y^2} = \sqrt{\mathbb{E}[X]^2 + \mathbb{E}[Y]^2}$, and where $\sigma^2 = var[X] = var[Y]$. In (M.106), $Q(\chi)$ is the Gaussian Q function or Gaussian probability function [AS65, p. 931] or Gaussian probability integral [Sim07, p. 5], defined as

$$Q(\chi) = \frac{1}{\sqrt{2\pi}} \int_{\chi}^{\infty} e^{-\frac{y^2}{2}} dy \tag{M.107}$$

Lemma M.0.17. *Let $Z = X + jY$ be a proper complex normal random variable, Definition M.0.23, and* (M.106) *be the marginal distribution of its phase $\Theta = Arg(Z) \in [0, 2\pi)$. Then, as stated in [GP95] and [HP08], for high SNR, defined by Equation* (M.100)*, i.e $\nu >> \sigma$, the pdf of the deviation of the disturbed phase angle from the signal's phase can be approximated by a zero mean normal distribution with variance $var[\Theta] = \frac{1}{\kappa^2} = (\frac{\sigma}{\nu})^2$:*

$$f_{\Delta\Theta}(\Delta\theta) \approx \frac{1}{\sqrt{2\pi(\frac{\sigma}{\nu})^2}} e^{-\frac{\Delta\theta^2}{2(\frac{\sigma}{\nu})^2}} \tag{M.108}$$

where $\Delta\theta = \theta - Arg(\mathbb{E}[Z])$.

Proof. Let $Z = X + jY$ be a proper complex normal random variable, and (M.106) be the marginal distribution of its phase $\Theta = Arg(Z) \in [0, 2\pi)$. Because, according to [AS65, p. 931]

$$\begin{aligned} \frac{1}{\sqrt{2\pi}} \int_{-\infty}^{\infty} e^{-\frac{y^2}{2}} dy &= \frac{1}{\sqrt{2\pi}} \int_{-\infty}^{\chi} e^{-\frac{y^2}{2}} dy + \frac{1}{\sqrt{2\pi}} \int_{\chi}^{\infty} e^{-\frac{y^2}{2}} dy \\ &= \frac{1}{\sqrt{2\pi}} \int_{-\infty}^{\chi} e^{-\frac{y^2}{2}} dy + Q(\chi) = 1 \end{aligned} \tag{M.109}$$

The term $1 - Q(\chi)$ in (M.106) with $\chi = \frac{\nu \cos\theta}{\sigma}$, is replaced by

$$1 - Q(\chi) = \frac{1}{\sqrt{2\pi}} \int_{-\infty}^{\chi} e^{-\frac{y^2}{2}} dy \tag{M.110}$$

For high SNR, i.e $\nu >> \sigma, \kappa = \frac{\nu}{\sigma} \to \infty$ the integral in (M.110) becomes 1:

$$\begin{aligned} \lim_{\kappa \to \infty} \chi(\kappa) &= \kappa \cos\theta = \infty \\ \lim_{\chi \to \infty} \frac{1}{\sqrt{2\pi}} \int_{-\infty}^{\chi} e^{-\frac{y^2}{2}} dy &= \frac{1}{\sqrt{2\pi}} \int_{-\infty}^{\infty} e^{-\frac{y^2}{2}} dy = 1 \end{aligned} \tag{M.111}$$

With these results the marginal distribution (M.106) can be approximated by

$$f_{\Theta}(\Theta) \approx \frac{1}{2\pi} e^{-\frac{\nu^2}{2\sigma^2}} \{1 + \frac{\nu}{\sigma} \sqrt{2\pi} \cos\theta e^{\frac{\nu^2}{2\sigma^2} \cos^2\theta}\} = \frac{1}{2\pi} e^{-\frac{\kappa^2}{2}} \{1 + \kappa\sqrt{2\pi} \cos\theta e^{\frac{\kappa^2}{2} \cos^2\theta}\} \tag{M.112}$$

For large SNR, i.e $\kappa \to \infty$ it is easy to see that the second term in the bracket in (M.112) will dominate the first term, which is the constant 1. We can therefore reduce (M.112) further to

$$\begin{aligned} f_\Theta(\theta) &\approx \frac{1}{2\pi} e^{-\frac{\kappa^2}{2}} \kappa\sqrt{2\pi}\cos\theta e^{\frac{\kappa^2}{2}\cos^2\theta} = \frac{\kappa\sqrt{2\pi}\cos\theta}{2\pi} e^{\frac{\kappa^2}{2}(\cos^2\theta - 1)} \\ &= \frac{\kappa\cos\theta}{\sqrt{2\pi}} e^{-\frac{\kappa^2}{2}\sin^2\theta} \end{aligned} \tag{M.113}$$

For very large SNR the deviation in the phase angle $\Delta\Theta$, will be very small [GP95]. Therefore, we can approximate:

$$\begin{aligned} \sin\Delta\Theta &= \Delta\Theta \\ \cos\Delta\Theta &= 1 \end{aligned} \tag{M.114}$$

Finally we obtain

$$f_{\Delta\Theta}(\Delta\theta) = \frac{\kappa}{\sqrt{2\pi}} e^{-\frac{\kappa^2}{2}\Delta\theta^2} = \frac{1}{\sqrt{2\pi(\frac{\sigma}{\nu})^2}} e^{-\frac{\Delta\theta^2}{2(\frac{\sigma}{\nu})^2}} \tag{M.115}$$

which corresponds to the pdf of a normal distribution with zero mean $\mathbb{E}[\Delta\Theta] = 0$ and variance $(\frac{\sigma}{\nu})^2$, see Appendix M.0.10. □

M.0.24 Circular-symmetry of Complex Random Variables

Definition M.0.24. *Let $Z = X + jY$ be a complex random variable and let the distribution of $e^{j\Phi}Z$ equal the distribution of Z for any $\Phi \in [-\pi, \pi]$, then the complex random variable Z is denoted* ***circularly symmetric****, [SS10, p. 53].*

Property M.0.8. *A circular symmetric complex random variable satisfies by definition [SS10, p. 53]*

$$\mathbb{E}[Z] = \mathbb{E}[e^{j\Phi}Z] = e^{j\Phi}\mathbb{E}[Z] \tag{M.116}$$

and

$$\mathbb{E}[ZZ] = \mathbb{E}[e^{j\Phi}Ze^{j\Phi}Z] = e^{2j\Phi}\mathbb{E}[ZZ] \tag{M.117}$$

Furthermore, the phase of Z is uniformly distributed over $[-\pi, \pi]$ and independent of the magnitude of Z.

Note, that from relation (M.116) it can be directly seen that the expected value of a circularly symmetric complex random variable is zero, $\mu_z = \mathbb{E}[Z] = 0$. Due to relation (M.117), $\mathbb{E}[ZZ]$ is zero: $\mathbb{E}[ZZ] = 0$. Consequently, the pseudo-variance of a circularly symmetric complex random variable is zero:

$$C = cov[Z, \bar{Z}] = \mathbb{E}[(Z - \mu_z)^2] = \mathbb{E}[Z^2] - \mathbb{E}[Z]^2 = 0 \tag{M.118}$$

where the pseudo variance of complex random variables was defined in Definition M.0.21.

M.0.25 Circular-symmetric Complex Normal Distribution

In Appendix M.0.19 the complex normal distribution was introduced. In most cases we consider circular symmetric complex Gaussian random variables $Z = X + jY$ which correspond to the special case of zero mean and zero pseudo-covariance matrix, i.e. $\mu_z = 0$ and $C = 0$, see Property M.0.8. The distribution is hence fully specified by the variance K, defined in Definition M.0.20. According to Equation (M.65): $C = \sigma_x^2 - \sigma_y^2 + 2jcov[X, Y]$, $C = 0$ implies that the covariance of the real and imaginary part is zero and that the two random variables X and Y have equal variance $\sigma_x^2 = \sigma_y^2 = \sigma^2$.

Lemma M.0.18. *A complex normal random variable Z is circularly symmetric if its mean and pseudo variance are zero, i.e. if $\Re(Z)$ and $\Im(Z)$ are i.i.d. with zero mean [SS10, p. 53].*

Lemma M.0.19. *Let $Z = X + jY$ be a circularly symmetric complex Gaussian random variable, then the probability density function of the complex normal distribution simplifies to*

$$f_z(z) = \frac{1}{2\pi\sigma^2} e^{-\frac{|z|^2}{2\sigma^2}} \tag{M.119}$$

Proof. The probability density function of the complex normal distribution, given in Equation (M.63) is

$$f_z(z) = \frac{1}{\pi\sqrt{JK}} e^{-\frac{1}{2}\begin{bmatrix}(\bar{z} - \bar{\mu}_z)\\(z - \mu_z)\end{bmatrix}^T \begin{bmatrix}K & C\\ \bar{C} & \bar{K}\end{bmatrix}^{-1} \begin{bmatrix}(z - \mu_z)\\(\bar{z} - \bar{\mu}_z)\end{bmatrix}} \tag{M.120}$$

For a circular symmetric normal distribution we insert $\mu_z = 0$, $C = 0$ and $J = \bar{K}$, see (M.66) and obtain

$$\begin{aligned} f_z(z) &= \frac{1}{\pi\sqrt{\bar{K}K}} e^{-\frac{1}{2}\begin{bmatrix}\bar{z}\\z\end{bmatrix}^T \begin{bmatrix}K & 0\\ 0 & \bar{K}\end{bmatrix}^{-1} \begin{bmatrix}z\\\bar{z}\end{bmatrix}} \\ &= \frac{1}{\pi\sqrt{\bar{K}K}} e^{-\frac{1}{2\bar{K}K}\begin{bmatrix}\bar{z}\\z\end{bmatrix}^T \begin{bmatrix}\bar{K} & 0\\ 0 & K\end{bmatrix} \begin{bmatrix}z\\\bar{z}\end{bmatrix}} \\ &= \frac{1}{\pi\sqrt{\bar{K}K}} e^{-\frac{1}{2\bar{K}K}\begin{bmatrix}\bar{z}\bar{K}\\zK\end{bmatrix}^T \begin{bmatrix}z\\\bar{z}\end{bmatrix}} \\ &= \frac{1}{\pi\sqrt{\bar{K}K}} e^{-\frac{\bar{z}\bar{K}z + zK\bar{z}}{2\bar{K}K}} \end{aligned} \tag{M.121}$$

Because by Property M.0.8, a circularly complex normal random variable is proper, Definition M.0.23, i.e $C = \sigma_x^2 - \sigma_y^2 + 2jcov[X,Y] = 0$, Equation (M.65), the real part X and imaginary part Y have identical variances, i.e. $var[X] = var[Y] = \sigma^2$. The variance K of the circularly complex normal random variable is hence given according to Lemma M.0.11 by $K = var[X] + var[Y] = 2\sigma^2$. Inserting this relation into (M.121) finally results in

$$f_z(z) = \frac{1}{\pi K} e^{-\frac{2\bar{z}\bar{K}z}{2K^2}} = \frac{1}{\pi K} e^{-\frac{\bar{z}z}{K}} = \frac{1}{2\pi\sigma^2} e^{-\frac{1}{2}\frac{\bar{z}z}{\sigma^2}} = \frac{1}{2\pi\sigma^2} e^{-\frac{1}{2}\frac{|z|^2}{\sigma^2}} \tag{M.122}$$

where Lemma M.0.21 for the product of a complex number with its conjugate complex was used to calculate $\bar{z}z$. □

Lemma M.0.20. *Let $Z = X + jY$ be a circularly symmetric complex Gaussian random variable, then in terms of real and imaginary part the probability density function of the complex normal distribution given in* (M.68) *simplifies to*

$$f_{x,y}(x,y) = \frac{1}{2\pi\sigma^2} e^{-\frac{1}{2}\frac{(x^2+y^2)}{\sigma^2}}. \tag{M.123}$$

Proof. The probability density function of the complex normal distribution in terms of real and imaginary part is given in Equation (M.68) as

$$f_{x,y}(x,y) = \frac{1}{2\pi\sqrt{det(\mathbf{\Sigma})}} e^{-\frac{1}{2}\begin{bmatrix}(x-\mu_x)\\(y-\mu_y)\end{bmatrix}^T \mathbf{\Sigma}^{-1} \begin{bmatrix}(x-\mu_x)\\(y-\mu_y)\end{bmatrix}} \tag{M.124}$$

For a circular symmetric complex normal random variable we know that $\mu_x = \mu_y = 0$, $\sigma_x = \sigma_y = \sigma$ and $cov[X,Y] = cov[Y,X] = 0$ by Lemma M.0.18. Hence, (M.124) becomes

$$\begin{aligned} f_{x,y}(x,y) =& \frac{1}{2\pi\sqrt{\sigma^4}} e^{-\frac{1}{2}\begin{bmatrix}x\\y\end{bmatrix}^T \begin{bmatrix}\sigma^2 & 0\\0 & \sigma^2\end{bmatrix}^{-1} \begin{bmatrix}x\\y\end{bmatrix}} \\ =& \frac{1}{2\pi\sigma^2} e^{-\frac{1}{2\sigma^4}\begin{bmatrix}x\sigma^2\\y\sigma^2\end{bmatrix}^T \begin{bmatrix}x\\y\end{bmatrix}} \\ =& \frac{1}{2\pi\sigma^2} e^{-\frac{1}{2\sigma^4}(x^2\sigma^2+y^2\sigma^2)} = \frac{1}{2\pi\sigma^2} e^{-\frac{x^2+y^2}{2\sigma^2}} \end{aligned} \tag{M.125}$$

□

M.0.26 Product of Complex Number with its Conjugate Complex

Lemma M.0.21. *For a complex number $z = x + jy$ the following relation holds*

$$z\bar{z} = |z|^2 = x^2 + y^2 \tag{M.126}$$

Proof.

$$z\bar{z} = (x + jy)(x - jy) = x^2 + y^2 + jyx - jxy = x^2 + y^2 \tag{M.127}$$

□

M.0.27 Sum of Complex Number with its Conjugate Complex

Lemma M.0.22. *For a complex number $z = x + jy$ the following relation holds*

$$z + \bar{z} = 2\Re(z) = 2x \tag{M.128}$$

Proof.

$$z + \bar{z} = (x + jy) + (x - jy) = 2x \tag{M.129}$$

□

M.0.28 Conjugate Complex of the Product of two Complex Numbers

Lemma M.0.23. *For two complex numbers $a = a_r + ja_j$ and $b = b_r + jb_j$ the following relation holds*

$$\overline{ab} = \bar{a}\bar{b} \tag{M.130}$$

Proof.

$$\begin{aligned} \overline{ab} &= \overline{(a_r + ja_j)(b_r + jb_j)} = \overline{(a_r b_r - a_j b_j) + j(b_r a_j + a_r b_j)} \\ &= (a_r b_r - a_j b_j) - j(b_r a_j + a_r b_j) \end{aligned} \tag{M.131}$$

which is the same as

$$\begin{aligned} \bar{a}\bar{b} &= \overline{(a_r + ja_j)(b_r + jb_j)} = (a_r - ja_j)(b_r - jb_j) \\ &= (a_r b_r - a_j b_j) - j(b_r a_j + a_r b_j) \end{aligned} \tag{M.132}$$

□

M.0.29 Conjugate Complex of the Ratio of two Complex Numbers

Lemma M.0.24. *For two complex numbers $a = a_r + ja_j$ and $b = b_r + jb_j$ the following relation holds*

$$\left(\frac{a}{b}\right)^* = \frac{a^*}{b^*} \tag{M.133}$$

Proof. Using Lemma M.0.21 and M.0.23 it is shown that

$$\left(\frac{a}{b}\right)^* = \left(\frac{ab^*}{bb^*}\right)^* = \left(\frac{ab^*}{|b|^2}\right)^* = \left(\frac{a^*b}{|b|^2}\right) \tag{M.134}$$

is the same as

$$\left(\frac{a^*}{b^*}\right) = \left(\frac{a^*b}{b^*b}\right) = \left(\frac{a^*b}{|b|^2}\right) \tag{M.135}$$

□

Appendix N

Characteristics of DFT of i.i.d. Normally Distributed Noise Sequence with Zero Mean

N.1 Mean and Variance

Lemma N.1.1. *Let the N discrete samples $n_y[n]$ be i.i.d. random variables, see Definition M.0.12, with normal distribution*

$$n_y[n] \sim \mathcal{N}(0, \sigma^2) \tag{N.1}$$

then the real and imaginary part of the DFT of $n_y[n]$ at frequency $\omega_k = \frac{2\pi}{NT_s}k$ will be also normally distributed as follows

$$\begin{aligned} \Re(N_{y,DFT}[k]) &\sim \mathcal{N}(0, \frac{\sigma^2}{2}) \\ \Im(N_{y,DFT}[k]) &\sim \mathcal{N}(0, \frac{\sigma^2}{2}) \end{aligned} \tag{N.2}$$

Proof. The DFT of the discrete real valued sequence $n_y[n]$ at frequency $\omega_k = \frac{2\pi}{NT_s}k$ is according to (2.9)

$$\begin{aligned} N_{y,DFT}[k] &= \frac{1}{\sqrt{N}} \sum_{n=0}^{N-1} n_y[n] e^{-j\frac{2\pi kn}{N}} \\ &= \frac{1}{\sqrt{N}} \sum_{n=0}^{N-1} n_y[n] \cos(\frac{2\pi kn}{N}) - j\frac{1}{\sqrt{N}} \sum_{n=0}^{N-1} n_y[n] \sin(\frac{2\pi kn}{N}) \\ &= \Re(N_{y,DFT}[k]) + j\Im(N_{y,DFT}[k]) \end{aligned} \tag{N.3}$$

which is complex. We define

$$\begin{aligned} x_{n,k} &= n_y[n] c_{n,k} \frac{1}{\sqrt{N}} \\ y_{n,k} &= n_y[n] s_{n,k} \frac{1}{\sqrt{N}} \end{aligned} \tag{N.4}$$

where

$$\begin{aligned} c_{n,k} &= \cos(\frac{2\pi kn}{N}) \\ s_{n,k} &= \sin(\frac{2\pi kn}{N}) \end{aligned} \tag{N.5}$$

are constants for a fixed n and k. Hence, we can express (N.3) as

$$N_{y,DFT}[k] = \sum_{n=0}^{N-1} x_{n,k} - j \sum_{n=0}^{N-1} y_{n,k} \tag{N.6}$$

Because the N discrete samples $n_y[n]$ are i.i.d. random variables with normal distribution

$$n_y[n] \sim \mathcal{N}(0, \sigma^2) \tag{N.7}$$

then $x_{n,k}$ and $y_{n,k}$ are also normally distributed as follows

$$\begin{aligned} x_{n,k} &\sim (0, \sigma^2 \frac{c_{n,k}^2}{N}) \\ y_{n,k} &\sim (0, \sigma^2 \frac{s_{n,k}^2}{N}) \end{aligned} \tag{N.8}$$

This follows directly from the linearity of the expectation and the second order homogeneity of the variance operator as stated in Property M.0.1 and Equation (M.11). Because $n_y[n]$ are independent and normally distributed, then by Lemma M.0.8, they are jointly normal. Consequently, the real and imaginary part of the DFT of $n_y[n]$, which are calculated as the sums of (N.4), are also normally distributed.

$$\begin{aligned} \sum_{n=0}^{N-1} x_{n,k} &\sim \mathcal{N} \\ \sum_{n=0}^{N-1} y_{n,k} &\sim \mathcal{N} \end{aligned} \tag{N.9}$$

Furthermore, because $n_y[n]$ are independent, then by Lemma M.0.5, $x_{n,k}$ will be uncorrelated for all $n = 0 \dots N-1$. The same holds for $y_{n,k}$. Because $x_{n,k}$ are uncorrelated, as well as $y_{n,k}$, then by Lemma M.0.2, the variance of the real and imaginary part of the DFT of $n_y[n]$, given as the sums in (N.6), equal $\sigma_x^2 = \sum_{n=0}^{N} \frac{\sigma^2}{N} c_{n,k}^2$ and $\sigma_y^2 = \sum_{n=0}^{N} \frac{\sigma^2}{N} s_{n,k}^2$. Because of the linearity of the expectation the respective mean values of the sums in (N.6)

remain zero. Hence,

$$\begin{aligned} \Re(N_{y,DFT}[k]) &\sim \mathcal{N}(0, \frac{\sigma^2}{N}\sum_{n=0}^{N} c_{n,k}^2) \\ \Im(N_{y,DFT}[k]) &\sim \mathcal{N}(0, \frac{\sigma^2}{N}\sum_{n=0}^{N} s_{n,k}^2) \end{aligned} \tag{N.10}$$

Because $k \in \mathbb{N}$, then by Lemma Q.1.1, $\sum_{n=0}^{N} s_{n,k}^2 = \sum_{n=0}^{N} c_{n,k}^2 = \frac{N}{2}$. Hence,

$$\begin{aligned} \Re(N_{y,DFT}[k]) &\sim \mathcal{N}(0, \frac{\sigma^2}{2}) \\ \Im(N_{y,DFT}[k]) &\sim \mathcal{N}(0, \frac{\sigma^2}{2}) \end{aligned} \tag{N.11}$$

□

N.2 Circular Symmetry of DFT of Noise Sequence

Lemma N.2.1. *Let $n_y[n]$ be an i.i.d. normally distributed, discrete noise sequence with N samples, zero mean and variance σ^2, then the DFT of the sequence, $N_{y,DFT}[k]$, is a circular-symmetric, normally distributed complex random variable.*

Proof. Circular symmetry of complex random variables is defined in Definition M.0.24 and a circular symmetric complex normal distribution is defined in Appendix M.0.25. A circular-symmetric complex Gaussian random variable $Z = X + jY$ satisfies according to Property M.0.8:

$$\mathbb{E}[X] = \mu_x = 0 \tag{N.12}$$

$$\mathbb{E}[Y] = \mu_y = 0 \tag{N.13}$$

$$C = 0 \tag{N.14}$$

where C is the pseudo covariance defined in Definition M.0.19. According to Lemma M.0.12

$$C = \sigma_x^2 - \sigma_y^2 + 2jcov[X, Y]. \tag{N.15}$$

In Equation (N.15) σ_x^2 and σ_x^2 are the variances of the real and imaginary part, respectively. The covariance $cov[X, Y]$ is defined in Definition M.0.8, as

$$cov[X, Y] = \mathbb{E}[(X - \mu_x)(Y - \mu_y)] \tag{N.16}$$

As was shown in the proof of Lemma N.1.1, Equation (N.11), the expected values of the real and imaginary part of $N_{y,DFT}[k]$ are zero:

$$\begin{aligned} \mu_x &= \mathbb{E}[\Re(N_{y,DFT}[k])] = 0 \\ \mu_y &= \mathbb{E}[\Im(N_{y,DFT}[k])] = 0 \end{aligned} \tag{N.17}$$

Furthermore, the variances of the real and imaginary part of $N_{y,DFT}[k]$ are equal and given in Equation (N.11) as

$$\sigma_x^2 = \sigma_y^2 = \frac{\sigma^2}{2} \tag{N.18}$$

where σ^2 is the variance of the noise sequence $n_y[n]$. The covariance of the real and imaginary part of $N_{y,DFT}[k]$ is

$$cov[X, Y] = \mathbb{E}[XY] \tag{N.19}$$

since $\mu_x = \mu_y = 0$, see (N.17) and (N.16). By Lemma N.3.1 the real and imaginary part of $N_{y,DFT}[k]$ are independent. Hence, according to Lemma M.0.5, their covariance is zero and

$$cov[X, Y] = \mathbb{E}[XY] = \mathbb{E}[X]\mathbb{E}[Y] = \mu_x\mu_y = 0. \tag{N.20}$$

see definition of mutual independence of two random variables in Appendix M.0.13. Since, as was shown, all conditions given by (N.12), (N.13) and (N.14) are satisfied, $N_{y,DFT}[k]$ is circular symmetric. Hence, Equation (N.15) is zero because of Equation (N.18) and (N.20), such that Equation (N.14) is satisfied. As shown in Equation (N.17), (N.12) and (N.13) are satisfied, too. Consequently, $N_{y,DFT}[k]$ is circular symmetric. Hence, the result.

□

N.3 Independence of Real and Imaginary part of DFT of i.i.d. Normally Distributed Noise Sequence

Lemma N.3.1. *Let $n_y[n]$ be an i.i.d. normally distributed, discrete noise sequence with N samples, zero mean and variance σ^2, then the real and imaginary part of the DFT of the sequence, $N_{y,DFT}[k]$, are independent.*

Proof. According to Lemma M.0.6 two real-valued random variables X_1 and X_2 are independent if they are uncorrelated, see Definition M.0.9, and jointly normal, see Definition M.0.16. Let $n_y[n]$ be an i.i.d. normally distributed, discrete noise sequence with N samples, zero mean and variance σ^2, then the real and imaginary part of the DFT of the sequence, $N_{y,DFT}[k]$, are uncorrelated, by Lemma N.4.1. Furthermore, they are jointly normal, by Lemma N.5.1. Hence, it follows from Lemma M.0.6, that they are independent.

□

N.4 Correlation of Real and Imaginary part of DFT of Noise Sequence

Lemma N.4.1. *Let $n_y[n]$ be an i.i.d. normally distributed, discrete noise sequence with N samples, zero mean and variance σ^2, then the real and imaginary part of the DFT of the sequence, $N_{y,DFT}[k]$, are uncorrelated.*

Proof. Let $n_y[n]$ be an i.i.d. normally distributed, discrete noise sequence with N samples, zero mean and variance σ^2, then according to Equation (N.3) the real and imaginary part of the DFT, $N_{y,DFT}[k]$, of the sequence $n_y[n]$, are calculated by

$$\begin{aligned} \Re(N_{y,DFT}[k]) = X[k] &= \frac{1}{\sqrt{N}} \sum_{n=0}^{N-1} n_y[n] c_{n,k} \\ \Im(N_{y,DFT}[k]) = Y[k] &= -\frac{1}{\sqrt{N}} \sum_{n=0}^{N-1} n_y[n] s_{n,k} \end{aligned} \tag{N.21}$$

with $c_{n,k}$ and $s_{n,k}$, given in Equation (N.5). $X[k]$ and $Y[k]$ are according to Lemma N.1.1 equally normally distributed, with zero mean. Hence, the covariance of the real and imaginary part, $cov[X, Y]$, Definition M.0.8, is calculated by Equation (M.15), using that the mean of the real and imaginary part is zero

$$\begin{aligned} cov[X, Y] &= \mathbb{E}[(X - \mu_x)(Y - \mu_y)] = \mathbb{E}[XY] \\ &= \mathbb{E}[-\frac{1}{N}(\sum_{n=0}^{N-1} n_y[n] c_{n,k})(\sum_{n=0}^{N-1} n_y[n] s_{n,k})] \\ &= \mathbb{E}[-\frac{1}{N} \sum_{n=0}^{N-1} \sum_{p=0}^{N-1} c_{n,k} n_y[n] s_{p,k} n_y[p]] \end{aligned} \tag{N.22}$$

Because of the linearity of the expected value operator, see Property M.0.1

$$cov[X, Y] = -\frac{1}{N} \sum_{n=0}^{N-1} \sum_{p=0}^{N-1} c_{n,k} s_{p,k} \mathbb{E}[n_y[n] n_y[p]] \tag{N.23}$$

Because $n_y[m] \sim \mathcal{N}(0, \sigma^2)$, has zero mean, i.e. $\mathbb{E}[n_y[m]] = 0$ for $m = 0, \ldots, N-1$, and $n_y[m]$ are mutually independent for $m = 0, \ldots, N-1$, then according to Lemma M.0.5

$$\mathbb{E}[n_y[n] n_y[p]] = \mathbb{E}[n_y[n]] \mathbb{E}[n_y[p]] = 0 \tag{N.24}$$

for $n \neq p$. Hence, Equation (N.23) simplifies to

$$cov[X, Y] = -\frac{1}{N} \sum_{n=0}^{N-1} c_{n,k} s_{n,k} \mathbb{E}[n_y[n] n_y[n]] \tag{N.25}$$

Because $n_y[n]$ have zero mean, $\mathbb{E}[n_y[n]n_y[n]]$ corresponds to the variance of $n_y[n]$, see Definition M.0.7, which is σ^2, i.e.

$$\mathbb{E}[n_y[n]n_y[n]] = \sigma^2 \tag{N.26}$$

Hence, the covariance of X and Y, Equation (N.25), results in

$$cov[X,Y] = -\frac{1}{N}\sigma^2 \sum_{n=0}^{N-1} c_{n,k}s_{n,k}. \tag{N.27}$$

By Lemma Q.2.1 this sum equals zero, such that

$$cov[X,Y] = 0 \tag{N.28}$$

Hence, the result. □

N.5 Joint Normality of Real and Imaginary part of DFT of Noise Sequence

Lemma N.5.1. *Let $n_y[n]$ be an i.i.d. normally distributed, discrete noise sequence with N samples, zero mean and variance σ^2, then the real and imaginary part of the DFT of the sequence, $N_{y,DFT}[k]$, are jointly normal.*

Proof. Let $n_y[n]$ be an i.i.d. normally distributed, discrete noise sequence with N samples, zero mean and variance σ^2, then according to Equation (N.3) the real and imaginary part of the DFT, $N_{y,DFT}[k]$, of the sequence $n_y[n]$, are calculated by

$$\begin{aligned} \Re(N_{y,DFT}[k]) = X[k] &= \frac{1}{N}\sum_{n=0}^{N-1} n_y[n]c_{n,k} \\ \Im(N_{y,DFT}[k]) = Y[k] &= -\frac{1}{N}\sum_{n=0}^{N-1} n_y[n]s_{n,k} \end{aligned} \tag{N.29}$$

with $c_{n,k}$ and $s_{n,k}$, given in Equation (N.5). By Definition M.0.16 two normally distributed random variables X_1 and X_2 are jointly normal, if for all $a, b \in \mathbb{R}$,

$$Y = aX_1 + bX_2 \tag{N.30}$$

is also normally distributed. $X[k]$ and $Y[k]$ are according to Lemma N.1.1 equally normally distributed. The sum of the normally distributed random variables X and Y with $a, b \in \mathbb{R}$ equals

$$\begin{aligned} aX[k] + bY[k] &= a\frac{1}{N}\sum_{n=0}^{N-1} n_y[n]c_{n,k} - b\frac{1}{N}\sum_{n=0}^{N-1} n_y[n]s_{n,k} \\ &= \frac{1}{N}\sum_{n=0}^{N-1}(ac_{n,k} - bs_{n,k})n_y[n] \\ &= \frac{1}{N}\sum_{n=0}^{N-1} l_{n,k}n_y[n] \end{aligned} \tag{N.31}$$

Because the sequence $n_y[n]$ is i.i.d with normal distribution, then by Lemma M.0.8, the samples $n_y[n]$ are jointly normal, meaning that $\frac{1}{N}\sum_{n=0}^{N-1} l_{n,k}n_y[n]$ will be also normally distributed. Hence, $X[k]$ and $Y[k]$ are jointly normal. □

N.6 Characteristics of Product of Complex Valued Constant with DFT of i.i.d. Normally Distributed Noise Sequence with Zero Mean

Lemma N.6.1. *Let $n_y[n]$ be an i.i.d. normally distributed, discrete noise sequence with N samples, zero mean and variance σ^2, then the product of a complex valued constant $S(j\omega_k)$ with the DFT of $n_y[n]$:*

$$S(j\omega_k)N_{y,DFT}(j\omega_k) \tag{N.32}$$

will have the following properties

- *The real and imaginary parts are normally distributed with zero mean and variance $\sigma_s^2 = \frac{\sigma^2}{2}|S(j\omega_k)|^2$, i.e.*

$$\Re(S(j\omega_k)N_{y,DFT}(j\omega_k)) \sim \Im(S(j\omega_k)N_{y,DFT}(j\omega_k)) \sim \mathcal{N}(0, \frac{\sigma^2}{2}|S(j\omega_k)|^2) \tag{N.33}$$

- *The real and imaginary parts are uncorrelated*

$$cov[\Re(S(j\omega_k)N_{y,DFT}(j\omega_k)), \Im(S(j\omega_k)N_{y,DFT}(j\omega_k))] = 0 \tag{N.34}$$

- *The real and imaginary parts are independent*
- *The real and imaginary parts are jointly normal*

Proof. For the DFT $N_{y,DFT}$ of the discrete real valued sequence $n_y[n]$ the following holds

- $N_{y,DFT}(j\omega_k)$ is a circular symmetric normally distributed complex random variable, according to Lemma N.2.1

- The real and imaginary parts of $N_{y,DFT}(j\omega_k)$ are independent, according to Lemma N.3

- The real and imaginary parts of $N_{y,DFT}(j\omega_k)$ are jointly normal, according to Lemma N.5.1

- The real and imaginary parts of $N_{y,DFT}(j\omega_k)$ are normally distributed with zero mean and variance $\sigma_n^2 = \frac{\sigma^2}{2}$, according to Lemma N.1.1

$$\Re(N_{y,DFT}(j\omega_k)) \sim \Im(N_{y,DFT}(j\omega_k)) \sim \mathcal{N}(0, \frac{\sigma^2}{2}) \tag{N.35}$$

- The real and imaginary parts of $N_{y,DFT}(j\omega_k)$ are uncorrelated, according to Lemma N.4.1

The complex valued constant $S(j\omega_k)$ can be expressed as

$$S(j\omega_k) = |S(j\omega_k)|e^{j\Phi_S} \tag{N.36}$$

such that

$$S(j\omega_k)N_{y,DFT}(j\omega_k) = |S(j\omega_k)|e^{j\Phi_S}N_{y,DFT}(j\omega_k) \tag{N.37}$$

Because $N_{y,DFT}(j\omega_k)$ is circular symmetric, the distribution of $e^{j\Phi_S}N_{y,DFT}(j\omega_k)$ will equal the distribution of $N_{y,DFT}(j\omega_k)$, according to Definition M.0.24, i.e.

$$\begin{aligned} \Re(e^{j\Phi_S}N_{y,DFT}(j\omega_k)) \sim \Im(e^{j\Phi_S}N_{y,DFT}(j\omega_k)) \sim \mathcal{N}(0, \frac{\sigma^2}{2}) \\ cov[\Re(e^{j\Phi_S}N_{y,DFT}(j\omega_k)), \Im(e^{j\Phi_S}N_{y,DFT}(j\omega_k))] = 0 \end{aligned} \tag{N.38}$$

The real and imaginary part of $e^{j\Phi_S}N_{y,DFT}(j\omega_k)$ will be jointly normal, according to Definition M.0.16, because the real and imaginary part of $N_{y,DFT}(j\omega_k)$ are jointly normal such that for all $a, b \in \mathcal{R}$,

$$\begin{aligned} &a\Re(e^{j\Phi_S}N_{y,DFT}) + b\Im(e^{j\Phi_S}N_{y,DFT}) = \\ &a(\cos\Phi_S\Re(N_{y,DFT}) - \sin\Phi_S\Im(N_{y,DFT})) \\ &+ b(\sin\Phi_S\Re(N_{y,DFT}) + \cos\Phi_S\Im(N_{y,DFT})) \end{aligned} \tag{N.39}$$

has a normal distribution. Because the real and imaginary part of $e^{j\Phi_S}N_{y,DFT}(j\omega_k)$ are uncorrelated and jointly normal, according to Lemma M.0.6 they are independent. Because of the linearity of the expected value operator and the second order homogenity of the vari-

ance operator, the real and imaginary part of $S(j\omega_k)N_{y,DFT}(j\omega_k) = |S(j\omega_k)|e^{j\Phi_S}N_{y,DFT}(j\omega_k)$ will be normally distributed with zero mean and variance $\sigma_s^2 = \frac{\sigma^2}{2}|S(j\omega_k)|^2$ and be uncorrelated.

□

Appendix O

Characteristics of DFT of a Stationary, Normally Distributed Noise Sequence

O.1 Expected Value

Lemma O.1.1. *Let $n_y[n]$ be a stationary sequence, Definition M.0.11, with a normal distribution $\mathcal{N}(\mu, \sigma^2)$ then*

$$\begin{aligned} \mathbb{E}[X(j\omega_k)] &= \mu_x = 0 \\ \mathbb{E}[Y(j\omega_k)] &= \mu_y = 0 \end{aligned} \tag{O.1}$$

where the real valued random variables $X(j\omega_k)$ and $Y(j\omega_k)$ are the real and imaginary parts of the DFT of the noise sequence $n_y[n]$.

Proof. According to (N.3), the real and imaginary value of the DFT of a real valued sequence $n_y[n]$ are calculated according to

$$\begin{aligned} X(j\omega_k) &= \sum_{n=0}^{N-1} \frac{1}{\sqrt{N}} n_y[n] c_{n,k} \\ Y(j\omega_k) &= \sum_{n=0}^{N-1} \frac{1}{\sqrt{N}} n_y[n] s_{n,k} \end{aligned} \tag{O.2}$$

where $c_{n,k}$ and $s_{n,k}$ are abbreviations for the cosine and sine term given in (N.5). Because $c_{n,k}$ is a constant for fixed n and k, the expected value of $X(j\omega_k)$ can be calculated using the linearity property of the expected value operator (Property M.0.1) by

$$\mathbb{E}[X(j\omega_k)] = \sum_{n=0}^{N-1} \frac{1}{\sqrt{N}} c_{n,k} \mathbb{E}[n_y[n]] = \frac{\mu}{\sqrt{N}} \sum_{n=0}^{N-1} c_{n,k} \tag{O.3}$$

Because of Lemma Q.3.1, $\sum_{n=0}^{N-1} c_{n,k} = 0$, thus

$$\mathbb{E}[X(j\omega_k)] = 0 \tag{O.4}$$

Similarly we obtain

$$\mathbb{E}[Y(j\omega_k)] = \frac{\mu}{\sqrt{N}} \sum_{n=0}^{N-1} s_{n,k} = 0 \tag{O.5}$$

Hence, the result. □

O.2 Second Order Moment Characteristics of Real and Imaginary Part for Uncorrelated Samples

Lemma O.2.1. *Let $n_y[n]$ be a stationary sequence, Definition M.0.11, with a normal distribution $\mathcal{N}(\mu, \sigma^2)$ and let the samples of $n_y[n]$ be uncorrelated, then for the real part $X(j\omega_k)$ and imaginary part $Y(j\omega_k)$ of the DFT, $N_{y,DFT}(j\omega_k) = X(j\omega_k) + jY(j\omega_k)$, of the noise sequence $n_y[n]$ the following holds*

$$\begin{aligned} var[X(j\omega_k)] &= \frac{\sigma^2}{2} - \mu_x^2 \\ var[Y(j\omega_k)] &= \frac{\sigma^2}{2} - \mu_y^2 \\ cov[X(j\omega_k), Y(j\omega_k)] &= -\mu_x \mu_y \end{aligned} \tag{O.6}$$

where μ_x and μ_y are the expected values of the real and imaginary part, respectively, which are by Lemma O.1.1 zero.

Proof. The variance of a real random variable X is according to Definition M.0.7

$$var[X] = \mathbb{E}[(X - \mu_x)^2] = \mathbb{E}[X^2] - \mathbb{E}[X]^2 \tag{O.7}$$

The real part $X(j\omega_k)$ of the DFT of the noise sequence $n_y[n]$ is according to (N.3)

$$X(j\omega_k) = \sum_{n=0}^{N-1} \frac{1}{\sqrt{N}} n_y[n] c_{n,k} \tag{O.8}$$

where $c_{n,k}$ is an abbreviation for the cosine term given in (N.5). For better readability $(j\omega_k)$ is omitted in the following. Because $c_{n,k}$ is a constant for fixed n and k, and because of the linearity property of the expected value operator, the following relation is obtained

$$\begin{aligned}\mathbb{E}[XX] &= \mathbb{E}\left[\frac{1}{\sqrt{N}}\left(\sum_{n=0}^{N-1} n_y[n]c_{n,k}\right)\frac{1}{\sqrt{N}}\left(\sum_{n=0}^{N-1} n_y[n]c_{n,k}\right)\right] \\ &= \frac{1}{N}\mathbb{E}\left[\sum_{n=0}^{N-1}\sum_{p=0}^{N-1} n_y[n]c_{n,k}n_y[p]c_{p,k}\right] \\ &= \frac{1}{N}\sum_{n=0}^{N-1}\sum_{p=0}^{N-1} c_{n,k}c_{p,k}\mathbb{E}\left[n_y[n]n_y[p]\right]\end{aligned} \tag{O.9}$$

Since the samples of $n_y[n]$ are uncorrelated, their covariance is according to Definition M.0.9 zero. Consequently, according to Property M.0.3

$$\mathbb{E}\left[n_y[n]n_y[p]\right] = \mathbb{E}\left[n_y[n]\right]\mathbb{E}\left[n_y[p]\right] = \mu^2 \tag{O.10}$$

because $cov[n_y[n], n_y[p]] = 0$ for $n \neq p$. For $n = p$

$$\mathbb{E}\left[n_y[n]n_y[n]\right] = var[n_y[n]] + \mathbb{E}\left[n_y[n]\right]^2 = \sigma^2 + \mu^2 \tag{O.11}$$

according to Definition M.0.7. Hence, Equation (O.9) simplifies to

$$\begin{aligned}\mathbb{E}[XX] &= \frac{1}{N}\left(\sum_{n=0}^{N-1}\sum_{p=0}^{N-1} c_{n,k}c_{p,k}(\mu^2)\right) + \frac{1}{N}\left(\sum_{n=0}^{N-1} c_{n,k}^2\sigma^2\right) \\ &= \frac{\mu^2}{N}\left(\sum_{n=0}^{N-1} c_{n,k}\right)\left(\sum_{p=0}^{N-1} c_{n,k}\right) + \frac{\sigma^2}{N}\left(\sum_{n=0}^{N-1} c_{n,k}^2\right)\end{aligned} \tag{O.12}$$

According to Lemma Q.3.1, $\sum_{n=0}^{N-1} c_{n,k} = 0$, and according to Lemma Q.1.1, $\sum_{n=0}^{N-1} c_{n,k}^2 = \frac{N}{2}$. Thus,

$$\mathbb{E}[XX] = \frac{\sigma^2}{2} \tag{O.13}$$

and with (O.7)

$$var[X] = \frac{\sigma^2}{2} - \mu_x^2 \tag{O.14}$$

Similarly it can be shown that

$$var[Y] = \frac{\sigma^2}{2} - \mu_y^2 \tag{O.15}$$

Hence, the first result.

The covariance of X and Y is according to Property M.0.3

$$cov(X, Y) = \mathbb{E}[XY] - \mathbb{E}[X]\mathbb{E}[Y] = \mathbb{E}[XY] - \mu_x\mu_y \tag{O.16}$$

With real part X and imaginary part Y given in (N.3)

$$\begin{aligned}\mathbb{E}[XY] &= \mathbb{E}\left[\left(\sum_{n=0}^{N-1}\frac{1}{\sqrt{N}}n_y[n]c_{n,k}\right)\left(\sum_{n=0}^{N-1}\frac{1}{\sqrt{N}}n_y[n]s_{n,k}\right)\right] \\ &= \mathbb{E}\left[\frac{1}{N}\sum_{n=0}^{N-1}\sum_{p=0}^{N-1}n_y[n]c_{n,k}n_y[p]s_{p,k}\right]\end{aligned} \tag{O.17}$$

where $c_{n,k}$ and $s_{n,k}$ are an abbreviation for the cosine and sine term given in (N.5). Because $c_{n,k}$ and $s_{n,k}$ are constant for fixed n and k, and because of the linearity property of the expected value operator, the following relation is obtained

$$\mathbb{E}[XY] = \frac{1}{N}\sum_{n=0}^{N-1}\sum_{p=0}^{N-1}c_{n,k}s_{p,k}\mathbb{E}\left[n_y[n]n_y[p]\right] \tag{O.18}$$

With Equation (O.10) and (O.11)

$$\begin{aligned}\mathbb{E}[XY] &= \frac{\mu^2}{N}\left(\sum_{n=0}^{N-1}\sum_{p=0}^{N-1}c_{n,k}s_{p,k}\right) + \frac{\sigma^2}{N}\left(\sum_{n=0}^{N-1}c_{n,k}s_{n,k}\right) \\ &= \frac{\mu^2}{N}\left(\sum_{n=0}^{N-1}c_{n,k}\right)\left(\sum_{n=0}^{N-1}s_{n,k}\right) + \frac{\sigma^2}{N}\left(\sum_{n=0}^{N-1}c_{n,k}s_{n,k}\right)\end{aligned} \tag{O.19}$$

According to Lemma Q.3.1, $\sum_{n=0}^{N-1}c_{n,k} = \sum_{n=0}^{N-1}s_{n,k} = 0$, and according to Lemma Q.2.1, $\sum_{n=0}^{N-1}c_{n,k}s_{n,k} = 0$. Thus,

$$\mathbb{E}[XY] = 0 \tag{O.20}$$

such that Equation (O.16) becomes

$$cov(X,Y) = -\mu_x\mu_y \tag{O.21}$$

Hence, the second result. □

O.3 Second Order Moment Characteristics of DFT for Uncorrelated Samples

Lemma O.3.1. *Let $n_y[n]$ be a stationary sequence, Definition M.0.11, with a normal distribution $\mathcal{N}(\mu,\sigma^2)$ and let the samples of $n_y[n]$ be uncorrelated. Let $N_{y,DFT}(j\omega_k) = Z(j\omega_k) = X(j\omega_k) + jY(j\omega_k)$ denote the DFT of the noise sequence $n_y[n]$. Then the following holds*

$$\begin{aligned}\mathbb{E}[Z(j\omega_k)Z(j\omega_k)^*] &= \sigma^2 \\ \mathbb{E}[Z(j\omega_k)Z(j\omega_k)] &= 0\end{aligned} \tag{O.22}$$

Proof. The variance of a complex random variable Z is according to Lemma M.0.9, and Lemma M.0.11

$$K_{ZZ} = \mathbb{E}[ZZ^*] - \mathbb{E}[Z]\mathbb{E}[Z^*] = var[X] + var[Y] \tag{O.23}$$

The variances of the real and imaginary part, X and Y, are given in Lemma O.2.1 by $var[X] = \frac{\sigma^2}{2} - \mu_x$ and $var[Y] = \frac{\sigma^2}{2} - \mu_y$. Thus, a relation for $\mathbb{E}[ZZ^*]$ can be obtained as follows,

$$\begin{aligned}
\mathbb{E}[ZZ^*] &= var[X] + var[Y] + \mathbb{E}[Z]\mathbb{E}[Z^*] \\
&= \frac{\sigma^2}{2} - \mu_x^2 + \frac{\sigma^2}{2} - \mu_y^2 + \mu_z\mu_z^* \\
&= \frac{\sigma^2}{2} - \mu_x^2 + \frac{\sigma^2}{2} - \mu_y^2 + \mu_x^2 + \mu_y^2 \\
&= \sigma^2
\end{aligned} \tag{O.24}$$

Hence, the first result.

The pseudo-variance on the other hand is according to Lemma M.0.10 and Lemma M.0.12

$$C_{ZZ} = \mathbb{E}[ZZ] - \mathbb{E}[Z]\mathbb{E}[Z] = var[X] - var[Y] + 2jcov[X, Y] \tag{O.25}$$

The variances of the real and imaginary part, X and Y, and their covariance is given in Lemma O.2.1. Thus, a relation for $\mathbb{E}[ZZ]$ can be obtained as follows,

$$\begin{aligned}
\mathbb{E}[ZZ] &= \frac{\sigma^2}{2} - \mu_x^2 - (\frac{\sigma^2}{2} - \mu_y^2) + 2j(-\mu_x\mu_y) + \mathbb{E}[Z]\mathbb{E}[Z] \\
&= \frac{\sigma^2}{2} - \mu_x^2 - (\frac{\sigma^2}{2} - \mu_y^2) + 2j(-\mu_x\mu_y) + \mu_x^2 - \mu_y^2 + 2j\mu_x\mu_y \\
&= 0
\end{aligned} \tag{O.26}$$

Hence, the second result. □

O.4 Second Order Moment Characteristics of Ratio with Complex Valued Constant

Lemma O.4.1. *Given $V = \frac{N}{u} = X + jY$ where N is a complex random variable with zero mean $\mu_n = 0$ and u is a complex valued constant, then the elements of the covariance matrix Σ_{XY}, given in Equation* (M.62)*, are calculated by Equation* (M.60) *as follows*

$$\begin{aligned} var[X] &= \frac{1}{2}\Re(K_{VV} + C_{VV}) = \frac{1}{2}\frac{\mathbb{E}\left[NN^*\right]}{|u|^2} + \frac{1}{2}\Re(\frac{\mathbb{E}[NN]}{u_r^2 - u_j^2 + 2ju_ru_j}) \\ var[Y] &= \frac{1}{2}\Re(K_{VV} - C_{VV}) = \frac{1}{2}\frac{\mathbb{E}\left[NN^*\right]}{|u|^2} - \frac{1}{2}\Re(\frac{\mathbb{E}[NN]}{u_r^2 - u_j^2 + 2ju_ru_j}) \\ cov[X,Y] &= \frac{1}{2}\Im(-K_{VV} + C_{VV}) = \frac{1}{2}\Im(\frac{\mathbb{E}[NN]}{u_r^2 - u_j^2 + 2ju_ru_j}) \\ cov[Y,X] &= \frac{1}{2}\Im(K_{VV} + C_{VV}) = \frac{1}{2}\Im(\frac{\mathbb{E}[NN]}{u_r^2 - u_j^2 + 2ju_ru_j}) \end{aligned} \tag{O.27}$$

Proof. The variance of the complex random variable V is calculated according to Definition M.0.20 as

$$K_{VV} = var[V] = \mathbb{E}[(V - \mu_v)(V - \mu_v)^*] \tag{O.28}$$

where $()^*$ denotes the conjugate complex transpose. Since $\mu_v = 0$, because $\mu_n = 0$, K_{VV} reduces to

$$K_{VV} = \mathbb{E}[VV^*] = \mathbb{E}\left[\frac{N}{u}\left(\frac{N}{u}\right)^*\right] \tag{O.29}$$

By Lemma M.0.24, $\left(\frac{N}{u}\right)^* = \frac{N^*}{u^*}$ holds, and by Lemma M.0.21 $uu^* = |u|^2$, such that the variance further simplifies to

$$K_{VV} = \mathbb{E}\left[\frac{NN^*}{uu^*}\right] = \mathbb{E}\left[\frac{NN^*}{|u|^2}\right] \tag{O.30}$$

Since u is a complex valued constant, the variance results in

$$K_{VV} = \frac{\mathbb{E}\left[NN^*\right]}{|u|^2} \tag{O.31}$$

where the linearity property (Property M.0.1) of the expected value operator was used. The pseudo variance of the complex random variable V is calculated according to Definition M.0.21 as

$$C_{VV} = \mathbb{E}\left[(V - \mu_v)^2\right] \tag{O.32}$$

Since $\mu_v = 0$, C_{VV} reduces to

$$C_{VV} = \mathbb{E}\left[V^2\right] = \mathbb{E}\left[\frac{NN}{uu}\right]. \tag{O.33}$$

Since u is a complex valued constant, using that the expected value operator is linear, the pseudo variance thus results in

$$C_{VV} = \frac{\mathbb{E}[NN]}{uu} = \frac{\mathbb{E}[NN]}{u_r^2 - u_j^2 + 2ju_r u_j} \tag{O.34}$$

where u_r and u_j are the real and imaginary parts of u. Finally, with the derived relations in O.31 and O.34 the equalities in O.27 are obtained as can be directly seen. □

Appendix P

Closed-loop Identification

P.1 Bias of Indirect Estimate

Lemma P.1.1. *Assume that the true plant $G_{cl}(j\omega_k)$ is related with the Controller C and closed-loop $G(j\omega)$ according to*

$$G(j\omega_k) = \frac{G_{cl}(j\omega_k)}{1 - G_{cl}(j\omega_k)C(j\omega_k)} \tag{P.1}$$

and the plant is estimated over

$$\hat{G}(j\omega_k) = \frac{\hat{G}_{cl}(j\omega_k)}{1 - \hat{G}_{cl}(j\omega_k)C(j\omega_k)} \tag{P.2}$$

where C is exactly known and the closed-loop estimate $\hat{G}_{cl}$ is given by

$$\hat{G}_{cl}(j\omega_k) = G_{cl}(j\omega_k) + G_{B,cl}(j\omega_k) + \epsilon(j\omega_k) \tag{P.3}$$

where $G_{cl}(j\omega_k)$ is the true closed-loop frequency response and $G_{B,cl}(j\omega_k)$ is a constant bias. The real and imaginary parts of $\epsilon(j\omega_k)$, are normally distributed with zero mean and

$$\begin{aligned} \mathbb{E}[\Re(\epsilon(j\omega_k))^2] &= r_{xx}(j\omega_k) \\ \mathbb{E}[\Im(\epsilon(j\omega_k))^2] &= r_{yy}(j\omega_k) \\ \mathbb{E}[\Re(\epsilon(j\omega_k))\Im(\epsilon(j\omega_k))] &= r_{xy}(j\omega_k) \end{aligned} \tag{P.4}$$

Then the expected value of the plant estimate $\hat{G}$ is given by [Hea01b]

$$\mathbb{E}[\hat{G}(j\omega_k)] = \alpha(j\omega_k)G_B(j\omega_k) + (1 - \alpha(j\omega_k))\left(-\frac{1}{C(j\omega_k)}\right) \tag{P.5}$$

where

$$G_B(j\omega_k) = \frac{G_{cl}(j\omega_k) + G_{B,cl}(j\omega_k)}{1 - C(j\omega_k)(G_{cl}(j\omega_k) + G_{B,cl}(j\omega_k))} \tag{P.6}$$

and α results from the line integral

$$\alpha = \int_0^{r_0} \frac{r}{\sqrt{1 - a^2 r^2}} e^{-\frac{r^2}{2}} dr \tag{P.7}$$

with

$$\begin{aligned}
\tan 2\Phi &= \frac{2r_{xy}}{r_{yy} - r_{xx}} \\
\sigma_{\bar{x}}^2 &= r_{xx}\cos^2\Phi + r_{yy}\sin^2\Phi - 2r_{xy}\cos\Phi\sin\Phi \\
\sigma_{\bar{y}}^2 &= r_{xx}\sin^2\Phi + r_{yy}\cos^2\Phi + 2r_{xy}\cos\Phi\sin\Phi \\
r_0^2(j\omega_k) &= \frac{1}{\sigma_{\bar{x}}^2}[\Re(e^{j\Phi}\frac{S_B}{C})]^2 + \frac{1}{\sigma_{\bar{y}}^2}[\Im(e^{j\Phi}\frac{S_B}{C})]^2 \\
a^2 &= (\sigma_{\bar{x}}^2 - \sigma_{\bar{y}}^2)\left(\frac{C}{S_B}\right)^2 e^{-2j\Phi} \\
S_B(j\omega_k) &= \frac{1}{1 + G_B C}
\end{aligned} \tag{P.8}$$

Note, that for better readability the dependency on $(j\omega_k)$ was omitted in the last equations.

Proof. The proof is given in [Hea01b]. □

P.2 Bias of Indirect Estimate - Special Case

Lemma P.2.1. *Assume that the true plant $G(j\omega_k)$ is related with the Controller C and closed-loop $G(j\omega)$ according to*

$$G(j\omega_k) = \frac{G_{cl}(j\omega_k)}{1 - G_{cl}(j\omega_k)C(j\omega_k)} \tag{P.9}$$

and the plant is estimated over

$$\hat{G}(j\omega_k) = \frac{\hat{G}_{cl}(j\omega_k)}{1 - \hat{G}_{cl}(j\omega_k)C(j\omega_k)} \tag{P.10}$$

where C is exactly known and the closed-loop estimate $\hat{G}_{cl}$ is given by

$$\hat{G}_{cl}(j\omega_k) = G_{cl}(j\omega_k) + \epsilon(j\omega_k) \tag{P.11}$$

where $G_{cl}(j\omega_k)$ is the true closed-loop frequency response. The real and imaginary parts of $\epsilon(j\omega_k)$, are equally normally distributed and uncorrelated with zero mean and

$$\begin{aligned}\mathbb{E}[\Re(\epsilon(j\omega_k))^2] &= \sigma(j\omega_k)^2 \\ \mathbb{E}[\Im(\epsilon(j\omega_k))^2] &= \sigma(j\omega_k)^2 \\ \mathbb{E}[\Re(\epsilon(j\omega_k))\Im(\epsilon(j\omega_k))] &= 0\end{aligned} \tag{P.12}$$

Then according to [Hea01b], the expected value of the plant estimate $\hat{G}$ is given by

$$\mathbb{E}[\hat{G}(j\omega_k)] = \alpha(j\omega_k)G(j\omega_k) + (1-\alpha(j\omega_k))\left(-\frac{1}{C(j\omega_k)}\right) \tag{P.13}$$

where α is

$$\alpha = 1 - e^{-\frac{1}{2}\frac{1}{\sigma(j\omega_k)^2}|\frac{S_c(j\omega_k)}{C(j\omega_k)}|^2} \tag{P.14}$$

and

$$S_c(j\omega_k) = \frac{1}{1+G(j\omega_k)C(j\omega_k)} \tag{P.15}$$

Proof. Using Lemma P.1.1 we calculate with the specified $\epsilon(j\omega_k)$:

$$\begin{aligned}\Phi &= 0 \\ \sigma_{\bar{x}}^2 &= \sigma_{\bar{y}}^2 = \sigma^2 \\ r_0^2(j\omega_k) &= \frac{1}{\sigma^2}[\Re\left(\frac{S_c}{C}\right)]^2 + \frac{1}{\sigma^2}[\Im\left(\frac{S_c}{C}\right)]^2 = \frac{1}{\sigma^2}|\frac{S_c}{C}|^2 \\ a^2 &= 0 \\ S_c &= \frac{1}{1+GC}\end{aligned} \tag{P.16}$$

and

$$\alpha = \int_0^{r_0} re^{-\frac{r^2}{2}}dr = [-e^{-\frac{r^2}{2}}]_0^{r_0} = 1 - e^{-\frac{r_0^2}{2}} = 1 - e^{-\frac{1}{2}\frac{1}{\sigma^2}|\frac{S_c}{C}|^2} \tag{P.17}$$

Note, that for better readability $(j\omega_k)$ was omitted. □

Appendix Q

Cosine and Sine Equalities

Q.1 Finite Sum of Cosine and Sine Squared

Lemma Q.1.1. *Let $k \in \mathbb{N}$, then*

$$\sum_{n=0}^{N-1} cos^2(2\pi \frac{n}{N} k) = \frac{N}{2} \tag{Q.1}$$

$$\sum_{n=0}^{N-1} sin^2(2\pi \frac{n}{N} k) = \frac{N}{2} \tag{Q.2}$$

Proof. A cosine can be expressed in terms of exponentials according to Equation (2.18) such that (Q.1) becomes

$$\begin{aligned} \sum_{n=0}^{N-1} cos^2(2\pi \frac{n}{N} k) &= \sum_{n=0}^{N-1} (\frac{e^{j2\pi \frac{n}{N} k} + e^{-j2\pi \frac{n}{N} k}}{2})^2 \\ &= \sum_{n=0}^{N-1} \frac{e^{2j2\pi \frac{n}{N} k} + e^{-2j2\pi \frac{n}{N} k} + 2e^0}{4} \\ &= \frac{1}{4} \sum_{n=0}^{N-1} e^{j2\pi \frac{n}{N} 2k} + \frac{1}{4} \sum_{n=0}^{N-1} e^{-j2\pi \frac{n}{N} 2k} + \sum_{n=0}^{N-1} \frac{1}{2} \end{aligned} \tag{Q.3}$$

where each of the first two summands is a geometric series with $r = e^{j2\pi \frac{n}{N} 2k}$ and $r = e^{-j2\pi \frac{n}{N} 2k}$, respectively. The geometric series is defined in Equation (2.21) and is repeated here for convenience

$$\sum_{n=0}^{N-1} r^n = \frac{1 - r^N}{1 - r} \tag{Q.4}$$

The sum in Equation (Q.3) can be hence expressed as

$$\begin{aligned}
&\frac{1}{4}\left(\frac{1-(e^{j2\pi\frac{n}{N}2k})^N}{1-e^{j2\pi\frac{n}{N}2k}}+\frac{1-(e^{-j2\pi\frac{n}{N}2k})^N}{1-e^{-j2\pi\frac{n}{N}2k}}\right)+\frac{N}{2}= \\
&\frac{1}{4}\left(\frac{1-e^{j2\pi\frac{n}{N}2kN}}{1-e^{j2\pi\frac{n}{N}2k}}+\frac{1-e^{-j2\pi\frac{n}{N}2kN}}{1-e^{-j2\pi\frac{n}{N}2k}}\right)+\frac{N}{2}= \\
&\frac{1}{4}\left(\frac{1-e^{j2\pi n2k}}{1-e^{j2\pi\frac{n}{N}2k}}+\frac{1-e^{-j2\pi n2k}}{1-e^{-j2\pi\frac{n}{N}2k}}\right)+\frac{N}{2}
\end{aligned} \tag{Q.5}$$

where $\sum_{n=0}^{N-1}\frac{1}{2}=\frac{N}{2}$ was used. Since $n\in\mathbb{N}$ and $k\in\mathbb{N}$ the exponents will be multiple integers of 2π. It holds that $e^{jp2\pi}=1$ with $p\in\mathbb{Z}$. This can be easily seen by drawing its phasor diagram and recognizing that if the phase is a multiple integer of 2π, the imaginary part $Im\{e^{jp2\pi}\}$ will be zero and the real part will be $Re\{e^{jp2\pi}\}=1$ since $|e^{jp2\pi}|=1$. Hence, we finally arrive at the relation

$$\sum_{n=0}^{N-1}cos^2(2\pi\frac{n}{N}k)=\frac{1}{4}(\frac{1-1}{1-e^{j2\pi\frac{n}{N}2k}}+\frac{1-1}{1-e^{-j2\pi\frac{n}{N}2k}})+\frac{N}{2}=\frac{N}{2} \tag{Q.6}$$

which we wanted to show. In the same manner the relation given in (Q.2) can be proven. □

Q.2 Finite Sum of Product of Cosine and Sine

Lemma Q.2.1. *Let $k\in\mathbb{N}$ then*

$$\sum_{n=0}^{N-1}cos(2\pi\frac{k}{N}n)sin(2\pi\frac{k}{N}n)=0 \tag{Q.7}$$

Proof. Let $k\in\mathbb{N}$ then using the trigonometric identity, known as the double angle formula $sin(2\Theta)=2sin(\Theta)cos(\Theta)$, we obtain

$$\begin{aligned}
\sum_{n=0}^{N-1}cos(2\pi\frac{k}{N}n)sin(2\pi\frac{k}{N}n)&=\frac{1}{2}\sum_{n=0}^{N-1}2cos(2\pi\frac{k}{N}n)sin(2\pi\frac{k}{N}n) \\
&=\frac{1}{2}\sum_{n=0}^{N-1}sin(2\pi\frac{k}{N}n\cdot 2)
\end{aligned} \tag{Q.8}$$

Using the relation $sin(\Theta) = \frac{e^{j\Theta} - e^{-j\Theta}}{2j}$ given in (2.19), results in

$$\begin{aligned} \frac{1}{2}\sum_{n=0}^{N-1} sin(2\pi\frac{k}{N}n \cdot 2) &= \frac{1}{2}\sum_{n=0}^{N-1} \frac{e^{j2\pi\frac{k}{N}n\cdot 2} - e^{-j2\pi\frac{k}{N}n\cdot 2}}{2j} \\ &= \frac{1}{2}\sum_{n=0}^{N-1} \frac{e^{j2\pi\frac{k}{N}n\cdot 2}}{2j} - \frac{1}{2}\sum_{n=0}^{N-1} \frac{e^{-j2\pi\frac{k}{N}n\cdot 2}}{2j} \end{aligned} \tag{Q.9}$$

where each summand is a geometric series:

$$\sum_{n=0}^{N-1} r^n = \frac{(1-r^N)}{1-r} \tag{Q.10}$$

with $r = e^{j2\pi\frac{k}{N}\cdot 2}$ and $r = e^{j2\pi\frac{k}{N}\cdot 2}$, respectively. Hence, we can write

$$\begin{aligned} \frac{1}{2}\sum_{n=0}^{N-1} \frac{e^{j2\pi\frac{k}{N}n\cdot 2}}{2j} - \frac{1}{2}\sum_{n=0}^{N-1} \frac{e^{-j2\pi\frac{k}{N}n\cdot 2}}{2j} &= \frac{1}{4j}(\frac{1-e^{j2\pi\frac{k}{N}N\cdot 2}}{1-e^{j2\pi\frac{k}{N}\cdot 2}} - \frac{1-e^{-j2\pi\frac{k}{N}N\cdot 2}}{1-e^{-j2\pi\frac{k}{N}\cdot 2}}) \\ &= \frac{1}{4j}(\frac{1-e^{j2\pi k\cdot 2}}{1-e^{j2\pi\frac{k}{N}\cdot 2}} - \frac{1-e^{-j2\pi k\cdot 2}}{1-e^{-j2\pi\frac{k}{N}\cdot 2}}) \\ &= 0 \end{aligned} \tag{Q.11}$$

since $k \in \mathbb{N}^+$ such that $e^{j2\pi k\cdot 2} = e^{-j2\pi k\cdot 2} = 1$. Hence, the result.

□

Q.3 Finite Sum of Sine and Cosine

Lemma Q.3.1. *Let $k \in \mathbb{N}$ then*

$$\sum_{n=0}^{N-1} \sin(j2\pi\frac{k}{N}n) = \sum_{n=0}^{N-1} cos(j2\pi\frac{k}{N}n) = 0 \tag{Q.12}$$

Proof. The sine can be expressed in terms of complex exponentials as

$$\sin(j2\pi\frac{k}{N}n) = \frac{e^{j2\pi\frac{k}{N}n} - e^{-j2\pi\frac{k}{N}n}}{2j} \tag{Q.13}$$

such that

$$\sum_{n=0}^{N-1} \sin(j2\pi\frac{k}{N}n) = \sum_{n=0}^{N-1} \frac{e^{j2\pi\frac{k}{N}n} - e^{-j2\pi\frac{k}{N}n}}{2j} = \frac{1}{2j}\sum_{n=0}^{N-1} e^{j2\pi\frac{k}{N}n} - \frac{1}{2j}\sum_{n=0}^{N-1} e^{-j2\pi\frac{k}{N}n} \tag{Q.14}$$

which is zero according to Lemma Q.4.1. Similarly, it can be shown that $\sum_{n=0}^{N-1} cos(j2\pi\frac{k}{N}n) = 0$, using the relation

$$\cos(j2\pi\frac{k}{N}n) = \frac{e^{j2\pi\frac{k}{N}n} + e^{-j2\pi\frac{k}{N}n}}{2} \tag{Q.15}$$

□

Q.4 Finite Sum of Complex Exponential

Lemma Q.4.1. *Let $k \in \mathbb{N}$ then*

$$\sum_{n=0}^{N-1} e^{j2\pi \frac{k}{N} n} = \sum_{n=0}^{N-1} e^{-j2\pi \frac{k}{N} n} = 0 \tag{Q.16}$$

Proof. Equation (Q.16) constitutes a geometric series with $r = e^{j2\pi \frac{k}{N} k}$ or $r = e^{-j2\pi \frac{k}{N}}$, respectively. The geometric series is defined in Equation (2.21) and is repeated here for convenience

$$\sum_{n=0}^{N-1} r^n = \frac{1 - r^N}{1 - r} \tag{Q.17}$$

For $r = e^{j2\pi \frac{k}{N}}$ this results in

$$\sum_{n=0}^{N-1} e^{(j2\pi \frac{k}{N})^n} = \frac{1 - e^{(j2\pi \frac{k}{N})^N}}{1 - e^{(j2\pi \frac{k}{N})}} = \frac{1 - e^{(j2\pi \frac{N}{N} k)}}{1 - e^{(j2\pi \frac{k}{N})}} = \frac{1 - e^{(j2\pi k)}}{1 - e^{(j2\pi \frac{k}{N})}} = 0 \tag{Q.18}$$

since $k \in \mathbb{N}$, such that $e^{j2\pi k} = 1$. Similarly, it can be shown that $\sum_{n=0}^{N-1} e^{-j2\pi \frac{k}{N} n} = 0$, since $e^{-j2\pi k} = 1$. Hence, the result. □

Appendix R

Scientific Publications

During the employment at the Institute of Flight System Dynamics at TUM, this author contributed to the following publications. Note, that in 2019 after marriage the surname of the author of this thesis changed from GABRYS to STEINERT. Besides, the author was involved in the notes for the lecture *Advanced Flight Control* [Adv22] and in the notes for the lab courses *Numerical Methods and Tools in Aerospace Engineering Lab* [NMT22] and *Flight Control Systems Lab* [FCL22].

- STEINERT, A. ; SPECKMAIER, M. ; GIERSZEWSKI, D. ; STEFFENSEN, R. ; HOLZAPFEL, F.: Experimental Results of Flight Test-Based Gain Retuning. In: *Accepted for AIAA Scitech 2022 Forum*

- STEINERT, A. ; STEFFENSEN, R. ; HOLZAPFEL, F.: Bias of Anticipated Non-Parametric Closed-loop Frequency Response for Controller Gain Re-tuning. In: *Manuscript submitted for publication*

- GABRYS, A. ; HOLZAPFEL, F. ; STEFFENSEN, R. ; MERKL, C.: Flight test based gain tuning using non-parametric frequency domain methods. In: *AIAA Scitech 2021 Forum*, 2021

- GOSSMANN, F.; GABRYS, A.; SVARICEK, F.: Longitudinal Short-Period Aircraft Motion Control under Loadcase Variation. In: *Proceedings of the American Control Conference*, 2020

- GABRYS, A.C. ; STEFFENSEN, R. ; DE ANGELIS CORDEIRO, R. ; MOUTINHO, A. ; HOLZAPFEL, F.: Integration of phase plane flight envelope protections in cascaded incremental flight control. In: *21st IFAC Symposium on Automatic Control in Aerospace ACA 2019*, 2019

- STEFFENSEN, R. ; STEINERT, A. ; HOLZAPFEL, F.: Flight envelope protections using phase plane limits and backstepping control. In: *5th CEAS Conf. Guid. Navig. Control*, 2019

- GOSSMANN, F. ; SVARICEKY, F. ; GABRYS, A.: Control of longitudinal aircraft motion with loadcase robustness using LPV-control with partly-measurable parameters. In: *AIAA Guidance, Navigation, and Control Conference*, 2018

- SCHATZ, S.P. ; GABRYS, A.C. ; GIERSZEWSKI, D.M. ; HOLZAPFEL, F.: Inner Loop Command Interface in a Modular Flight Control Architecture for Trajectory Flights of General Aviation Aircraft. In: *5th International Conference on Control, Decision and Information Technologies, CoDIT*, 2018

- KARLSSON, E. ; SCHATZ, S. ; BAIER, T. ; DÖRHÖFER, C. ; GABRYS, A. ; HOCHSTRASSER, M. ; KRAUSE, C. ; LAUFFS, P. ; MUMM, C. ; NÜRNBERGER, K. ; PETER, L. ; SCHNEIDER, V. ; SPIEGEL, P. ; STEINERT, L. ; ZOLLITSCH, A. ; HOLZAPFEL, F.: Development of an automatic flight path controller for a DA42 general aviation aircraft. In: *Advances in Aerospace Guidance, Navigation and Control*. (pp.121-139). Springer, 2018

- KARLSSON, E. ; BAIER, T. ; DÖRHÖFER, C. ; GABRYS, A. ; HOCHSTRASSER, M. ; KRAUSE, C. ; LAUFFS, P. ; MUMM, C. ; NÜRNBERGER, K. ; PETER, L. ; SCHATZ, S. ; SCHNEIDER, V. ; SPIEGEL, P. ; STEINERT, L. ; ZOLLITSCH, A. ; HOLZAPFEL, F.: Active control objective prioritization for high-bandwidth automatic flight path control. In: *Advances in Aerospace Guidance, Navigation and Control*. (pp.141-161). Springer, 2018

- KARLSSON, E. ; GABRYS, A. ; SCHATZ, S.P. ; HOLZAPFEL, F.: Dynamic flight path control coupling for energy and maneuvering integrity. In: *14th International Conference on Control, Automation, Robotics and Vision, ICARCV 2016*, 2016

- SCHATZ, S.P. ; SCHNEIDER, V. ; KARLSSON, E. ; HOLZAPFEL,F. ; BAIER, T. ; DÖRHÖFER, C. ; HOCHSTRASSER, M. ; GABRYS, A. ; KRAUSE, C. ; LAUFFS, P. ; MUMM, C. ; NÜRNBERGER, K. ; PETER, L. ; SPIEGEL, P. ; STEINERT, L. ; ZOLLITSCH, A.: Flightplan flight tests of an experimental DA42 general aviation aircraft. In: *14th International Conference on Control, Automation, Robotics and Vision, ICARCV 2016*, 2016

- SCHNEIDER, V. ; PIPREK, P. ; SCHATZ, S.P. ; BAIER, T. ; DÖRHÖFER, C. ; HOCHSTRASSER, M. ; GABRYS, A. ; KARLSSON, E. ; KRAUSE, C. ; LAUFFS, P. ; MUMM, C. ; NÜRNBERGER, K. ; PETER, L. ; SPIEGEL, P. ; STEINERT, L. ; ZOLLITSCH, A. ; HOLZAPFEL,F.: Online trajectory generation using clothoid segments. In: *14th International Conference on Control, Automation, Robotics and Vision, ICARCV 2016*, 2016

- KARLSSON, E. ; SCHATZ, S. ; BAIER, T. ; DÖRHÖFER, C. ; GABRYS, A. ; HOCHSTRASSER, M. ; KRAUSE, C. ; LAUFFS, P. ; MUMM, C. ; NÜRNBERGER, K. ; PETER, L. ; SCHNEIDER, V. ; SPIEGEL, P. ; STEINERT, L. ; ZOLLITSCH, A. ; HOLZAPFEL, F.: Automatic flight path control of an experimental DA42 general aviation aircraft. In: *14th International Conference on Control, Automation, Robotics and Vision, ICARCV 2016*, 2016

- DIEPOLDER, J. ; Ben-Asher, J.Z. ; GABRYS, A. ; SCHATZ, S. ; BITTNER, M. ; RIECK, M. ; GRÜTER, B. ; HOLZAPFEL, F.: Flight control law clearance using worst-case inputs. In: *30th Congress of the International Council of the Aeronautical Sciences, ICAS 2016*, 2016

Bibliography

[Adv22] *Advanced Flight Control. Lecture Notes.* München: Lehrstuhl für Flugsystemdynamik, Technische Universität München, 2022

[AM07] Anderson, B.D.O. ; Moore, J.B.: *Optimal Control: Linear Quadratic Methods.* Dover Publications, 2007 (Dover Books on Engineering)

[AS65] Abramowitz, M. ; Stegun, I.A.: *Handbook of Mathematical Functions: With Formulas, Graphs, and Mathematical Tables.* Dover Publications, 1965 (Applied mathematics series). https://books.google.de/books?id=MtU8uP7XMvoC. – ISBN 9780486612720

[Bal03] Balas, Gary J.: Flight control law design: An industry perspective. In: *European Journal of Control* 9 (2003), Nr. 2-3, S. 207–226

[BAL11] Brockhaus, Rudolf ; Alles, Wolfgang ; Luckner, Robert: *Flugregelung.* Berlin and Heidelberg : Springer Verlag, 2011

[BB90] Bongers, P. M. M. ; Bosgra, O. H.: Low order robust H/sub infinity / controller synthesis. In: *29th IEEE Conference on Decision and Control*, 1990, S. 194–199 vol.1

[Bra11] Brandt, Anders: Unbiased Estimation of Frequency Response in the Presence of Input and Output Noise. In: *Conference Proceedings of the Society for Experimental Mechanics Series* 3 (2011), 01. http://dx.doi.org/10.1007/978-1-4419-9299-4-26. – DOI 10.1007/978–1–4419–9299–4–26. ISBN 978–1–4419–9298–7

[Bri81] Brillinger, D.R.: *Time Series: Data Analysis and Theory.* Holden-Day, 1981 (Holden-Day series in time analysis and digital signal processing). https://books.google.de/books?id=iOdQAAAAMAAJ. – ISBN 9780816211500

[Bri88] Brigham, E.O.: *The Fast Fourier Transform and Its Applications.* Prentice Hall, 1988 (Prentice-Hall Signal Processing Series: Advanced monographs). https://books.google.de/books?id=XfJQAAAAMAAJ

[CEGB11] Campestrini, L. ; Eckhard, D. ; Gevers, M. ; Bazanella, A.S.: Virtual Reference Feedback Tuning for non-minimum phase plants. In: *Automatica* 47 (2011), Nr. 8, 1778 - 1784. http://dx.doi.org/https://doi.org/10.1016/j.automatica.2011.04.002. – DOI https://doi.org/10.1016/j.automatica.2011.04.002. – ISSN 0005–1098

[CLS00] Campi, M. ; Lecchini, A. ; Savaresi, S.: Virtual reference feedback tuning (VRFT): a new direct approach to the design of feedback controllers. In: *Proceedings of the 39th IEEE Conference on Decision and Control (Cat. No.00CH37187)* 1 (2000), S. 623–629 vol.1

[DB90] Douce, JL ; Balmer, L: Statistics of frequency-response estimates. In: *IEE Proceedings D-Control Theory and Applications* Bd. 137 IET, 1990, S. 290–296

[DBAG+16] Diepolder, Johannes ; Ben-Asher, Joseph Z. ; Gabrys, Agnes C. ; Schatz, Simon P. ; Bittner, Matthias ; Rieck, Matthias ; Grüter, Benedikt ; Holzapfel, Florian: Flight control law clearance using worst-case inputs. In: *ICAS 30th International Congress of the International Council of the Aeronautical Sciences. ICAS*, 2016

[DFT13] Doyle, John C. ; Francis, Bruce A. ; Tannenbaum, Allen R.: *Feedback control theory*. Courier Corporation, 2013

[Dou80] Douce, JL: Bias of frequency-response estimates in closed-loop systems. In: *IEE Proceedings D-Control Theory and Applications* Bd. 127 IET, 1980, S. 149–152

[dv95] de Vries, Douwe K. ; van den Hof, Paul M.: Quantification of uncertainty in transfer function estimation: a mixed probabilistic-worst-case approach. In: *Automatica* 31 (1995), Nr. 4, 543-557. http://dx.doi.org/https://doi.org/10.1016/0005-1098(95)98483-M. – DOI https://doi.org/10.1016/0005–1098(95)98483–M. – ISSN 0005–1098

[El-85] El-Sakkary, A.: The gap metric: Robustness of stabilization of feedback systems. In: *IEEE Transactions on Automatic Control* 30 (1985), Nr. 3, S. 240–247

[FCL22] *Flight Control Systems Lab. Lab Notes*. München: Lehrstuhl für Flugsystemdynamik, Technische Universität München, 2022

[FHK14] Formentin, Simone ; Heusden, Klaske ; Karimi, Alireza: A comparison of model-based and data-driven controller tuning. In: *International Journal of Adaptive Control and Signal Processing* 28 (2014), 10. http://dx.doi.org/10.1002/acs.2415. – DOI 10.1002/acs.2415

[FL99] Forssell, Urban ; Ljung, Lennart: Closed-loop identification revisited. In: *Automatica* 35 (1999), Nr. 7, 1215-1241. http://dx.doi.org/https://doi.org/10.1016/S0005-1098(99)00022-9. – DOI https://doi.org/10.1016/S0005–1098(99)00022–9. – ISSN 0005–1098

[FVBS02] Fielding, Chris ; Varga, Andras ; Bennani, Samir ; Selier, Michiel: *Advanced techniques for clearance of flight control laws*. Bd. 283. Springer Science & Business Media, 2002

[Gev92] Gevers, M.: Connecting Identification and Robust Control: A New Challenge. In: *IFAC Proceedings Volumes* 25 (1992), Nr. 15, 1 - 10. http://dx.doi.org/https://doi.org/10.1016/S1474-6670(17)50604-7. – DOI https://doi.org/10.1016/S1474–6670(17)50604–7. – ISSN 1474–6670. – 9th IFAC/IFORS Symposium on Identification and System Parameter Estimation 1991 , Budapest, Hungary, 8-12 July 1991

[Gev93] Gevers, Michel: Towards a joint design of identification and control? In: *Essays on Control*. Springer, 1993, S. 111–151

[Gev05] Gevers, Michel: Identification for Control: From the Early Achievements to the Revival of Experiment Design*. In: *European Journal of Control* 11 (2005), Nr. 4, 335 - 352. http://dx.doi.org/https://doi.org/10.3166/ejc.11.335-352. – DOI https://doi.org/10.3166/ejc.11.335–352. – ISSN 0947–3580

[GGS20] Gossmann, Felix ; Gabrys, Agnes ; Svaricek, Ferdinand: Longitudinal Short-Period Aircraft Motion Control Under Loadcase Variation. In: *2020 American Control Conference (ACC)*, 2020, S. 4188–4194

[GHSM21] Gabrys, Agnes ; Holzapfel, Florian ; Steffensen, Rasmus ; Merkl, Christian: Flight Test Based Gain Tuning using non-parametric Frequency Domain Methods. In: *AIAA Scitech 2021 Forum*, 2021, 1424

[GKP96a] Guillaume, P. ; Kollar, I. ; Pintelon, R.: Statistical analysis of nonparametric transfer function estimates. In: *IEEE Transactions on Instrumentation and Measurement* 45 (1996), Nr. 2, S. 594–600. http://dx.doi.org/10.1109/19.492794. – DOI 10.1109/19.492794

[GKP96b] Guillaume, P. ; Kollar, I. ; Pintelon, R.: Statistical analysis of nonparametric transfer function estimates. In: *IEEE Transactions on Instrumentation and Measurement* 45 (1996), Nr. 2, S. 594–600. http://dx.doi.org/10.1109/19.492794. – DOI 10.1109/19.492794

[GL86] Gevers, Michel ; Ljung, Lennart: Optimal experiment designs with respect to the intended model application. In: *Automatica* 22 (1986), Nr. 5, 543 - 554. http://dx.doi.org/https://doi.org/10.1016/0005-1098(86)90064-6. – DOI https://doi.org/10.1016/0005–1098(86)90064–6. – ISSN 0005–1098

[GM89] Glover, K. ; McFarlane, D. C.: *Robust Controller Design Using Normalized Coprime Factor Plant Descriptions*. Springer-Verlag, 1989

[Goo60] Goodman, Leo A.: On the Exact Variance of Products. In: *Journal of the American Statistical Association* 55 (1960), Nr. 292, 708–713. http://www.jstor.org/stable/2281592. – ISSN 01621459

[GP95] Gudbjartsson, Hákon ; Patz, Samuel: The Rician distribution of noisy MRI data. In: *Magnetic resonance in medicine* 34 (1995), Nr. 6, S. 910–914

[GPS92] Guillaume, P. ; Pintelon, R. ; Schoukens, J.: Nonparametric frequency response function estimators based on nonlinear averaging techniques. In: *IEEE Transactions on Instrumentation and Measurement* 41 (1992), Nr. 6, S. 739–746. http://dx.doi.org/10.1109/19.199393. – DOI 10.1109/19.199393

[Gra15] Grauer, Jared: Real-Time Data-Compatibility Analysis Using Output-Error Parameter Estimation. In: *Journal of Aircraft* 52 (2015), 01, S. 1–8. http://dx.doi.org/10.2514/1.C033182. – DOI 10.2514/1.C033182

[Gra18] Grauer, Jared A.: A Learn-to-Fly Approach for Adaptively Tuning Flight Control Systems. In: *2018 Atmospheric Flight Mechanics Conference*, 2018, S. 3312

[GSG18] Gossmann, Felix ; Svaricek, Ferdinand ; Gabrys, Agnes: Control of longitudinal aircraft motion with loadcase robustness using LPV-control with partly-measurable parameters. In: *2018 AIAA Guidance, Navigation, and Control Conference*, 2018, 0854

[Hea00] Heath, W.P.: Probability Density Function of Indirect Non-Parametric Transfer Function Estimates for Plants in Closed-Loop. In: *IFAC Proceedings Volumes* 33 (2000), Nr. 15, 709-714. http://dx.doi.org/https://doi.org/10.1016/S1474-6670(17)39835-X. – DOI

https://doi.org/10.1016/S1474–6670(17)39835–X. – ISSN 1474–6670. – 12th IFAC Symposium on System Identification (SYSID 2000), Santa Barbara, CA, USA, 21-23 June 2000

[Hea01a] Heath, W. P.: Characterising non-parametric estimators in closed-loop: The finite data case. In: *2001 European Control Conference (ECC)*, 2001, S. 3558–3563

[Hea01b] Heath, W.P.: Bias of indirect non-parametric transfer function estimates for plants in closed loop. In: *Automatica* 37 (2001), Nr. 10, 1529 - 1540. http://dx.doi.org/https://doi.org/10.1016/S0005-1098(01)00105-4. – DOI https://doi.org/10.1016/S0005–1098(01)00105–4. – ISSN 0005–1098

[Hea02] Heath, W. P.: Two measures of variation for non-parametric estimates in closed-loop. In: *Proceedings of the 41st IEEE Conference on Decision and Control, 2002.* Bd. 3, 2002, S. 2627–2632 vol.3

[Hea03] Heath, W.P.: The variation of non-parametric estimates in closed-loop. In: *Automatica* 39 (2003), Nr. 11, 1849-1863. http://dx.doi.org/https://doi.org/10.1016/S0005-1098(03)00194-8. – DOI https://doi.org/10.1016/S0005–1098(03)00194–8. – ISSN 0005–1098

[HGd96] Hjalmarsson, Håkan ; Gevers, Michel ; de Bruyne, Franky: For model-based control design, closed-loop identification gives better performance. In: *Automatica* 32 (1996), Nr. 12, 1659-1673. http://dx.doi.org/https://doi.org/10.1016/S0005-1098(96)80003-3. – DOI https://doi.org/10.1016/S0005–1098(96)80003–3. – ISSN 0005–1098

[HGG94] Hjalmarsson, Håkan ; Gunnarsson, Svante ; Gevers, Michel: A convergent iterative restricted complexity control design scheme. In: *Proceedings of 1994 33rd IEEE Conference on Decision and Control* Bd. 2 IEEE, 1994. – ISBN 0–7803–1968–0, S. 1735–1740

[HGG95] Hjalmarsson, H. ; Gunnarsson, S. ; Gevers, M.: Optimality and sub-optimality of iterative identification and control design schemes. In: *Proceedings of 1995 American Control Conference - ACC'95* 4 (1995), S. 2559–2563 vol.4

[HGGL98] Hjalmarsson, H. ; Gevers, M. ; Gunnarsson, S. ; Lequin, O.: Iterative feedback tuning: theory and applications. In: *IEEE Control Systems Magazine* 18 (1998), Nr. 4, S. 26–41. http://dx.doi.org/10.1109/37.710876. – DOI 10.1109/37.710876

[Hja98] Hjalmarsson, Håkan: Iterative Feedback Tuning. In: *IFAC Proceedings Volumes* 31 (1998), Nr. 22, 101 - 108. http://dx.doi.org/https://doi.org/10.1016/S1474-6670(17)35928-1. – DOI https://doi.org/10.1016/S1474–6670(17)35928–1. – ISSN 1474–6670. – IFAC Workshop on Adaptive Systems in Control and Signal Processing 1998, Glasgow, Scotland, 26-28 August 1998

[Hja02] Hjalmarsson, H.: Iterative feedback tuning-an overview. In: *International Journal of Adaptive Control and Signal Processing* 16 (2002), S. 373–395

[HP08] Hua Fu ; Pooi Yuen Kam: Exact phase noise model and its application to linear minimum variance estimation of frequency and phase of a noisy sinusoid. In: *2008 IEEE 19th International Symposium on Personal, Indoor and Mobile Radio Communications*, 2008, S. 1–5

[IPR+16] Invernizzi, Davide ; Panizza, Pietro ; Riccardi, Fabio ; Formentin, Simone ; Lovera, Marco: Data-driven attitude control law of a variable-pitch quadrotor: a comparison study. In: *IFAC-PapersOnLine* 49 (2016), Nr. 17, 236 - 241. http://dx.doi.org/https://doi.org/10.1016/j.ifacol.2016.09.041. – DOI https://doi.org/10.1016/j.ifacol.2016.09.041. – ISSN 2405–8963. – 20th IFAC Symposium on Automatic Control in AerospaceACA 2016

[Kan13] Kaneko, Osamu: Data-Driven Controller Tuning: FRIT approach. In: *IFAC Proceedings Volumes* 46 (2013), Nr. 11, 326 - 336. http://dx.doi.org/https://doi.org/10.3182/20130703-3-FR-4038.00122. – DOI https://doi.org/10.3182/20130703–3–FR–4038.00122. – ISSN 1474–6670. – 11th IFAC Workshop on Adaptation and Learning in Control and Signal Processing

[kar]

[KBD+18] Karlsson, Erik ; Baier, Thaddäus ; Dörhöfer, Christoph ; Gabrys, Agnes ; Hochstrasser, Markus ; Krause, Christoph ; Lauffs, Patrick J. ; Mumm, Nils C. ; Nürnberger, Kajetan ; Peter, Lars ; Schatz, Simon P. ; Schneider, Volker ; Spiegel, Philip ; Steinert, Lukas ; Zollitsch, Alexander W. ; Holzapfel, Florian: Active Control Objective Prioritization for High-Bandwidth Automatic Flight Path Control. In: *Advances in Aerospace Guidance, Navigation and Control*, Springer International Publishing, 2018. – ISBN 978–3–319–65283–2, S. 141–161

[KGH18] Krause, Christoph ; Goettlicher, Christoph ; Holzapfel, Florian: Development of a generic Flight Test Maneuver Injection Module. In: *ICAS 31st Congress of the International Council of the Aeronautical Science*, 2018

[KGSH16] Karlsson, Erik ; Gabrys, Agnes ; Schatz, Simon P. ; Holzapfel, Florian: Dynamic flight path control coupling for energy and maneuvering integrity. In: *2016 14th International Conference on Control, Automation, Robotics and Vision (ICARCV)*, 2016, S. 1–6

[KH18] Krause, Christoph ; Holzapfel, Florian: System Automation of a DA42 General Aviation Aircraft. In: *2018 Aviation Technology, Integration, and Operations Conference*, 2018, S. 3984

[KM06] Klein, V. ; Morelli, E.A.: *Aircraft System Identification: Theory and Practice*. American Institute of Aeronautics and Astronautics, 2006 (AIAA education series)

[KMH+19] Kügler, Martin E. ; Mumm, Nils C. ; Holzapfel, Florian ; Schwithal, Alexander ; Angermann, Maik: Vision-Augmented Automatic Landing of a General Aviation Fly-by-Wire Demonstrator. In: *AIAA Scitech 2019 Forum*, 2019, S. 1641

[KPVDF17] Kergus, P. ; Poussot-Vassal, C. ; Demourant, F. ; Formentin, S.: Frequency-domain data-driven control design in the Loewner framework. In: *IFAC-PapersOnLine* 50 (2017), Nr. 1, 2095 - 2100. http://dx.doi.org/https://doi.org/10.1016/j.ifacol.2017.08.531. – DOI https://doi.org/10.1016/j.ifacol.2017.08.531. – ISSN 2405–8963. – 20th IFAC World Congress

[Kra20] Krause, Christoph: *Safe and Robust Automation of Aircraft and System Operation*. München, Technische Universität München, Dissertation, 2020

[KS72] Kwakernaak, Huibert ; Sivan, Raphael: *Linear Optimal Control Systems*. John Wiley & Sons, Inc., 1972

[KSB+16] Karlsson, Erik ; Schatz, Simon P. ; Baier, Thaddäus ; Dörhöfer, Christoph ; Gabrys, Agnes ; Hochstrasser, Markus ; Krause, Christoph ; Lauffs, Patrick J. ; Mumm, Nils C. ; Nürnberger, Kajetan ; Peter, Lars ; Schneider, Volker ; Spiegel, Philip ; Steinert, Lukas ; Zollitsch, Alexander W. ; Holzapfel, Florian: Automatic flight path control of an experimental DA42 general aviation aircraft. In: *2016 14th International Conference on Control, Automation, Robotics and Vision (ICARCV)*, 2016, S. 1–6

[KSB+18] Karlsson, Erik ; Schatz, Simon P. ; Baier, Thaddäus ; Dörhöfer, Christoph ; Gabrys, Agnes ; Hochstrasser, Markus ; Krause, Christoph ; Lauffs, Patrick J. ; Mumm, Nils C. ; Nürnberger, Kajetan u. a.: De-

velopment of an automatic flight path controller for a DA42 general aviation aircraft. In: *Advances in Aerospace Guidance, Navigation and Control*. Springer, 2018, S. 121–139

[KvB07] Karimi, A. ; van Heusden, K. ; Bonvin, D.: Non-iterative data-driven controller tuning using the correlation approach. In: *2007 European Control Conference (ECC)*, 2007, S. 5189–5195

[LAKM93] Lee, W. S. ; Anderson, B. D. O. ; Kosut, R. L. ; Mareels, I. M. Y.: On robust performance improvement through the windsurfer approach to adaptive robust control. In: *Proceedings of 32nd IEEE Conference on Decision and Control*, 1993, S. 2821–2827 vol.3

[Lat98] Lathi, Bhagwandas P.: *Modern Digital and Analog Communication Systems 3e Osece*. Oxford University Press, Inc., 1998

[Lju99] Ljung, L.: *System Identification: Theory for the User*. Prentice Hall PTR, 1999 (Prentice Hall information and system sciences series)

[Lop09] Lopez-Salcedo, J. A.: Simple Closed-Form Approximation to Ricean Sum Distributions. In: *IEEE Signal Processing Letters* 16 (2009), Nr. 3, S. 153–155. http://dx.doi.org/10.1109/LSP.2008.2012223. – DOI 10.1109/LSP.2008.2012223

[LW13] Lavretsky, Eugene ; Wise, Kevin A.: Optimal control and the linear quadratic regulator. In: *Robust and Adaptive Control*. Springer, 2013, S. 27–50

[MC04] Miller, S. ; Childers, D.: *Probability and Random Processes: With Applications to Signal Processing and Communications*. Elsevier Science, 2004 https://books.google.de/books?id=fhs73nnLQYEC. – ISBN 9780080470429

[Mer19] Merkl, Christian: *Frequency Response Estimation for Integrity Monitoring*. München, Technische Universität München, Dissertation, 2019

[MG92] McFarlane, D. ; Glover, K.: A loop-shaping design procedure using H/sub infinity / synthesis. In: *IEEE Transactions on Automatic Control* 37 (1992), June, Nr. 6, S. 759–769

[MH17] Mumm, Nils C. ; Holzapfel, Florian: Development of an automatic landing system for diamond da 42 aircraft utilizing a load factor inner loop command system. In: *CEAS˜ EuroGNC*, 2017

[Moo85] In: Mooij, H. A.: *Criteria Based on the Results of the Experiments*. Dordrecht : Springer Netherlands, 1985. – ISBN 978–94–017–1193–7, 101–128

[Mor12] Morelli, Eugene A.: Flight Test Maneuvers for Efficient Aerodynamic Modeling. In: *Journal of Aircraft* 49 (2012), Nr. 6, S. 1857–1867. http://dx.doi.org/10.2514/1.C031699. – DOI 10.2514/1.C031699

[MZS+17] Mumm, Nils C. ; Zollitsch, Alexander W. ; Schatz, Simon P. ; Wulf, Simona ; Holzapfel, Florian ; Lauffs, Patrick J. ; Peter, Lars: Design and testing of a ground roll runway centerline tracking controller for a general aviation research aircraft. In: *2017 11th Asian Control Conference (ASCC)* IEEE, 2017, S. 1689–1694

[NMT22] *Numerical Methods and Tools in Aerospace Engineering Lab. Lab Notes*. Singapore: Technical University of Munich Asia, 2022

[OBS01] Oppenheim, Alan V. ; Buck, John R. ; Schafer, Ronald W.: *Discrete-time signal processing. Vol. 2*. Upper Saddle River, NJ: Prentice Hall, 2001

[OM12] O'Donoughue, N. ; Moura, J. M. F.: On the Product of Independent Complex Gaussians. In: *IEEE Transactions on Signal Processing* 60 (2012), Nr. 3, S. 1050–1063. http://dx.doi.org/10.1109/TSP.2011.2177264. – DOI 10.1109/TSP.2011.2177264

[OMS10] Oldham, K.B. ; Myland, J. ; Spanier, J.: *An Atlas of Functions: with Equator, the Atlas Function Calculator*. Springer New York, 2010 (An Atlas of Functions). https://books.google.de/books?id=UrSnNeJW10YC. – ISBN 9780387488073

[Osg19] Osgood, Brad G.: *Lectures on the Fourier Transform and Its Applications*. Bd. 33. American Mathematical Soc., 2019

[PA03] Phillips, Allyn W. ; Allemang, Randall J.: An overview of MIMO-FRF excitation/averaging/processing techniques. In: *Journal of Sound and Vibration* 262 (2003), Nr. 3, 651 - 675. http://dx.doi.org/https://doi.org/10.1016/S0022-460X(03)00116-0. – DOI https://doi.org/10.1016/S0022–460X(03)00116–0. – ISSN 0022–460X. – 2001 India-USA Symposium on Emerging Trends in Vibration and Noise Engineering

[Pap62] Papoulis, Athanasios: The Fourier integral and its applications. In: *Polytechnic Institute of Brooklyn, McCraw-Hill Book Company Inc., USA, ISBN: 67-048447-3* (1962)

[Par61] Park, J. H.: Moments of the generalized rayleigh distribution. In: *Quarterly of Applied Mathematics* 19 (1961), Nr. 1, 45–49. http://www.jstor.org/stable/43634840. – ISSN 0033569X, 15524485

[Pou18] Poularikas, Alexander D.: *Transforms and applications handbook*. CRC press, 2018

[PP18] Park, Kun I. ; Park: *Fundamentals of Probability and Stochastic Processes with Applications to Communications*. Springer, 2018

[PS01] Pintelon, R. ; Schoukens, J.: Measurement of frequency response functions using periodic excitations, corrupted by correlated input/output errors. In: *IEEE Transactions on Instrumentation and Measurement* 50 (2001), Nr. 6, S. 1753–1760. http://dx.doi.org/10.1109/19.982976. – DOI 10.1109/19.982976

[PS12] Pintelon, Rik ; Schoukens, Johan: *System identification: a frequency domain approach*. John Wiley & Sons, 2012

[Rao08] Rao, Ramakrishna P.: *Signals and Systems*. Tata McGraw Hill, 2008

[Ric44] Rice, S. O.: Mathematical analysis of random noise. In: *The Bell System Technical Journal* 23 (1944), Nr. 3, S. 282–332. http://dx.doi.org/10.1002/j.1538-7305.1944.tb00874.x. – DOI 10.1002/j.1538–7305.1944.tb00874.x

[RT06] Remple, Robert K. ; Tischler, Mark B.: *Aircraft and rotorcraft system identification: engineering methods with flight-test examples*. American Institute of Aeronautics and Astronautics, 2006

[SAE07] SAE International: *Aerospace - Flight Control Systems - Design, Installation and Test of Piloted Military Aircraft, General Specification for,. SAE Aerospace Standard 94900 (SAE AS94900)*. 2007

[SAE12] SAE International: *Aerospace - Vehicle Management Systems - Flight Control Design, Installation and Test of, Military Unmanned Aircraft, Specification Guide For., SAE Aerospace recommended Practices 94910 (SAE ARP 94910)*. 2012

[SB93] Schrama, Ruud J. P. ; Bosgra, Okko H.: Adaptive performance enhancement by iterative identification and control design. In: *International Journal of Adaptive Control and Signal Processing* 7 (1993), Nr. 5, 475-487. http://dx.doi.org/https://doi.org/10.1002/acs.4480070513. – DOI https://doi.org/10.1002/acs.4480070513

[Sch92] Schrama, Rudolphus Johannes P.: *Approximate identification and control design*, Delft University of Technology, Faculty of Mechanical Engineering and Marine, Dissertation, 1992

[Sch18a] Schatz, Simon: *Development and Flight-Testing of a Trajectory Controller Employing Full Nonlinear Kinematics*. München, Technische Universität München, Dissertation, 2018

[Sch18b] Schneider, Volker: *Trajectory Generation for Integrated Flight Guidance*. München, Technische Universität München, Dissertation, 2018

[SGGH18] Schatz, Simon P. ; Gabrys, Agnes C. ; Gierszewski, Daniel M. ; Holzapfel, Florian: Inner Loop Command Interface in a Modular Flight Control Architecture for Trajectory Flights of General Aviation Aircraft. In: *2018 5th International Conference on Control, Decision and Information Technologies (CoDIT)*, 2018, S. 86–91

[SGS18] Schoukens, J. ; Godfrey, K. ; Schoukens, M.: Nonparametric Data-Driven Modeling of Linear Systems: Estimating the Frequency Response and Impulse Response Function. In: *IEEE Control Systems Magazine* 38 (2018), Nr. 4, S. 49–88. http://dx.doi.org/10.1109/MCS.2018.2830080. – DOI 10.1109/MCS.2018.2830080

[sH84] Åström, K.J. ; Hägglund, T.: Automatic Tuning of Simple Regulators. In: *IFAC Proceedings Volumes* 17 (1984), Nr. 2, 1867 - 1872. http://dx.doi.org/https://doi.org/10.1016/S1474-6670(17)61248-5. – DOI https://doi.org/10.1016/S1474–6670(17)61248–5. – ISSN 1474–6670. – 9th IFAC World Congress: A Bridge Between Control Science and Technology, Budapest, Hungary, 2-6 July 1984

[Sim07] Simon, M.K.: *Probability Distributions Involving Gaussian Random Variables: A Handbook for Engineers and Scientists*. Springer US, 2007 (Springer International Series in Engineering and Computer Sc). https://books.google.de/books?id=zjJdP0CJUAYC. – ISBN 9780387476940

[SKFL03] Selier, Michiel ; Korte, Udo ; Fielding, Chris ; Luckner, Robert: New analysis techniques for clearance of flight control laws. In: *AIAA Guidance, Navigation, and Control Conference and Exhibit*, 2003, S. 5476

[SM+05] Stoica, Petre ; Moses, Randolph L. u. a.: *Spectral analysis of signals*. Pearson Prentice Hall Upper Saddle River, NJ, 2005

[SP07] Skogestad, Sigurd ; Postlethwaite, Ian: *Multivariable feedback control: analysis and design*. Bd. 2. Wiley New York, 2007

[SPB18] Selvi, D. ; Piga, D. ; Bemporad, A.: Towards direct data-driven model-free design of optimal controllers. In: *2018 European Control Conference (ECC)*, 2018, S. 2836–2841

[SPG94] Schoukens, J. ; Pintelon, R. ; Guillaume, P.: On the Advantages of Periodic Excitation in System Identification. In: *IFAC Proceedings Volumes* 27 (1994), Nr. 8, 1115 - 1120. http://dx.doi.org/https://doi.org/10.1016/S1474-6670(17)47857-8. – DOI https://doi.org/10.1016/S1474–6670(17)47857–8. – ISSN 1474–6670. – IFAC Symposium on System Identification (SYSID'94), Copenhagen, Denmark, 4-6 July

[SPRD01] Schoukens, J. ; Pintelon, R. ; Rolain, Y. ; Dobrowiecki, T.: Frequency response function measurements in the presence of nonlinear distortions. In: *Automatica* 37 (2001), Nr. 6, 939-946. http://dx.doi.org/https://doi.org/10.1016/S0005-1098(01)00037-1. – DOI https://doi.org/10.1016/S0005–1098(01)00037–1. – ISSN 0005–1098

[SPS+16a] Schneider, Volker ; Piprek, Patrick ; Schatz, Simon P. ; Baier, Thäddaus ; Dörhöfer, Christoph ; Hochstrasser, Markus ; Gabrys, Agnes ; Karlsson, Erik ; Krause, Christoph ; Lauffs, Patrick J. u. a.: Online trajectory generation using clothoid segments. In: *2016 14th International Conference on Control, Automation, Robotics and Vision (ICARCV)* IEEE, 2016, S. 1–6

[SPS+16b] Schneider, Volker ; Piprek, Patrick ; Schatz, Simon P. ; Baier, Thäddaus ; Dörhöfer, Christoph ; Hochstrasser, Markus ; Gabrys, Agnes ; Karlsson, Erik ; Krause, Christoph ; Lauffs, Patrick J. ; Mumm, Nils C. ; Nürnberger, Kajetan ; Peter, Lars ; Spiegel, Phillip ; Steinert, Lukas ; Zollitsch, Alexander ; Holzapfel, Florian: Online trajectory generation using clothoid segments. In: *2016 14th International Conference on Control, Automation, Robotics and Vision (ICARCV)*, 2016, S. 1–6

[SS10] Schreier, Peter J. ; Scharf, Louis L.: *Statistical Signal Processing of Complex-Valued Data: The Theory of Improper and Noncircular Signals*. Cambridge University Press, 2010. http://dx.doi.org/10.1017/CBO9780511815911. http://dx.doi.org/10.1017/CBO9780511815911

[SSG+] Steinert, Agnes C. ; Speckmaier, Moritz ; Gierszewski, Daniel ; Steffensen, Rasmus ; Holzapfel, Florian: Experimental Results of Flight Test Based Gain Retuning. In: *Manuscript for AIAA Scitech 2022 Forum*

[SSH] Steinert, A. ; Steffensen, R. ; Holzapfel, F.: *Bias of Anticipated Non-Parametric Closed-loop Frequency Response for Controller Gain Re-Tuning*. Manuscript

[SSK+16] Schatz, Simon P. ; Schneider, Volker ; Karlsson, Erik ; Holzapfel, Florian ; Baier, Thaddäus ; Dörhöfer, Christoph ; Hochstrasser, Markus ; Gabrys, Agnes ; Krause, Christoph ; Lauffs, Patrick J. ; Mumm, Nils C. ; Nürnberger, Kajetan ; Peter, Lars ; Spiegel, Philip ; Steinert, Lukas ; Zollitsch, Alexander W.: Flightplan flight tests of an experimental DA42 general aviation aircraft. In: *2016 14th International Conference on Control, Automation, Robotics and Vision (ICARCV)*, 2016, S. 1–6

[Sta02] Stark, Henry: *Probability and random processes with applications to signal processing / Henry Stark, John W. Woods.* 3rd ed. Upper Saddle River, N.J : Prentice Hall, 2002. – ISBN 0130200719

[SVBP09] Schoukens, Johan ; Vandersteen, G. ; Barbé, Kurt ; Pintelon, Rik: Nonparametric Preprocessing in System Identification: a Powerful Tool. In: *EUROPEAN JOURNAL OF CONTROL* 15 (2009), 12, S. 260–274. http://dx.doi.org/10.3166/EJC.15.260-274. – DOI 10.3166/EJC.15.260–274

[TLW96] Tan, K. K. ; Lee, T. H. ; Wang, Q. G.: Enhanced automatic tuning procedure for process control of PI/PID controllers. In: *AIChE Journal* 42 (1996), Nr. 9, 2555-2562. http://dx.doi.org/https://doi.org/10.1002/aic.690420916. – DOI https://doi.org/10.1002/aic.690420916

[TZ95] Tranter, William H. ; Ziemer, Rodger E.: *Principles of communications: systems, modulation, and noise.* Wiley, 1995

[US 80] US Department of Defense: *Flying Qualities of Piloted Airplaneys. Military Specification MIL-F-8785C.* 1980

[US 97] US Department of Defense: *Flying Qualities of Piloted Aircraft. Military Handbook MIL-HDBK-1797.* 1997

[Vid11] Vidyasagar, Mathukumalli: Control system synthesis: a factorization approach, part ii. In: *Synthesis lectures on control and mechatronics* 2 (2011), Nr. 1, S. 1–227

[Vin93] Vinnicombe, G.: Frequency domain uncertainty and the graph topology. In: *IEEE Transactions on Automatic Control* 38 (1993), Nr. 9, S. 1371–1383

[VS95] Van Den Hof, Paul M. ; Schrama, Ruud J.: Identification and control — Closed-loop issues. In: *Automatica* 31 (1995), Nr. 12, 1751 - 1770. http://dx.doi.org/https://doi.org/10.1016/0005-1098(95)00094-X. – DOI https://doi.org/10.1016/0005–1098(95)00094–X. – ISSN 0005–1098. – Trends in System Identification

[WG02] Welsh, J. S. ; Goodwin, G. C.: Finite sample properties of indirect non-parametric closed-loop identification. In: *IEEE Transactions on Automatic Control* 47 (2002), Nr. 8, S. 1277–1292. http://dx.doi.org/10.1109/TAC.2002.800768. – DOI 10.1109/TAC.2002.800768

[WG04] Welsh, J. S. ; Goodwin, G. C.: An alternative regularisation technique in closed loop non-parametric frequency domain system identification. In: *2004 5th Asian Control Conference (IEEE Cat. No.04EX904)* Bd. 3, 2004, S. 1651–1657 Vol.3

[Yak19] Yakovleva, Tatiana: Nonlinear Properties of the Rice Statistical Distribution: Theory and Applications in Stochastic Data Analysis. In: *Journal of Applied Mathematics and Physics* 07 (2019), 01, S. 2767–2779. http://dx.doi.org/10.4236/jamp.2019.711190. – DOI 10.4236/jamp.2019.711190

[ZBG91] Zhuquan Zang ; Bitmead, R. R. ; Gevers, M.: H/sub 2/ iterative model refinement and control robustness enhancement. In: *[1991] Proceedings of the 30th IEEE Conference on Decision and Control*, 1991, S. 279–284 vol.1

[ZD98] Zhou, Kemin ; Doyle, John C.: *Essentials of robust control*. Bd. 104. Prentice hall Upper Saddle River, NJ, 1998

[ZIPL20] Zangarini, Angelo ; Invernizzi, Davide ; Panizza, P. ; Lovera, Marco: Closed-loop MIMO data-driven attitude control design for a multirotor UAV. In: *CEAS Aeronautical Journal* 11 (2020), 06. http://dx.doi.org/10.1007/s13272-020-00456-9. – DOI 10.1007/s13272–020–00456–9

[ZMW+17] Zollitsch, Alexander W. ; Mumm, Nils C. ; Wulf, Simona ; Holzapfel, Florian ; Hochstrasser, Markus ; Lauffs, Patrick J. ; Peter, Lars: Automatic takeoff of a general aviation research aircraft. In: *2017 11th Asian Control Conference (ASCC)* IEEE, 2017, S. 1683–1688

[ZSMH18] Zollitsch, Alexander W. ; Schatz, Simon P. ; Mumm, Nils C. ; Holzapfel, Florian: Model-in-the-loop simulation of experimental flight control software. In: *2018 AIAA Modeling and Simulation Technologies Conference*, 2018, S. 0425